2020

Pressure tuning of correlated electron systems

Li Xiang
Iowa State University

Pressure tuning of correlated electron systems

by

Li Xiang

A dissertation submitted to the graduate faculty

in partial fulfillment of the requirements for the degree of

DOCTOR OF PHILOSOPHY

Major: Condensed Matter Physics

Program of Study Committee:
Paul C. Canfield, Co-major Professor
Sergey L. Bud'ko, Co-major Professor
Adam Kaminski
Peter Orth
Gordon Miller
John Lajoie

The student author, whose presentation of the scholarship herein was approved by the program of study committee, is solely responsible for the content of this dissertation. The Graduate College will ensure this dissertation is globally accessible and will not permit alterations after a degree is conferred.

Iowa State University

Ames, Iowa

2020

DEDICATION

I would like to dedicate this thesis to my parents, my beloved wife Jinjing Luo and boy Eason Xiang.

TABLE OF CONTENTS

Page

LIST OF FIGURES

Page

ACKNOWLEDGEMENTS

Looking back to the more than 6 years of life at Ames, besides my graduate research at Iowa State University, big steps are also achieved with my life, getting married to my beloved wife and have a beatiful son. I feel very lucky that I have shared part of my life journey with friends, families and especially the Canfield's Army in Ames. I am so grateful for the support and company. Approaching graduation, I would like to take this opportunity to express my thanks to those who helped me with various aspects of conducting research, writing of this thesis as well as my life during my journey in Ames.

First of all, I would like to express my sincere and greatest thanks to to my advisors, Dr. Paul C. Canfield and Dr. Sergey L. Bud'ko (with the "L." still being a mystery to me) for their extreme patience, guidance and support throughout my Ph.D. research. Their care also helped me through some struggling times. When I first met Dr. Canfield as a first year graduate student, I was immediately attracted by his passion and his way of making research understandable to beginners or outsiders. During my research in his group, he has kept inspired me with the passion in science as well as broad and deep knowledge. I would like to thank Dr. Bud'ko for his enormous guidance and support with various research instruments, especially the pressure devices. The discussions with him are always insightful and his skepticism has pushed me further in understanding the physics.

I would like to thank all my committee members, Dr. Adam Kaminski, Dr. Peter Orth, Dr. Gordon Miller, Dr. John Lajoie as well as my previous committee member Dr. Sanjeevi Sivasankar for their guidance and comments during my Ph.D.

I am greatly thankful to Dr. Udhara Kaluarachchi (the "Great Dark Master" or "GDM") for teaching me the high-pressure techniques and also the good friendship. He is a true master on handling (making contacts) tiny samples. His eyebrows are also the best eyebrows (soft and thin) for making eyebrow-tool. I would like to thank all my colleagues in the Canfield's Army and

researchers I have collaborated with for their research support as well as friendship: Dr. Nahyun Jo (the nicest and most "naive" person I have met, often happens to be the happy source), Dr. Tai Kong (who is a reliable big brother), Dr. William Meier (full of energy and enthusiasm, who also provided the great shooting experience), Mingyu Xu (the meat master who started the KFC chicken tradition), Dr. Xiaojuan Xi (amazing cook), Dr. Elena Gati (smart Elena full of sarcasm), Brinda Kuthanazhi, Atreyee Das, Dr. Raquel A. Ribeiro, Dr. Paula Herrera-Siklody, Buck the Deer, Dr. Anna Böhmer (who guided me in conducting and writing my first first-author paper), Scott Saunders (my torch work teacher), Dr. Tej Lamichhane, Dr. Valentin Taufour, Dr. Soham Manni, Dr. Gil Drachuck, Dr. Andreas Kreyssig, John Wilde, Dr. Gang Wang, Dr. Dominic Ryan (great flying experience), Dr. Andriy Palasyuk, Dr. Guilherme Gorgen, Juan Schmidt, Dr. Nestor Haberkorn, Caiden Abel, Morgan Masters, Connor Schmidt, Kathryn Neilson, Savannah Downing, Michael Onyszczak, Victor Barrena, Saba Sharikadze, Dr. Makariy Tanatar, Dr. Ruslan Prozorov, Dr. Vladimir Kogan, Dr. Yuji Furukawa, Khusboo Rana, Dr. Priscila Rosa, Dr. Mario Piva.

I would like to thank Dr. Viktor Struzhkin and Dr. Jianjun Ying from Geophysical Laboratory in Washington DC for their guidance in using the miniature Diamond Anvil Cell.

I would like to thank my friends in Ames, who have accompanied me and brought me joy.

Mostly importantly, I would like to thank my parents, brother for their support, my beloved wife Jinjing Luo for her encouragement and company, my son Eason Xiang who has brought and continue bringing enormous happiness to my family.

The work included in this thesis is supported by Ames Laboratory, US DOE, under Contract No. DE-AC02-07CH11358. In addition, I have received support from the W. M. Keck Foundation for publications Xiang et al. (2017, 2018a); Lamichhane et al. (2018); Kaluarachchi et al. (2018); Gati et al. (2018); Xiang et al. (2018b); Gati et al. (2019a,b); Xiang et al. (2019b); Bud'ko et al. (2020); Saunders et al. (2020) and the Gordon and Betty Moore Foundations EPiQS Initiative (Grant No. GBMF4411) for publications Gati et al. (2019b); Xiang et al. (2019b); Bud'ko et al. (2020); Gati et al. (2020b); Rana et al. (2020).

ABSTRACT

The research described in this thesis is focused on utilizing physical pressure as a tuning parameter to modify and study various phase transitions and their associated ground states, including superconductivity, spin/charge density waves, structural transitions etc. Pressure provides a strong and unique way to tune these ground states as well as investigate the interplay between them. The thesis contains 9 chapters and 4 appendices outlined as follows.

Chapter 1 introduces the concept of physical pressure as well as some theoretical background to ideas that are encountered in this thesis.

Chapter 2 provides a detailed explanation and description of the measurement techniques used in this work. This includes resistivity measurements as well as various pressure cells that are used to perform electrical transport measurements under pressure.

Chapters 3-8 are research papers that have been published (Chaps. 3-6, Chap. 8) or are being drafted (Chap. 7). Chapters 3-7 are devoted to pressure tuning of a varity of correlated electron systems, which is the main topic of the thesis. In Chaps. 3, 4 and 5, studies of Fe-based superconductors including $FeSe_{1-x}S_x$, $CaK(Fe_{1-x}Ni_xAs)_4$ and $EuRbFe_4As_4$ are presented. In Fe-based superconductors, different ground states related to electronic, magnetic, and structural degrees of freedom emerge in close proximity. Pressure tunability of these ground states provides great opportunity to investigate the interplay between them.

Chapter 6 presents the effects of pressure on a Kondo heavy fermion system, $CeBi_2$. It is demonstrated that the antiferromagnetic transition T_N of $CeBi_2$ is moderately modified, whereas the pressure induced superconductivity is suggested to be extrinsic and due to Bi flux in the specimen.

Chapter 7 focuses on the effect of pressure on a newly discovered metallic ferromagnetic material, $La_5Co_2Ge_3$. It is demonstrated that the ferromagnetic quantum critical point is avoided by the emergence of a new phase under pressure. The analysis and interpretation of the data is on-going.

Chapter 8 focuses on an important technical aspect of measuring pressure as a function of temperature in piston-cylinder pressure cells and the characterization of the pressure coefficient for manganin as well as the temperature evolution of pressure in a piston-cylinder cell. This work provides two main findings that are important for the pressure community in general. First, it is demonstrated that the temperature and pressure dependence of the pressure coefficient for manganin has to be taken into account for an accurate determination of pressure values at any given tempearture. Second, a detailed analysis of the temperature dependent pressure in a piston-cylinder cell is done to estimate the pressure value at any given temperature. Measurement results and analysis of other manometers such as InSb and Zeranin are further discussed in this work.

Chapter 9 summarizes the thesis as well as suggests some possible further research aspects that could address open questions or improve understandings of the work presented.

Appendix A describes the detailed process of assembling a piston-cylinder cell which enables electrical transport measurements of specimen under hydrostatic pressure up to $\sim$ 2.5 GPa.

Appendix B describes the detailed process of assembling a modifield Bridgman Anvil Cell which enables electrical transport measurements of specimen under hydrostatic pressure up to $\sim$ 6 -7 GPa.

Appendix C describes the detailed process of assembling a miniature Diamond Anvil Cell which enables electrical transport measurements of specimen under pressure up to $\sim$ 20 - 30 GPa.

Appendix D briefly summarizes other projects that I led or was involved in and provides a full publication list during my Ph.D.

CHAPTER 1. GENERAL INTRODUCTION

It is of general interest to modify materials' properties by external tuning parameters as it provides the opportunity to (i) study how their properties respond to perturbation or (ii) induce new ground states. Some of the common tuning parameters are temperature, magnetic field, chemical substitution and pressure. Each of the tuning parameter has its own characteristics in terms of perturbation. For instance, decreasing temperature suppresses thermal fluctuations, and when other interaction energy becomes dominating, materials can enter into an ordered state. Magnetic field breaks time reversal symmetry and directly interacts with magnetic moments thus modifying the magnetic properties. Chemical substitution, in the case of non-isovalent substitution, affects the band filling and thereby modifies the density of states at the Fermi level. In the case of isovalent substition, it can change the lattice parameters. Note that in both cases, substitution induces degrees of disorder into the system. Pressure, to first order, changes lattice parameters of the system, which in turn affects the electronic band structure as well as density of states at the Fermi level. These changes with pressure can furthermore influence the microscopic interactions (electron-phonon, electron-electron interactions) and thus suppress the formation of a ground state or the stabilization of a new one. In many cases, pressure and chemical substitution, especially isovalent substitution as it does not introduce electron or hole doping, are considered to be similar tuning parameters and in many systems as they modify systems' properties very similarly. However, the biggest advantage of pressure is that pressure does not introduce extra disorder into the system as substitution does. Therefore pressure is often referred as a "clean" tuning parameter in comparison to chemical substitution.

To put materials under pressure, the specimen is typically placed into a pressure cell and surrounded by a pressure-transmitting medium (gas, liquid or solid). When a force is applied to the medium via e.g. a piston or an anvil, high pressure is generated and transmitted to the

sample. Despite the simplicity of pressure application mechanism, high pressure study has historically not been widely done due to technical difficulties of measuring physical properties under high pressure. The area of high-pressure physics started to expand at the beginning of 20th century as P. W. Bridgman developed a new apparatus called Bridgman anvil cell which enables physical property measurements under high pressure Bridgman (1941). This new technique enhanced the maximum achieved pressure by orders of magnitude (from $\sim$ 0.3 GPa to $\sim$ 10 GPa) at that time. P. W. Bridgman was awarded the Nobel Prize in 1946 "for the invention of an apparatus to produce extremely high pressures, and for the discoveries he made therewith in the field of high pressure physics". Nowadays the maximum laboratory-achieved static pressure is as large as $\sim$700 GPa Dubrovinsky et al. (2015) and high-pressure science becomes a well defined sub-field of physical science. Among them, recently discovered high-temperature superconductivity in hydrides under high pressure is intensively discussed and still holds the record for the highest superconducting transition temperature (at $\sim$250 K for LaH_{10} under $\sim$170 GPa)Haug et al. (2019); Kostrzewa et al. (2020); Drozdov et al. (2019). Pressure has been combined with various other tuning parameters as well as measurement techniques to probe properties of materials, such as transport (resistivity, thermopower), scattering (X-ray scattering, neutron scattering, Raman scattering), thermodynamic (magnetic susceptibility, specific heat), Nuclear Magnetic Resonance (NMR), Muon Spin Resnance (μSR), etc. Eremets (1996). It should be noted that in parallel with these advances, high pressure synthesis (at temperatures of several thousands of centigrade degrees) has been used to grow compounds ranging from diamond to LaFeAsO, MgB_2, and other novel materials, often by using pressure to shift or tune composition-temperature phase diagrams or allow for the creation and preservation of metastable states Friedrich (2016); Liu (2017).

In this thesis, I use high-pressure measurement techniques, focused on electrical transport, to study several classes of materials and to modify and better understand their properties. In the following, I will first review the basic physical concepts that are encountered in this thesis.

1.1 Superconductivity

1.1.1 Phenomenon of superconductivity

The phenomena of superconductivity was first discovered in Mercury by H. K. Onnes in 1911 when he observed a sudden drop of resistance to below $10^{-5}\Omega$ (an experimental value indistinguishable from zero, Fig. 1.1 (a)) at 4.2 K Onnes (1911). This zero resistive behavior manifests one of the characteristics of superconductivity. What distinguishes superconductors from a hypothetical perfect conductor is another characteristic feature, which is the complete expulsion of an applied magnetic field, also know as Meissner-Ochsenfeld effect (Fig. 1.1 (b)) Meissner and Ochsenfeld (1933). This effect describes the observation that when cooling down a superconductor through its critical temperature in an applied, external magnetic field, the superconductor expels the magnetic field when entering the superconducting state. Whereas, a hypothetical perfect conductor in the same situation would preserve the magnetic field inside.

Extensive theoretic efforts were made to understand superconductivity since its discovery. Among them, London theory, proposed in 1935, provides a first satisfactory classical phenomenological description of superconductivity London et al. (1935). However, since superconductivity is a quantum phonomenon, the London theory only provided a good qualitative agreement with the experimental observations rather than a quantitative one. Ginzburg-Landau theory was introduced in 1950 as a macroscopic theory to describe superconductivity Ginzburg and Landau (1950). Ginzburg-Landau theory combines Landau's second-order phase transition theory and quantum mechanics by introducing a complex order parameter, $\phi(r)$, which describes the wave function of superconducting electrons. Without knowing the microscopic mechanism, Ginzburg-Landau theory successfully describes many behaviors of superconductors. The successful microscopic description of superconductivity comes with **BCS** theory by **B**ardeen, **C**ooper and **S**chrieffer in 1957 Cooper (1956); Bardeen et al. (1957a,b). In BCS theory, electrons near the Fermi surface with opposite momentum $\vec{k}$ and spin $\vec{\sigma}$ form a bound state (Cooper pairs Cooper (1956)) via an electron-phonon attractive interaction. This pairing increases the kinetic

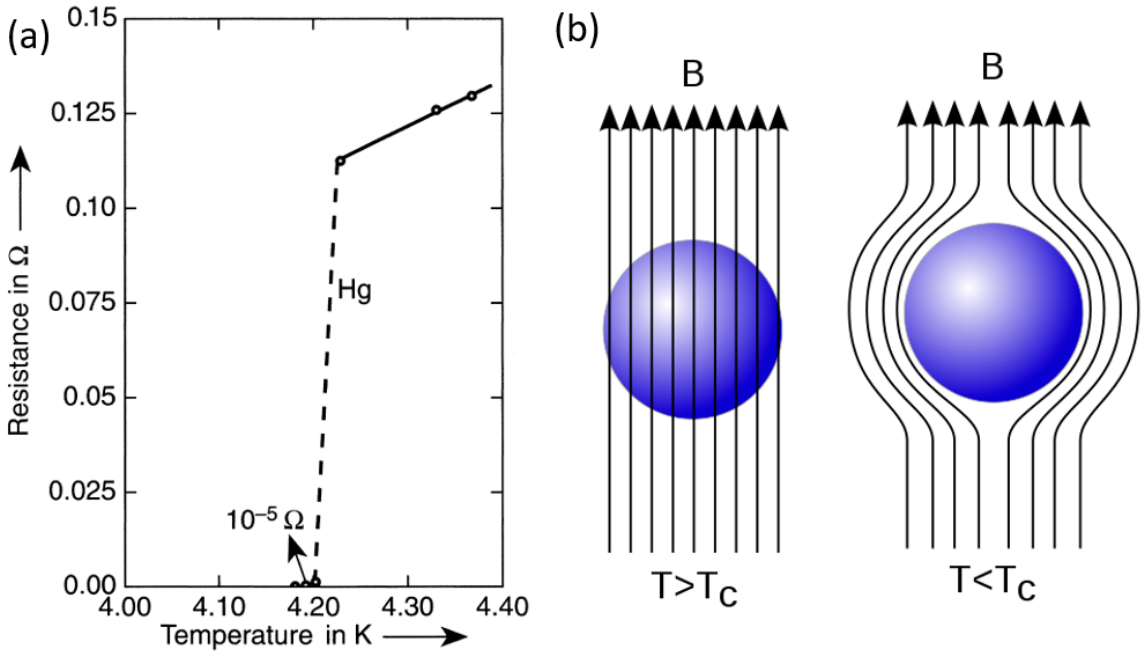

Figure 1.1 (a) Low temperature resistance of Mercury showing superconductivity Onnes (1911). (b) Schematic diagram of Meissner-Ochsenfeld effect showing that the external magnetic field is expelled when a superconductor is cooled through its transition temperature T_c. Figure is adapted from wikipedia "Meissner effect".

energy and lowers the potential energy. If the decrease of the potential energy is larger than the increase of the kinetic energy, then the total energy of the two electrons is smaller than $2E_F$ and a new ground state (superconductivity) can be formed. To break the cooper pair, a minimum amount of energy 2Δ is required, which is called the superconducting energy gap. The energy gap at the superconducting transition temperature is zero. At zero temperature it is given by,

$$\Delta(0) = \frac{\hbar\omega_D}{\sinh(\frac{1}{N(E_F)V_{eff}})} \tag{1.1}$$

where $\hbar$, ω_D, $N(E_F)$ and V_{eff} are the Plank's constant, the Debye frequency, the density of states at Fermi energy and the the effective electron-phonon interaction potential. In the weak coupling limit, $N(E_F)V_{eff} \ll 1$, the energy gap and the superconducting transition temperature are given

by,

$$\Delta(0) = 2\hbar\omega_{\mathrm{D}} e^{\frac{-1}{N(E_{\mathrm{F}})V_{\mathrm{eff}}}} \tag{1.2}$$

$$T_{\mathrm{c}} = \frac{1.13\hbar\omega_{\mathrm{D}}}{k_{\mathrm{B}}} e^{\frac{-1}{N(E_{\mathrm{F}})V_{\mathrm{eff}}}} \tag{1.3}$$

where k_{B} is the Boltzman's constant.

BCS theory deals with a weak electron-phonon coupling and interaction energy, V_{eff}, is assumed to be constant across the Fermi surface. To addresses the case for a strong phonon-mediated pairing interaction, the Eliashberg theory extended the BCS theory by introducing a variant electron-phonon coupling parameter λ ($\lambda = N(E_{\mathrm{F}})V_{\mathrm{eff}}$ in BCS theory) Eliashberg (1960),

$$\lambda = 2\int_0^\infty \frac{\alpha^2(\omega)F(\omega)}{\omega} d\omega \tag{1.4}$$

where $\alpha^2(\omega)$ is the strength of the electron-phonon interaction and $F(\omega)$ is the phonon density of states. $\alpha^2(\omega)F(\omega)$ is defined as the electron-phonon spectral function (Eliashberg function). In the Eliashberg theory, information about the band structure and the phonon spectrum is included. Later work by McMillan and Dynes expanded the Eliashberg theory again by taking electron-electron Coulomb interaction into account McMillan (1968); Dynes (1972). A phenomenological Coulomb pseudopotential μ^* is introduced and the superconducting transition temperature is expressed as,

$$T_{\mathrm{c}} = \frac{\hbar\omega_0}{1.20k_{\mathrm{B}}} \exp[-\frac{1.04(1+\lambda)}{\lambda - \mu^*(1+0.62\lambda)}] \tag{1.5}$$

There are two characteristic lengths associated with superconductivity. One is the coherence length, ξ, beyond which the order parameter $\phi(r)$ varies significantly in real spaceGinzburg and Landau (1950) (Also effective size of Cooper pair in BCS theory Bardeen et al. (1957a)). The other one is the penetration depth (previously introduced in London theory), λ, over which the magnetic field penetrates the surface of a superconductor London and London (1935). The ratio of these two characteristic lengths (also known as Ginzburg-Landau parameter), defined as $\kappa = \frac{\lambda}{\xi}$, determines whether superconductors fall into one category or the other:

$$\text{Type-I} : \kappa < \frac{1}{\sqrt{2}} \tag{1.6}$$

$$\text{Type-II} : \kappa > \frac{1}{\sqrt{2}} \tag{1.7}$$

For a type-I superconductor, a small external magnetic field is completely expelled in its superconducting state (Meissner state). When the external field exceeds certain critical field, H_c, the magnetic field penetrates through the material and superconductivity is destroyed. For a type-II superconductor, above a certain critical field, H_{c1}, magnetic field partially penetrates through the material in the form of magnetic vortices. For each of the vortex, it carries a quantized magnetic flux, $\Phi_0 = \frac{h}{2e}$. Thus superconductivity in this region is no longer continuous across the materials and this state is known as a "mixed state" (Shubnikov/vortex state). Above a higher critical field (upper critical field), H_{c2}, superconductivity is completely destroyed and material enters its normal state. The categorization of type-I and type-II superconductors can be understood in the energetic point of view. Assume there is a boundary layer between the the superconducting area and the normal state area in the external field H. At the boundary layer, we compare energy from two contributions, namely the energy, E_B, associated with the expulsion of the external magnetic field, and the energy, E_C, from electrons forming Cooper pairs. One one hand, the penetration depth of the magnetic field is characterized by λ, the decrease of the expulsion energy $\Delta E_B \propto \lambda$. On the other hand, the length over which the number of Cooper pairs can vary significantly is characterized by ξ, the reduction of the condensation energy due to the boundary $\Delta E_C \propto -\xi$. As a result, the sign of the interface energy, $\sigma_{ns} \propto \Delta E_B + \Delta E_C$, is determined by the relative sizes of λ and ξ, or κ. Specifically, it was demonstrated that $\sigma_{ns} > 0$ (< 0) for $\kappa < \frac{1}{\sqrt{2}}$ ($> \frac{1}{\sqrt{2}}$). In the case of $\sigma_{ns} > 0$, the formation of the interface is not energetically favorable and thus only formed at the surface of the superconductor (type-I superconductor). Whereas in the case of $\sigma_{ns} < 0$, the formation of the interface becomes energetically favorable. As a result, in certain conditions ($H_{c1} < H < H_{c2}$) magnetic field penetrate through the superconductor in the form of vortices and mixed state is establised (type-II superconductor). The corresponding magnetization curves for type-I and type-II superconductors as well as schematic $H - T$ phase diagrams are shown in Fig. 1.2. In addition, an intermediate state for a

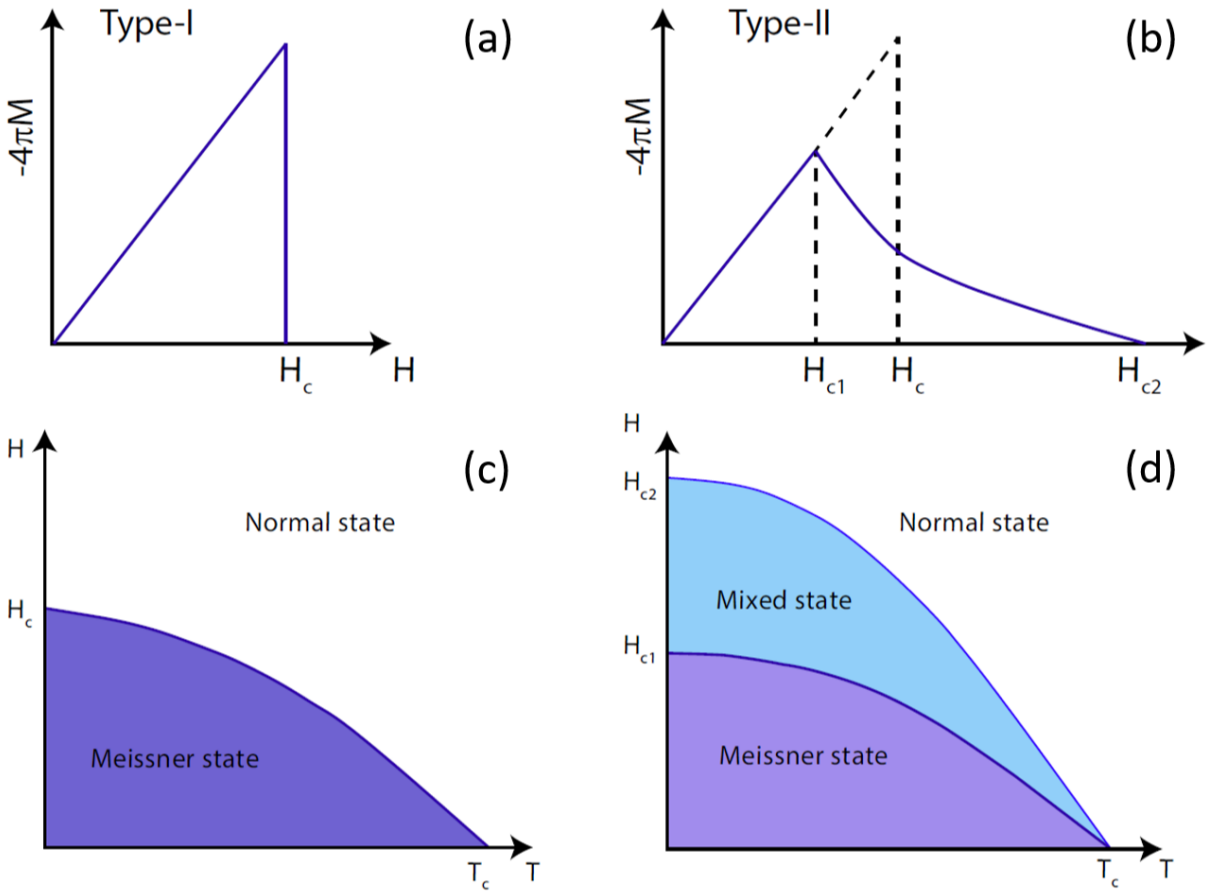

Figure 1.2 Magnetization curves for (a) type-I and (b) type-II superconductors in their superconducting state. H_C represents the thermodynamic critical field. $H-T$ phase diagrams for (c) type-I and (d) type-II superconductors.

type-I superconductor can be realized in which the superconductor splits up into superconducting and normal conducting domains. This can be understood in the simplified picture that when a superconductor is placed in a homogeneous external field, the expulsion of the magnetic field results in different effective field near the surface which dependes on the geometric shape of the superconductor (see Fig. 1.3 for the example of a sphere superconductor). Thus superconducting (normal conducting) domains can be generated in regions where the effective field is smaller (larger) than the critical field.

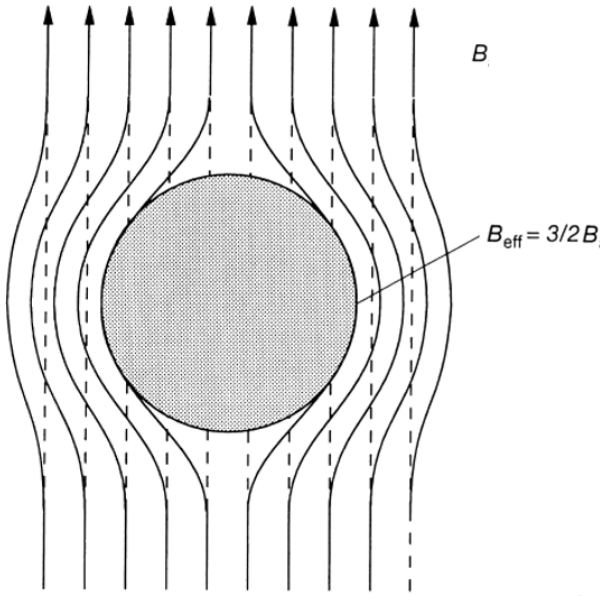

Figure 1.3 In the absence of the superconducting sphere, the field is homogenous (dashed field lines). Expulsion of magnetic field (solid field lines) from a superconducting sphere, where $B_{\text{eff}} = 3/2B$ at the equator of the surface.

The temperature dependence of the upper critical field has been approached by various theories. Generally, the low temperature limit of the upper critical field, $H_{c2}(0)$, is determined through the effects of Pauli spin pair breaking and spin-orbit coupling. With applied magnetic field, the energy of the electrons with spin 1/2 and spin -1/2 is split to $2\mu_B H$ due to Zeeman splitting. Since it requires the energy of $2\Delta = 3.53 k_B T_c$ to break the Cooper pair, assuming Zeeman interaction is the only interaction between electrons and external field, we get the Pauli limiting field as, $H_{\text{Pauli}} = 1.84 T_c(\text{Tesla})$ Clogston (1962). The theory developed by N. R. Werthamer and co-authors (WHH theory) later provides a description for the temperature-dependent upper critical field, taking in the effects of Zeeman splitting, spin-orbit interaction as well as impurity scattering Helfand and Werthamer (1964, 1966); Werthamer et al. (1966). WHH theory calculates that for an isotropic type-II superconductor,

$$\text{clean limit} : H_{c2}(0) = -0.727 T_c \frac{dH_{c2}}{dT_c}|_{T_c} \tag{1.8}$$

$$\text{dirty limit} : H_{c2}(0) = -0.693 T_c \frac{dH_{c2}}{dT_c}|_{T_c} \tag{1.9}$$

The critical magnetic field can be analyzed from a thermodynamic point of view, where a thermodynamic critical field, H_C, is referred to. In the case of a type-I superconductor, the thermodynamic field H_C is the same as the critical field (Fig. 1.2 (a)). For a type-II superconductor, the thermodynamic critical field H_C, which is defined by the thermodynamic properties of the material, is between H_{c1} and H_{c2}, i.e. $H_{c1} < H_C < H_{c2}$ (Fig. 1.2 (b)). It can be further related to these critical fields as,

$$H_{c1} = H_c \frac{\ln \kappa}{\kappa\sqrt{2}} \tag{1.10}$$

$$H_{c2} = \kappa\sqrt{2} H_c \tag{1.11}$$

On one hand, the free energy change, ΔE, during the transition can be obtained by integrating the area under the magnetization curve ($M(H)$ curves in Figs. 1.2 (a) and (b)) from zero up to the field where SC is destroyed and thus is proportional to H_c^2. On the other hand, as mentioned before, the transition from normal state to superconductivity opens up a energy gap Δ and decrease the overall energy of the system. The condensation energy density in the low temperature limit is proportional to Δ^2. Thus the thermodynamic critical field is directly related to the superconducting gap and it is shown that at zero Kelvin,

$$H_c(0) = \sqrt{2\pi N(E_F)}\Delta(0) \tag{1.12}$$

where $H_c(0)$ is the thermodynamic critical field at T=0.

1.1.2 Fe-based superconductors

BCS theory is important as the first successful microscopic theory of superconductivity for which the authors received the Nobel Prize in 1972. In later years, more classes of superconductors were discovered, the properties of which can not be explained by BCS theory or its extensions. These superconductors are often know as unconventional superconductors, such as heavy fermion superconductors, cuprate superconductors and Fe-based (pnictide) superconductors

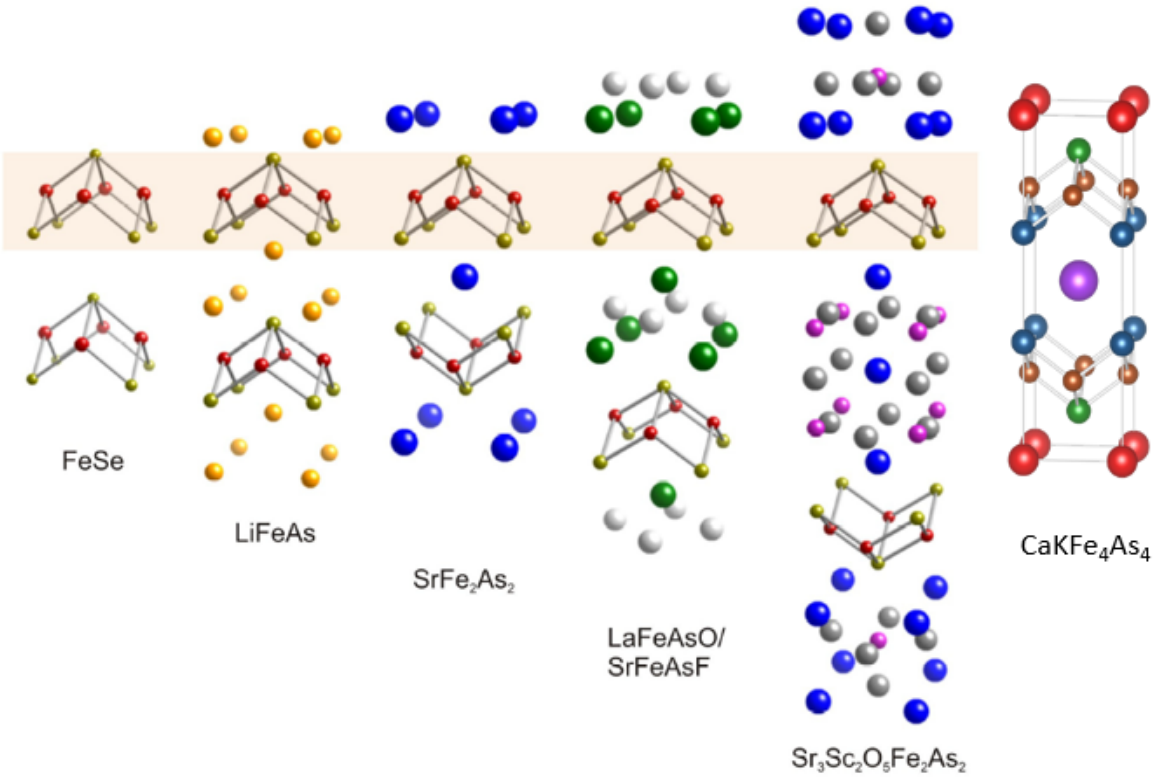

Figure 1.4 Crystallographic structures of Fe-based superconductors in representive members of the 11 (FeSe), 111 (LiFeAs), 122 ($SrFe_2As_2$), 1111 (LaFeAsO/SrFeAsF), 32522 ($Sr_3Sc_2O_5Fe_2As_2$), and 1144 ($CaKFe_4As_4$) families. Figure is adapted from Refs. Paglione and Greene (2010); Iyo et al. (2016); Meier et al. (2016)

(FeSCs) Paglione and Greene (2010); Iyo et al. (2016); Steglich et al. (1979); Walker et al. (1997); Tateiwa et al. (2000); Petrovic et al. (2001); Bednorz and Müller (1986); Maeda et al. (1988); Sheng and Hermann (1988); Schilling et al. (1993); Kamihara et al. (2008). Among them, the first FeSC was discovered in 2008 with $T_c \sim 26$ K in $LaFeAsO_{1-x}F_x$ Kamihara et al. (2008). Later on, many other FeSCs were discovered and classified according to their structure-related stoichiometry. As indicated in Fig. 1.4, FeSCs share a common layered structure based on a planar layer of iron atoms coordinated tetrahedrally by pnictogen or chalcogen atoms arranged in a stacked sequence and separated by alkali, alkaline-earth, rare-earth and oxygen/fluorine layers Paglione and Greene (2010); Iyo et al. (2016); Meier et al. (2016). In addition to the structural

similarities, the physical properties of different FeSC families also have lots in common, as ground states related to electronic, magnetic as well as structural degrees of freedom emerge in close proximity in this class of material Paglione and Greene (2010); Fernandes et al. (2014). With moderate perturbation via tuning parameters such as chemical substitution or pressure, different ground states coexist or compete with other. Figure 1.5 presents the canonical phase diagram of FeSCs determined from the most intensively investigated $BaFe_2As_2$ system, which is widely believed to capture the main physics of the FeSCsPaglione and Greene (2010); Canfield and Bud'ko (2010). As shown in the figure, the parent compound $BaFe_2As_2$ at ambient pressure undergoes a transition from a paramagnetic state to a stripe-type antiferromagnetic state upon cooling at T_N, this magnetic transition is slightly preceded but closely coupled to a structural transition at T_S from tetragonal to orthorhombic structure Canfield and Bud'ko (2010); Huang et al. (2008). The structural transition is widely believed to be driven by electronic degrees of freedom Fernandes et al. (2014) and the orthorhombic state is now often referred to as a nematic state based on an analogy to liquid crystals. In FeScs nematic order breaks the lattice rotational symmetry by making the x and y directions in the iron plane non-equivalent, in liquid crystals rotational symmetry is broken due to the alignment of the rod-shape molecules in the nematic state. Upon electron doping or applying physical pressure, the magnetic-structural transition is suppressed and a dome of superconducting region emerges in the phase diagram Canfield and Bud'ko (2010); Colombier et al. (2009). The fact the maximum of the superconducting critical temperature T_c is located in close proximity to where the magnetic-structural phase lines from the normal state extrapolate to zero Kelvin promoted ideas of a magnetically-driven mechanism of superconductivity in FeSCs. It was suggested that in the context of magnetism, Cooper pairing could arise from fluctuations emanating from a quantum critical point, or an alternative pairing mechanism may simply benefit from the suppression of a long range magnetically ordered state Paglione and Greene (2010); Mazin (2010); Chubukov (2012); Dai (2015). In addition, superconductivy and magnetic-orthorhombic order are widely believed to compete with each other in FeSCs. The idea was further supported by experimental evidence that clear suppression of both

the ordered moment size and the orthorhombic distortion upon entering into the superconducting state was observed Canfield and Bud'ko (2010); Pratt et al. (2009); Nandi et al. (2010).

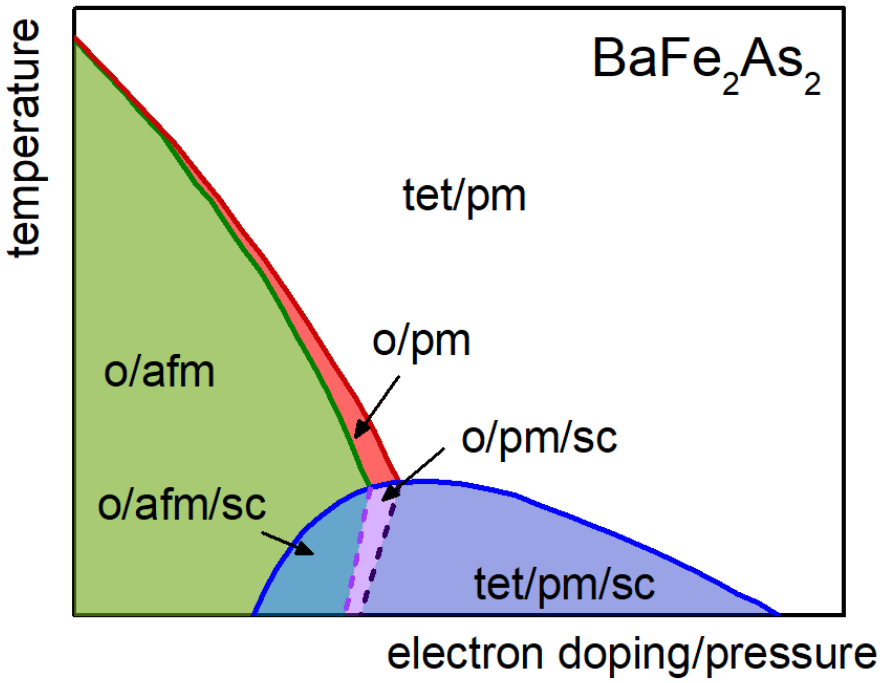

Figure 1.5 Schematic phase diagram of $BaFe_2As_2$ upon electron doping or applying physical pressure, which is considered as a generic phase diagram for Fe-based superconductors; tet (o) stands for tetragonal (orthorhombic), pm (afm) for paramagnetic (antiferromagnetic), sc for superconducting Canfield and Bud'ko (2010).

1.1.3 Superconductivity and magnetism

The interplay between magnetism and superconductivity has been a hotly discussed topic since the discovery of superconductivity. The BCS theory is successful at explaining the properties of conventional superconductors where two electrons with opposite momentum and spins form Cooper pairs via electron-phonon interaction. Early experimental studies showed that even a small amount of magnetic impurities in a superconductor strongly reduces the superconducting transition temperature T_c Matthias et al. (1958); Finnemore et al. (1965); Maple (1968). It was

proposed that the exchange interaction between the conduction electron spin and the spin of the local impurity accounts for the suppression of T_c Matthias et al. (1958); Herring (1958); Suhl and Matthias (1959), which can be intuitively understood that the magnetic impurities cause spin-flip scatterings of electrons in Cooper pairs and thus break Cooper pairs. Abrikosov and Gor'kov developed a theory (AG theory) to quantitatively account for the suppression of T_c due to this exchange scattering Abrikosov and Gor'kov (1960). In AG theory, a pair breaking parameter, α, which is proportional to the impurity concentration is introduced and written as,

$$\alpha = \frac{n_i}{\hbar}[\frac{N(E_F)}{2k_B}]I^2(g_J-1)J(J+1) \tag{1.13}$$

where n_i is the impurity concentration, I is the coupling between the spin of the impurity atoms and the spin of the conduction electrons giving rise to the superconductivity, $(g_J-1)J(J+1)$ is the de Gennes factor. Then the suppression of T_c due to magnetic impurity is written as,

$$\ln\frac{T_{c,0}}{T_c} = \varphi(\frac{1}{2}+0.14\frac{\alpha T_{c,0}}{\alpha_c T_c}) \tag{1.14}$$

where $T_{c,0}$ is the superconducting critical temperature without impurity, α_c is the critical pair breaking parameter value where T_c is suppressed to zero, φ is the digamma function. It was further demonstrated that for dilute magnetic impurity limit, T_c is linearly suppressed with impurity concentration n_i and the suppression rate is given by,

$$\frac{dT_c}{dn_i}|_{n_i\to 0} = -[\frac{\pi^2 N(E_F)}{2k_B}]I^2(g_J-1)J(J+1) \tag{1.15}$$

The AG theory has achieved good agreement with experimental results (see Fig. 1.6 for example) and became a classic theory for superconductors containing magnetic impurities Matthias et al. (1958); Herring (1958); Suhl and Matthias (1959).

On the other hand, the coexistence of superconductivity and long range magnetic ordering is found in several classes of superconductors, such as $R\mathrm{Rh_4B_4}$, $R\mathrm{Ni_2B_2C}$ (R is different rare earth elements for each specific serie), heavy fermion superconductors, Fe-based superconductors etc. Paglione and Greene (2010); Steglich et al. (1979); Canfield and Bud'ko (2010); Chubukov (2012); Canfield et al. (1998); Shrivastava and Sinha (1984); Fischer (1990); Maple (1976); Bud'ko and

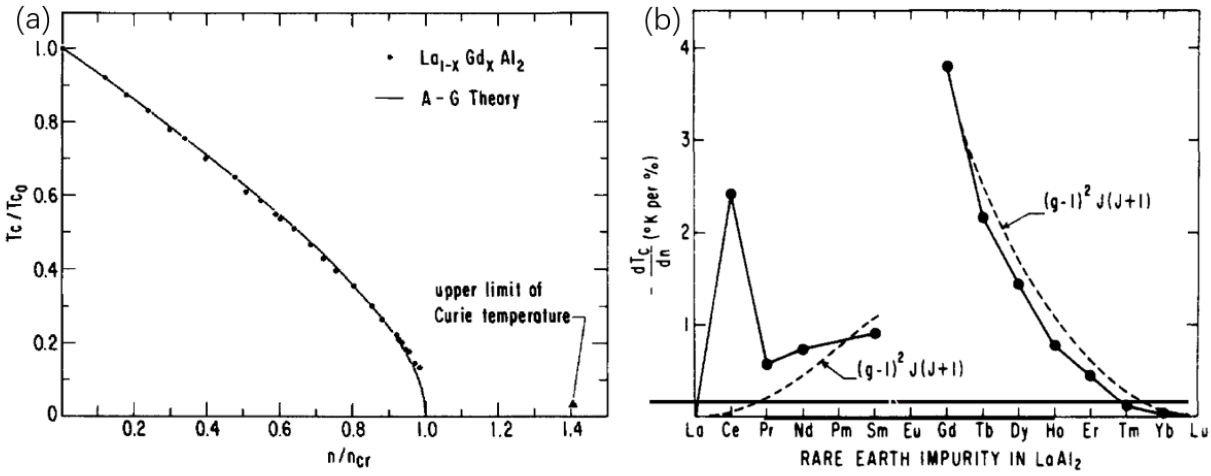

Figure 1.6 (a) Suppressed superconducting transition temperature $\frac{T_{c0}}{T_c}$ vs. Gd impurity concentration in the $La_{1-x}Gd_xAl_2$ system. Dots are experimental data from Ref. Maple (1968) and line is from the AG theory. Figure is adapted from Ref. Maple (1968). (b) Initial suppression rate of the superconducting transition temperature of $La_{1-x}R_xAl_2$ (R is rare earth elements) systems. Dots are experimental data from Ref. Maple (1970) and line is from the AG theory. Figure is adapted from Ref. Maple (1970).

Canfield (2006); Muramatsu et al. (2001); Basov and Chubukov (2011); Steglich and Wirth (2016); Johnston (2010). In the case of $R\mathrm{Rh_4B_4}$ and $R\mathrm{Ni_2B_2C}$, the magnetism originates from the local moment associated with the well isolated and localized $4f$-shell and the superconductivity comes from a separate conduction electron band, it was suggested that for these compounds the coupling was weak enough that even a compound with concentrated magnetic ions could establish superconducting ground state. They can still be understood in the frame work of AG theory as T_c of these compounds scales with the de Gennes factor to some extent (for $T_c > T_N$) Canfield and Bud'ko (2010); Canfield et al. (1998); Shrivastava and Sinha (1984); Bud'ko and Canfield (2006). In addition, the superconductivity in these compounds is believed to be conventional phonon-mediated SC Shrivastava and Sinha (1984); Cheon et al. (1999). In contrast, in many of the heavy fermion, Fe-based superconductors, the superconductivity and magnetism are believed to come from the same, shared electron subsystem and the superconductity in these compounds

are unconventional. Specifically, in the FeSCs, which is one of the main topics of this thesis, the superconductivity and magnetism are believed to strongly interact with each other. It has been established/suggested that in many of the FeSCs, the magnetism is itinerant spin-density-wave like antiferromagnetism.

Long before the discovery of FeSCs, theories have already been proposed to describe the coexistence of superconductivity and magnetism Smit and Vertogen (1973); Machida (1981); Bulaevskii et al. (1985); Ozaki and Machida (1989). Among them, the theory proposed by Machida addresses the coexistence of the spin density wave (SDW) and superconductivity (SC) Machida (1981). The model, which follows a theory developed by Bilbro and McMillan to describe the coexistence of charge density wave and superconductivity Bilbro and McMillan (1976), was developed in the anisotropic, three-dimensional single band case. In the model, two scenarios are discussed. In the case that SC would form at a temperature higher than SDW, it is demonstrated that SDW will actually be prohibited below the superconducting transition temperature and SC and SDW does not coexist. The physical reason is that the SC state opens up the energy gap Δ over the whole Fermi surface and thus prohibited the formation of SDW. In the other case that the SDW is formed at a temperature higher than the superconducting transition temperature, it is shown that SDW and SC can coexist and compete with each other. In this scenario, the Fermi surface is divided into two regions 1 and 2. Region 1 with density of states N_1 satisfies a certain nesting condition which allows for the formation of the SDW gap M, whereas SC is formed in region 2 with density of states N_2 ($N_2 = N_0 - N_1$ where N_0 is the total density of states at the Fermi surface) and gap Δ. When both orders exists, the gaps of SDW, $M(T)$, and SC, $\Delta(T)$, satisfy two self-consistency equations,

$$\ln\frac{T}{T_{s0}} = 2\pi T\sum_{\omega>0}^{\omega_s}[\frac{1}{2M}(\frac{M+\Delta}{\sqrt{\omega^2+(M+\Delta)^2}}+\frac{M-\Delta}{\sqrt{\omega^2+(M-\Delta)^2}})-\frac{1}{\omega}] \tag{1.16}$$

$$\ln\frac{T}{T_{c0}} = n_1 2\pi T\sum_{\omega>0}^{\omega_D}[\frac{1}{2\Delta}(\frac{M+\Delta}{\sqrt{\omega^2+(M+\Delta)^2}}+\frac{M-\Delta}{\sqrt{\omega^2+(M-\Delta)^2}})-\frac{1}{\omega}]+n_2 2\pi T\sum_{\omega>0}^{\omega_D}(\frac{1}{\sqrt{\omega^2+\Delta^2}}-\frac{1}{\omega}) \tag{1.17}$$

where T_{s0} (T_{c0}) is the SDW (SC) transition temperature without SC (SDW), $n_1 = \frac{N_1}{N_0}$ ($n_2 = \frac{N_2}{N_0} = 1 - n_1$) is the relative density of states of region 1 (region 2), $\omega = \pi T(2n+1)$ are Matsubara frequencies with integer $n \geq 0$, ω_s is the cutoff frequency of SDW. The two equations can be solved numerically given relative densitity of states, n_1, and the SDW SC transition temperature ratio, $\frac{T_{c0}}{T_{s0}}$. Figures 1.7 (a-c) show the temperature dependence of the SDW and SC order parameters for three different sets of n_1 and T_{c0}/T_{s0} values. The plots clearly demonstrate that the order parameter of SDW is suppressed when SC is formed, indicating an overall competition relation between SDW and SC. This is explicitly demonstrated in several FeSCs as neutron scattering experiments showed a reduction of the Fe moments and Fe Mössbauer study showed a decrease of magnetic hyperfine field, when entering superconducting state (see Fig. 1.7 (d) for example) Pratt et al. (2009); Christianson et al. (2009); Luo et al. (2012); Munevar et al. (2013); Bud'ko et al. (2018).

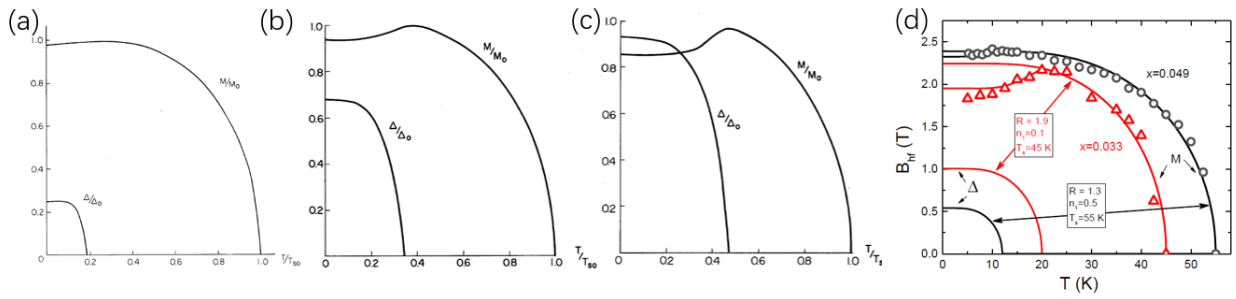

Figure 1.7 (a-c) The temperature dependence of the order parameter M/M_0 and Δ/Δ_0 for (a) T_{c0}/T_{s0} =0.7, n_1=0.5, (b) T_{c0}/T_{s0} =0.5, n_1=0.2 and (c) T_{c0}/T_{s0} =0.5, n_1=0.05. M_0 (Δ_0) is the order parameter without the SC (SDW) state. The temperature is normalized by T_{s0}. Figures are adapted from Ref. Maple (1970). (d) Experimental data (symbols) of the magnetic hyperfine field, $B_{hf}(T)$, measured by ^{57}Fe Mössbauer spectroscopy for $CaK(Fe_{0.967}Ni_{0.033})_4As_4$, and $CaK(Fe_{0.951}Ni_{0.049})_4As_4$ overlaid with temperature dependence of scaled magnetic, M, and superconducting, Δ, order parameters (lines) from fits using model of Ref. Machida (1981) (with $B_{hf}(T)$ serving as a proxy for magnetization). Obtained fitting parameters are listed on the plot, where $R = 1/n_1$. Figure is adapted from Ref. Bud'ko et al. (2018).

1.1.4 Superconductivity under pressure

The effect of pressure on superconductivity has been intensively studied over the years. Based on the BCS theory, we can have a first glance of how pressure could change superconducting transition temperature T_c in a simple argument. According to the BCS theory, in the weak coupling limit, $T_c = \frac{1.13\hbar\omega_D}{k_B} e^{\frac{-1}{N(E_F)V_{eff}}}$. Generally, the Debye temperature, ω_D, increases upon increasing pressure Brandt and Ginzburg (1969). However, the pressure dependence of $N(E_F)$ depends on the detailed band structure. In addition, pressure dependence of the electron-phonon coupling, V_{eff}, is also complex and hard to determine. Thus even in elemental superconductors that are conventional BCS type superconductors, the pressure dependence of T_c has different behavior, with T_c that either increases or decreases with pressure Brandt and Ginzburg (1969); Smith and Chu (1967); SEIDEN (1969); Smith (1972); Lorenz and Chu (2005). For instance, the pressure dependence of the superconducting critical temperature, T_C, of lead was investigated thoroughly. Experimentally, it was demonstrated that T_C was linearly suppressed with p (with the rate of $dT_C/dp \simeq$ -0.365 K/GPa) up to $\sim$ 5 GPa and became more nonlinear with p at higher pressures (see Fig. 1.8) Eichler and Wittig (1968); Smith et al. (1969); Clark and Smith (1978); Eiling and Schilling (1981); Bireckoven and Wittig (1988). Theoretically, the $T_C(p)$ behavior of lead was well explained based on the extended BCS theory of strong-coupling superconductivity Lorenz and Chu (2005); Clark and Smith (1978); Hodder (1969). As a matter of fact, due to the easily avaible high purity (99.9999%), sharp superconducting transition and well resolvable pressure dependence of T_C, elemental Pb has been widely used as a low-temperature manometer in the high pressure research. A more detailed discussion regarding this aspect is included in Chap. 8 of this thesis work. For unconventional superconductors where the pairing mechanism is argued to be not a simple electron-phonon interaction, pressure was often and is continuously being used as an important tuning parameter for modifying physical properties to investigate the relation between different ordered states as well as pairing mechanism of superconductivity Paglione and Greene (2010); Steglich et al. (1979); Lorenz and Chu (2005).

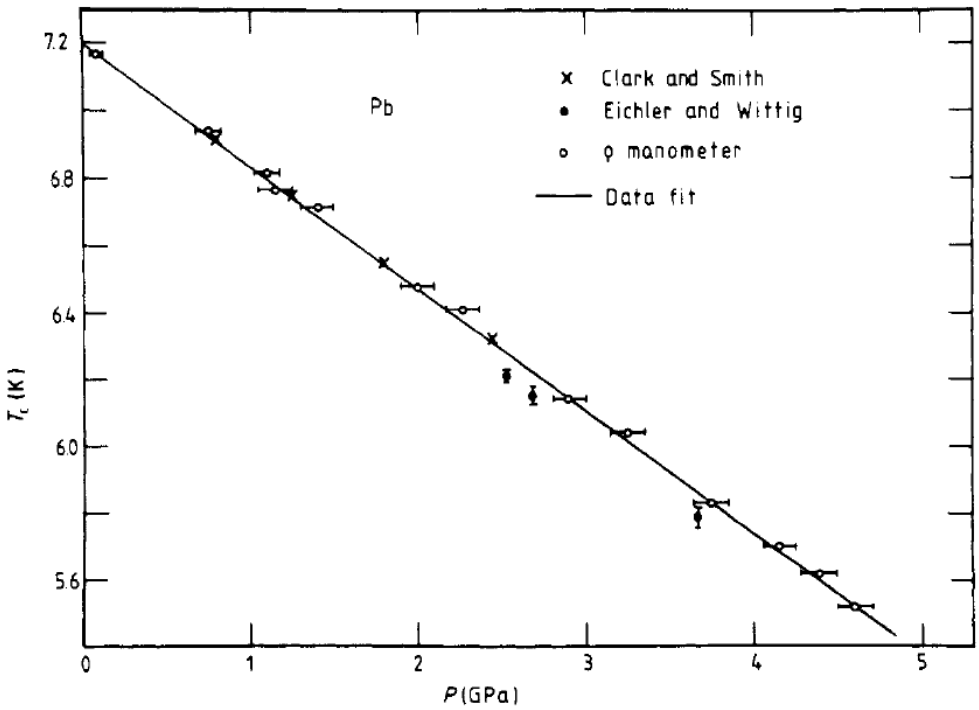

Figure 1.8 Pressure dependence of the superconducting transtion temperature T_c of Pb. Data points are obtained from Ref. Clark and Smith (1978) (cross symbols), Ref. Eichler and Wittig (1968) (solid circle) and Ref. Eiling and Schilling (1981) (open circle). The solid line is a linear fit of the data. Figure is adapted from Ref. Eiling and Schilling (1981).

1.2 Kondo effect and heavy fermions

What is now known as "Kondo physics" started in the 1930s with the puzzling experimental observation that the resistance in noble metals had a minimum at low temperature when containing small concentrations of transition metals de Haas et al. (1934) (Fig. 1.9 (a)). This observation violated the understanding based on the "Matthiessen's rule". It was expected that resistivity of metal decreases with temperature as inelastic scattering of electrons is reduced and reaches a constant, additive residual resistivity ρ_0 for $T \to 0$, which is governed by impurities and imperfections. In the early 1960s it was recognized that the resistivity minima are associated with magnetic impurities in the metallic host and in 1961, P. W. Anderson proposed a model to describe magnetic impurities embedded in metals by considering the interactions between local

spins and the conduction electrons Anderson (1961). Later on in 1964, J. Kondo, by using a perturbation theory, showed in detail how certain scattering on magnetic spins give rise to a resistivity contribution as $\rho_{\text{im}} \propto JN(E_{\text{F}})\ln\frac{k_{\text{B}}T}{D}$, which explains the observed resistivity minima and logarithmic increase of resistivity in certain temperature range Kondo (1964) (Fig. 1.9 (b)). Here, J is the exchange interaction, $N(E_{\text{F}})$ is the density of states at the Fermi level and D is the width of the conduction band. However, this calculation made by Kondo gives a non-physical diverging resistivity at zero temperature (the "Kondo problem") and turns out to be valid above a characteristic Kondo temperature, $T_{\text{K}} \propto De^{-\frac{1}{2}JN(E_{\text{F}})}$ Hewson (1993).

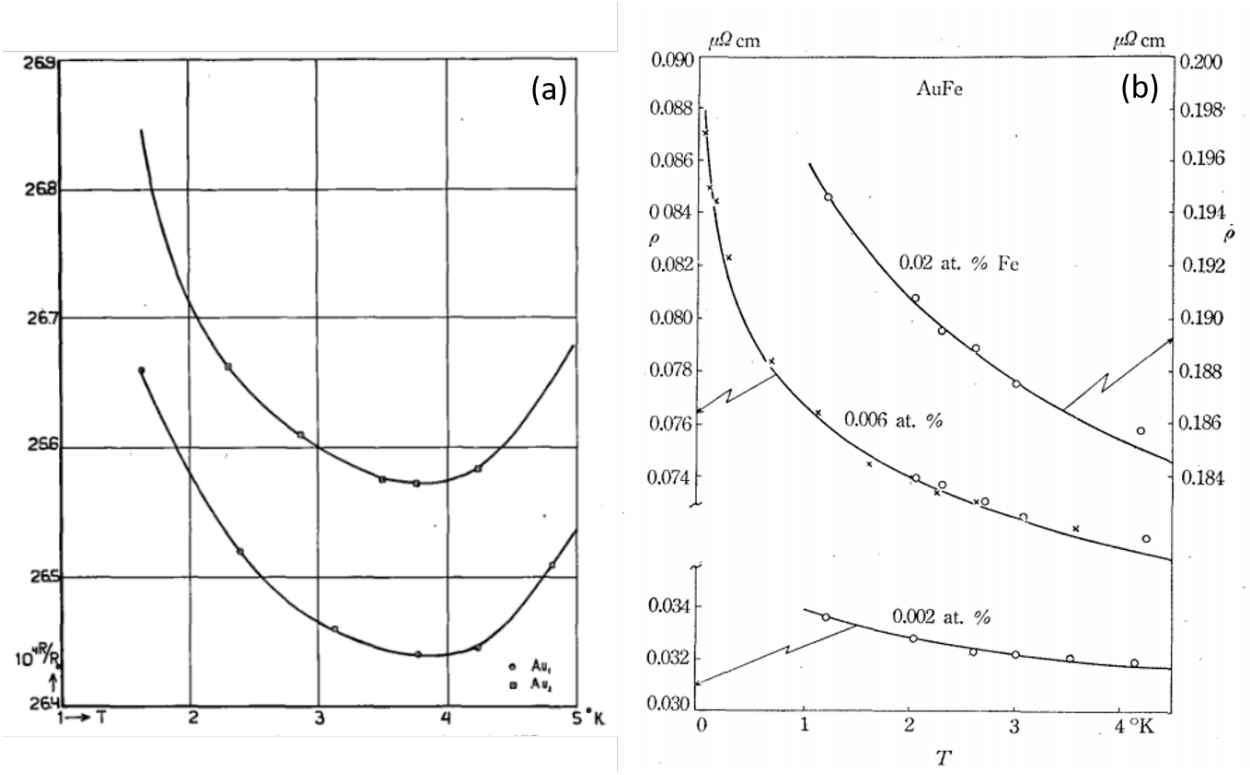

Figure 1.9 (a) Temperature dependent resistance of Au wires (not very pure) at low temperature region de Haas et al. (1934). (b) Comparison of experimental (open symbols) and theoretical (solid lines) temperature-dependent resistivity curves for dilute AuFe alloys Kondo (1964).

Solving the Kondo problem attracted the attention of many theorists to the field. The physical picture, in the simplest case where the magnetic impurity has an unpaired spin $S = 1/2$

(2-fold degenerate), is that this spin is gradually screened out by the conduction electrons as the temperature is lowered, with an associated increasing resistivity, such that as $T \to 0$, it becomes non-magnetic spin-singlet (Kondo singlet) and giving a temperature independent, but large, contribution to the resistivity in this regime. Furthermore it was concluded that the impurity contributions to the magnetic susceptibility, specific heat, and other thermodynamic properties, could all be expressed as universal functions of $T/T_{\rm K}$. Mathematical confirmation of this picture was obtained by Wilson (1975) using a non-perturbative renormalization group method Wilson (1975) and further confirmation by Andrei (1980) and Wiegmann (1981) via applying the Bethe Ansatz method Andrei (1980); Wiegmann (1981). This picture provides an explanation why the anomalous scattering from magnetic impurities leads to an enhanced contribution to the specific heat coefficient and magnetic susceptibility at low temperatures $T << T_{\rm K}$, whereas, at high temperatures $T >> T_{\rm K}$, the magnetic impurities act as local moments and susceptibility manifests Curie-Weiss behavior.

The single impurity Kondo model, outlined above, is for very dilute, non-interacting impurities dissolved in a metallic matrix. Moving away from this limit, as the so-called magnetic impurities get denser, they can completely occupy a certain periodic lattice site and form what is called a Kondo lattice system where a new ground state, heavy fermion, can sometimes emerge. In the Kondo lattice system at low temperature, the scattering of the electrons off the periodic magnetic impurities becomes coherent which results in a sharp resistance decrease with temperature. This drop of resistance at low temperature is also associated with the formation of Fermi liquid with strongly enhanced effectively mass (heavy) quasiparticles. The effective mass, m^*, can be of the order 1000 times that of the real mass of the electrons.

On one hand, the screening of local moments by the conduction electrons at low temperature results in a non-magnetic ground state as discussed above. On the other hand, the RKKY interaction between local moments and conductions electrons can give rise to an intersite exchange interaction between the local moments, which results in a magnetic ordered ground state. The competition of the Kondo-screening and RKKY-ordering can therefore result in

different ground states. Based on this, Doniach in 1977 proposed the generic phase diagram Doniach (1977) as shown in Fig. 1.10, where the energy scales of Kondo and RKKY are represented by their characteristic temperature $T_{\mathrm{K}} \propto De^{-\frac{1}{2}JN(E_{\mathrm{F}})}$ and $T_{\mathrm{RKKY}} \propto J^2N(E_{\mathrm{F}})$. As shown in the figure, changing $JN(E_{\mathrm{F}})$ can result in different dominating interaction energy and therefore different ground states. The tuning of $JN(E_{\mathrm{F}})$ via various tuning parameter (chemical substitution, magnetic field, physical pressure) may lead to a quantum phase transition (phase transition at $T = 0$ K) and is of great interest to scientists.

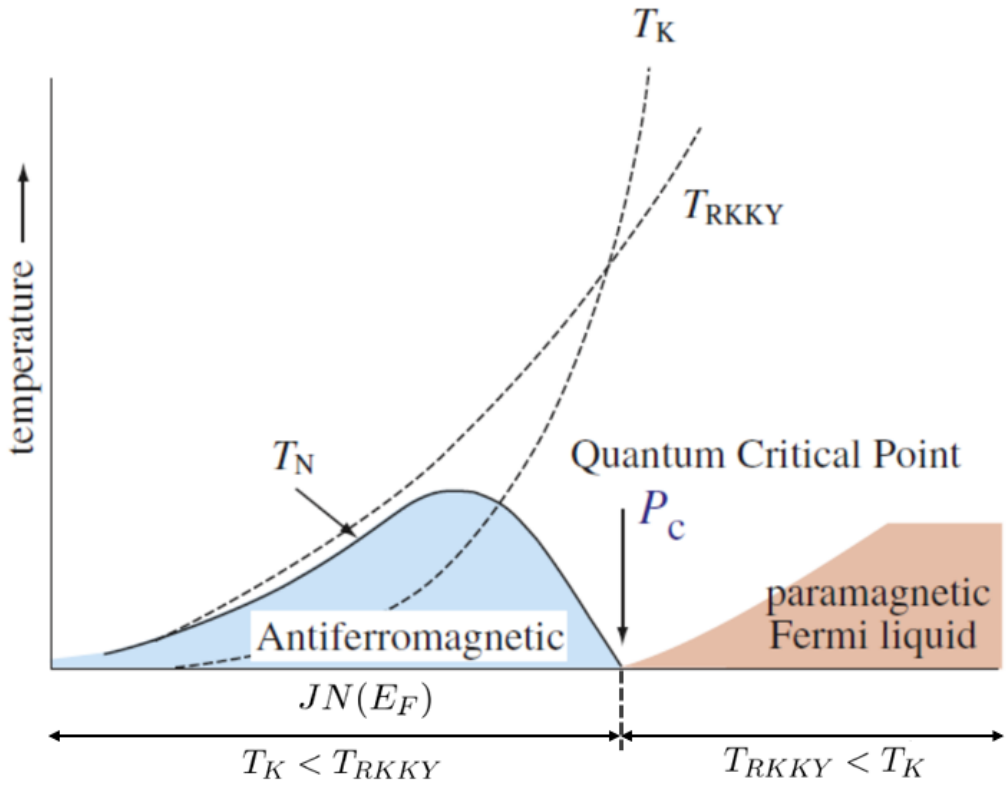

Figure 1.10 Doniach phase diagram Doniach (1977), illustrating the antiferromagnetic regime, where $T_{\mathrm{K}} < T_{\mathrm{RKKY}}$ and the heavy fermion regime, where $T_{\mathrm{K}} > T_{\mathrm{RKKY}}$. The green and brown dashed lines represent the Kondo and RKKY energy scale, T_{K} and T_{RKKY}, as a function of interaction, $JN(E_{\mathrm{F}})$ respectively. Transition between these two regions can be done through a quantum critical point (QCP).

1.3 Phase transitions

A phase is a description of a state of matter which establishes uniform physical properties. Phase transitions describe the process of a system changing from one phase to another as a result of the change of external conditions, such as temperature, pressure or others. Phase transitions are often classified based on the behavior of the thermodynamic free energy as a function of other thermodynamic variables, which was first introduced by Paul Ehrenfest Jaeger (1998). In this classification, phase transitions are labeled by the lowest derivative of the free energy that is discontinuous at the transition. A first-order phase transition is a transition for which the first derivative of the free energy with respect to some thermodynamic variable is discontinuous. Such transition also involves a latent heat and can establish a "mixed-phase regime" in which both phases co-exists under certain conditions. An example of a first-order transition is a solid to liquid transition. Similarly, a second-order phase transition is continuous in the first derivative and discontinuous in the second derivative. In these transitions, no latent heat or phase co-existence regime is observed. Paramagnetic to ferromagnetic transition when sample is cooled through the Curie temperature is a good example of a second-order phase transition. Later in 1936, Landau theory was introduced by Lev Landau to formulate a general theory of second-order phase transitions, which can also be used as a quantitative model for first-order transitions Landau (1936, 1937). In the Landau theory, phase transitions often involve a symmetry breaking process and an order parameter is introduced to describe this process. The free energy is then written as an analytical function of the order parameter and stable state(s) are obtained by the minimization of the free energy with respect to the order parameter (Fig. 1.11 (a)). In the case of a phase transition across a critical temperature, T_{cri}, the order parameter changes abruptly or continuously from zero to non-zero across T_{cri} for a first- and second-order transition, respectively (Figs. 1.11 (b) and (c)).

When phase transition happens at finite temperature with temperature being the control parameter, its behavior near the transition is often governed by thermal fluctuations. In contrast to that, quantum phase transition (QPT), driven by a non-thermal control parameter such as

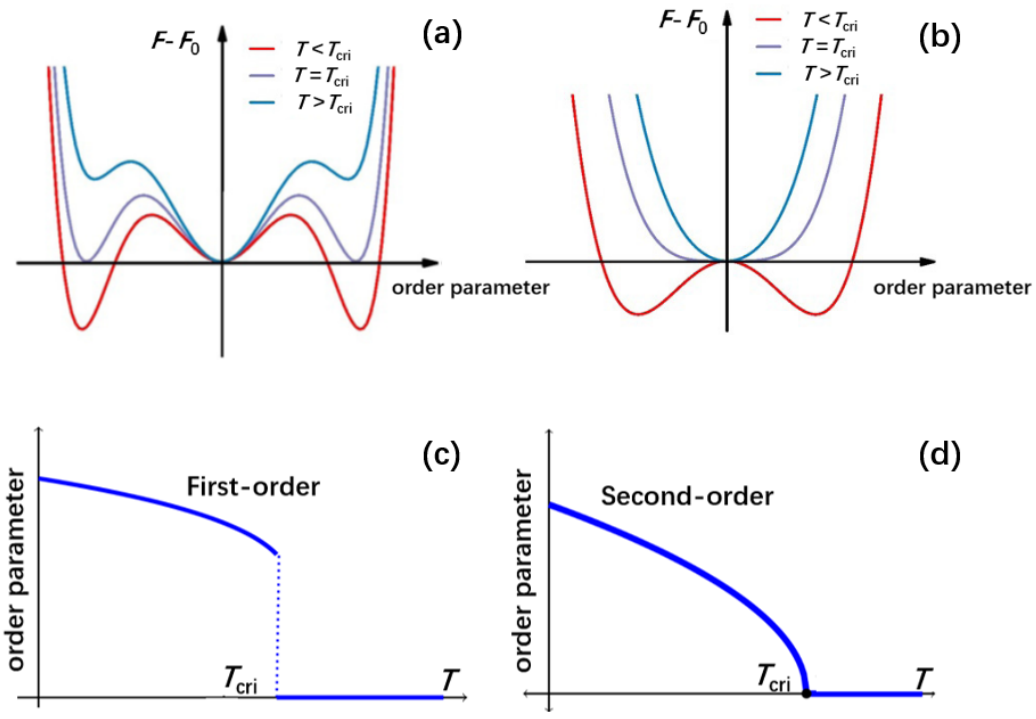

Figure 1.11 (a) Schematic plot of free energy as a function of order parameter for temperature above, equal and below critical transition temperature, T_{cri}, for a first- (a) and second-order (b) phase transition, respectively. Order parameter as a function of temperature for a first- (c) and second-order (d) phase transition, respectively.

pressure, doping or magnetic field, occurs at $T = 0$ and is governed by quantum fluctuations Hertz (1976); Sondhi et al. (1997); Vojta (2003). Though absolute zero Kelvin is not achievable experimentally, often at low but finite temperatures near the quantum phase transition region, the behavior of materials can still be dominated or strong influenced by quantum fluctuations Sachdev (2011). Quantum phase transitions have received great attention as novel ground states, such as unconventional superconductivity, heavy fermion liquid and two-dimensional electron gas, are often found in the vicinity of quantum phase transitions Paglione and Greene (2010); Steglich et al. (1979); Sondhi et al. (1997); Dagotto (1994); Sachdev (2000). Practically, one can tune a finite-temperature second-order phase transition to close to zero temperature by external tuning parameters (pressure, doping or magnetic field). When the transition is continuously suppressed and maintains its second-order nature, quantum phase transition happens through a quantum critical point (QCP). Near the QCP, the physical properties of the system are governed by the fluctuations of the order parameter and strongly related with the symmetry of the order parameter, the spatial dimensionality and the correlation length Vojta (2003); Sachdev (2011). For the cases of magnetic phase transitions (AFM and FM), the combined body of work by Hertz, Millis and Moriya (HMM theory), based on a self-consistent renormalized, studied the behavior near the magnetic QCP and make several predictions about the measurable physical properties Hertz (1976); Moriya (1985); Millis (1993). Whereas the the predictions of the HMM theory are observed in many magnetic systems with AFM transitions Sachdev (2011); Umeo et al. (1996); Wilhelm et al. (1999); Gegenwart et al. (2008); Sachdev and Keimer (2011), qualitative discrepancies are observed when one refers to metallic ferromagnetic systems. In the latter case, the second-order ferromagnetic transitions at finite temperatures, when suppressed to low enough temperatures, either become first-order in nature or are encountered by other modulated magnetic phases (spin-density wave, AFM order), given that the systems is "clean" enough (Figs. 1.12 (a) and (c)) Brando et al. (2016); Goto et al. (1998); Uhlarz et al. (2004); Kotegawa et al. (2011, 2013); Taufour et al. (2016). This near universal behavior in metallic ferromagnets is now often referred as avoided quantum criticality. Theories have been proposed to understand this

striking difference of the behavior between AFM and FM QPT. On one hand, in 1999 a general mechanism for first-order transitions was proposed by Belitz, Kirkpatrick and Vojta (BKV theory). It is shown that in two- and three-dimensional metallic systems, a second-order FM transition becomes first order through a tricritical point when suppressed to low enough temperature, provided the system is sufficiently clean Belitz et al. (1999). The striking difference between the predications of BKV theory and HMM theory is due to a coupling of the magnetic fluctuations to electronic soft modes, which leads to a fluctuation-induced first-order transition. In addition, BKV theory also showed that strong enough nonmagnetic disorder suppresses the tricritical temperature and FM transition remains second order down to zero Kelvin. On the other hand, different theories are proposed to explain the appearance of modulated magnetic phases between the paramagnetic and FM ordered region as well Chubukov et al. (2004); Conduit et al. (2009); Karahasanovic et al. (2012); Pedder et al. (2013). Nevertheless, the avoided quantum criticality in metallic ferromagnets has continued being an intriguing topic for researchers as i) the mechanism behind this is not fully understood with open questions, ii) a very recent theory work by Kirkpatrick and Belitz proposes that FM QCP can be realized in clean noncentrosymmetric metallic FM with strong spin-orbit coupling Kirkpatrick and Belitz (2020), iii) approaching QPT can sometimes realize novel ground states Brando et al. (2016).

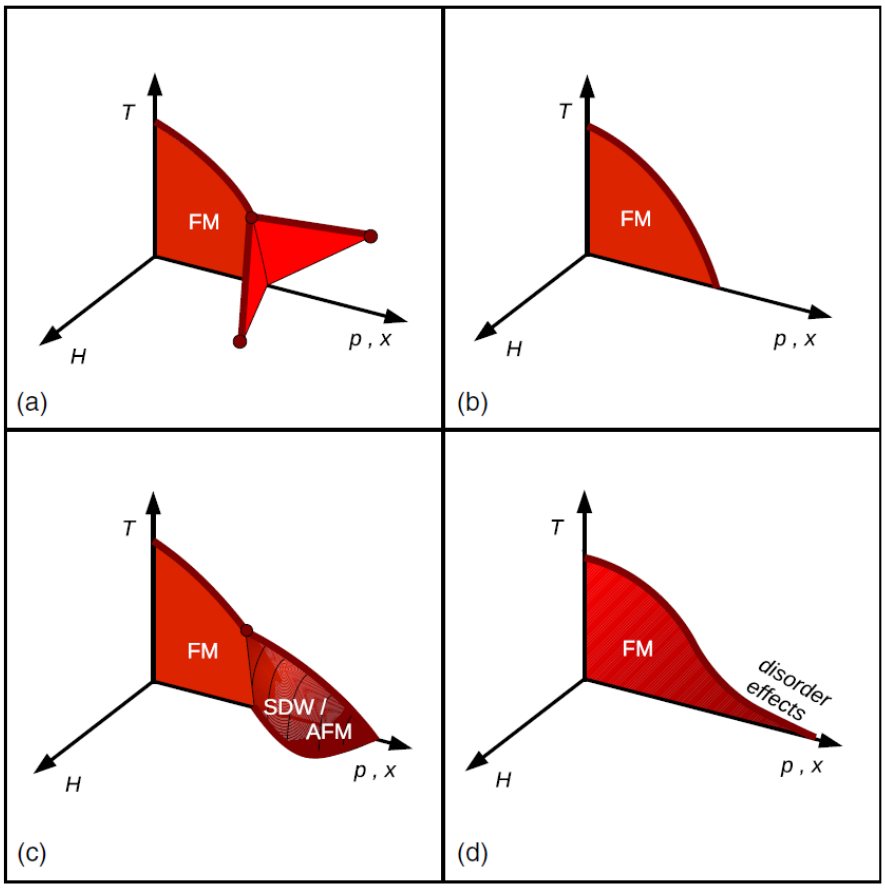

Figure 1.12 Schematic phase diagrams observed in ferromagnetic (FM) systems that show, at the lowest temperatures realized, (a) a discontinuous transition and tricritical wings in a magnetic field, (b) a continuous transition, (c) a change to spin-density-wave (SDW) or antiferromagnetic (AFM) order, and (d) a continuous transition in strongly disordered systems. Figure is adapted from Ref. Brando et al. (2016).

CHAPTER 2. EXPERIMENTAL METHODS

This section is an overview of the experimental methods for pressure-related measurements, focusing on electrical transport measurements. Two different pressure cells (piston cylinder and modified Bridgman anvil), with different sample spaces and maximum pressures, were extensively used to perform high-pressure electrical transport measurements during my research. An introduction to these two pressure cells is presented in the following sections. The details of the assembling process for each of the pressure cells are described in the appendix sections A, B and C.

2.1 Piston Cylinder Cell

The piston-cylinder cell (PCC) is a type of self-clamping cell with maximum pressure as high as ∼4 GPa, but in many incarnations operates with a maximum pressure of 2-3 GPa, depending upon details of construction Fujiwara et al. (2014, 2007). It typically uses a pressure medium that is liquid at room temperature, at least at lower pressures, thus offering good hydrostaticity, and has a sample space of ∼100 mm^3. This type of pressure cell is one of the most commonly used due to its relative ease of use, wide pressure range (up to ∼ 4 GPa, depending on the specific design and materials) as well as the relatively large volume that allows for the performance of a variety of measurements Fujiwara et al. (2007); Kadomatsu and Fujiwara (1979); Fujiwara et al. (1980); Kamishima et al. (2001); Gati et al. (2019a, 2020b). The PCC used in this thesis work is similar to the one described in Ref. Bud'ko et al. (1984) with the maximum low-temperature pressure ∼2.5 GPa.

A diagram of the PCC is shown in Fig. 2.1. The cell body is made of a non-magnetic Be-Cu alloy (C17200-copper alloy with 1.8-2% Be and ≪1% of Co,Ni,Fe) or Ti alloy (Ti 6Al-4V) and is reinforced by a Ni-Cr-Al alloy inner cylinder. A feed-through, made out of Ni-Cr-Al alloy,

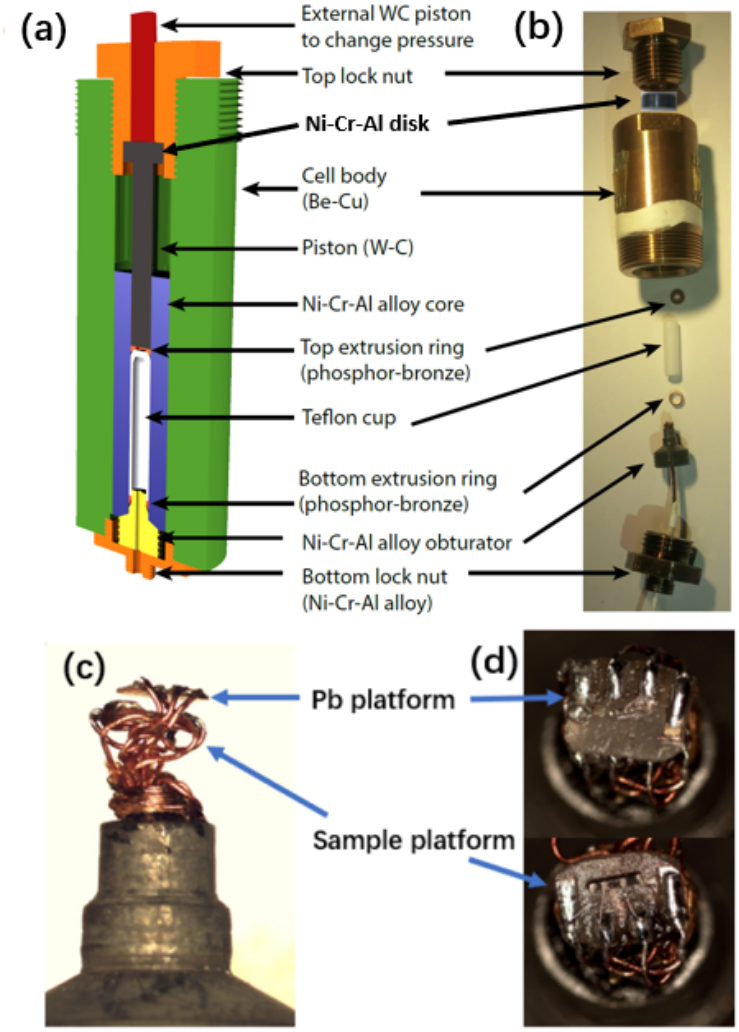

Figure 2.1 (a) Schematic diagram of the piston cylinder cell (PCC). Figure is adapted from Kaluarachchi (2018). (b) Individual parts of the PCC (c) A enlarged view of the feed-through showing various Cu wiring, Pb and Sample platforms. (d) Details of Pb (Upper figure) and sample (lower figure) platforms.

provides access for the electrical leads that connect sample and other components within the sample space to the outside. The feed-through is sealed with black stycast (2850FT with catalyst 9). The sample space is contained in a Teflon cup filled with liquid pressure medium. A mixture of 4:6 light mineral oil: n-pentane Bud'ko et al. (1984) was used as the pressure medium, which solidifies at room temperature at $\sim$ 3-4 GPa Torikachvili et al. (2015), i.e. at pressures above our maximum pressure. Two anti-extrusion rings, made out of 510 phosphor-bronze, are placed above and below the Teflon cup to prevent Teflon from flowing through the interstices when it is compressed. High pressure is generated by compressing the medium in the Teflon cup with a inner-piston which is a tungsten carbide (WC) rod, Ni-Cr-Al disk, outside-piston (WC rod) assemblage via a hydraulic press. Pressure is then maintained by tightening the top lock-nut. After that the pressure cell is removed from the hydraulic pressure (i.e. self-clamping) and measured elsewhere. Details of the process of assembling PCC can be found in Appx. A.

Pressure inside the pressure cell is usually determined by two manometers. At low temperature, pressure is determined by the superconducting transition temperature, T_c, of Pb Bireckoven and Wittig (1988) (elemental Sn or In could be used as well Smith and Chu (1967); Smith et al. (1969); Eiling and Schilling (1981)). At room temperature, the pressure can be determined by measuring the resistance of a manganin wire, which follows $R_p = R_0(1 + \alpha p)$, where R_p, R_0 are resistance at pressure p and ambient pressure ($p = 0$). The pressure coefficient, α, is determined independently for a particular manufacturer and batch. The room-temperature values of α for different manganin pressure gauges were reported to be $(2.35\pm0.15)\times10^{-2}$ /GPa Wang (1967); Zeto and Vanfleet (1969); Fujioka et al. (1978); Andersson and Sundqvist (1997); Dmowski and Litwin-Staszewska (1999). Note that in clamp piston-cylinder pressure cells, due to differential thermal expansion of the cell materials, Teflon and the medium, the pressure values depend on temperature and the difference of pressure values at room temperature and low temperature can be as large as 0.4 GPa. In Chap. 8, we will have a detailed discussion of the temperature-dependent pressure inside this pressure cell utilizing multiple manometers.

2.2 Modified Bridgman Anvil Cell

To reach higher static pressures the anvil cells are usually used. The anvil cell was first developed by P. W. Bridgman Bridgman (1941) and Bridgman cells can generate pressures up $\sim$ 10 GPa, using tungsten carbide (WC) alloy as anvils Bridgman (1952) with solid pressure medium. Later on, Bridgman cells were further adjusted to utilize liquid pressure medium to have better hydrostaticity Rüetschi and Jaccard (2007); Colombier and Braithwaite (2007). In this thesis, a modified Bridgman Anvil Cell (mBAC) similar to the one described in Ref. Colombier and Braithwaite (2007) was used to perform electrical resistance measurements under pressure up to $\sim$6 GPa.

A schematic diagram as well as pictures of various components of mBAC is shown in Fig. 2.2. The cell body and anvil holders are made of Be-Cu alloy (same as the alloy for PCC cell body). The anvils are made out of WC (purchased from Ceratizit, contains $\sim$ 8% of Ni) with culet size diameter 3.2 mm (maximum pressure 6$\sim$7 GPa) or 3.6 mm (maximum pressure 4$\sim$5 GPa). The sample space between the two anvils is further confined by sets of gaskets. The outside gasket is made out of pyrophyllite to support the inner gaskets, which are Teflon rings. Pyrophyllite is chosen for the following reasons: it is an electrical insulating material, thus good for insulation of wires for electrical measurements, it has a yield strength that increases with pressure Eremets (1996), it does not extrude significantly under compression and has a high friction coefficient Wentorf (1967). When setting up the cell, the pyrophyllite gasket is glued to the bottom WC anvil via GE varnish and is supported by Araldite epoxy resin surrounding the gasket on the outside. Inside the pyrophyllite gasket, two teflon rings are carefully placed on top of each other to seal the liquid pressure medium under compression. To perform electrical transport measurement, eight 12.5 μm diameter Au wires (four for Pb manometer, four for sample) are spot weldered to the surface of the Pb manometer and sample, which are further electrically connected to the outside measurement devices via Cu wires (Fig. 2.2 (d)). Typically a liquid pressure medium of 1:1 mixture of n-pentane:iso-pentane is used, which solidifies at $\sim$ 6 - 7 GPa at room temperature Torikachvili et al. (2015); Colombier and Braithwaite (2007). The pressure values at low

temperature are determined by the superconducting transition temperature, T_c, of Pb Bireckoven and Wittig (1988). Comparing with the PCC, assembling a mBAC takes more time and has a higher failure rate. Details of the process of assembling mBAC can be found in Appx. B.

2.3 Resistivity measurements

Temperature- and field-dependent resistance measurements were performed in Quantum Design Physical Property Measurement Systems (PPMS) with temperature range 1.8 K$\leq T \leq$ 300 K and magnetic field range $|H| \leq$ 140 kOe. Most of the time, the measurement option is used with f = 17 Hz and I = 1-3 mA. A standard four-probe method is used where current is passed through the outer two wires and voltage is measured across the inner two wires. This method ensures that the contact and wiring resistance are not measured and thus only measures the resistance from the sample itself. Prior to making contacts, samples are preferably made into bar shape via cutting, polishing and/or cleaving to ensure reasonably uniform current flow across the sample and to reduce the error in determination of the resistivity. For samples that only need to be characterized at ambient pressure, large sample dimensions can used (a maximum length of $\sim$ 8 mm to fit onto the PPMS puck). For samples need to be measured under high pressure, sample dimensions are limited by the pressure cell sample space. For PCC and mBAC, typical sizes of samples are 1.5×0.2×0.1 mm^3 and 0.7×0.1×0.03 mm^3, respectively. Electrical contacts to the sample were made via different methods, depending on the sample size and properties. For relative large samples (samples characterized at ambient pressure or in PCC), silver epoxy (Epotek-H20E) or silver paint (DuPont 4929N) was used to attach Pt wires onto the sample surface. Silver epoxy needs to be cured at 120°C for $\sim$ 20 mins and provides a strong mechanical bond between sample surface and the contact leads. Silver paint only needs only 5-10 mins to dry in air and typically provides a good electrical contact. However, it does not provide as strong of mechanical bond as silver epoxy. For samples measured under high pressure, due to limited sample space, contacts are preferably made with spot welding where Au wires (12.5 μm diameter) are spot welded to the sample surface. After spot welding, the mechanical strength of the

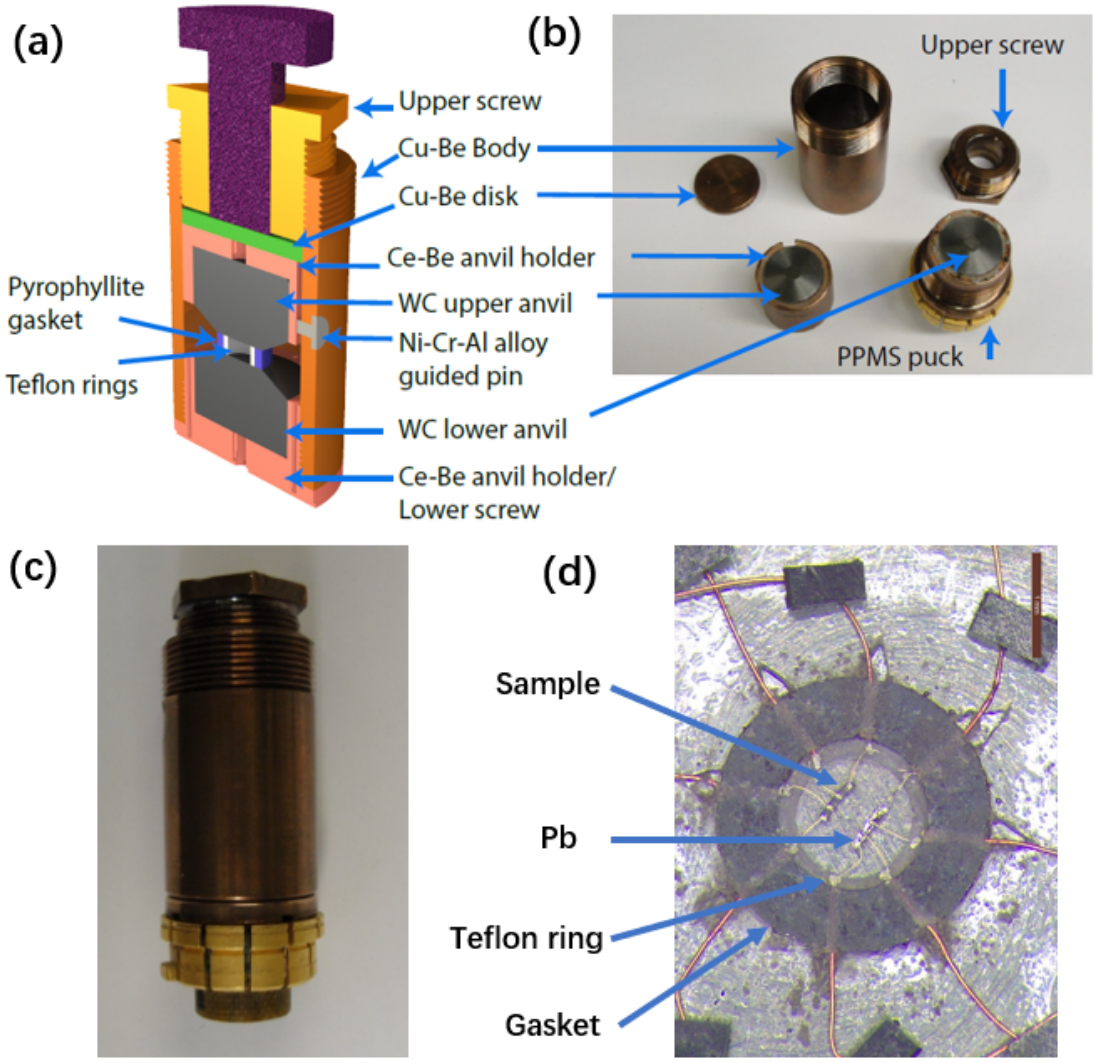

Figure 2.2 (a) Schematic diagram of the modified Bridgman anvil cell (mBAC). Figure is adapted from Kaluarachchi (2018). (b) Individual parts of the mBAC (c) Closed mBAC with PPMS puck attached at the bottom for electrical transport measurements in the Quantum Design PPMS. (d) Details of the sample space showing the gasket, Teflon ring, sample, Pb manometer as well as the Cu wires used for electrical connection.

contacts is enhanced by applying a small amount of silver epoxy (cured at 120°C for $\sim$ 20 mins). In this way, spot welding provides a good electrical contact (contact resistance typically less than 1 Ω for metallic samples) and silver epoxy provides a good mechanical strength. For air sensitive samples, contacts are made by silver paint inside an inert-atmosphere-filled glove box.

CHAPTER 3. DOME OF MAGNETIC ORDER INSIDE THE NEMATIC PHASE OF SULFUR-SUBSTITUTED FeSe UNDER PRESSURE

The following context is a slightly modified version of the published work in Ref. Xiang et al. (2017). DOI: https://link.aps.org/doi/10.1103/PhysRevB.96.024511. Reprinted (abstract/excerpt/figure) with permission from [L. Xiang *et. al.*, Phys. Rev. B 96, 024511 (2017)]

3.1 Introduction

Despite a large number of different compounds, many iron-based superconductors share similar physical properties. A characteristic feature of this material class is rich phase diagrams, containing an antiferromagnetic phase, which is suppressed upon substitution or pressure, and superconductivity, which emerges at a critical value of this tuning parameterCanfield and Bud'ko (2010); Paglione and Greene (2010). Usually, the antiferromagnetic ordering is of stripe-type and is preceded or accompanied by a structural tetragonal-to-orthorhombic distortion, associated with electronic nematic orderFernandes et al. (2014). The magnetic and structural transitions typically extrapolate to zero temperature near the maximum of the superconducting T_c dome, suggesting the possibility that magnetic or nematic fluctuations surrounding a quantum critical point mediate superconductivityKasahara et al. (2010); Putzke et al. (2014).

Among all the iron-based superconductors, the structurally most simple binary compound, FeSe, does not share this common behavior. First, the structural and magnetic transitions are well separatedMcQueen et al. (2009); at ambient pressure, a tetragonal-to-orthorhombic structural transition occurs at $T_s = 90$ K. The low-temperature phase has been identified as nematic due to the similarity of this transition with the structural transition typical of many iron-based superconductorsMcQueen et al. (2009); Baek et al. (2014); Böhmer et al. (2015);

Watson et al. (2015b). However, there is no signature of with no signature of magnetic order observed at ambient pressure down to 0.24 K (Ref. Bendele et al. (2010)). Very recent specific heat indicates a possible antiferromagnetic transition at 1.08 K (Ref. Chen et al. (2017)). However, their results contradict previous resultsLin et al. (2011), in which no anomaly in the specific measurement near this temperature was observed.

Second, under approximately 0.8 GPa of applied pressure, magnetic order clearly emergesBendele et al. (2010, 2012); Terashima et al. (2015); Kaluarachchi et al. (2016) above T_c and the magnetic transition temperature T_m exhibits a dome-like pressure dependence between 0.8 GPa and 6 GPaSun et al. (2016, 2017). Strong coupling between orthorhombic distortion and magnetic order under pressure was demonstratedKothapalli et al. (2016). Nevertheless, the large separation of T_s and T_m at ambient pressure raises the question of how the nematic order and magnetism are related in this compoundGlasbrenner et al. (2015); Yu and Si (2015); Wang et al. (2015); Chubukov et al. (2016).

Third, the pressure dependence of superconducting transition temperature T_c shows a remarkable non-monotonic structure, with a local maximum of T_c around 0.8 GPa, a local minimum around 1.2 GPa, a plateau around 4 GPa and finally a maximum of 37 K around 6 GPa, before T_c decreases at even higher pressures Miyoshi (2014); Kaluarachchi et al. (2016); Sun et al. (2016). Moreover, recent studies found that monolayer thin films of FeSe on STO shows superconducting behavior at temperatures higher than 100 KGe et al. (2015). Hence, FeSe gives us a unique opportunity to study how nematicity, magnetism and superconductivity interact with each other.

The maximum T_c of bulk FeSe under pressure is achieved in the pressure range above 5 GPa. However, FeSe has a complex and interesting phase interplay in the pressure range below 2 GPa. In this pressure range falls the intersection of the nematic phase, magnetic order and superconductivityTerashima et al. (2015); Kaluarachchi et al. (2016); Sun et al. (2016). Several studies have investigated the effect of sulfur substitution on FeSeMizuguchi et al. (2009); Watson et al. (2015a); Coldea et al. (2016); Hosoi et al. (2016); Ovchenkov et al. (2016). Similar to

applied pressure, sulfur substitution suppresses T_s. In contrast to pressurized FeSe, no magnetic ordering is found in the substitution-temperature phase diagram of $Fe(Se_{1-x}S_x)$ and T_c is only moderately enhanced to 11 K by substitutionWatson et al. (2015a). In this work, we combine chemical pressure through sulfur substitution up to 12% and physical pressure up to 1.8 GPa and show that the pressure-induced magnetic phase is strongly suppressed upon substitution in this pressure range. In contrast, the nematic phase and superconducting phase are quite robust and their behaviors under pressure do not change qualitatively.

3.2 Experimental details

High quality single crystals of $FeSe_{1-x}S_x$ ($x = 0.043(5)$, $x = 0.096(1)$, $x = 0.12(2)$) with sharp superconducting transitions at ambient pressure (see Figs. 1, 2-5 (b) below), were grown using chemical vapor transport, similar to Ref. Böhmer et al. (2016). The substitution level x was determined by energy-dispersive x-ray spectroscopy (EDS) and the given values and errors correspond to the average and standard deviation of EDS results obtained on ~ 10 spots from typically 3 different samples per batch, respectively. The c-axis resistance was measured on samples with substitution level $x = 0.043$ and 0.096 of approximate dimensions of $(0.5 \times 0.5 \times 0.1)$ mm^3, using a two-probe technique similar to Refs. Kaluarachchi et al. (2016); Tanatar et al. (2009). Two Ag wires were attached to the samples by soldering with In-Ag alloyKaluarachchi et al. (2016); Tanatar et al. (2016). The contact resistance is less than 50 $\mu\Omega$ which is much smaller than the sample resistance of approximately 10 mΩ. Four-probe wiring was used down to the sample contacts. The in-plane resistance was measured on a sample with substitution level $x = 0.12$ of approximate dimensions of $(1 \times 0.5 \times 0.1)$ mm^3 in a standard four-contact configuration, with contacts prepared using silver epoxy. AC resistance measurement were performed in a Quantum Design Physical Property Measurement System using 1 mA; 17 Hz excitation, on cooling and warming at a rate of 0.25 K/min. A Be-Cu/Ni-Cr-Al hybrid piston-cylinder cell similar to the one described in Ref. Bud'ko et al. (1984) was used to apply pressure. Pressure values at low temperature were inferred from the $T_c(p)$ of leadBireckoven and

Wittig (1988). Good hydrostatic conditions were achieved by using a 4:6 mixture of light mineral oil:n-pentane as pressure medium, which solidifies at room temperature in the range $3-4$ GPa, i.e., well above our maximum pressureBud'ko et al. (1984); Kim et al. (2011); Torikachvili et al. (2015).

3.3 Pressure-temperature phase diagrams

Figure 3.1 shows the ambient-pressure resistance of the studied $Fe(Se_{1-x}S_x)$ samples. The resistance is normalized at 300 K. The c-axis and in-plane resistance data on the parent compound FeSe are taken from Ref. Kaluarachchi et al. (2016) and Tanatar et al. (2016) respectively. T_c increases slightly from 8.9 K for undoped FeSe to 10.1 K for $x = 0.12$. The structural transition, visible as a kink in the resistance data, is suppressed from 90 K to 60 K at the highest studied substitution level. Note that in this work, the in-plane resistance is studied for the $x = 0.12$ sample, but c-axis resistance for the other three substitution levels. The features at T_s in in-plane and inter-plane resistance are rather similar. The positions of the studied compositions are indicated in the composition-temperature phase diagram in Fig. 3.1(c).

Figures 3.2-3.5 (a) show the pressure dependence of the resistance of $Fe(Se_{1-x}S_x)$ for $x = 0$, $x = 0.043$, 0.096 and 0.12, respectively. In these plots the resistance is normalized by dividing it by the ambient-pressure, room-temperature value for each sample. In general, the resistance decreases under applied pressure. A non-monotonic change of the high-temperature resistance value for the $x = 0.12$ sample is possibly due to contacting between the outside wiring and the piston cylinder pressure cell body in the first three pressure runs. The kink-like anomaly, associated with the structural phase transition T_s, is clearly visible in the lower pressure data and appears as a step-like anomaly in the temperature derivative dR/dT (Figs. 3.2-3.5 (c)). With increasing pressure, T_s is suppressed in all compounds. The blow up of the low temperature region, presented in Figs. 3.2-3.5 (b), highlights non-monotonic changes of T_c under increasing pressure. Furthermore, the superconducting transition broadens systematically under pressure, a tendency observed in the parent compound in the magnetically ordered phase. The increasing

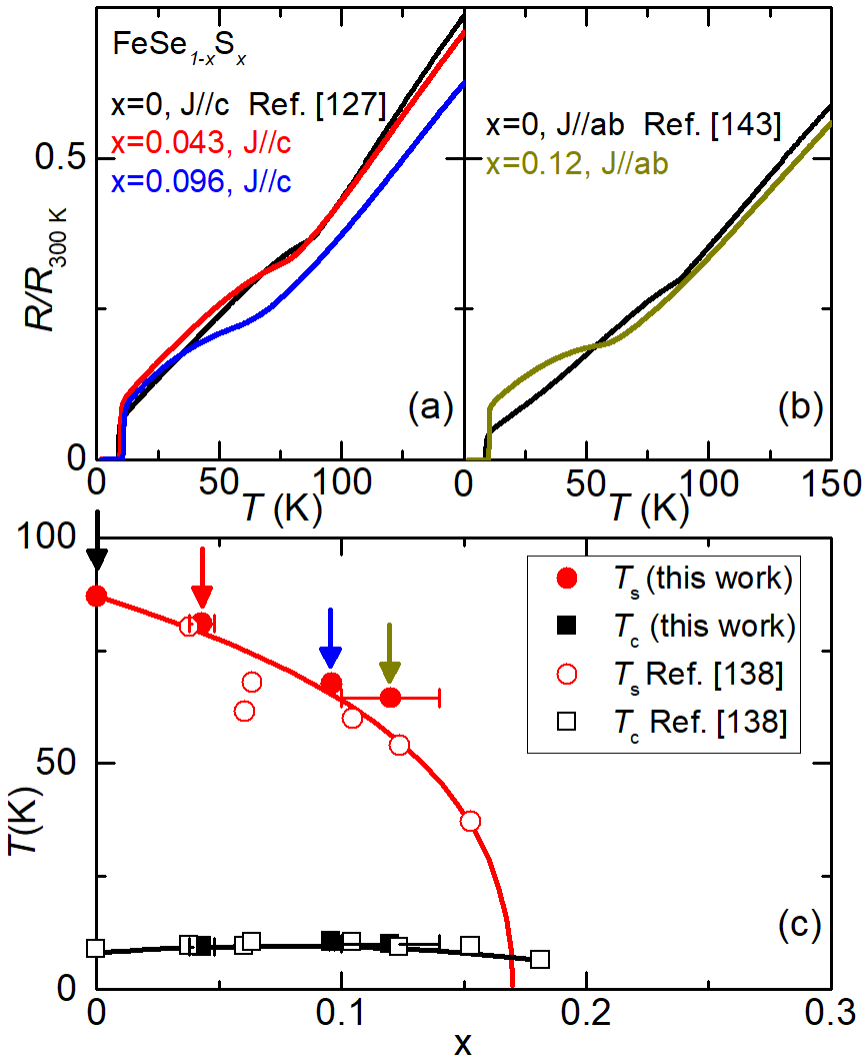

Figure 3.1 (a) Temperature dependence of the normalized resistance of $Fe(Se_{1-x}S_x)$ single crystals with current applied along c-axis for $x = 0$, $x = 0.043$ and $x = 0.096$. The data on the parent compound FeSe are taken from Ref. Kaluarachchi et al. (2016). (b) Temperature dependence of the normalized resistance of $Fe(Se_{1-x}S_x)$ single crystals with current applied in the ab plane for $x = 0$ and $x = 0.12$. The data on the parent compound FeSe are taken from Ref. Tanatar et al. (2016). (c) Substitution-temperature phase diagram of $Fe(Se_{1-x}S_x)$. The four compounds we used in this work are marked. Open symbols are data taken from Ref. Coldea et al. (2016).

broadening of the superconducting transition under pressure could also be due to inherent inhomogeneity of pressure when larger loads are applied and the substituted samples may be increasingly sensitive to this inhomogeneity.

The magnified scale in Figs 3.2-3.5 (b) reveals the effect of S-substitution on T_m. For $x = 0.043$, an increase of resistance upon cooling is observed below 15 K for pressures between $0.71 - 1.03$ GPa. This anomaly is reminiscent of the resistance increase at T_m of the parent compound at low pressures, shown in Fig. 3.2(b). We therefore associate it with the magnetic transition temperature T_m. In contrast to the parent compound, however, T_m is much less prominent in the S-substituted samples.

A magnetic field suppresses T_c but does not measurably affect T_mKaluarachchi et al. (2016), allowing for the study the magnetic transition in the absence of superconductivity. The application of a 9 T magnetic field, parallel to the c axis, permits us to discern T_m at pressures up to 1.28 GPa for the $x = 0.043$ sample (Fig. 3.6). An additional anomaly at temperatures slightly above T_m is observed for pressures greater than 0.95 GPa and is discussed in the appendix.

No feature corresponding to a possible magnetic transition is observed in the resistance data for $x = 0.096$ and $x = 0.12$ in zero magnetic field. However, the application of a 9 T magnetic field reveals a subtle resistance anomaly between $0.27 - 0.54$ GPa for the $x = 0.096$ sample (Fig. 3.6(b)), which may be associated with T_m. For the $x = 0.12$ sample, even in a 9 T magnetic field, no anomaly that could be associated with magnetic ordering is observed in the resistance measurement with pressure up to 1.81 GPa. It is possible that the anomaly at T_m is less pronounced in the in-plane resistance, which was measured for the $x = 0.12$ sample, and therefore not resolved in these data.

The values of T_c, T_m and T_s were obtained using the criteria outlined in Ref. Kaluarachchi et al. (2016) and shown in Figs. 3.2 and 3.3. T_c is defined as the intersection between highest slope of $R(T)$ and zero resistance. T_s is defined as the midpoint of the step in $\mathrm{d}R/\mathrm{d}T$, i.e., the midpoint of the kink in $R(T)$, and T_m is defined as the point of the highest slope of the resistance. The resulting $p - T$ phase diagrams of $Fe(Se_{1-x}S_x)$, $x = 0 - 0.12$, are presented in Fig 3.7.

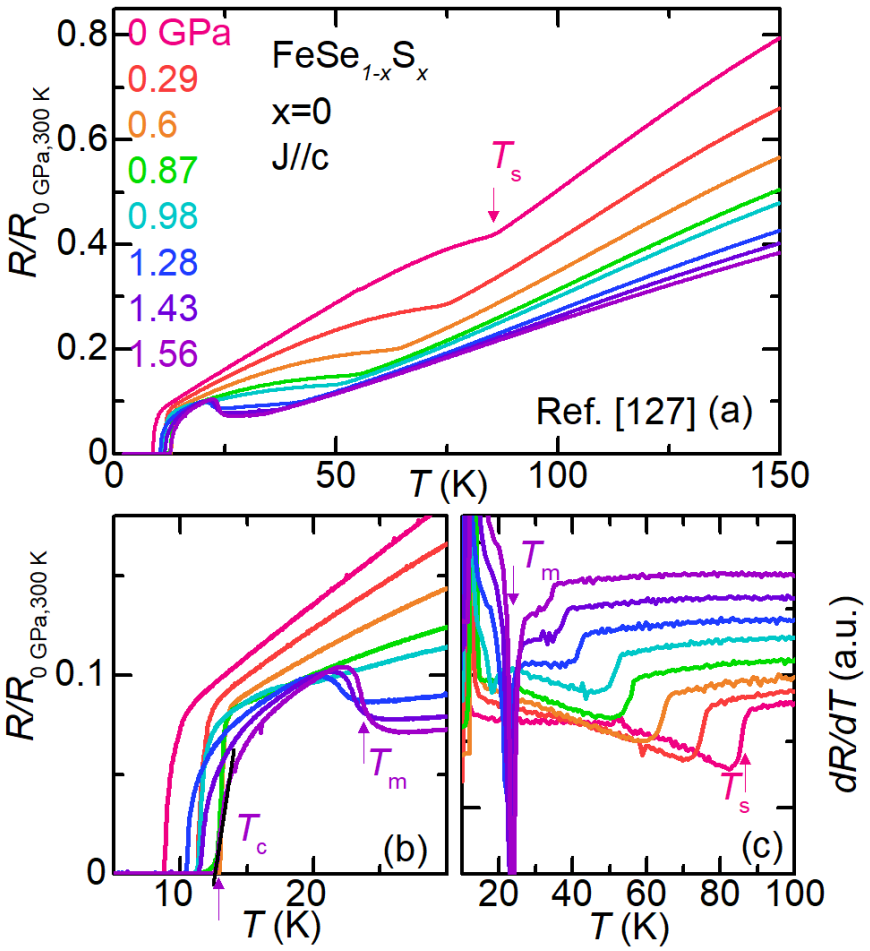

Figure 3.2 (a) Evolution of the c-axis resistance with hydrostatic pressure for pure FeSe. Data were normalized at room temperature, ambient pressure. (b) Blow up of the low-temperature region. (c) Temperature derivative dR/dT showing the evolution of structural transition T_s. Data are taken from Ref. Kaluarachchi et al. (2016). Examples of transition temperatures T_s, T_m and T_c are indicated by arrows.

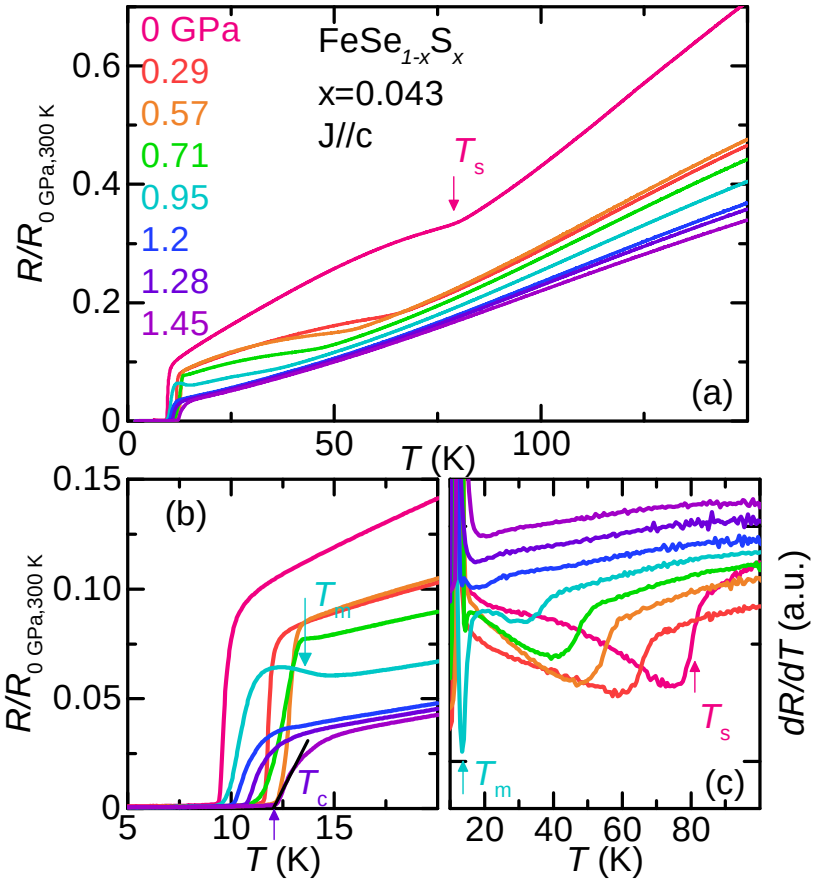

Figure 3.3 (a) Evolution of the c-axis resistance with hydrostatic pressure for $Fe(Se_{1-x}S_x)$, $x = 0.043$. Data were normalized at room temperature, ambient pressure. (b) Blow up of the low-temperature region. (c) Temperature derivative dR/dT showing the evolution of structural transition T_s. Examples of transition temperatures T_s, T_m and T_c are indicated by arrows.

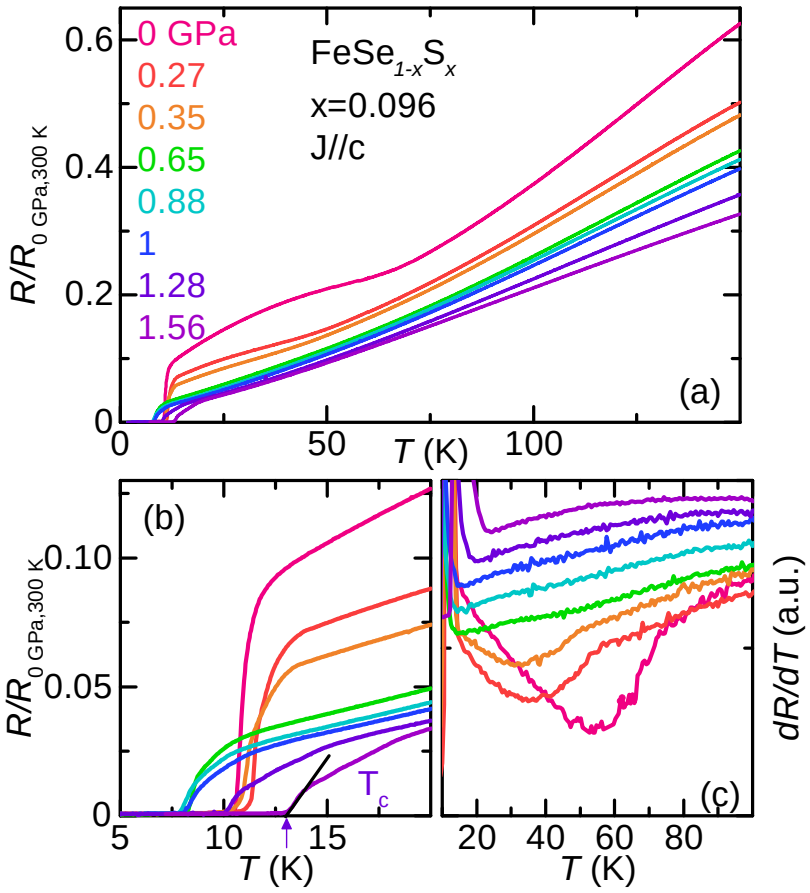

Figure 3.4 (a) Evolution of the c-axis resistance with hydrostatic pressure for $Fe(Se_{1-x}S_x)$, $x = 0.096$. Data were normalized at room temperature, ambient pressure. (b) Blow up of the low-temperature region. (c) Temperature derivative dR/dT showing the evolution of structural transition T_s.

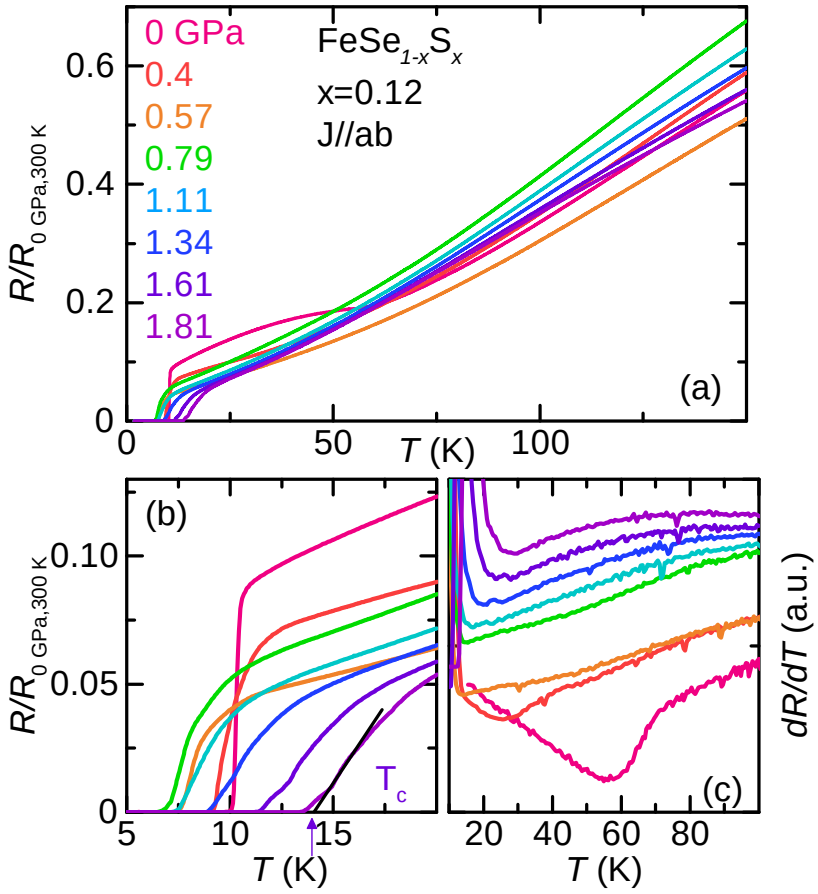

Figure 3.5 (a) Evolution of the c-axis resistance with hydrostatic pressure for $Fe(Se_{1-x}S_x)$, $x = 0.12$, with in-plane current. Data were normalized at room temperature, ambient pressure. (b) Blow up of the low-temperature region. (c) Temperature derivative dR/dT showing the evolution of structural transition T_s.

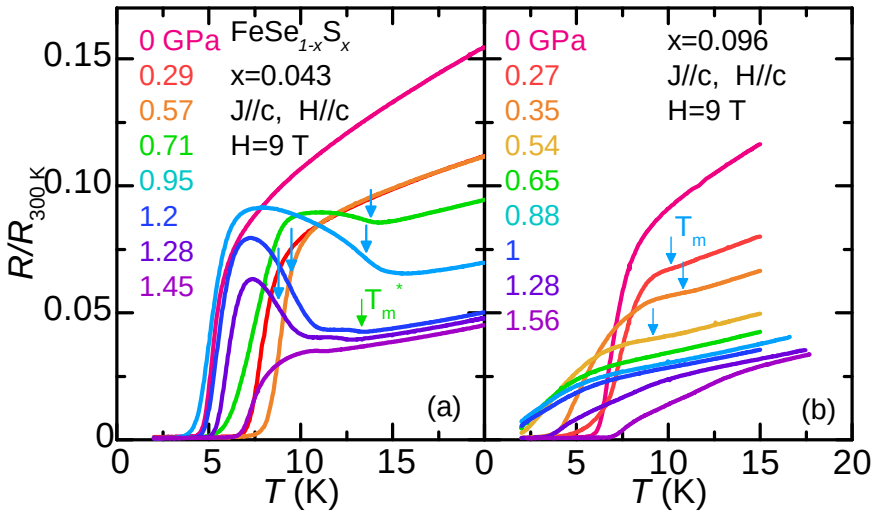

Figure 3.6 Evolution of the temperature dependence of normalized resistance under various pressures with $H = 9$ T magnetic field applied parallel to c axis for (a) $x = 0.043$ and (b) $x = 0.096$. For the $x = 0.043$ sample, the magnetic phase transition indicated by blue arrows is more pronounced in field and a second anomaly is observed at slightly higher temperatures. This anomaly, at T_m^*, is indicated by green arrow and will be discussed in the Appendix. For $x = 0.096$, magnetic field reveals a subtle anomaly between $0.27 - 0.54$ GPa, associated with the magnetic transition at T_m.

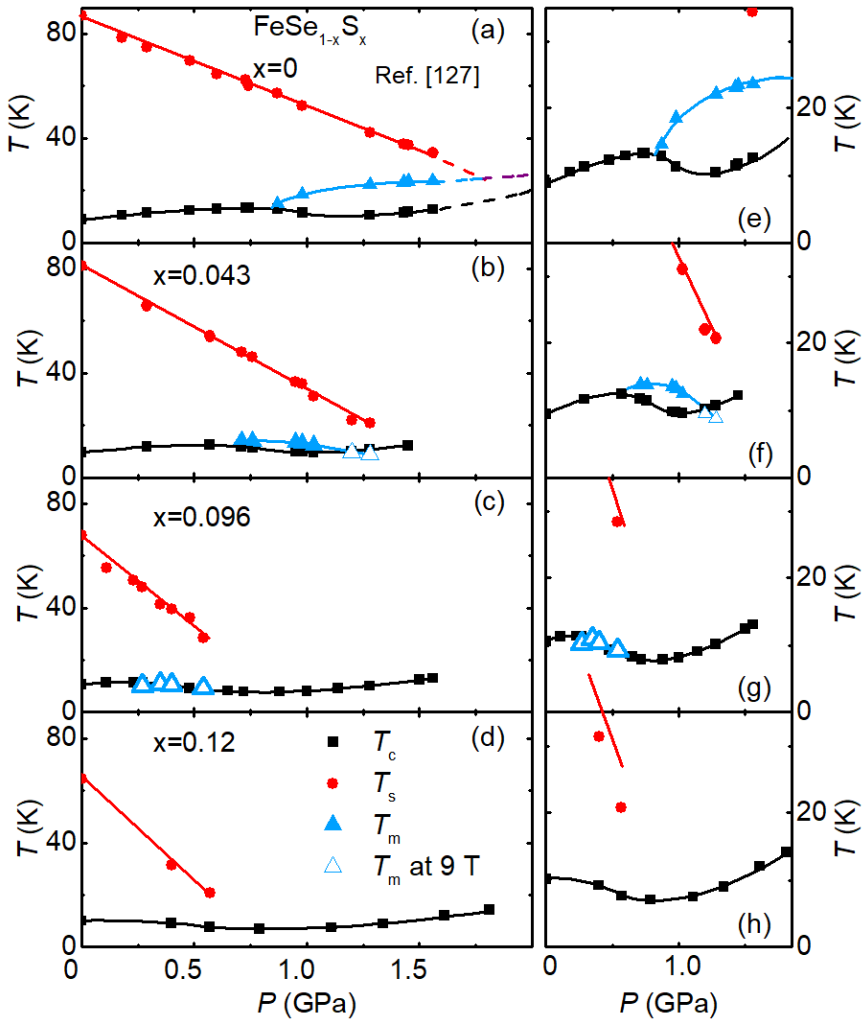

Figure 3.7 Temperature - pressure phase diagrams of $Fe(Se_{1-x}S_x)$ as determined from resistance measurements. The squares, circles and triangles circles represent the superconducting T_c, structural T_s and magnetic T_m phase transitions respectively. The solid lines are guides to the eye. Data in (a),(e) are taken from Ref. Kaluarachchi et al. (2016). The dashed lines in (a) represent extrapolations based of Refs. Terashima et al. (2015); Kothapalli et al. (2016). As shown in the left panels (a)-(d), for all compounds T_s is suppressed linearly with increasing pressure. Panels (e)-(h) show the data on an expanded temperature scale. T_c shows similar non-monotonic dependence on pressure with a local maximum and minimum. The magnetic order appears strongly suppressed upon substitution. The intersection of the T_s lines and T_c lines is not unique and does not coincide universally with either the minimum or the maximum of T_c.

The orthorhombic phase line is clearly resolved in all of the phase diagrams in the pressure range below $\sim 0.5 - 1.5$ GPa. At ambient pressure, T_s is suppressed by 12% S-substitution from 90 K to 60 K. Pressure suppresses T_s almost linearly for all x, but as shown in Fig. 3.8(a), with increased rate dT_s/dP for higher x.

For the parent compound FeSe, the magnetic transition at T_m is observed for pressures greater than 0.8 GPaKaluarachchi et al. (2016); Terashima et al. (2015). Subsequent work has shown the magnetic phase to persist up to 6 GPa, with a dome-like dependence of T_m on pressureSun et al. (2016, 2017). For the $x = 0.043$ sample, a similar phase line emerges above 0.5 GPa, and we tentatively associate it with T_m, pending confirmation by microscopic magnetic probes. But in contrast to pure FeSe, T_m increases only slightly to a maximum of 13.8 K at 0.71 GPa and is suppressed to below T_c already by 1.2 GPa. For higher S-content, $x = 0.096$, this transition seems to occur within the small pressure range $0.27 - 0.57$ GPa and with a dome-like shape barely exceeding T_c at its maximum. For $x = 0.12$, no corresponding transition is resolved in the in-plane resistance measurement.

For all measured substitution levels, T_c of $Fe(Se_{1-x}S_x)$ shows a similar non-monotonic dependence on pressure. The local maximum of T_c shifts to lower pressure on increasing sulfur content, from $P_{Tc,\max} = 0.73$ GPa for $x = 0$ to 0.23 GPa for $x = 0.096$ and close to ambient pressure for $x = 0.12$. Likewise, the local minimum of T_c shifts from $P_{Tc,\min} = 1.28$ GPa for $x = 0$ to 0.79 GPa for $x = 0.12$, as presented in Fig. 3.8(b).

The clear suppression of T_c below its local maximum in the intermediate pressure range is similar for all studied substitution levels. The onset of this suppression correlates with the emergence of the magnetic phase for $x = 0 - 0.096$, even though in the $x = 0.096$ sample, T_m is indicated only by an extremely weak feature in resistivity and practically coincides with T_c. For $x = 0.12$, T_m is not visible at all. It seems likely that the competing order setting in at T_m suppresses T_c for $x = 0 - 0.096$. However, whether this is still the case at higher substitution levels remains an open question and possibly another mechanism for the partial suppression of T_c needs to be invoked.

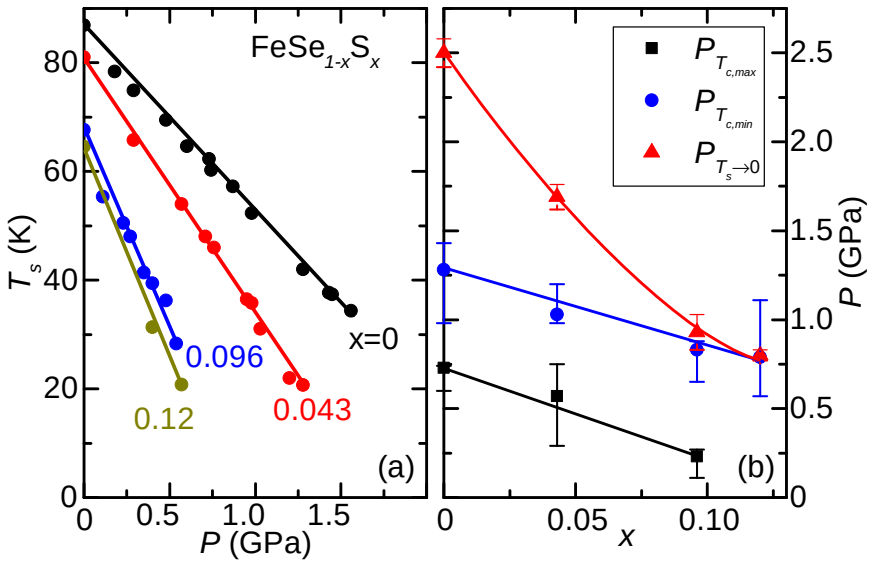

Figure 3.8 (a) Pressure dependence of the structural transition temperature T_s for $Fe(Se_{1-x}S_x)$ with different substitution levels x. (b) Substitution dependence of the pressures $P_{Tc,\max}$, $P_{Tc,\min}$ and $P_{T_s\to 0}$ which correspond to the local maximum of T_c, minimum of T_c and the extrapolation of T_s to zero temperature, respectively. Solid lines are guides to the eyes. Data for $x = 0$ are taken from Ref. Kaluarachchi et al. (2016)

The minimum of T_c of pure FeSe at 1.3 GPa likely coincides with a change of the Fermi-surface under pressureKaluarachchi et al. (2016); Terashima et al. (2016). It is plausible that a similar change of Fermi surface occurs in the doped samples and is the origin of the local minimum of T_c. In contrast, the extrapolations of the T_s phase lines intersect T_c at non-unique positions for the different substitution levels. The extrapolation does not correlate universally with either the maximum or the minimum of T_c in $Fe(Se_{1-x}S_x)$, $x = 0 - 0.12$ (Fig.3.8(b)). This behavior differs from many other iron-based superconductor phase diagrams, where T_s and T_c typically intersect near the maximum of T_c (Ref. Paglione and Greene (2010)).

$Fe(Se_{0.904}S_{0.096})$ provides an example in which the structural transition extrapolates to the minimum of T_c. Several theories have discussed the influence of a nematic phase, and in particular of a nematic quantum critical point, on superconductivityLederer et al. (2015); Labat and Paul (2017). In all cases, the nematic fluctuations are assumed to enhance (or induce) superconducting pairing and correlate with a maximum in T_c, opposite to the observed behavior. This is a sign that nematic fluctuations may not be involved in the superconducting pairing in this compound.

The magnetic phase in the low-pressure range is extremely sensitive to S-substitution, but the orthorhombic/nematic phase is not. For example, in $Fe(Se_{0.957}S_{0.043})$ we observe only a tiny magnetic dome, contained entirely inside the nematic phase. In pure FeSe, T_m increases under applied pressure until T_s and T_m merge. The increase of orthorhombic distortion below T_m in FeSe demonstrates the cooperative coupling of the two types of orderKothapalli et al. (2016), similar to many iron-arsenide materialsKim et al. (2011). In the well-known spin-nematic scenario for iron-arsenide materialsFernandes and Schmalian (2012), the nematic transition is believed to be a consequence of incipient stripe-type magnetic order. The strikingly different response of nematic and magnetic order to sulfur substitution in FeSe suggests, however, that the nematic phase in $Fe(Se_{1-x}S_x)$ may not be related to the magnetic order observed in the low pressure range. A number of alternative scenarios for the origin of nematic order in FeSe have been put forward, including quadrupolar orderYu and Si (2015); Wang et al. (2016), frustrated quantum paramagnetismWang et al. (2015) and a Pomeranchuk instabilityChubukov et al. (2016).

Isovalent substitution, as the replacement of selenium by sulfur, may be thought of as chemical pressure. Well-known examples in the iron-arsenide systems are $BaFe_2(As_{1-x}P_x)_2$ and $Ba(Fe_{1-x}Ru_x)_2As_2$Klintberg et al. (2010); Jiang et al. (2009c); Colombier et al. (2009); Thaler et al. (2010). If pressure and substitution were simply additive, the $p-T$ phase diagrams for different substitution levels would be shifted with respect to each other. This is clearly not the case for the transition at T_m in $Fe(Se_{1-x}S_x)$, whose maximum temperature is strongly suppressed with increasing x. Sulfur substitution and pressure are not additive concerning T_s either. Fig. 3.8(a) shows the T_s phase lines for the four substitution levels $x = 0$, 0.043, 0.096 and $x = 0.12$. Both substitution and pressure suppress T_s, but the rate of suppression of T_s under pressure depends on the substitution level. This would not be the case if S-substitution was simply additive to pressure. Similarly, an overlap of the "S-shaped" pressure dependence of T_c for different x can not be achieved by a simple shift. Even though $P_{Tc,\max}$ and $P_{Tc,\min}$ are suppressed at a similar rate by sulfur substitution (Fig.3.8(b)), this "S" changes shape for increasing sulfur content. These comparisons demonstrate that sulfur substitution and physical pressure are not equivalent in FeSe concerning any phase transition and likely modify the electronic structure as well as any salient coupling constants in different ways.

3.4 Pressure-dependence of the upper critical field

To better understand the superconducting properties of $Fe(Se_{1-x}S_x)$, including the non-monotonic pressure dependence of T_c, the superconducting upper critical field is analyzed following Refs. Kaluarachchi et al. (2016); Taufour et al. (2014). Figs 3.9, 3.10 and 3.11 show the temperature dependence of the upper critical field H_{c2} for $H||c$ of $Fe(Se_{1-x}S_x)$ for $x = 0.043$, $x = 0.096$ and $x = 0.12$ at various pressures. The insets show the temperature dependence of resistance in magnetic fields $H \parallel c$ between $0-9$ T, from which these data are obtained, for representative pressure values. Notably, for the $x = 0.12$ sample, the current was applied along the ab plane, whereas the current was along the c-axis for the other compounds. In principle, the $j||H||c$ configuration can minimize the contribution of flux flow to the superconducting

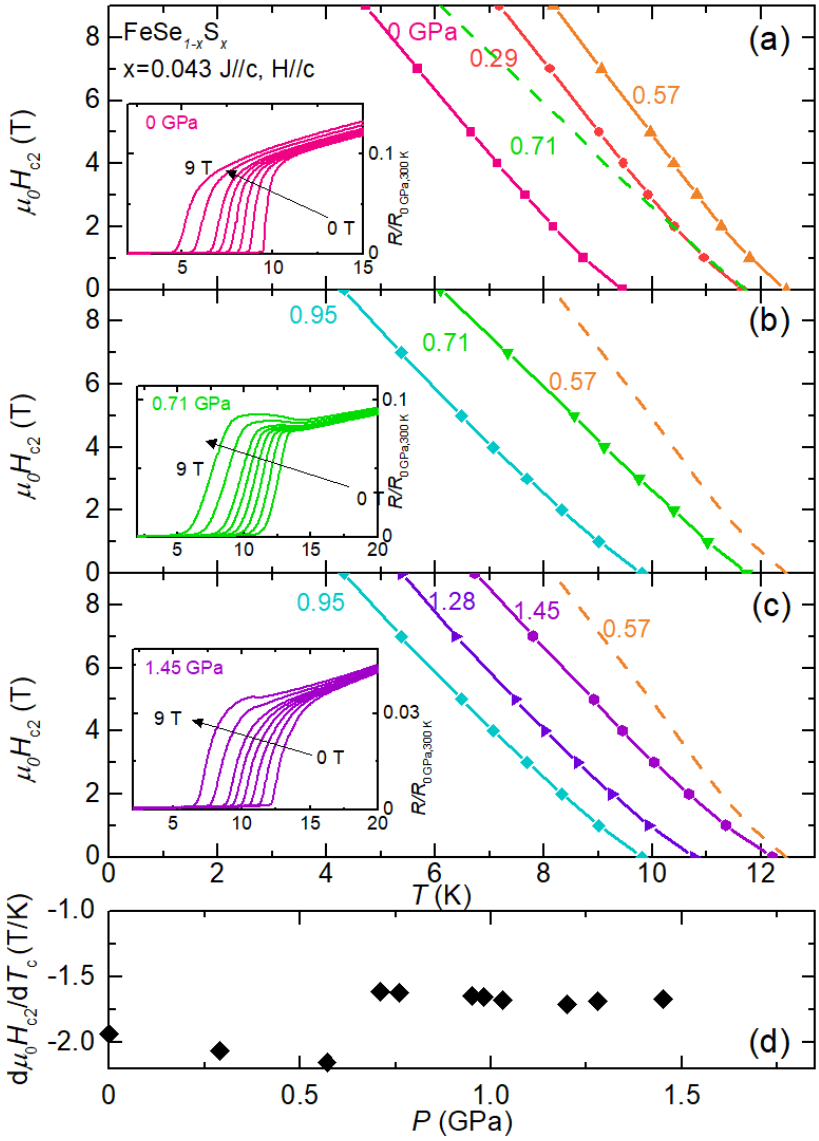

Figure 3.9 Temperature dependence of the upper critical field $H_{c2}(T)$ measured in $j \parallel H \parallel c$ configuration under various pressures for the $x = 0.043$ sample. Three regions are identified and separated by the local maximum and minimum of T_c under pressure (panels (a), (b) and (c), respectively). A clear change of the $H_{c2}(T)$ slope is observed between the first and second region only (panel (d)). Insets show representative resistance data under magnetic fields up to 9 T.

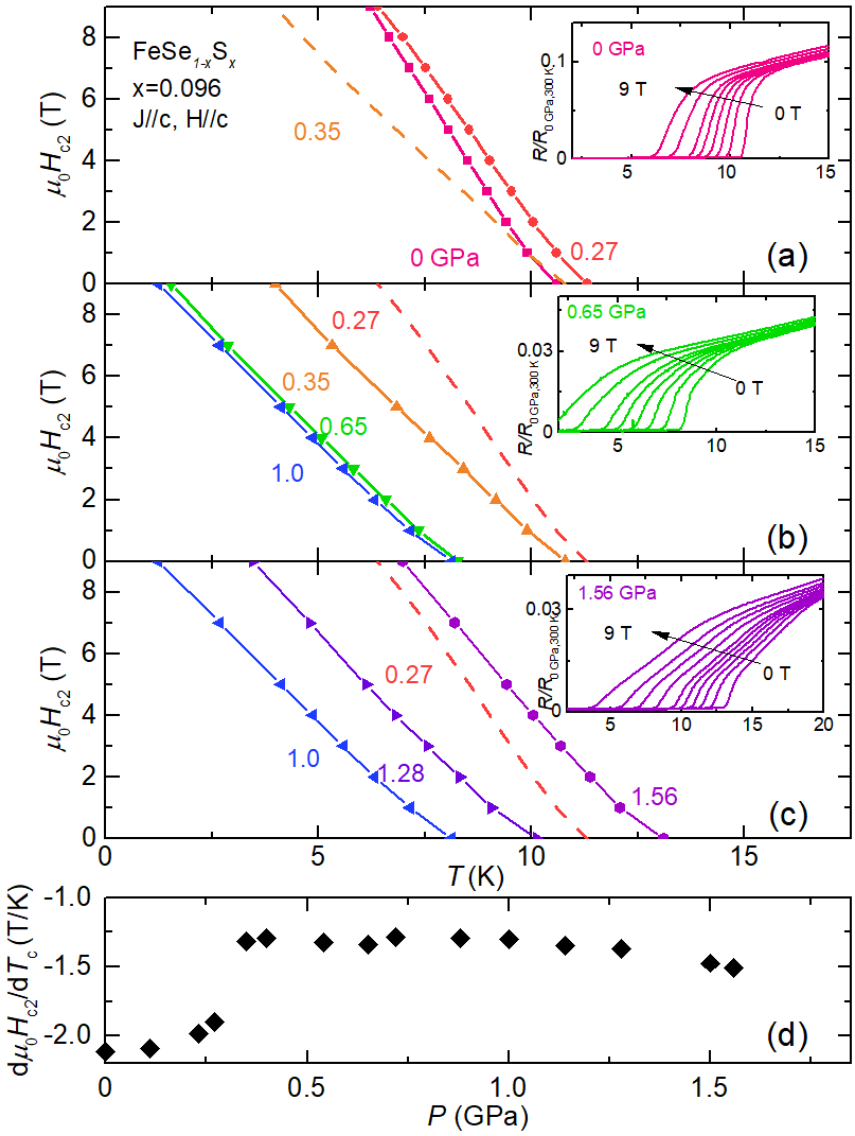

Figure 3.10 Temperature dependence of the upper critical field $H_{c2}(T)$ measured in $j \parallel H \parallel c$configuration under various pressures for the $x = 0.096$ sample. Three regions are identified and separated by the local maximum and minimum of T_c under pressure (panels (a), (b) and (c), respectively). A clear change of the $H_{c2}(T)$ slope is observed between the first and second region only (panel (d)). Insets show representative resistance data under magnetic fields up to 9 T.

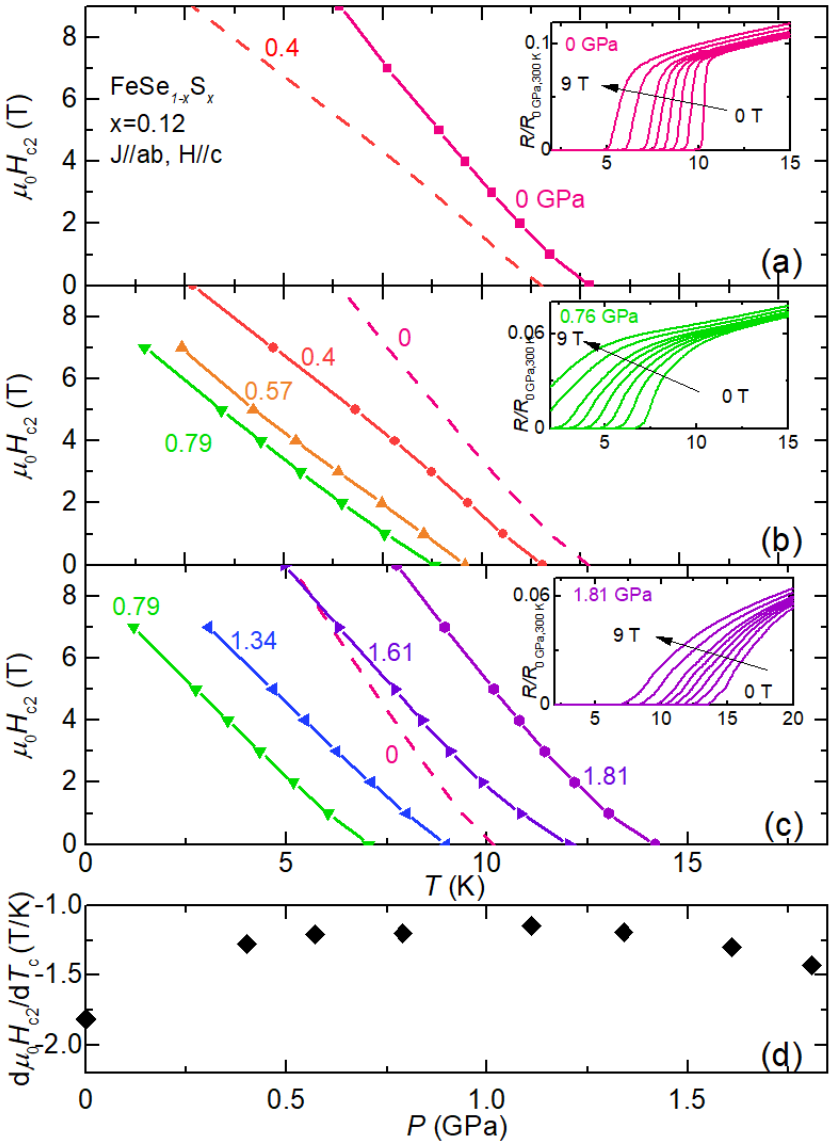

Figure 3.11 Temperature dependence of the upper critical field $H_{c2}(T)$ measured in $H \parallel c$, $j \parallel ab$ configuration under various pressures for the $x = 0.12$ sample. Three regions are identified and separated by the local maximum and minimum of T_c under pressure (panels (a), (b) and (c), respectively). A clear change of the $H_{c2}(T)$ slope is observed between the first and second region only (panel (d)). Insets show representative resistance data under magnetic fields up to 9 T.

transitions, but no fundamental difference with different current directions was observed between the measurements. At ambient pressure, the superconducting transition remains sharp for all field values. As the pressure is increased the superconducting transition becomes broader, especially in the $x = 0.096$ and $x = 0.12$ samples.

A distinct change of the slope of $H_{c2}(T)$, which is abtained by fitting the 0-9 T date, is observed between 0.57 GPa and 0.71 GPa (between 0.27 GPa and 0.35 GPa) for $x = 0.043$ ($x = 0.096$). For $x = 0.12$, a slope change occurs between ambient pressure and 0.4 GPa (Figures 9-11 (d)). These pressure ranges are close to the local maximum of T_c and, for $x = 0.043$ and $x = 0.096$, the onset of magnetic order. No abrupt slope change of H_{c2} occurs around the pressure associated local minimum of T_c.

Fig 3.12 shows the pressure evolution of the upper critical field slope normalized by T_c, -$[d\mu_o H_{c2}/dT_c]/T_c$, and of the transition temperatures T_c, T_s, T_m for $x = 0$ (Ref. Kaluarachchi et al. (2016)), $x = 0.043$, $x = 0.096$ and $x = 0.12$. For all substitution levels, -$[d\mu_o H_{c2}/dT_c]/T_c$ exhibits a sudden decrease near the local maximum of T_c under pressure. For the substituted compounds, a more continuous change is observed near the local minimum of T_c at which point -$[d\mu_o H_{c2}/dT_c]/T_c$ has a broad maximum.

Generally speaking, the slope of the upper critical field normalized by T_c, is related to the Fermi velocity and superconducting gap of the systemKogan and Prozorov (2012). In the clean limit for a single-band case,

$$-[d\mu_o H_{c2}/dT_c]/T_c \propto 1/v_F^2, \tag{3.1}$$

where v_F is the Fermi velocity. Note that the mass enhancement expected at a quantum critical point should result in an increase of -$[d\mu_o H_{c2}/dT_c]/T_c$ (Ref. Putzke et al. (2014)). The superconducting gap structure and, in a multiband-case, the coupling constants for the different bands are also involvedKogan and Prozorov (2012). A change of the normalized slope of H_{c2} may result from changes of the Fermi surface, of the superconducting gap structure or of the pairing mechanismTaufour et al. (2014); Kogan and Prozorov (2012). In addition, a change of scattering rates can also change H_{c2} (Ref. Kogan and Prozorov (2014)). It was previously shown in pure

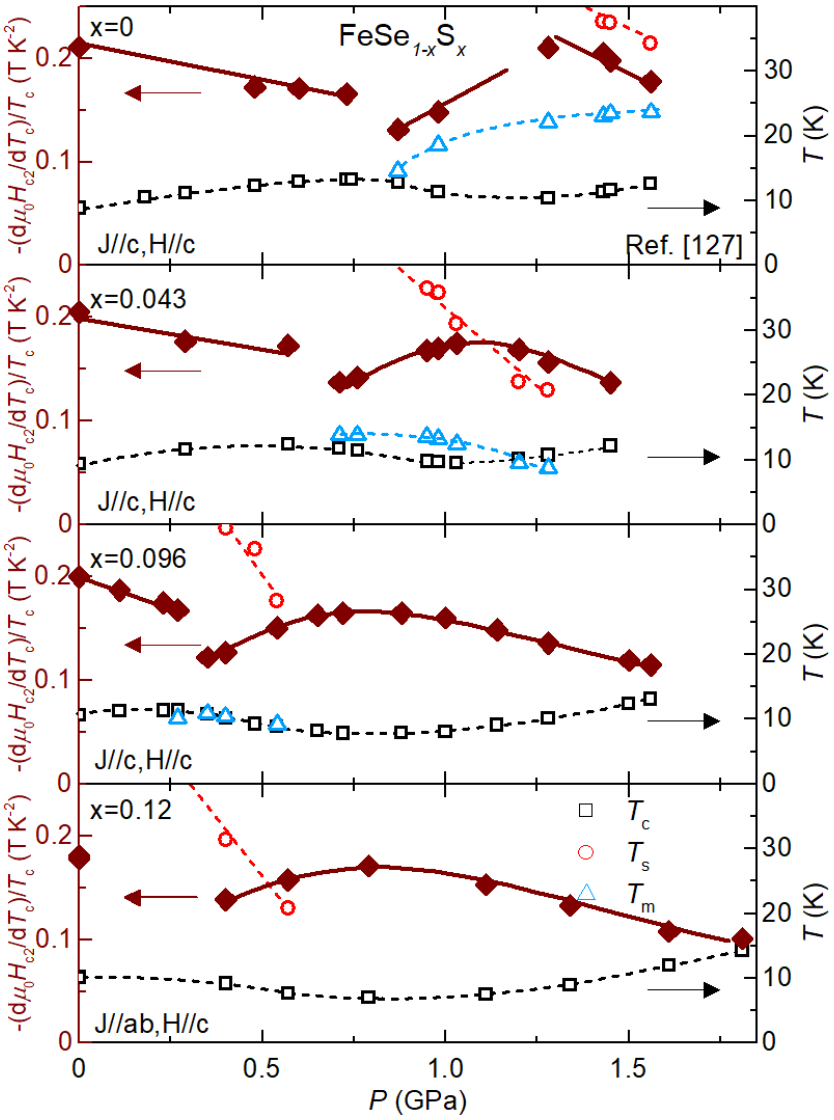

Figure 3.12 Pressure dependence of the normalized upper critical field slope $-[d\mu_o H_{c2}/dT_c]/T_c$, plotted together with T_c, T_s and T_m. For all compounds, an abrupt change of slope is observed near the local maximum of T_c. For the sulfur-containing compounds, a more continuous change of the slope occurs near the local minimum of T_c. Date in (a) is taken from Ref. Kaluarachchi et al. (2016).

FeSe that both the decrease of -$[d\mu_o H_{c2}/dT_c]/T_c$ close to the local maximum of T_c as well as its increase close to the local minimum of T_c under pressure can be explained by changes in the Fermi velocity Kaluarachchi et al. (2016).

Similarly to pure FeSe, -$[d\mu_o H_{c2}/dT_c]/T_c$ of $Fe(Se_{1-x}S_x)$ displays an abrupt decrease close to the local maximum of T_c under pressure for all studied substitution levels. This points to a similar change of Fermi velocity as in the parent compound and supports the identification of this pressure level with the emergence of magnetic order entailing a reconstruction of the Fermi surface. Possibly, a change of electronic scattering rates at the onset of magnetic order also influences H_{c2}. The subsequent broad maximum of -$[d\mu_o H_{c2}/dT_c]/T_c$ results from dividing an almost pressure independent $d\mu_o H_{c2}/dT_c$ (Figs 9-11 (d)) by T_c, since T_c displays a minimum in this pressure range. This maximum of the normalized slope of H_{c2} may also be associated with a pressure-induced Fermi surface change or with a gradual mass enhancement at this pressure. Note that a pressure-independent $d\mu_o H_{c2}/dT_c$ indicates that $T_c \propto v_F^2$, according to equation 5.1.

3.5 Conclusion

In conclusion, the resistance of sulfur-substituted $FeSe_{1-x}S_x$ ($x = 0.043, 0.096, 0.12$) has been studied under pressures up to 1.8 GPa and in magnetic fields up to 9 T. T_c exhibits a similar, non-monotonic pressure dependence with a local maximum and a local minimum for all substitution levels. T_s is suppressed by pressure, at increasing rates for higher sulfur contents. The magnetic phase in the low-pressure range is strongly suppressed by substitution, which raises the question of how closely magnetic order and orthorhombic phase are related. Abrupt changes in the normalized slope of the upper critical field -$[d\mu_o H_{c2}/dT_c]/T_c$ near the local maximum of T_c may indicate a Fermi-surface reconstruction coinciding with the transition at T_m for $x = 0 - 0.096$ and suggest its existence in $x = 0.12$ as well. Another change of Fermi surface likely occurs near the local minimum of T_c at slightly higher pressures. These results highlight the differences between chemical pressure and physical pressure as tuning parameters for FeSe.

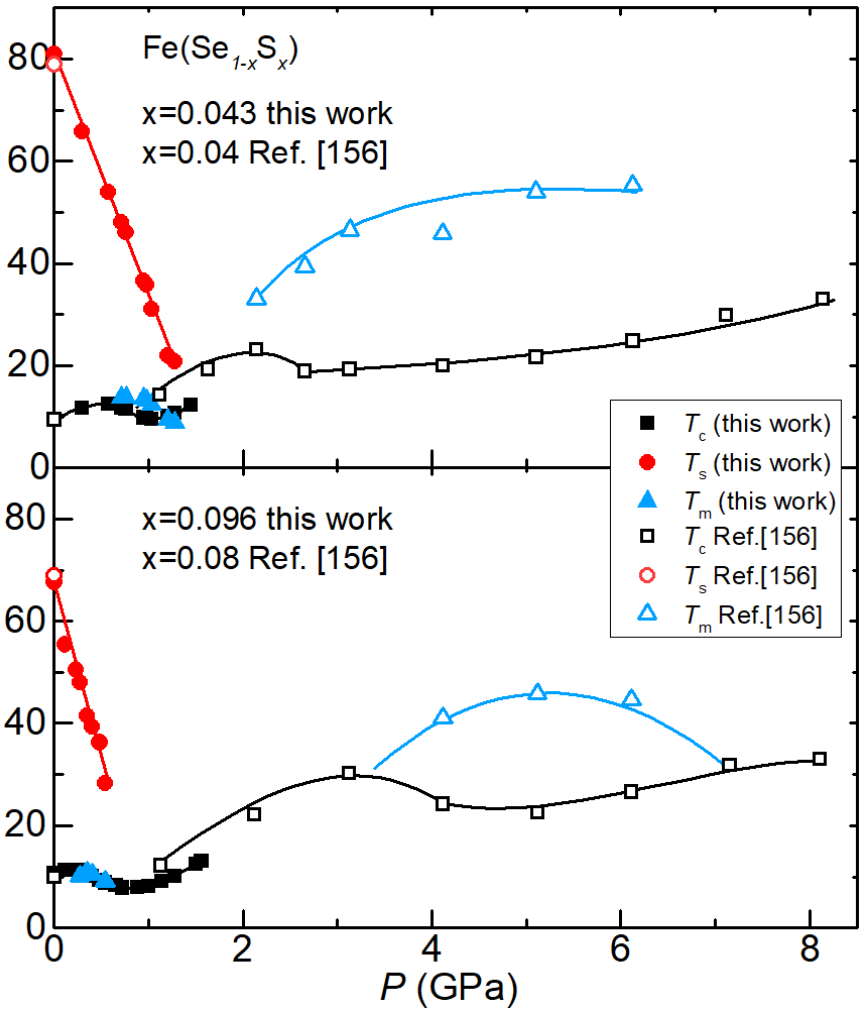

Figure 3.13 Temperature - pressure phase diagrams of $Fe(Se_{1-x}S_x)$ up to 8 GPa, including data from Ref. Matsuura et al. (2017). The squares, circles and triangles circles represent the superconducting T_c, structural T_s and magnetic T_m phase transitions respectively. Data from samples with similar T_s value at ambient pressure are combined. The solid lines are guides to the eye. This represents an extension of our detailed low-pressure phase diagrams presented in Fig. 3.7.

Note added: During the finalization of this manuscript, related results on the pressure-temperature phase diagrams of $Fe(Se_{1-x}S_x)$ ($x = 0.04 - 0.17$) with a focus on the higher pressure range 2-8 GPa were made availableMatsuura et al. (2017). By means of resistivity measurements in a cubic anvil cell, a prominent dome of likely magnetic order was found to exist in the higher pressure range, detached from the nematic phase for $x \geq 0.04$. Taken together with the results presented here, this indicates that the pressure-temperature phase diagram of lightly S-substituted $Fe(Se_{1-x}S_x)$ features two magnetic phases (see Fig. 3.13), possibly resulting from a splitting of the single pressure-induced magnetic dome of pure FeSe. The mechanism by such a splitting would occur remains to be studied, as indeed, the microscopic nature of the pressure-induced phases and their relation to each other. Altogether, the recent results reveal the astounding complexity of pressure- and substitution-tuned FeSe.

3.6 Appendix

Fig. 3.14 presents the low-temperature resistance data for $FeSe_{0.904}S_{0.096}$ in the pressure range 0.27 - 0.54 GPa and under applied magnetic fields up to 9 T. The superconductivity is suppressed by the applied magnetic field. For fields greater than 7 T, a slight upturn of the resistance is observed. We associate this anomaly with magnetic phase transition and the corresponding T_m at 9 T is indicated by an arrow.

An additional anomaly is observed in the resistance measurement for $FeSe_{0.957}S_{0.043}$ under pressure. As shown in Fig. 3.15, in pressure range 0.95 - 1.45 GPa, two anomalies emerge above the superconducting transition. We associated the lower-temperature anomaly with the magnetic transition T_m due to its similarities with the parent compound FeSeSun et al. (2016). The other anomaly, labeled T_m^*, occurs slightly above T_m and is indicated in Figs. 3.6 and 3.15. For 0.71 GPa, only T_m is observed. From 0.95 - 1.03 GPa, both of these anomalies can be seen in zero field resistance measurements. Furthermore, with application of magnetic fields up to 9 T, these two anomalies barely shift. At higher pressures 1.2 - 1.45 GPa, those anomalies are no longer discernible in the zero field resistance measurements. However, by suppressing the

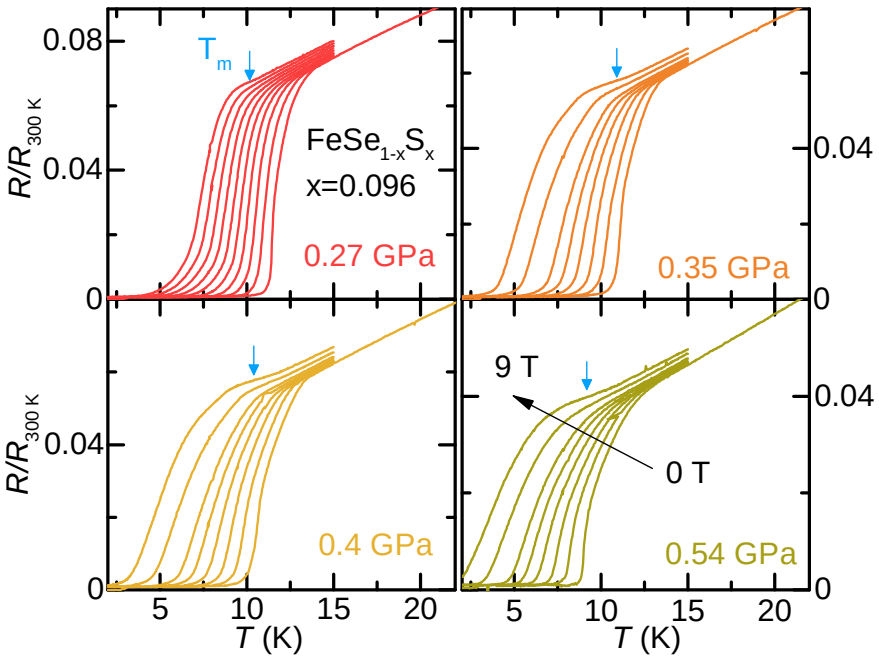

Figure 3.14 Temperature dependence of the normalized resistance under magnetic field up to 9 T for selected pressures for compound $FeSe_{1-x}S_x$, $x = 0.096$. The anomaly associated with magnetic transition T_m is indicated by arrow.

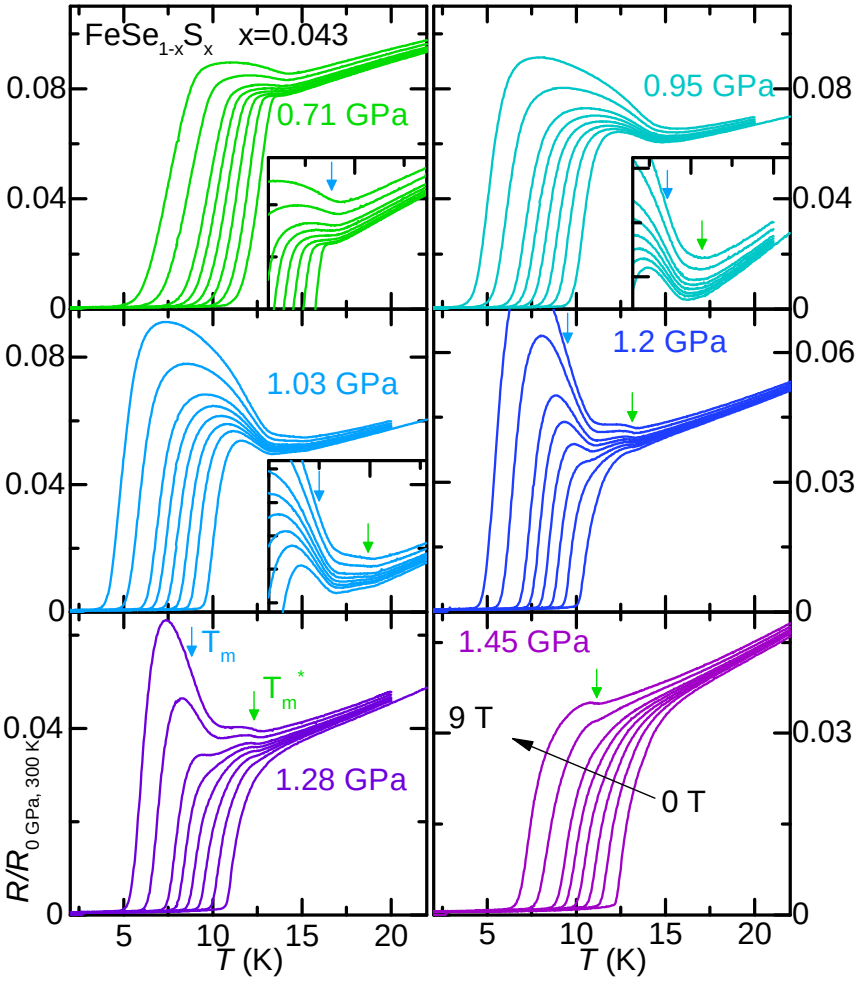

Figure 3.15 Temperature dependence of the normalized resistance under magnetic field up to 9 T for selected pressures for compound $FeSe_{1-x}S_x$, $x = 0.043$. Two anomalies associated with magnetic transition T_m and possibly another magnetic transition T_m^* are indicated by arrows.

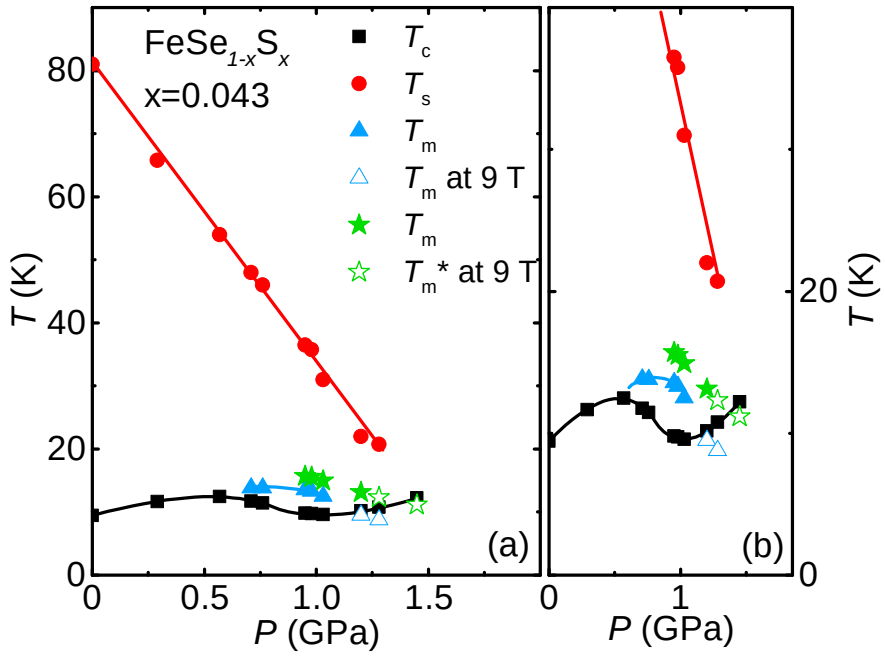

Figure 3.16 Extended temperature - pressure phase diagram of $FeSe_{0.957}S_{0.043}$ as determined from resistance measurement as in Fig. 3.7. The T_m^*, indicated by green stars, represents the new anomaly we observed in this compound. The solid lines are guides for the eye.

superconducting transition with magnetic field, they are revealed in resistance for 1.2 GPa and 1.28 GPa. At our highest pressure of 1.45 GPa, only T_m^* could be observed.

The temperature - pressure phase diagram of $FeSe_{0.957}S_{0.043}$ complemented by including T_m^* is presented in Fig. 3.16. T_m exhibits a dome-like pressure dependence, whereas T_m^* emerges on the high-pressure side of this dome. Whether this new anomaly T_m^* is related to a possible incommensurate magnetic transition or a different phase transition needs further studies.

CHAPTER 4. PRESSURE-TEMPERATURE PHASE DIAGRAM OF $CaK(Fe_{1-x}Ni_x)_4As_4$ SUPERCONDUCTORS

The following context is a slightly modified version of the published work in Ref. Xiang et al. (2018a). DOI: https://link.aps.org/doi/10.1103/PhysRevB.97.174517. Reprinted (abstract/excerpt/figure) with permission from [L. Xiang *et. al.*, Phys. Rev. B 97, 174517 (2018)]

4.1 Introduction

Since the discovery of Fe-based superconductors (FeSC) Kamihara et al. (2008); Ren et al. (2008); Rotter et al. (2008); Takahashi et al. (2008), many studies have been done on them and they have expanded into a large family. Among them the $Ae Fe_2As_2$ compounds (Ae=Ca, Sr, Ba, Eu) have received significant attention because large, high-quality single crystals can be obtained with a variety of chemical substitutionCanfield and Bud'ko (2010); Ni and Bud'ko (2011). Studies have revealed that members of this family share a global phase diagram upon tuning by substitution or pressurePaglione and Greene (2010); Canfield and Bud'ko (2010). At ambient pressure, the parent compounds undergo a structural/magnetic transition upon cooling; substitution or pressure induce superconductivity after sufficiently suppressing the structural/magnetic transitionsCanfield and Bud'ko (2010); Ni and Bud'ko (2011); Torikachvili et al. (2008a); Alireza et al. (2009); Kimber et al. (2009); Colombier et al. (2009). This suggests a competition between the magnetism and superconductivity, and that magnetic fluctuations play an important role in forming superconductivity in this systemPratt et al. (2009); Christianson et al. (2009); Fernandes et al. (2010); Christianson et al. (2008); Yu et al. (2009a); Paglione and Greene (2010).

Recently, a new FeSC $AeA\mathrm{Fe_4As_4}$ (A=K, Rb, Cs) structural type ($P4/mmm$) was discovered by Iyo *et al*Iyo et al. (2016). This is not a homogeneous substitution as in $(Ae_{0.5}A_{0.5})\mathrm{Fe_2As_2}$ where Ae/A share the same crystallographic site. Each Ae and A in the $AeA\mathrm{Fe_4As_4}$ structure has a unique, well-defined, crystallographic site, forming alternating Ae and A planes along the c-axisIyo et al. (2016); Meier et al. (2016). Among them, single crystals of $\mathrm{CaKFe_4As_4}$ were synthesized and found to be superconducting at $\sim$ 35 K and no other phase transition from 1.8 K to 300 K at ambient pressureMeier et al. (2016, 2017). A pressure study up to 6 GPa shows that the superconducting transition temperature, T_c, is suppressed to about 28.5 K before it undergoes half-collapsed-tetragonal (hcT) phase transition at $\sim$ 4 GPa and loses bulk superconductivityKaluarachchi et al. (2017b). The hcT phase transition occurs due to the As-As bonding across the Ca-layer under pressure, like the collapsed-tetragonal transition in $\mathrm{CaFe_2As_2}$ at $\sim$0.35 GPaTorikachvili et al. (2008b); Yu et al. (2009b); Kreyssig et al. (2008).

From the perspective of electron count, $\mathrm{CaKFe_4As_4}$ is analogous to $(\mathrm{Ba_{0.5}K_{0.5}})\mathrm{Fe_2As_2}$ and many of its properties are consistent with thisMeier et al. (2016). In the later compound, the stripe-type spin density wave associated with $\mathrm{BaFe_2As_2}$ is suppressed by hole dopingPaglione and Greene (2010) (substitution K for Ba). A recent study revealed that adding electrons to $\mathrm{CaKFe_4As_4}$ via Ni or Co substitution drives the system back towards a magnetic phase. In contrast to the stripe-type antiferromagnetism in the "122" systems, the order in the Ni- or Co-substituted $\mathrm{CaKFe_4As_4}$ is experimentally identified as a new hedgehog spin-vortex-crystal (SVC) magnetism that has no structural phase transition associated with itMeier et al. (2018). This type of magnetic order had been theoretically predicted but until the discovery of Ni- or Co-substituted $\mathrm{CaKFe_4As_4}$, was considered to be a "missing link"Fernandes et al. (2016); Cvetkovic and Vafek (2013); O'Halloran et al. (2017). Increasing the substitution level of Ni or Co in $\mathrm{CaK(Fe_{1-x}}T_x)_4\mathrm{As_4}$ leads to the suppression of the superconducting transition temperature T_c and stabilizing the SVC magnetism and increasing T_NMeier et al. (2018).

The application of pressure to $\mathrm{Ba(Fe_{1-x}Co_{\mathit{x}})_2As_2}$ suppresses AFM (T_N falls) and increases T_cColombier et al. (2010). This has been taken as an indication that pressure, like doping, can

tune T_N and the associated AFM fluctuations to favor the superconducting state when $T_N > T_c$. Therefore, it is natural to study how the SVC magnetic order behaves under pressure, specifically, how the magnetism and superconductivity interact in this system and whether this interaction is similar to $Ba(Fe_{1-x}Co_x)_2As_2$.

In this work, we present the first pressure study on Ni-substituted $CaK(Fe_{1-x}Ni_x)_4As_4$ ($x = 0.033$ and 0.050) up to 5.12 GPa. The pressure-temperature ($p-T$) phase diagrams inferred from resistance measurements allow comparison of $T_N(p)$ and $T_c(p)$. Specifically, $p-T$ phase diagrams reveal that T_N is suppressed with pressure for both substitution levels. In contrast to $Ba(Fe_{1-x}Co_x)_2As_2$, T_c is suppressed as well, although more slowly. For $x = 0.050$, it exhibits an anomaly at the pressure where T_c and T_N cross. At ~ 4 GPa both compositions appear to undergo the hcT transition as was observed in the undoped $CaKFe_4As_4$. Furthermore, superconducting upper critical fields studied up to 9 T suggests a Fermi-surface reconstruction when $T_N(p)$ crosses $T_c(p)$.

4.2 Experimental details

Single crystals of $CaK(Fe_{1-x}Ni_x)_4As_4$ ($x = 0.033$ and 0.050) with sharp superconducting transitions at ambient pressure [See Figs 1(b)-3(b)] were grown using high-temperature solution growthMeier et al. (2016, 2017). The substitution level, x, was determined by performing wavelength-dispersive x-ray spectroscopy (WDS) as described in Ref. Meier et al. (2018).

The in-plane ab resistance was measured using standard four-probe configuration. The 25 μm Pt wires were soldered to the samples using a Sn:Pb-60:40 alloy. For $x = 0.033$, two samples, #1 and #2, were cut from one single crystal. They were then measured in a piston-cylinder cell (PCC)Bud'ko et al. (1984) and a modified Bridgman Anvil Cell (mBAC)Colombier and Braithwaite (2007) respectively. For $x = 0.050$, a single sample was prepared and measured in the mBAC. Pressure values for both cells, at low temperature, were inferred from the $T_c(p)$ of leadBireckoven and Wittig (1988). For the PCC, a 4:6 mixture of light mineral oil:n-pentane was used as the pressure medium, which solidifies, at room temperature, in the range of 3-4 GPa. For

the mBAC, a 1:1 mixture of iso-pentane:n-pentane was used as the pressure medium, which solidifies, at room temperature, in the range of 6-7 GPa. Both of the solidification pressures are well above the maximum pressures achieved in the pressure cells, which suggests good hydrostatic conditionsBud'ko et al. (1984); Kim et al. (2011); Torikachvili et al. (2015).

The ac resistance measurements were performed in a Quantum Design Physical Property Measurement System using $I = 1$ mA; $f = 17$ Hz excitation, on cooling with the rate of 0.25 K/min and the magnetic field was applied along the c axis.

4.3 Results and discussions

Figs. 1(a) and 2(a) show the pressure dependence of the temperature dependent resistance for $CaK(Fe_{1-x}Ni_x)_4As_4$, $x = 0.033$. Sample #1 was measured in the PCC for pressures up to 1.83 GPa. Sample #2 was measured in the mBAC for pressures up to 5.12 GPa. For both samples, the 0 GPa resistance was corrected for geometric changes to the sample via normalization. (Details of the normalization are described in the Appendix.) Fig. 3(a) shows the pressure dependence of the temperature dependent resistance for the $x = 0.050$ sample that was measured in the mBAC for pressures up to 5.12 GPa. In general, for all samples, the resistance decreases under applied pressure.

For both compositions, the magnetic phase transition T_N appears as a kink-like anomaly in the lower temperature data and is more pronounced in the $x = 0.050$ compound. This feature is more clearly revealed as a step-like anomaly in the temperature derivative dR/dT [Figs. 1(c),2(c) and 3(c)]. These plots demonstrate that T_N is suppressed by increasing pressure before it disappears at higher pressures.

The blowups of the low temperature resistance [Figs. 1(b), 2(b) and 3(b)] show how T_c changes under increasing pressure. For $x = 0.033$, T_c monotonically decreases in the studied pressure range. In contrast, for $x = 0.050$, after 2.41 GPa there is a slight enhancement of the T_c before it is suppressed again at higher pressures.

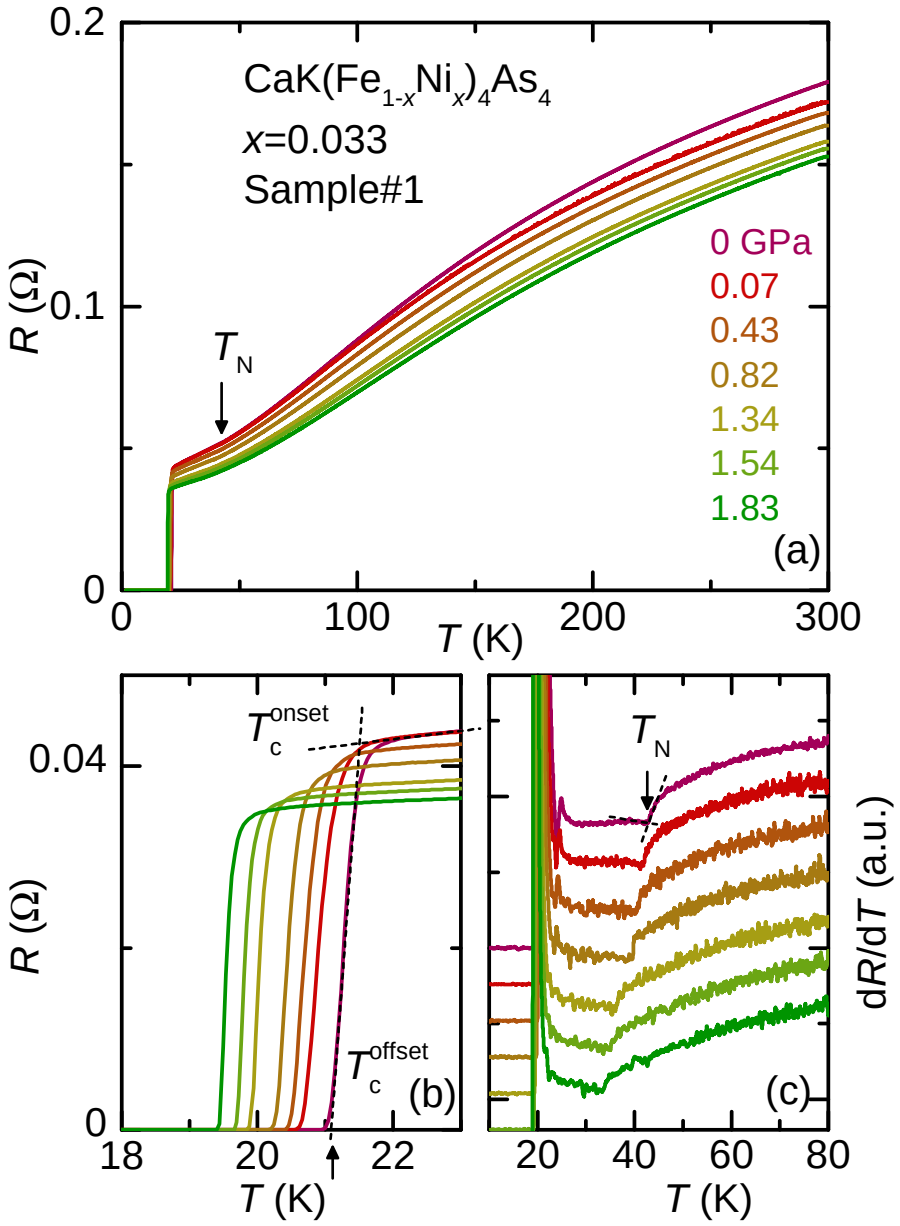

Figure 4.1 (a) Evolution of the in-plane resistance with hydrostatic pressures up to 1.83 GPa measured in a PCC for the $CaK(Fe_{0.967}Ni_{0.033})_4As_4$, sample#1. (b) Blowup of the low temperature region. Criteria for T_c^{onset} and T_c^{offset} are indicated in the figure. (c) Temperature derivative, dR/dT, showing the evolution of the magnetic transition T_N with offset criteria as shown in the figure.

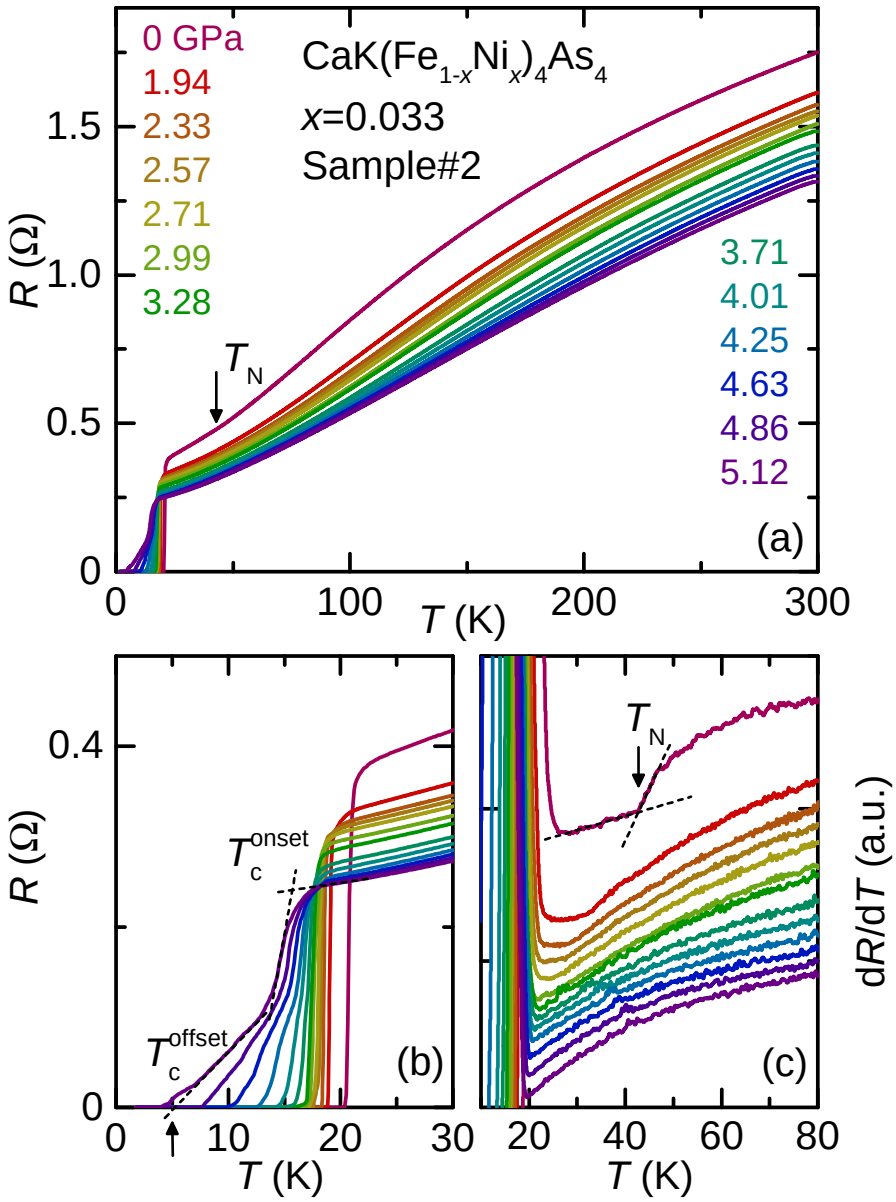

Figure 4.2 (a) Evolution of the in-plane resistance with hydrostatic pressures up to 5.12 GPa measured in a mBAC for $CaK(Fe_{0.967}Ni_{0.033})_4As_4$, sample#2. (b) Blowup of the low temperature region. (c) Temperature derivative, dR/dT, showing the evolution of magnetic transition T_N.

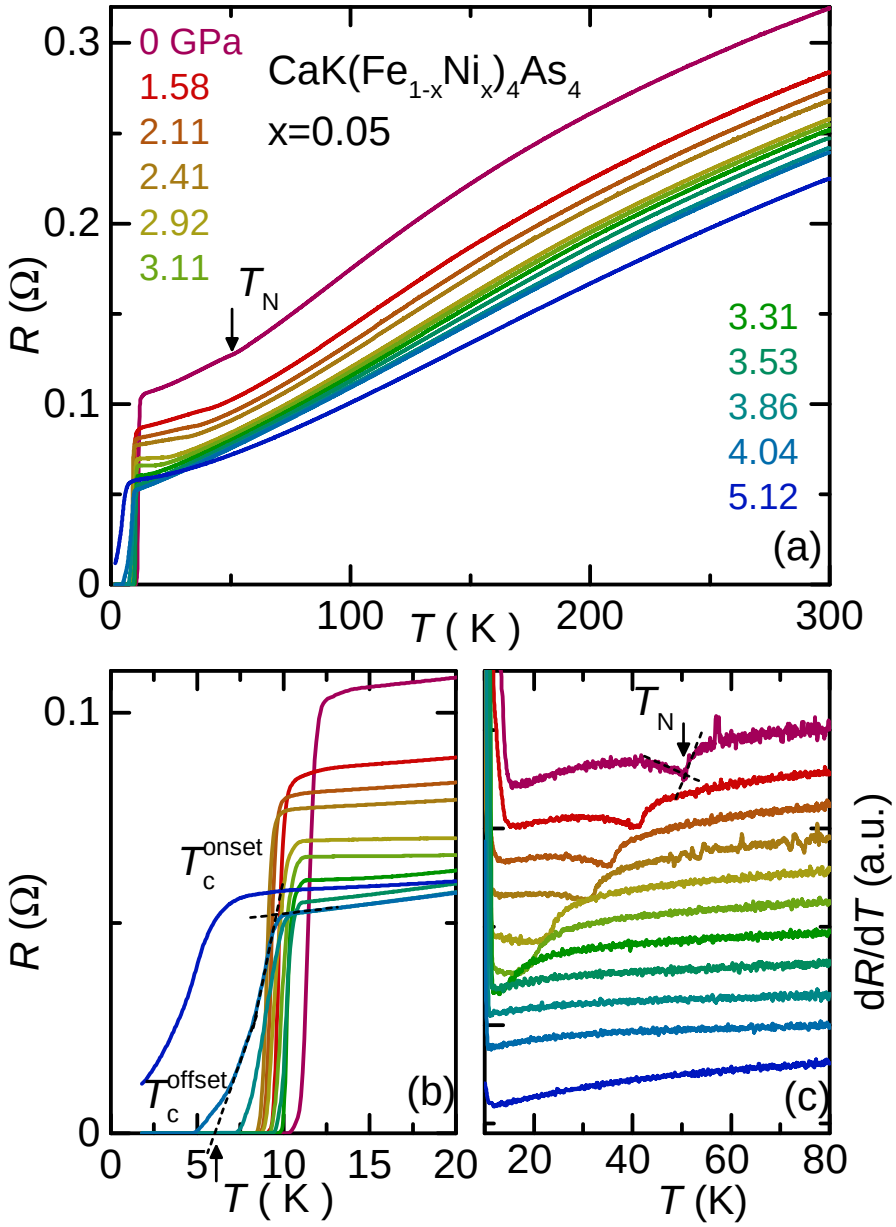

Figure 4.3 (a) Evolution of the in-plane resistance with hydrostatic pressures up to 5.12 GPa measured in a mBAC for $CaK(Fe_{0.95}Ni_{0.05})_4As_4$. (b) Blowup of the low temperature region. (c) Temperature derivative, dR/dT, showing the evolution of magnetic transition T_N.

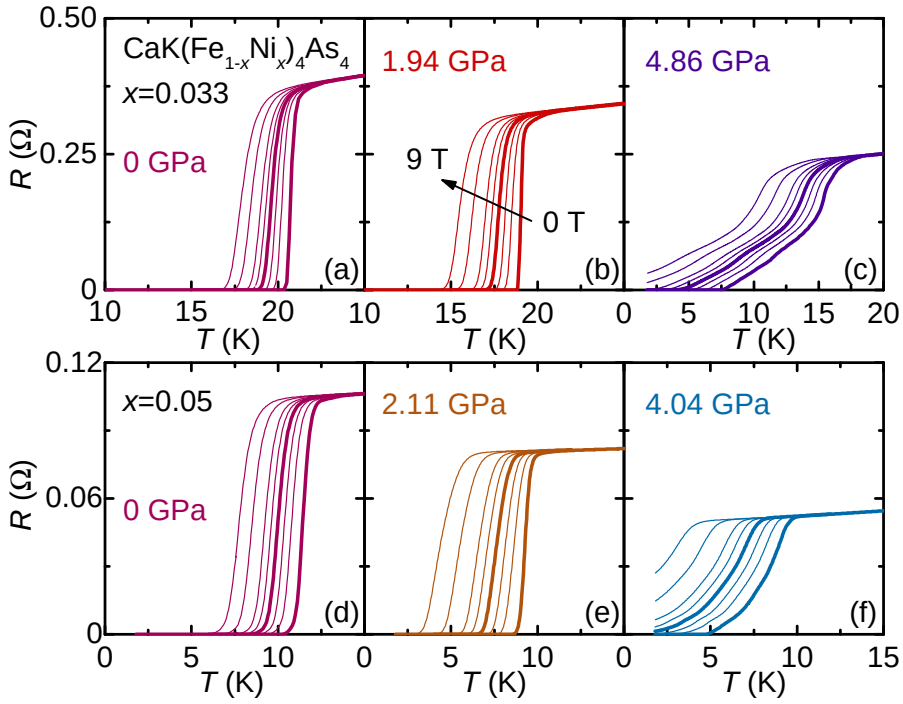

Figure 4.4 Temperature dependence of resistance under magnetic field up to 9 T for selective pressures for $CaK(Fe_{1-x}Ni_x)_4As_4$, $x = 0.033$ ((a)-(c)), $x = 0.050$ ((d)-(f)). Superconducting transition becomes broader as pressure is increased for both compounds, to explore the nature of the broadening, transition width at 0 T and 3 T (indicated by thick lines in the figures) were analyzed and described in details in the text.

Upon increasing pressures above ~ 4 GPa, the sharp superconducting transition at lower pressures becomes broadened at higher pressures. A similar behavior was also observed in the parent compound $CaKFe_4As_4$ and has been associated with the hcT phase transition at $p \gtrsim 4$ GPaKaluarachchi et al. (2017b). In order to understand the nature of the broadening in the substituted system, analysis similar to that in Ref. Kaluarachchi et al. (2017b) was carried out.

Fig. 4.4 presents the temperature dependence of the resistance under magnetic field up to 9 T for selected pressures. The superconducting transition width, $\Delta T = T_c^{\text{onset}} - T_c^{\text{offset}}$, is broadened with increasing pressure, with the criteria for T_c^{onset} and T_c^{offset} shown in Figs. 1(b), 2(b) and 3(b). In order to determine whether the broadening is associated with any sort of phase transition, or is simply due to pressure inhomogeneities in the pressure medium when larger loads

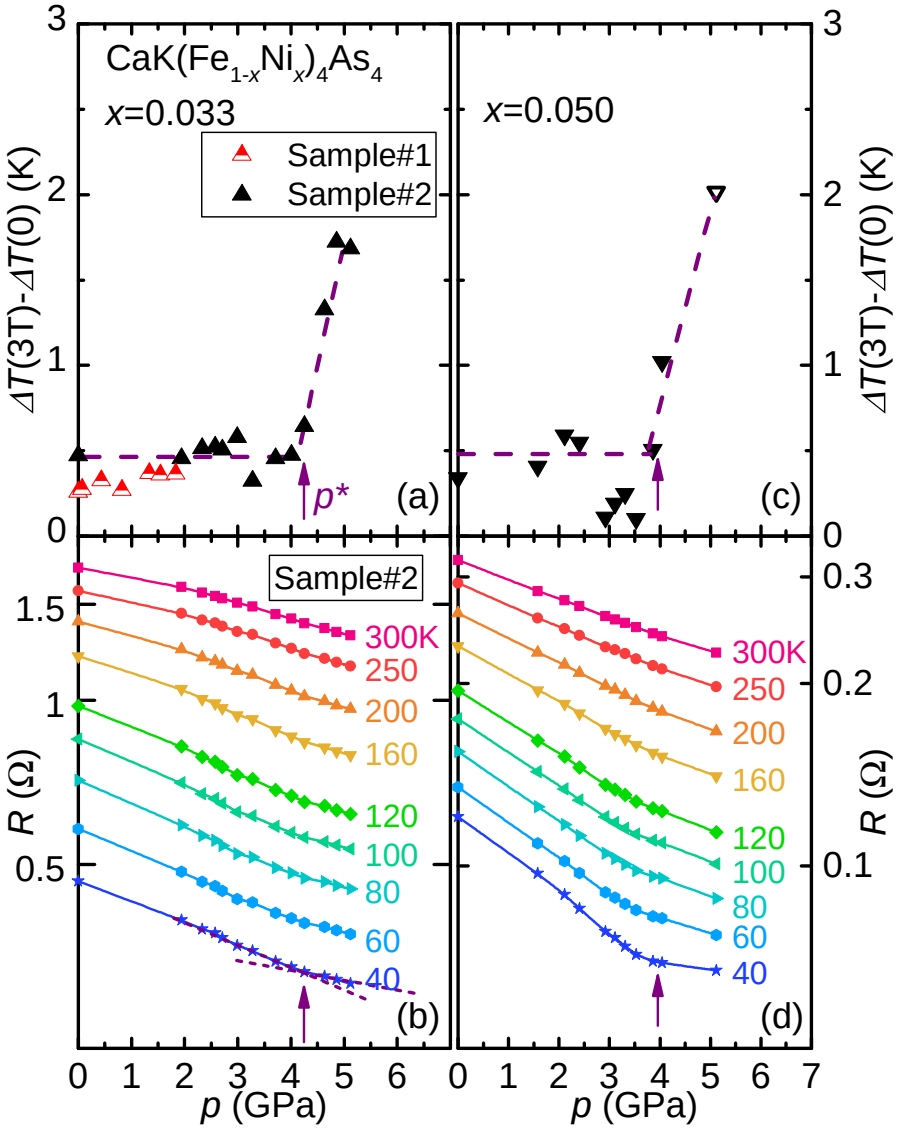

Figure 4.5 (a),(c) Pressure dependence of the superconducting transition widths difference for $CaK(Fe_{1-x}Ni_x)_4As_4$, $x = 0.033$ and 0.050 respectively. The superconducting transition widths is $\Delta T = T_c^{onset} - T_c^{offset}$ and the widths difference is taken between 0 field and 3 T. Open symbol in panel (c) is the widths difference taken between 0 field and 1 T because of no clear definition of T_c^{offset} at 3 T for 5.12 GPa. (b), (d) Pressure dependence of resistance at $R(p)$ fixed temperatures for $CaK(Fe_{1-x}Ni_x)_4As_4$, $x = 0.033$ and 0.050 respectively. The critical pressure p^*(Arrows in the figure) which is associated with the hcT phase is described in details in the text.

are applied, the field dependence of the superconducting transition width $\Delta T(H)$ was studiedKaluarachchi et al. (2017b). Specifically, the transition width at magnetic fields 0 T and at 3 T (indicated by thicker lines in Figs. 4.4) were determined, and then the difference between them, $\Delta T(3\mathrm{T}) - \Delta T(0)$, was calculated. Any broadening due to the pressure inhomogeneities are expected to be equally present in the $H = 0$ T and 3 T data. Figs. 4.5(a) and (c) present the pressure dependence of the transition width difference. As it is clearly shown, for both compositions, $\Delta T(3\mathrm{T}) - \Delta T(0)$ increases dramatically as pressure goes above $p^* \sim 4$ GPa (indicated by arrows in Figs. 4.5(a), (c)). Note that for $x = 0.050$, at 5.12 GPa, the transition width difference was taken between $H = 0$ T and 1 T, because T_c^{offset} is not clearly defined at $H = 3$T. But we would expect the transition width difference between $H = 0$ T and 3 T to be even larger at this pressure. Furthermore, the pressure dependence of the resistance $R(p)$ at fixed temperatures for both compositions (Figs. 4.5(b), (d)) shows anomaly at the same pressure at 40 K (indicated by arrows in the figure), though subtle for $x = 0.033$. Based on the analogy with the parent compound $CaKFe_4As_4$Kaluarachchi et al. (2017b), we identify this anomaly as an indication of the hcT phase transition that exists from base temperature up to at least 40 K. As was the case for pure $CaKFe_4As_4$, we believe that superconductivity is not bulk for $p \gtrsim 4$ GPa (i.e. in the hcT phase).

The upper superconducting critical field H_{c2} can be evaluated from Fig. 4.4 at pressures lower than p^*, where superconductivity is considered bulk, using the offset criteria defined in Figs. 1-3. The temperature dependence of H_{c2} at various pressures is presented in Figs. 4.6 and 4.7 for $CaK(Fe_{1-x}Ni_x)_4As_4$, $x = 0.033$ and 0.050 respectively. For $x = 0.033$, both Sample#1 and Sample#2 were analyzed and plotted in Fig 4.6. Note that at ambient pressure, T_c^{offset} values for two samples differ by ∼0.5 K, possibly due to a small difference of the substitution level at different positions of the crystal they were cut from. As is shown in Figs. 4.6 and 4.7, for $x = 0.033$, H_{c2} is systematically suppressed by increasing pressure, whereas, for $x = 0.050$, the evolution of the temperature dependent H_{c2} is nonmonotonic. For both compositions, H_{c2} is linear in temperature except for magnetic fields below 1 T. The curvature at low fields has been

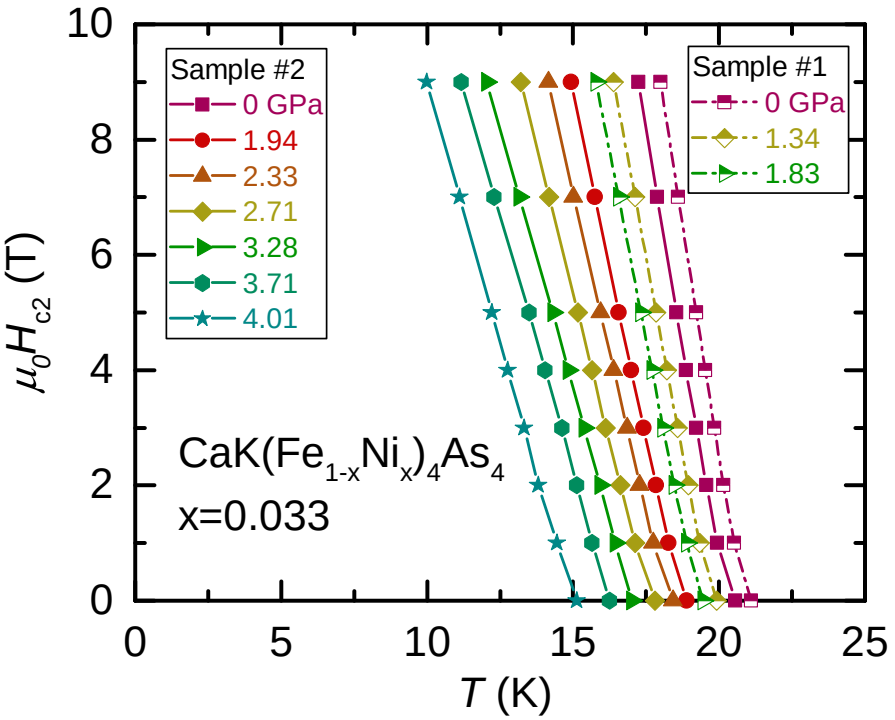

Figure 4.6 Temperature dependence of the upper superconducting critical field, $H_{c2}(T)$, under selected pressures for $CaK(Fe_{1-x}Ni_x)_4As_4$, $x = 0.033$. T_c^{offset} is used for the figure. Half filled and solid symbols are two samples measured in PCC and mBAC respectively.

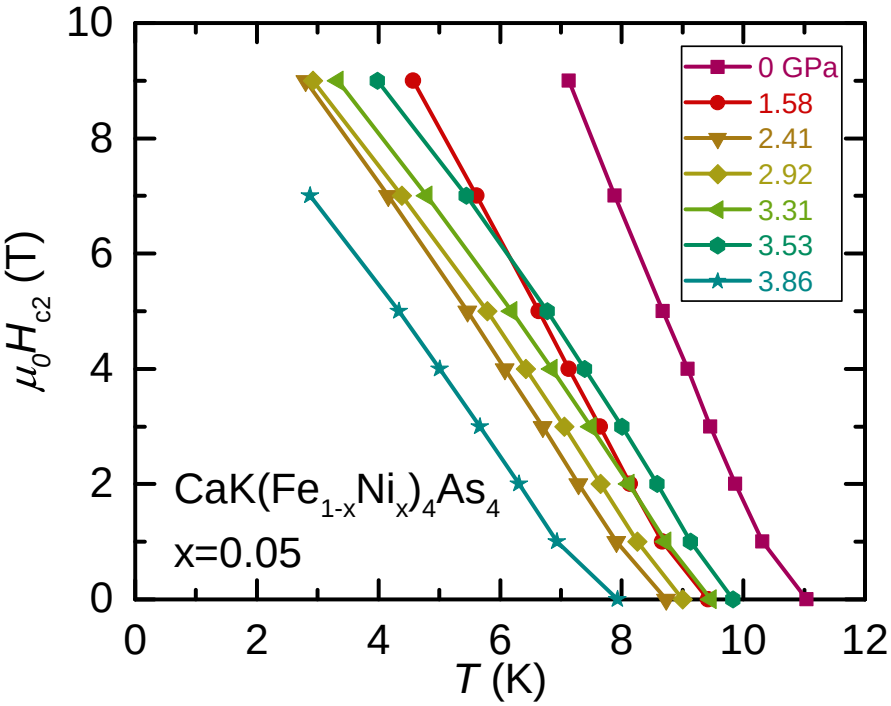

Figure 4.7 Temperature dependence of the upper superconducting critical field, $H_{c2}(T)$, under selected pressures for $CaK(Fe_{1-x}Ni_x)_4As_4$, $x = 0.050$. T_c^{offset} is used for the figure.

observed in other FeSC and can be explained by nature of superconductivityKogan and Prozorov (2012); Kaluarachchi et al. (2016); Xiang et al. (2017), which is also the case for the parent compound $CaKFe_4As_4$Mou et al. (2016).

Figs. 4.8(a) and 4.9(a) present the $p-T$ phase diagrams for $CaK(Fe_{1-x}Ni_x)_4As_4$, $x = 0.033$ and 0.050 respectively, with T_c^{offset} and T_N values obtained using the criteria shown in Figs. 1-3 and the indication of non-bulk superconductivity above p^*. For both compositions, T_N is suppressed by pressure, specifically, T_N is suppressed from 43 K to 25 K at 2.71 GPa for $x = 0.033$ and suppressed from 51 K to 13.8 K at 3.31 GPa for $x = 0.050$.

In terms of superconductivity, for x=0.033, T_c^{offset} is monotonically suppressed with increasing pressure. It drops from 20.5 K to 15.1 K at 4.01 GPa before superconductivity becomes non-bulk. A closer examination reveals that T_c^{offset} is initially linearly suppressed by pressure up to 2.71 GPa, then a small, but clear deviation from the linear suppression was observed above 2.99 GPa. An extrapolation of T_N shows that the deviation happens near the crossing of T_N and T_c^{offset} lines. For $x = 0.050$, the behavior of $T_c^{\text{offset}}(p)$ is distinctly non-monotonic. T_c^{offset} is initially linearly suppressed from 11 K to a local minimum of 8.7 K at 2.41 GPa. Then it rises to a maximum of 10 K at 3.31 GPa, exhibiting a dome shape. This dome of enhanced T_c^{offset} coincides with the disappearance of T_N. After the local maximum in T_c^{offset} there is a much more rapid suppression of T_c^{offset} with increasing p until the hcT transition at p^*. For both compositions, a change in $T_c^{\text{offset}}(p)$ happens at the pressure where T_N and T_c^{offset} lines cross.

Both compositions show signatures of non-bulk superconductivity above $p^* \sim 4$ GPa (blue symbols in Figs. 4.8(a), 4.9(a)) similar to the parent compound $CaKFe_4As_4$Kaluarachchi et al. (2017b), suggesting the same hcT phase transition. Pressure dependent resistance data in Fig. 4.5 demonstrates that the hcT phase transition is discernable up to at least 40 K for the substituted compounds. The transition pressure does not appear to change with Ni-substitution. This is not too surprising given the fact that the hcT transition does not involve the Fe-plane but is, instead As-As bonding across the Ca plane.

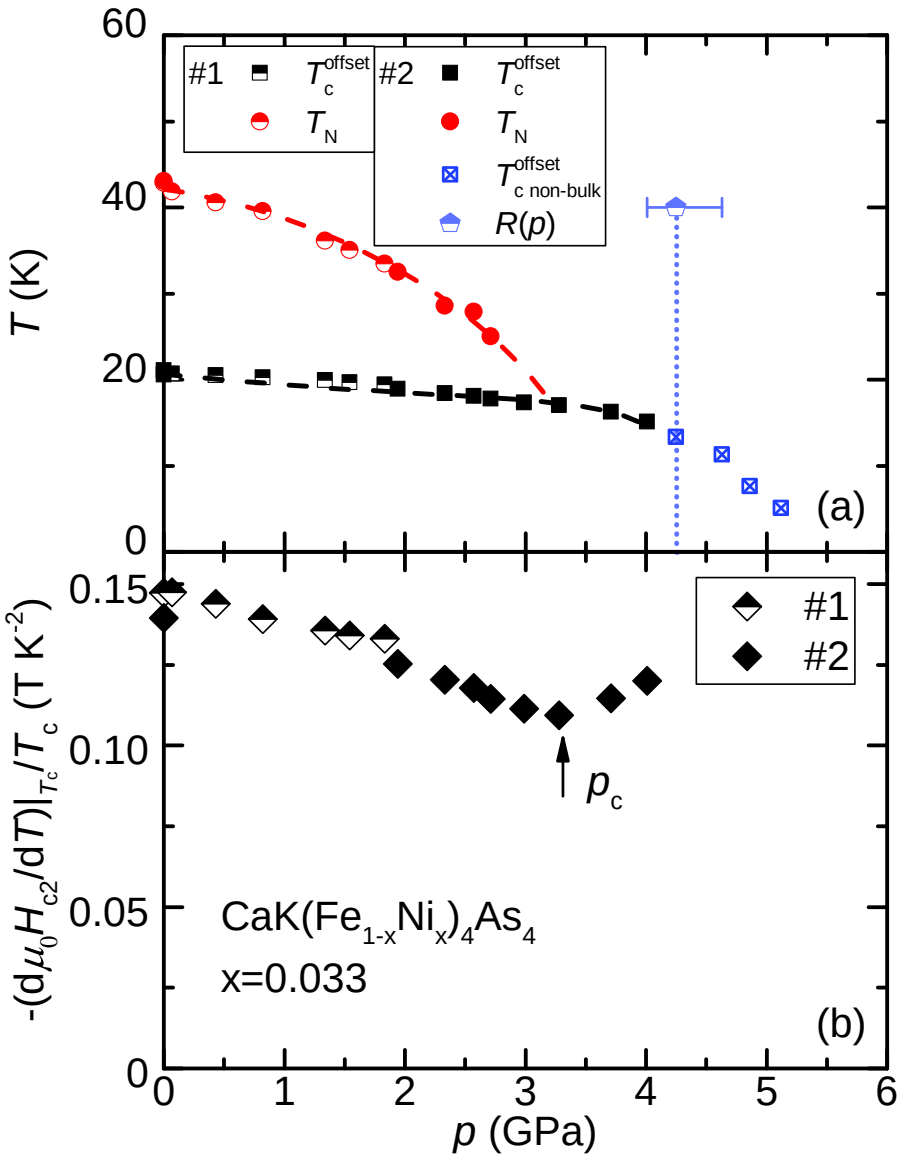

Figure 4.8 (a) Temperature-pressure phase diagram of $CaK(Fe_{1-x}Ni_x)_4As_4$, $x = 0.033$, as determined from resistance measurement. The squares and circles represent the superconducting T_c^{offset} and magnetic T_N phase transition. Half filled and solid symbols are two samples measured in the PCC and the mBAC respectively. Blue symbols represent T_c^{offset} for filamentary superconductivity. Dashed lines are guides to the eye. Blue dotted line indicates the half-collapsed-tetragonal phase transition up to 40 K, inferred from the pressure dependent resistance $R(p)$ data in Fig. 4.5. (b) Pressure dependence of the normalized upper critical field slope $-(1/T_c)(d\mu_o H_{c2}/dT)|_{T_c}$. A local minimum in the slope at p_c (indicated by arrow) is observed near the pressure where T_c^{offset} and T_N lines cross.

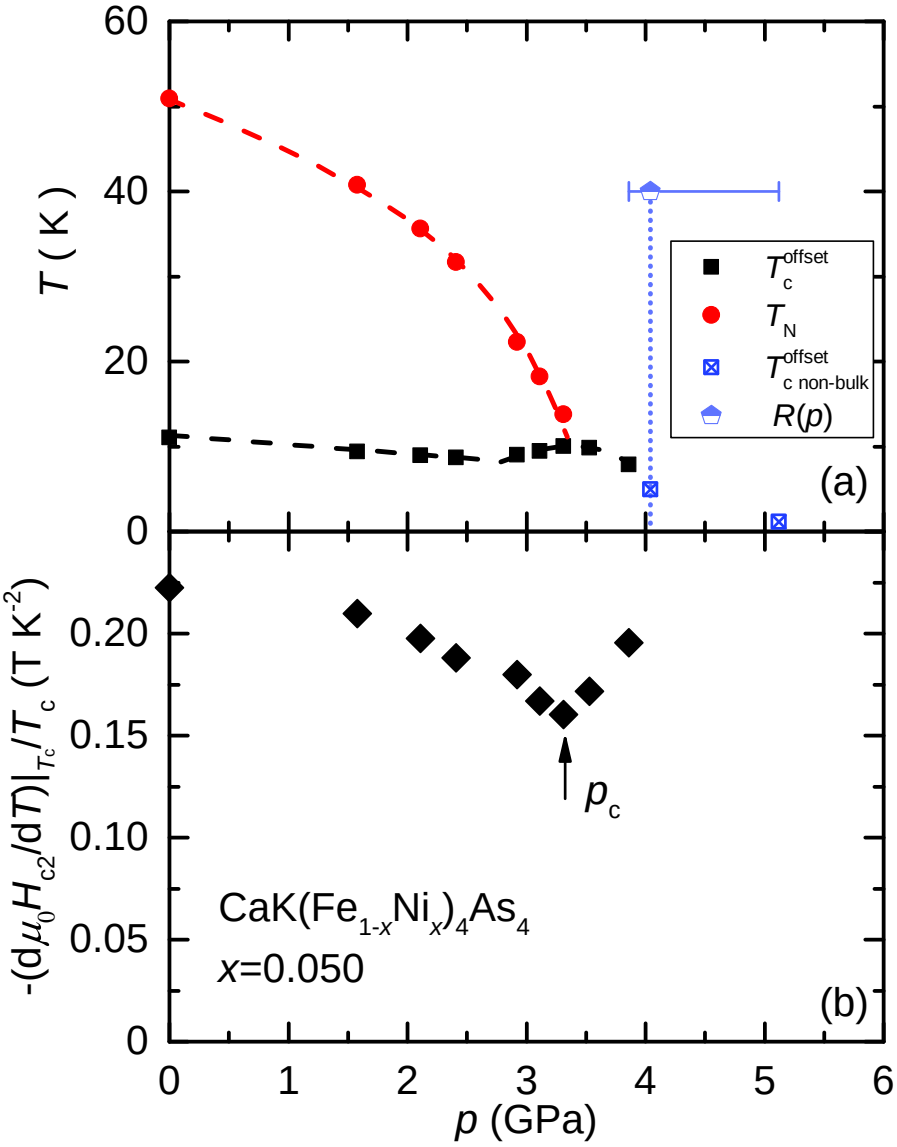

Figure 4.9 (a) Temperature-pressure phase diagram of $CaK(Fe_{1-x}Ni_x)_4As_4$, $x = 0.050$, as determined from resistance measurement. The squares and circles represent the superconducting T_c^{offset} and magnetic T_N phase transition. Blue symbols represent T_c^{offset} for filamentary superconductivity. Dashed lines are guides to the eye. Blue dotted line indicates the half-collapsed-tetragonal phase transition up to 40 K, inferred from the pressure dependent resistance $R(p)$ data in Fig. 4.5. (b) Pressure dependence of the normalized upper critical field slope $-(1/T_c)(d\mu_o H_{c2}/dT)|_{T_c}$. A local minimum in the slope at p_c (indicated by arrow) is observed near the pressure where T_c^{offset} and T_N lines cross.

To better understand the superconducting properties of $CaK(Fe_{1-x}Ni_x)_4As_4$, the superconducting upper critical field H_{c2} was analyzed following Refs.Taufour et al. (2014); Kaluarachchi et al. (2016); Xiang et al. (2017). Generally speaking, the slope of the upper critical field normalized by T_c, is related to the Fermi velocity and superconducting gap of the systemKogan and Prozorov (2012). In the clean limit, for a single-band,

$$-(1/T_c)(d\mu_o H_{c2}/dT)|_{T_c} \propto 1/v_F^2, \tag{4.1}$$

where v_F is the Fermi velocity. Even though the superconductivity in $CaKFe_4As_4$ compounds is multiband, Eq. 5.1 can give qualitative insight into changes induced by pressure.

As is shown in Figs. 4.8(b) and 4.9(b), the normalized slope of the upper critical field -$(1/T_c)(d\mu_o H_{c2}/dT)|_{T_c}$ (the slope $d\mu_o H_{c2}/dT|_{T_c}$) is calculated by linear fitting the data from 1-5 T in Figs. 4.6 and 4.7) exhibits a similar pressure dependence for $x = 0.033$ and 0.050. It initially decreases upon increasing pressure and then begins to increase above pressure p_c, resulting in a minimum of -$(1/T_c)(d\mu_o H_{c2}/dT)|_{T_c}$ in the studied pressure range. In both compositions, p_c coincides with the crossing of T_N and T_c^{offset} lines, suggesting a common origin of this feature.

In Fe-based superconductors, especially the "122" system, Fermi-surface nesting can lead to a partial opening of a gap at the Fermi-surface below T_N. By tuning with doping or applying pressure, a Fermi-surface reconstruction could happen due to the disappearance of magnetismJiang et al. (2009c); Dai et al. (2009); Gooch et al. (2009, 2010); Maiwald et al. (2012); Arsenijević et al. (2013); Liu et al. (2009a,b); Dhaka et al. (2013). For $CaK(Fe_{1-x}Ni_x)_4As_4$ ($x = 0.033$ and 0.050), a clear change of the pressure dependence of the normalized slope -$(1/T_c)(d\mu_o H_{c2}/dT)|_{T_c}$ is observed at p_c, indicating a possible Fermi-surface reconstruction near p_c. Note that for $x = 0.050$, there appears to be a discontinuous change in the normalized slope -$(1/T_c)(d\mu_o H_{c2}/dT)|_{T_c}$ and a subtle anomaly in $T_c(p)$ from 2.41 GPa to 2.92 GP, suggesting there may be a Liftshiz transition near this pressure. Such features are not observed for $x = 0.033$.

Figs. 4.8 and 4.9, then, combine surprising and not unexpected features. The hcT phase transition pressure appears insensitive to Ni subsititution. This is reasonable because this transition involves bonding of As atoms across the Ca-plane. The clear feature at p_c in

-$(1/T_c)(d\mu_o H_{c2}/dT)|_{T_c}$, as well as the more subtle features in $T_c(p)$, are again not too surprising and can be associated with the change (with increasing p) from $T_N > T_c$ to $T_N < T_c$, i.e. T_c occurring in an AFM ordered state to T_c occurring in a state lacking the AFM order and associated additional periodicities. The surprising feature shown in Figs. 4.8 and 4.9 is the weak suppression of T_c concurrent with the strong suppression of T_N. This is contrary to what is seen in Co substitution and pressure study on $BaFe_2As_2$(where T_c increases, as T_N is suppressed)Colombier et al. (2009, 2010); Canfield and Bud'ko (2010); Ni and Bud'ko (2011) and brings into question the exact effects suppression of T_N has on the magnetic fluctuations that the superconducting state is nominally built out of.

4.4 Conclusion

In conclusion, the resistance of Ni-substituted iron-based superconductor $CaK(Fe_{1-x}Ni_x)_4As_4$ ($x = 0.033$ and 0.050) has been studied under pressures up to 5.12 GPa and in magnetic fields up to 9 T. For both substitution levels, hedgehog spin-vortex-crystal magnetic transition temperature, T_N, is suppressed with increasing pressure. In both compositions, T_c is initially suppressed as well and exhibits a weak anomaly near the crossing of T_N and T_c lines. As pressure exceeds $\sim$ 4 GPa, both compositions likely go through the half-collapsed-tetragonal phase transition, similar to the one observed in the parent compound. This demonstrates the insensitivity of the hcT transition pressure to Ni-substitution. The minimum observed in the normalized slope of the upper critical field, -$(1/T_c)(d\mu_o H_{c2}/dT)|_{T_c}$, at the pressure where T_N and T_c lines cross indicate a possible Fermi-surface reconstruction associated with the disappearance of antiferromagnetism.

4.5 Appendix

Fig. 4.10 presents the evolution of the in-plane resistance with hydrostatic pressure for $CaK(Fe_{1-x}Ni_x)_4As_4$, $x = 0.033$, solid lines in the figure are the actual measured resistance data, dashed lines are the resistance after normalization. Sample#1 was measured in a PCC for

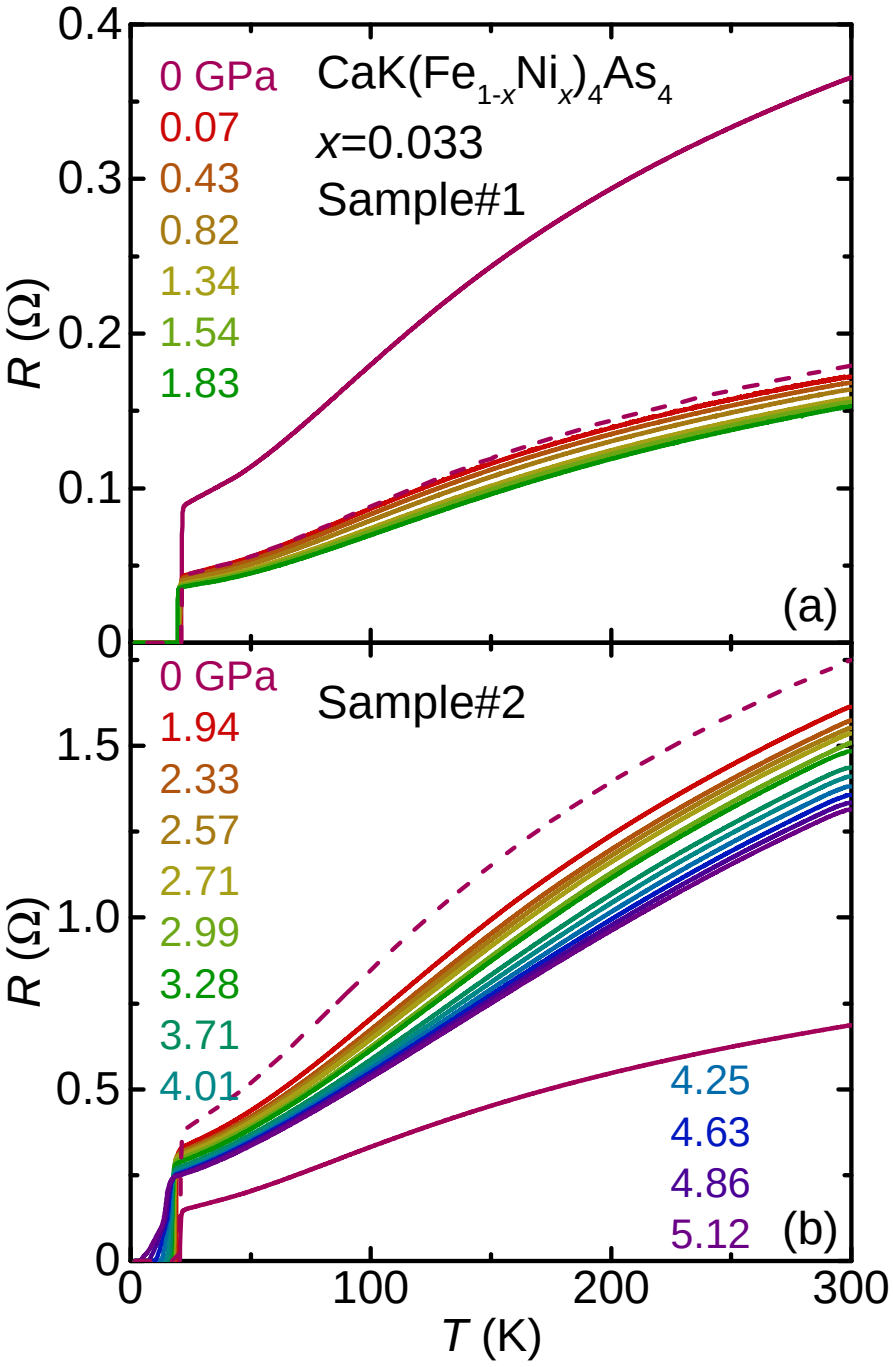

Figure 4.10 Evolution of the in-plane resistance with hydrostatic pressure of Sample#1 measured in a PCC (a) and Sample#2 measured in a mBAC (b) for $CaK(Fe_{1-x}Ni_x)_4As_4$, $x = 0.033$. Solid lines are the actual resistance data measured, dashed lines are the normalized resistance for 0 GPa. Notice that the 0 GPa resistance is measured on PPMS puck outside of either pressure cell (i.e. ambient pressure); in both cases there is a sudden change between the resistance measured at ambient pressure and inside pressure cell. Possible reasons for the sudden change and details of normalization are explained in details in the text.

pressures up to 1.83 GPa and Sample#2 was measured in a mBAC for pressures up to 5.12 GPa. Note that the 0 GPa resistance data was measured on a PPMS puck outside of either pressure cell (i.e. ambient pressure), a sudden change of resistance between ambient pressure and inside pressure cell was observed in both samples. For Sample#1, when the sample was moved from PPMS puck and mounted onto the PCC, one contact of the voltage channel became detached from the sample and that contact had to be re-attached. As a result, the changed position of the contact led to changes in the resistance before and after. For Sample#2, nothing was intentionally done to the sample before and after it was put into the mBAC, the sudden change of the resistance is most likely due to the exfoliation or cracking of the sample when pressure was first applied as the pressure cell was closed. Despite the abrupt change of resistance from ambient pressure to the first finite pressures inside the pressure cell, the resistance of $CaK(Fe_{1-x}Ni_x)_4As_4$ ($x = 0.033$ and 0.05) continuously and systematically decreases upon increasing pressure, consistent with the behavior that is observed in parent compound $CaKFe_4As_4$Meier et al. (2018) and many "122" systemsHassinger et al. (2012, 2016); Taufour et al. (2014).

To better evaluate the resistance evolution with pressure, especially the pressure dependence of resistance at various temperatures (Fig. 4.5 (b)(d)), the ambient pressure resistance is shifted via normalization (assuming in each case that the shift was due to geometric changes). Fig. 4.11 presents the pressure dependence of the resistance at $T = 60$ K for Sample#1 and Sample#2 (solid symbols). Note $T = 60$K was chosen because the pressure values are determined from the the $T_c(p)$ of leadBireckoven and Wittig (1988) at ∼7 K, and the pressure cells are known to have pressure changes with temperature. With the pressure cells and liquid medium we used in this study, the pressure change from room temperature to 7 K can be $0.2 \sim 0.3$ GPaThompson (1984); Colombier and Braithwaite (2007). 60 K was chosen based on the idea that at this temperature, the pressure medium has already solidifiedTorikachvili et al. (2015), the temperature dependence of the thermal expansion of cell materials flattens at low temperature, and the pressure difference between 60 K and 7 K should be smallThompson (1984). The fact that 60 K is still above the magnetic transition temperature T_N guarantees that pressure dependence of resistance at this

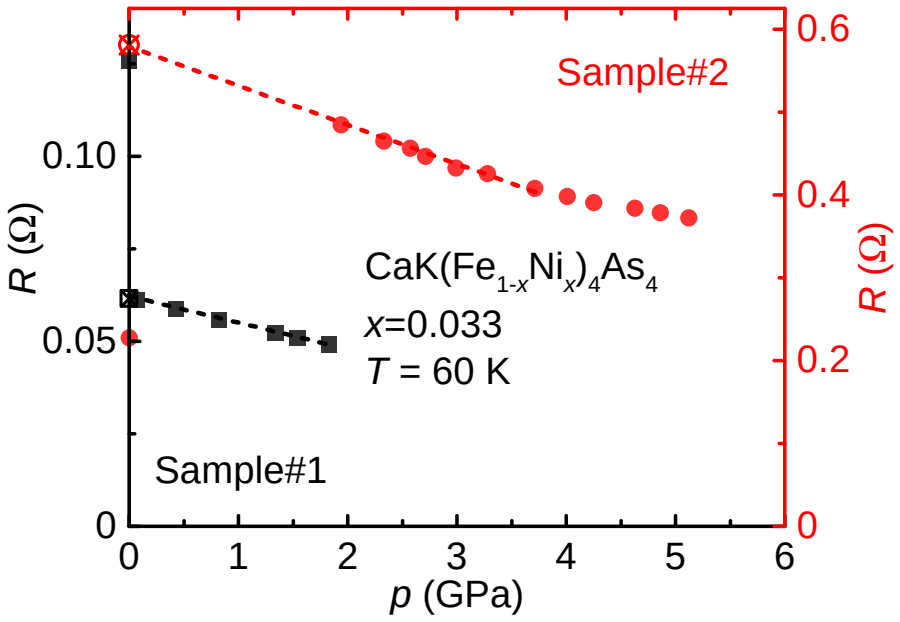

Figure 4.11 Pressure dependence of resistance at 60 K for $CaK(Fe_{1-x}Ni_x)_4As_4$, $x = 0.033$, black solid squares are data from Sample#1 measured in PCC, red solid circles are data from Sample#2 measured in mBAC. Dashed lines are linear fitting of the data before 4 GPa (not including 0 GPa), notice the clear deviation from the linear fitting for the 0 GPa data. Open symbols are the corresponding normalized 0 GPa resistance for Sample#1 and Sample#2 at 60 K.

temperature gives no feature related to magnetism. As shown in Fig. 4.11, except the ambient pressure data, the 60 K resistance for both samples are linearly suppressed by pressure before 4 GPa, so it is assumed that the ambient pressure resistance should also follow this pressure dependence (open symbols in Fig. 4.11). To do that, the ambient pressure resistance curves for the two samples are multiplied by two corresponding factors and moved to the dashed lines as shown in Fig. 4.10.

CHAPTER 5. PRESSURE-TEMPERATURE PHASE DIAGRAM OF THE $EuRbFe_4As_4$ SUPERCONDUCTOR

The following context is a slightly modified version of the published work in Ref. Xiang et al. (2019a). DOI: https://doi.org/10.1103/PhysRevB.99.144509. Reprinted (abstract/excerpt/figure) with permission from [L. Xiang *et. al.*, Phys. Rev. B 99, 144509 (2019)]

5.1 Introduction

New members of the Fe-based superconductors (FeSC) family, $AeAFe_4As_4$ (Ae=Ca, Sr; A=K, Rb, Cs), the so-called 1144-compounds were discovered by Iyo *et al* in 2016Iyo et al. (2016). Different from a homogeneous, random substitution, as in $(Ae_{0.5}A_{0.5})Fe_2As_2$ where Ae/A share the same crystallographic site and retains the parent-compound symmetry $I4/mmm$, these new members crystallize into structural type $P4/mmm$ where Ae and A have their own unique crystallographic sites and form alternating layers along the c axisIyo et al. (2016); Kawashima et al. (2016). Since discovery, the 1144-compounds have received significant attention because these stoichiometric compounds offer new, clean platforms for the study of, among other things, the relation between superconductivity and possible long-range magnetic order in the FeSC. Moreover, a new type of magnetic order, spin-vortex-crystal-order, has been realized in Co- and Ni-substituted $CaKFe_4As_4$, which was argued to be strongly related to its structureMeier et al. (2018).

Among the new 1144 compounds, the Eu(Rb,Cs)Fe_4As_4 compounds have been studied intensively due to the possible coexistence of superconductivity and ferromagnetism Kawashima et al. (2016); Liu et al. (2016); Bao et al. (2018); Smylie et al. (2018); Stolyarov et al. (2018); Albedah et al. (2018); Stolyarov et al. (2018). Polycrystalline Eu(Rb,Cs)Fe_4As_4 compounds were

first discovered in 2016 and were shown to be superconductors with $T_c \sim 35$ K and a magnetic transition temperature $T_M \sim 15$ KKawashima et al. (2016). Different from the undoped $EuFe_2As_2$ where Eu^{2+} orders antiferromagneticallyRen et al. (2008); Jeevan et al. (2008); Jiang et al. (2009a), the magnetic transition in $RbEuFe_4As_4$ is suggested to be ferromagnetic which is associated with the ordering of the Eu^{2+} moments perpendicular to the crystallographic c axisLiu et al. (2016); Albedah et al. (2018). Though the exact magnetic structure of $EuRbFe_4As_4$ has not been established so far, the possible coexistence of superconductivity and ferromagnetism makes $EuRbFe_4As_4$ one of the systems where the relation between these states may be studiedFertig et al. (1977); Ishikawa and Fischer (1977); Canfield et al. (1996); Saxena et al. (2000); Aoki et al. (2001); Pfleiderer et al. (2001); Huy et al. (2007); Jiang et al. (2009b); Nowik et al. (2011); Jiao et al. (2011, 2013); Jin et al. (2013, 2015).

Two substitution studies on polycrystalline $EuRbFe_4As_4$ were published. On one hand, Ni-substitution on the Fe-site suppresses T_c whereas T_M is almost unchangedLiu et al. (2017). On the other hand, substitution of non-magnetic Ca on the Eu-site suppresses T_M while T_c is almost unchangedKawashima et al. (2018). Both of these results suggest that superconductivity and ferromagnetism are almost independent of each other in this system. An optical investigation on single crystalline $EuRbFe_4As_4$ suggests weak interaction between superconductivity and ferromagnetism and that superconductivity is affected by the in-plane ferromagnetism mainly at domain boundariesStolyarov et al. (2018).

Pressure, as another commonly used tuning parameter, is considered less perturbing than substitution because it does not introduce chemical disorder into the system. A high pressure study up to ~ 30 GPa on polycrystalline $Eu(Rb,Cs)Fe_4As_4$ shows that for both compositions, upon increasing pressure, T_c is suppressed while T_M is enhanced and they cross near 7 GPaJackson et al. (2018). In addition, half-collapsed-tetragonal (hcT) phase transition, similar to the one observed in the $CaKFe_4As_4$ seriesKaluarachchi et al. (2017b); Xiang et al. (2018a), is suggested to take place at ~ 10 GPa for $EuRbFe_4As_4$ and ~ 12 GPa for $EuCsFe_4As_4$, respectivelyJackson et al. (2018), which is roughly consistent with theoretical calculationsBorisov

et al. (2018). In this high-pressure study, signatures of transitions are broad and zero resistance was never achieved below T_c due, most likely, to the use of polycrystalline samples.

In this work, we present a pressure study on single crystalline $EuRbFe_4As_4$ up to 6.21 GPa. From resistance measurements up to 6.21 GPa and magnetization measurements up to 1.24 GPa, T_c and T_M are tracked and presented in a pressure-temperature ($p-T$) phase diagram. Our results show that T_c is monotonically suppressed and T_M is linearly increased. Further superconducting upper critical field analysis indicates no qualitative change of Fermi surface within the studied pressure range.

5.2 Experimental details

High-quality single crystals of $EuRbFe_4As_4$ with sharp superconducting transitions at ambient pressure (see Figs. 5.1 (c) (d) and Fig. 5.5 (b) below) were grown as described in Ref. Bao et al. (2018). The *ab*-in-plane ac resistance measurements under pressure for two samples, #1 and #2, were performed in a Quantum Design Physical Property Measurement System (PPMS) using a 1 mA excitation with frequency of 17 Hz, on cooling rate of 0.25 K/min. A standard, linear four-contact configuration was used. Contacts were made by soldering 25 μm Pt wires to the samples using a Sn:Pb-60:40 alloy. The magnetic field was applied along the c axis. A modified Bridgman Anvil Cell (mBAC)Colombier and Braithwaite (2007) was used to apply pressure up to 6.21 GPa. Pressure values at low temperature were inferred from the $T_c(p)$ of leadBireckoven and Wittig (1988). Hydrostatic conditions were achieved by using a 1:1 mixture of iso-pentane:n-pentane as the pressure medium for the mBAC, which solidifies at $\sim$ 6.5 GPa at room temperatureTorikachvili et al. (2015).

Low-field (20 mT) dc magnetization measurements under pressure were performed on several pieces of single crystals (referred together as sample #3) in a Quantum Design Magnetic Property Measurement System (MPMS-3) SQUID magnetometer. A commercially-available HDM Be-Cu piston-cylinder pressure cellHDM was used to apply pressures up to 1.24 GPa. Daphne oil 7373 was used as a pressure medium, which solidifies at 2.2 GPa at room temperatureYokogawa et al.

(2007), ensuring hydrostatic conditions. Superconducting Sn was used as a low-temperature pressure gaugeEiling and Schilling (1981).

5.3 Results and discussions

Figures 5.1 (a) and (b) present the pressure dependence of the temperature-dependent resistance for $EuRbFe_4As_4$. Two samples, sample #1 and sample #2, were measured in the mBAC for pressures up to 4.69 GPa or 6.21 GPa. For both samples, resistance decreases upon increasing pressure. At ambient pressure for $T \sim 35$ K, a superconducting transition was observed and zero resistance was achieved for both samples. Below T_c, no features associated with the magnetic transition T_M are observed in the $R(T)$ curves down to 1.8 K. Figs. 5.1 (c) and (d) show blowups of the low-temperature resistance. For both samples, the superconducting transition at ambient pressure is very sharp, demonstrating good homogeneity of the single crystals. As shown in the figures, upon increasing pressure, T_c monotonically decreases in the studied pressure range. A gradually broadening of the superconducting transition was also observed in both samples. Similar behavior has been observed in many other superconductors that are measured in the mBAC cell and is likely due to the pressure inhomogeneity when high loads are applied.

To better visualize the pressure evolution of resistance, we present in Fig. 5.2 the pressure dependent resistance $R(p)$ at fixed temperatures. As shown in the figure, different from the $CaKFe_4As_4$ seriesKaluarachchi et al. (2017b); Xiang et al. (2018a), resistance of $EuRbFe_4As_4$ at various temperatures shows a smooth decrease as a function of pressure without any obvious anomalies. This implies the absence of structural transition up to 6.21 GPa, which is consistent with the results in Ref. Jackson et al. (2018) and predictions in Ref. Borisov et al. (2018) where the hcT phase transtion is suggested to take place at ~ 10 GPa. The total suppression of resistance at 40 K under pressure, $\sim 55\%$ up to 4 GPa and $\sim 65\%$ up to 6.21 GPa, is rather large compared with the $CaKFe_4As_4$ series, where the suppression at 40 K is 30% - 40% up to 4 GPa, i.e., before hcT happensKaluarachchi et al. (2017b); Xiang et al. (2018a). Another indication that a potential hcT phase transition has not been reached is the fact that the superconducting

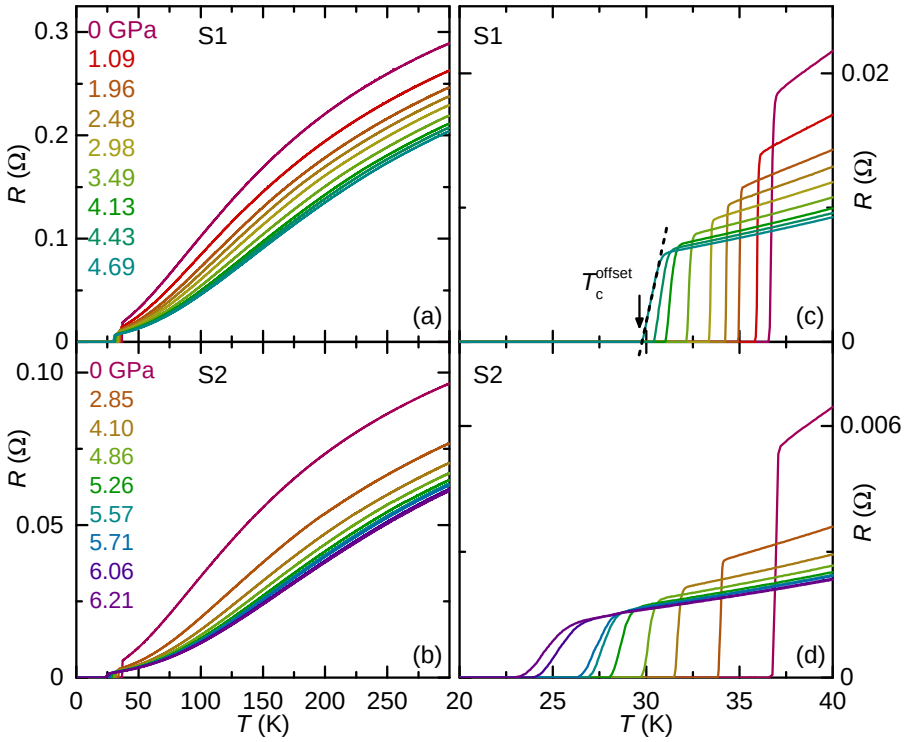

Figure 5.1 (a) (b) Evolution of the in-plane resistance with hydrostatic pressures up to 6.21 GPa measured in a mBAC for $EuRbFe_4As_4$ sample #1 and sample #2, respectively. (c) (d) Blowups of the low temperature region showing the superconducting transition. Criterion for T_c^{offset} is indicated by arrow in (c).

transitions shown in Figs. 5.1 and 5.3 are not significantly broadened and the upper critical fields, H_{c2}, remain high over our pressure range. Both $CaKFe_4As_4$ seriesKaluarachchi et al. (2017b); Xiang et al. (2018a) as well as Co-substituted $CaFe_2As_2$Ran et al. (2012); Gati et al. (2012) show loss of bulk superconductivity at the collapsed-tetragonal or lowest hcT transitions.

Temperature dependent resistance under magnetic fields up to 9 T applied along the c-axis was studied and the results are presented in Fig. 5.3 for selected pressures for sample #2. As shown in the figure, below T_c, no features associated with the magnetic transition T_M are observed and zero resistance persists down to 1.8 K with fields up to 9 T under all pressures. For temperatures above the superconducting transition, a decrease of resistance under applied magnetic field is observed. The upper superconducting critical field, H_{c2}, can be obtained from Fig. 5.3 using the offset criteria defined in Figs. 5.1-5.3. The temperature dependence of H_{c2} at various pressures for sample #1 and sample #2 is presented in Fig. 5.4. For both samples, H_{c2} is systematically suppressed by increasing pressure. H_{c2} is linear in temperature except for magnetic fields below 2 T, the bending of $H_{c2}(T)$ curves are more obvious at higher pressures. The curvature at low fields has been observed in other FeSCColombier et al. (2009, 2010); Kaluarachchi et al. (2016); Xiang et al. (2017, 2018a) and can be explained by the multi-bands nature of superconductivityKogan and Prozorov (2012), which is likely the case of $EuRbFe_4As_4$Stolyarov et al. (2018).

To study the evolution of the magnetic transition with pressure, we present, in Fig. 5.5, the dependence of the zero-field-cool magnetization $M(T)$ data. During the measurements, pressure was increased up to 1.24 GPa under 20 mT applied magnetic field. As shown in Figs. 5.5 (a) and (b), the superconducting transition of $EuRbFe_4As_4$ is determined from the onset of diamagnetism at $T \sim 35$ K. Whereas T_c monotonically decreases with pressure (Fig. 5.6 (a)), there is a highly non-monotonic change in the diamagnetism associated with the superconducting state (Figs. 5.5 (a), (b)); we attribute this variation to the likely change of the de-magnetization factor, which happens as a result of the sample position changes when pressure is changed. Another kink-like anomaly is observed at $T \sim 16$ K. We associated this anomaly with the magnetic transition T_M.

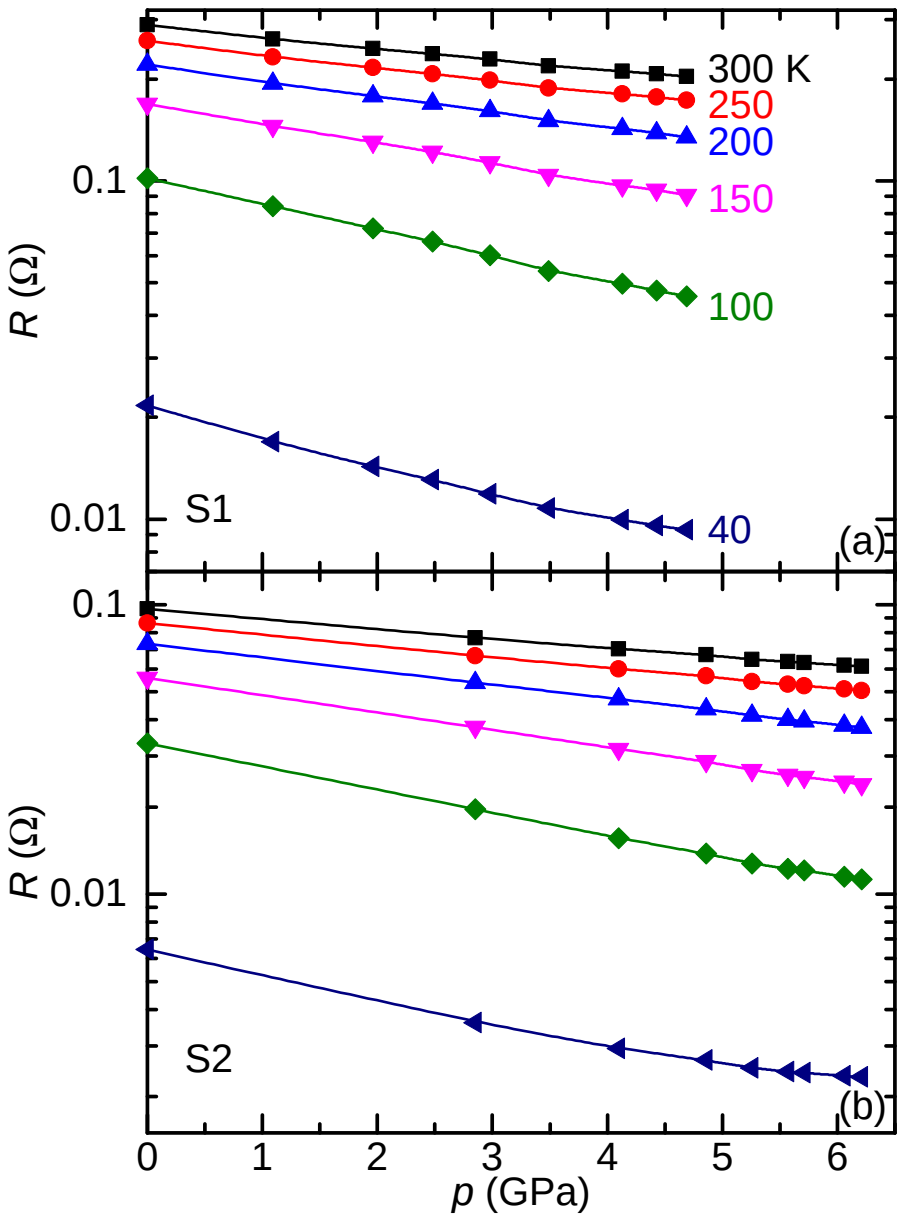

Figure 5.2 Pressure dependence of resistance $R(p)$ at fixed temperatures for $EuRbFe_4As_4$ sample #1 (a) and sample #2 (b).

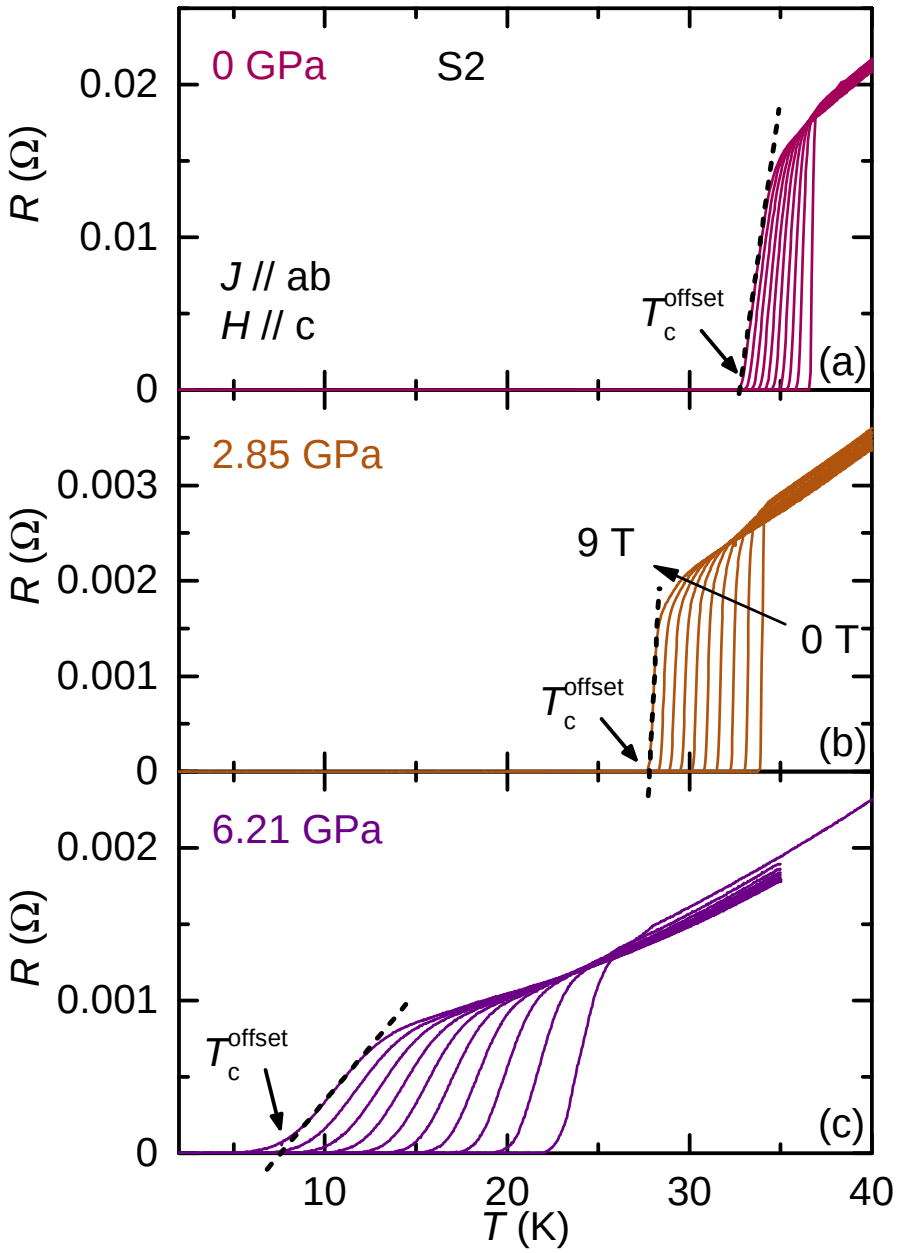

Figure 5.3 Temperature dependence of resistance under magnetic field up to 9 T for selective pressures for sample #2. Criteria for T_c^{offset} under magnetic fields are indicated by arrows. Current was applied in-plane and magnetic field was applied along c axis.

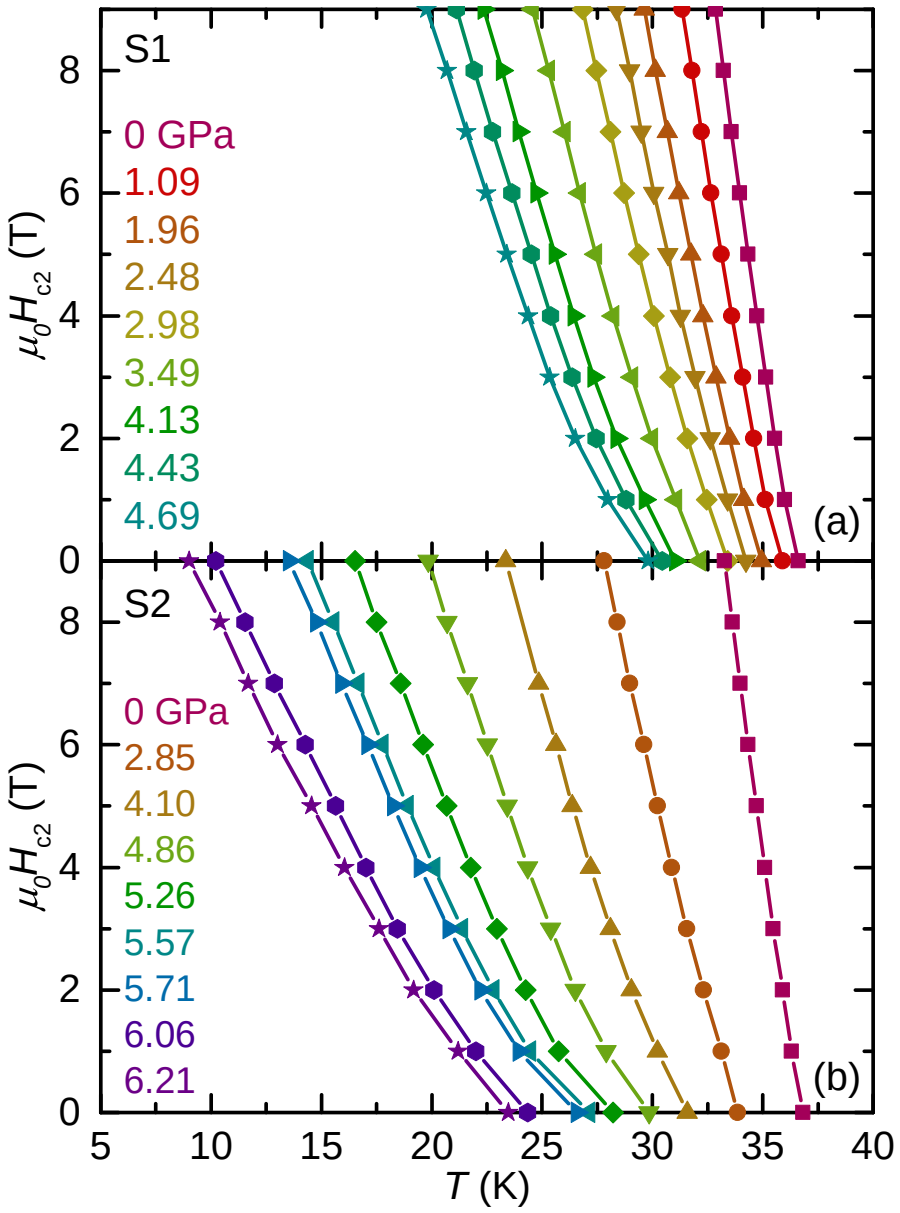

Figure 5.4 Temperature dependence of the upper superconducting critical field, $H_{c2}(T)$, under selected pressures for (a) sample #1 and (b) sample #2.

Pressure values at low temperature were inferred from the superconducting transition of Sn which also shown up in the data set at $T \sim 3.7$ K, i.e., way below T_c and T_M of $EuRbFe_4As_4$ (as indicated inside the pink circle in the figure). Fig. 5.5 (b) shows the blowup of the superconducting transition region of $EuRbFe_4As_4$, demonstrating that T_c is suppressed as pressure is increased. To determine the magnetic transition temperature T_M, temperature derivative of the magnetization, dM/dT, was calculated and presented in Fig. 5.5 (c). The temperature corresponding to the minimum in dM/dT was taken as T_M, as indicated in the figure. It is clearly seen that T_M is increased upon increasing pressure.

We summarize the T_c and T_M values inferred from both resistance and magnetization measurements in the pressure-temperature ($p-T$) phase diagram shown in Fig. 5.6 (a). To be consistent, T_c^{offset} determined from resistance measurements (Fig. 5.1 (c)) and T_c^{onset} determined from magnetization measurements (Fig. 5.5 (b)) were used and they match with each very well. As shown in Fig. 5.6 (a), T_c of $EuRbFe_4As_4$ is monotonically suppressed upon increasing pressure up to 6.21 GPa. Starting with $T_c = 36.6$ K at ambient pressure, T_c is suppressed to 23.5 K at 6.21 GPa. In terms of magnetic transition T_M, it is linearly increased from 16.2 K at ambient pressure to 18.2 K at 1.24 GPa, with the rate of $dT_M/dp = 1.64$ K/GPa. To better understand the superconducting properties of $EuRbFe_4As_4$, we further analyze the superconducting upper critical fieldTaufour et al. (2014); Kaluarachchi et al. (2016); Xiang et al. (2017, 2018a). Generally speaking, the slope of the upper critical field normalized by T_c, is related to the Fermi velocity and superconducting gap of the systemKogan and Prozorov (2012). In the clean limit, for a single-band,

$$-(1/T_c)(d\mu_o H_{c2}/dT)|_{T_c} \propto 1/v_F^2, \tag{5.1}$$

where v_F is the Fermi velocity. Even though the superconductivity in $EuRbFe_4As_4$ compounds is likely to be multiband, Eq. 5.1 can give qualitative insight into changes induced by pressure. As shown in Fig. 5.6 (b), the normalized slope of the upper critical field $-(1/T_c)(d\mu_o H_{c2}/dT)|_{T_c}$ (the slope $d\mu_o H_{c2}/dT$ is obtained by linearly fitting the data above 2 T in Fig. 5.4) is gradually suppressed by a factor of ~ 2.5 upon increasing pressure up to 6.21 GPa. No features in the

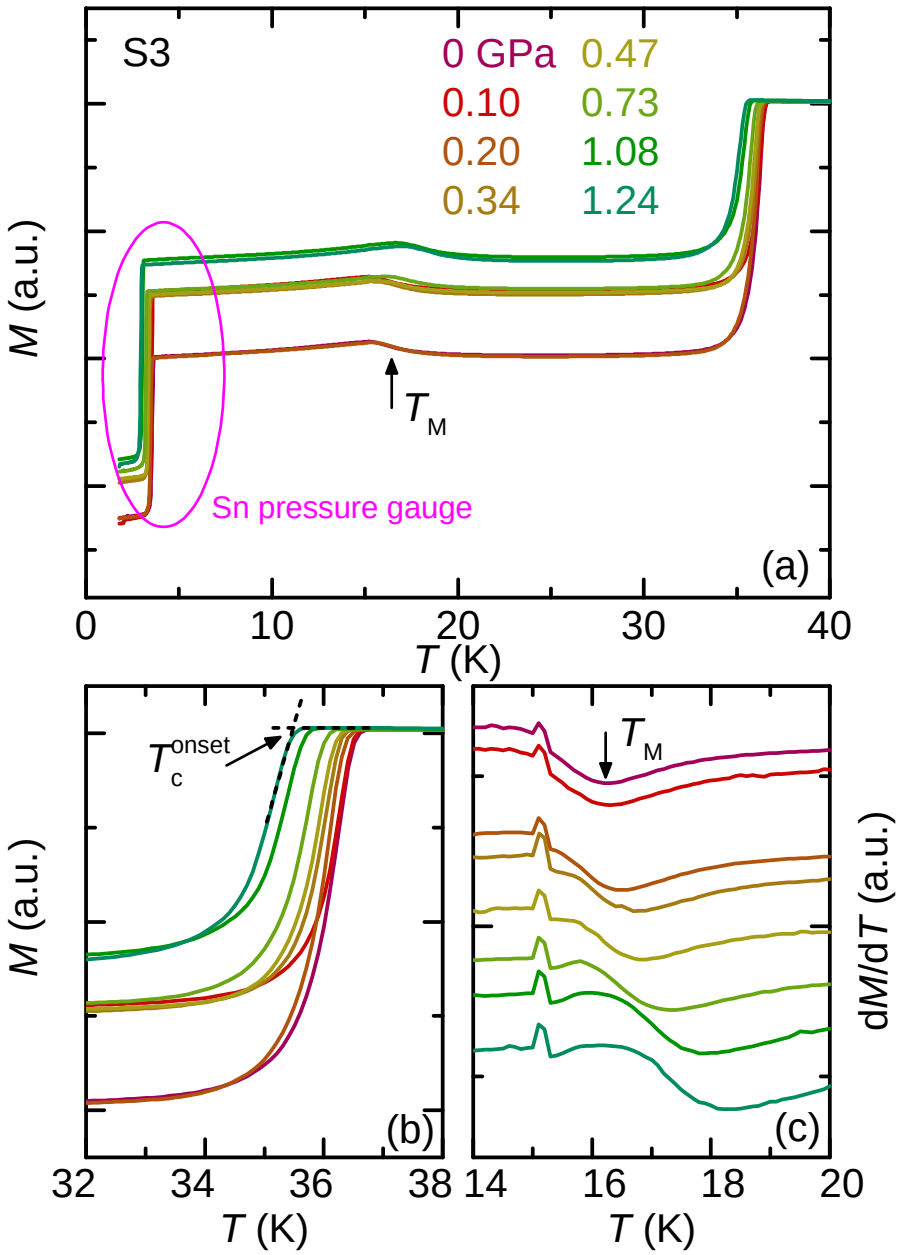

Figure 5.5 (a) Evolution of the zero-field-cool (ZFC) magnetization $M(T)$ with hydrostatic pressures up to 1.24 GPa under 20 mT applied field. Superconducting transition of Sn is used to determined the low temperature pressure, as indicated by the pink circle. (b) Blow up of the superconducting transition region for $EuRbFe_4As_4$. Criterion for T_c^{onset} is indicated by arrow. (c) Temperature derivative of the magnetization, dM/dT, showing the evolution of the magnetic transition $T_{\rm M}$. Criterion is indicated by arrow. The small feature just above 15 K is an artifact caused by the combination of small temperature steps and details of the temperature control in MPMS-3.

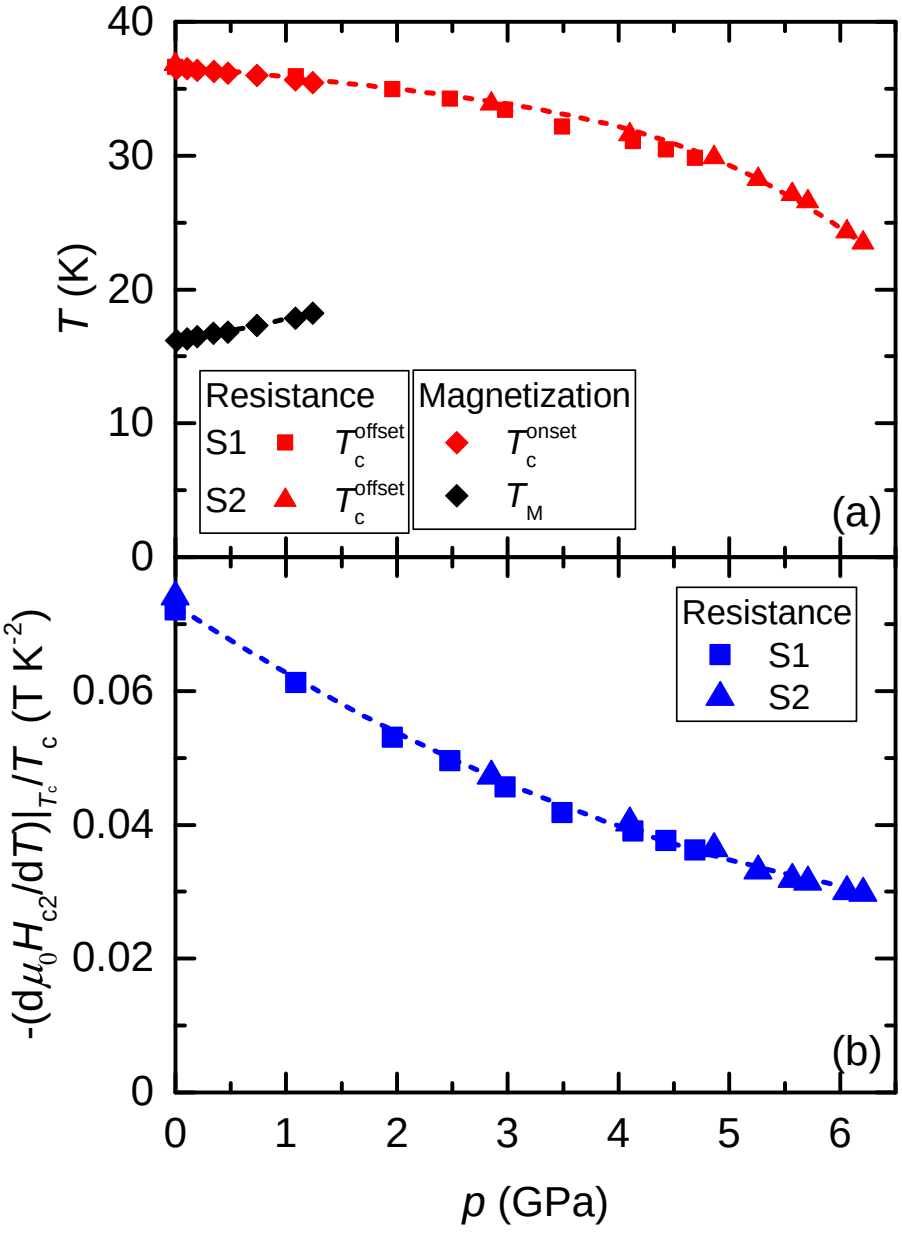

Figure 5.6 (a) Pressure-temperature phase diagram of $EuRbFe_4As_4$, as determined from resistance and magnetization measurements. Red and black symbols represent the superconducting T_c^{offset} and magnetic T_M phase transitions. (b) Pressure dependence of the normalized upper critical field slope $-(1/T_c)(d\mu_o H_{c2}/dT)|_{T_c}$. The squares and triangles are data obtained from resistance measurement for sample #1 and sample #2, respectively. The diamonds are data obtained from magnetization measurement. Dashed lines are guides to the eye.

normalized slope that could be associated with band structure change or Lifshitz transition, like the cases in many other Fe-based superconductorsTaufour et al. (2014); Kaluarachchi et al. (2016); Xiang et al. (2017, 2018a), are observed over the studied pressure range. Furthermore, the $R(p)$ curve at 40 K (Fig. 5.2 (b)), a temperature that is close to T_c but still above T_c and T_M, implies that resistivity is suppressed by a factor of ~ 2.7 as well. In a simple argumentKasap (2006),

$$\rho \propto 1/(g_{\epsilon_F} \tau v_F^2) \tag{5.2}$$

where g_{ϵ_F} is density of states at the Fermi level and τ is the scattering time of these Fermi electrons. Eq. 5.1 and 5.2, combined together, suggest that the decrease of both resistivity and $-(1/T_{\rm C})(d\mu_o H_{\rm C2}/dT)|_{T_{\rm C}}$ with pressure can be explained by pressure induced increase of the Fermi velocity.

Data from this study, on single crystalline samples, and from the study on polycrystalline samples in Ref. Jackson et al. (2018) are plotted together and presented in the combined $p-T$ phase diagram in Fig. 5.7. As shown in the figure, T_c from this study (determined by the offset of the transition via resistance measurement or onset of diamagnetism) matches very well with the T_c determined by the onset of diamagnetism in Ref. Jackson et al. (2018). T_M data also match with each other over the studied pressure range.

The extrapolation of our $T_M(p)$ line in Fig. 5.6(a) as well as the data in Fig. 5.7 suggest that $T_c(p)$ and $T_M(p)$ should cross near 6 GPa. On one hand, the suppression of T_c with pressure gets stronger when pressure is increased, which might be related to the fact that $T_c(p)$ and $T_M(p)$ are getting closer at higher pressures. On the other hand, neither our pressure dependent T_c nor $-(1/T_{\rm C})(d\mu_o H_{\rm C2}/dT)|_{T_{\rm C}}$ data show any clear signature potentially associated with $T_c(p)$ and $T_M(p)$ crossing. Either they cross at a pressure higher than 6.21 GPa or their crossing does not have qualitative effect on $T_c(p)$ or $H_{c2}(T,p)$.

5.4 Conclusion

In conclusion, the resistance and magnetization of single crystalline $EuRbFe_4As_4$ has been studied under pressure. In-plane resistance measurements under pressure up to 6.21 GPa reveal

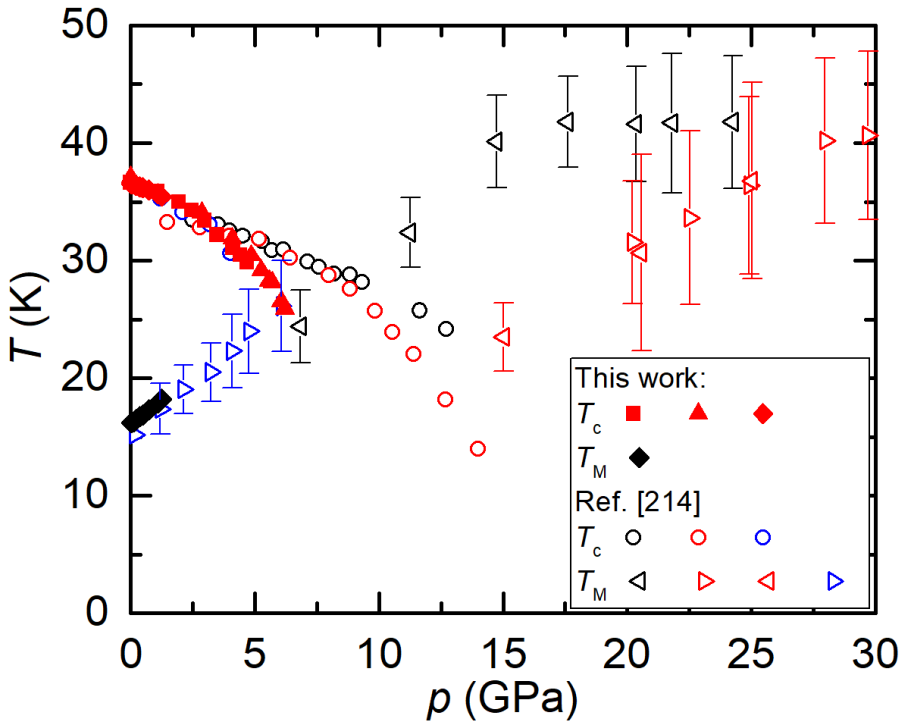

Figure 5.7 Pressure-temperature phase diagram of $EuRbFe_4As_4$ up to ~ 30 GPa, including data from Ref. Jackson et al. (2018) (open symbols). Open circles corresponds to the onset of the superconducting transition measured via resistivity or magnetic susceptibility. Open triangles corresponds to the magnetic transition determined from magnetic susceptibility or feature in $\mathrm{d}\rho/\mathrm{d}T$.

that superconducting transition T_c is monotonically suppressed. Magnetization measurements under pressure up to 1.24 GPa reveal that magnetic transition T_M is linearly increased. No indications of half-collapsed-tetragonal phase transition is observed up to 6.21 GPa. Further upper critical field analysis shows that the normalized slope, $-(1/T_{\mathrm{C}})(d\mu_o H_{\mathrm{c2}}/dT)|_{T_{\mathrm{C}}}$, is continuously suppressed upon increasing pressure up to 6.21 GPa, which is likely due to the continuous change of the Fermi velocity with pressure. Our results suggest that the magnetism of Eu sub-lattice does not have significant influence on the superconducting behavior of FeAs layer in $EuRbFe_4As_4$.

CHAPTER 6. PHYSICAL PROPERTIES OF RBi$_2$ (R = La, Ce) UNDER PRESSURE

The following context is a slightly modified version of the published work in Ref. Xiang et al. (2019b). DOI: https://doi.org/10.1103/PhysRevMaterials.3.095006. Reprinted (abstract/excerpt/figure) with permission from [L. Xiang *et. al.*, Phys. Rev. Materials 3, 095006 (2019)]

6.1 Introduction

Bi-rich compounds manifest a rich variety of ground states. For example, Bi-based families such as ABi (A = Li and Na)Sambongi (1971); Kushwaha et al. (2014), ABi$_2$ (A = K, Rb, Cs and Ca)Roberts (1976); Winiarski et al. (2016) and ABi$_3$ (A = Sr, Ba, Ca, Ni, Co, and La) are superconducting (SC) at low temperature Matthias and Hulm (1952); Shao et al. (2016); Kinjo et al. (2016); Xiang et al. (2018b); Gati et al. (2018); Tencé et al. (2014). RBi (R = Ce, Nd, Tb and Dy) and RBi$_2$ (R = La-Nd, Sm) families have low-temperature magnetic ground states with complex $H-T$ phase diagramsNereson and Arnold (1971); Petrovic et al. (2002). Moreover, due to the strong spin-orbit coupling of Bi-6p electrons they can have substantial ferromagnetic anisotropy, like MnBiIsaeva et al. (2013); Taufour et al. (2015), or, more recently, they have became candidates for realizing novel topological phases, such as topological insulators or topological superconductorsHasan and Kane (2010); Qi and Zhang (2011); Hor et al. (2010); Xia et al. (2009); Chen et al. (2009).

Among these, the RBi$_2$ family displays different magnetic ground states depending on the choice of RPetrovic et al. (2002). Structurally, RBi$_2$ forms in an orthorhombic structure with single layers of Bi separated from each other by RBi bilayers that are stacked along the crystallographic b axisPetrovic et al. (2002); Zhou et al. (2018). When R is chosen to be the

moment-bearing Ce ion, an antiferromagnetic (AFM) ground state below $T_N \sim 3.3$ K can be stabilizedPetrovic et al. (2002). A recent study shows that $CeBi_2$ is a Kondo system with a Sommerfeld coefficient γ over 200 mJ/mol K^2 and Kondo temperature of an order of ~ 2 KZhou et al. (2018). On the other hand, for $R =$ La (non-moment bearing), $LaBi_2$ reveals metallic behavior without indications of magnetic ordering or superconductivity down to 1.8 KPetrovic et al. (2002).

In this study, we perform a comparative study of the ground-state tunability of these two members by external pressure. We explore the temperature-pressure phase diagram of $CeBi_2$ and $LaBi_2$ by resistance measurements and complement these, in case of $CeBi_2$, with specific heat measurements. Our results show that T_N of $CeBi_2$ is moderately increased upon increasing pressure. Surprisingly, resistance measurements of both $CeBi_2$ and $LaBi_2$ show signatures pressure-induced superconductivity at low temperature ($T \lesssim 4$ K) above very similar threshold pressures ($p \gtrsim 1.68$ GPa). However, specific heat measurement of $CeBi_2$ does not reveal any anomaly that could be associated with a transition into the superconducting state. We assign these effects to filamentary SC that likely originates from traces of Bi flux, either on the surface of the plate-like samples, or trapped inside the sample as laminar inclusions. Finally, the analysis of pressure-dependent resistance data at fixed temperatures for $CeBi_2$ suggests that there might be a pressure-induced crossover most likely associated with pressure-induced changes in the Kondo temperature and crystal electric field splitting.

6.2 Experimental details

Single crystals of $CeBi_2$ and $LaBi_2$ were grown by a Bi self-flux technique with the help of a frit-disk alumina crucible setCanfield and Fisk (1992); Canfield et al. (2016). For $CeBi_2$, Ce and Bi in the molar ratio 9:91 were loaded into a crucible set and sealed into a fused silica ampoule under partial argon atmosphere. The ampoule was heated to 1000 °C in 5 h and dwelled at this temperature for another 4 h. It was then slowly cooled to 600 °C over 45 h. At this temperature, the ampoule was removed from the furnace and excess liquid was decanted by the help of a

centrifuge. For $LaBi_2$, La and Bi in the molar ratio 8:92 were loaded into the crucible set, heated to 1000 °C in 5h, dwelled at 1000 °C for 2 h, and slowly cooled to 350 °C over 80 h. The resulting crystals of $CeBi_2$ and $LaBi_2$ are millimeter-size and plate-shaped. Both $CeBi_2$ and $LaBi_2$ crystals are air-sensitive, the preparation of experiments was therefore performed in a N_2 glovebox.

The *ac*, in-plane resistance measurements were performed in a Quantum Design Physical Property Measurement System (PPMS) using a 1 mA excitation with frequency of 17 Hz, on cooling using a rate of - 0.25 K/min. The magnetic field was applied perpendicular to the current direction. For $CeBi_2$, two different samples (labeled as S1 and S2) were used in resistance measurements. S1 was measured at ambient condition outside pressure cell and S2 was measured under pressure. The temperature-dependent resistance data for S1 is normalized by extrapolating $p \leq 1.23GPa$ pressure-dependent resistance data, $R(p)$, at 300 K from S2 back to 0 GPa (see Fig. 6.1). For $LaBi_2$, only one sample was measured under pressure with the pressures 0.60 GPa $\leq p \leq$ 2.52 GPa. For both compounds, a standard four-contact configuration was used with contacts made by Dupont 4929N silver paint. Specific heat measurements under pressure were performed using an ac calorimetry technique on a third sample (sample S3) in a cryogen-free cryostat from ICEOxford (Lemon-Dry) with base temperature of 1.4 K. Details of the setup used and the measurement protocol are described in Ref. Gati et al. (2019a).

In this study, a Be-Cu/Ni-Cr-Al hybrid piston-cylinder cell, similar to the one described in Ref. Bud'ko et al. (1984), was used to apply pressure. Good hydrostatic conditions were achieved by using a 4:6 mixture of light mineral oil:n-pentane as pressure medium, which solidifies, at room temperature, in the range $3 - 4$ GPa, i.e., well above our maximum pressureBud'ko et al. (1984); Kim et al. (2011); Torikachvili et al. (2015). Pressure values were inferred from the $T_c(p)$ of leadBireckoven and Wittig (1988), determined via resistance measurements.

6.3 Results

6.3.1 $CeBi_2$

Figure 6.1 shows the temperature-dependent resistance of $CeBi_2$ at ambient pressure (sample S1) and pressure up to 2.44 GPa (sample S2). The temperature-dependent resistance data for S1 is normalized by extrapolating the 300 K pressure-dependent resistance data ($R(p)$ for $p \leq 1.23$ GPa) measured from S2 back to 0 GPa. As shown in the figure, the resistance decreases upon cooling, showing a metallic behavior. At $T \sim 50$ K, a broad drop of resistance is observed. In an earlier work, it was suggested that this drop in $R(T)$ is associated with either the coherence in Kondo scattering or crystal electric-field (CEF) splitting of Ce atomsZhou et al. (2018). At $T \sim 3.3$ K, the resistance shows a kink-like anomaly due to loss of spin-disorder scattering as $CeBi_2$ undergoes an AFM transition at T_NPetrovic et al. (2002); Zhou et al. (2018). Sample S2 was measured under pressure and at lowest pressure (0.12 GPa), resistance of S2 shows very similar feature as S1. Upon increasing pressure, the resistance gradually increases over a large temperature range (essentially everywhere in the paramagnetic state). This behavior is seen in many other Ce-based Kondo lattice systems as well and is often attributed to pressure-induced shift of characteristic spin-fluctuation temperature and spin-fluctuation scattering to higher temperaturesThompson and Lawrence (1994); Hegger et al. (2000); Nicklas et al. (2001, 2003). The broad drop of resistance at ambient pressure becomes progressively more pronounced, as pressure is increased, and evolves into a local maximum at highest pressures. The temperature of this broad drop/hump feature is labeled as T' and indicated by arrow in the figure (see below for the description of the criterion used). The evolution of this feature will be analyzed and discussed in more details below. As we move to the low-temperature region (inset to Fig. 6.1), for $p \leq 1.23$ GPa, the kink-like anomaly, which is associated with the magnetic transitionPetrovic et al. (2002); Zhou et al. (2018), is shifted to higher temperatures upon increasing pressure. Even with this slight increase in T_N, the loss of spin disorder scattering below T_N remains fundamentally the same. As a result, the resistance at 1.8 K, $R(1.8\ \text{K})$, does not show a significant change. Upon

increasing from 1.23 GPa to 1.68 GPa, R(1.8 K) shows a sudden decrease. For $p > 1.68$ GPa, the resistance as a function of temperature, $R(T)$, undergoes a much sharper drop and reaches a zero value, suggesting a pressure-induced superconducting phase at low temperature. The critical temperature of this phase is increased upon increasing pressure.

The temperature-derivative of the resistance data is shown in Fig, 6.2 to better differentiate between the low p and high p feature at low temperature as well as to trace the broad feature at $T \sim 50$ K. As shown in Fig.6.2 (a), at low pressures ($p \leq 1.23$ GPa), the magnetic transition shows up as a jump-like feature in the $\mathrm{d}R/\mathrm{d}T$. We therefore define T_N as the midpoint of the jump-like feature in $\mathrm{d}R/\mathrm{d}T$ (see dotted lines and arrow in Fig. 6.2 (a) as well as Figs. 6.5 (b) and (c) below). As a result, T_N increases with increasing p with a slope of ~ 0.48 K/GPa. At higher pressures ($p \geq 1.68$ GPa), the superconducting transition can be seen as a sharp peak in $\mathrm{d}R/\mathrm{d}T$. Figure 6.2 (b) shows $\mathrm{d}R/\mathrm{d}T$ curves over a larger temperature range. As shown in the figure, the broad drop/hump features in $R(T)$ are reflected in minima $\mathrm{d}R/\mathrm{d}T$. We therefore define the crossover temperature T', which marks the change between two different resistance regimes, by the minima in the the $\mathrm{d}R/\mathrm{d}T$ as indicated by the dashed lines in the figure. It is clearly seen that T' decreases upon increasing pressure.

To trace the magnetic transition to higher pressures, the temperature-dependent resistance under magnetic fields up to 9 T applied along the b-axis was studied. The applied field can suppress the superconducting transition which masks the signature of the magnetic transition for $p \geq 1.68$ GPa. The results for selected pressures are presented in Fig. 6.3. As shown in Figs. 6.3 (a) and (c), at 0.12 GPa the kink-like anomaly in $R(T)$ associated with magnetic transition is broadened in higher fields, yet not much shifted with an applied field of 3 T. In the temperature derivative of the resistance data, the corresponding jump-like feature is suppressed with increasing magnetic fields until it disappears at higher fields. At 2.44 GPa, the sharp drop of the resistance in $R(T)$ associated with superconducting transition at ~ 5 K is suppressed to lower temperatures with magnetic fields and the kink-like anomaly re-emerges at ~ 4 K. Further increasing magnetic fields broadens the kink-like anomaly until it disappears. Similarly, in the

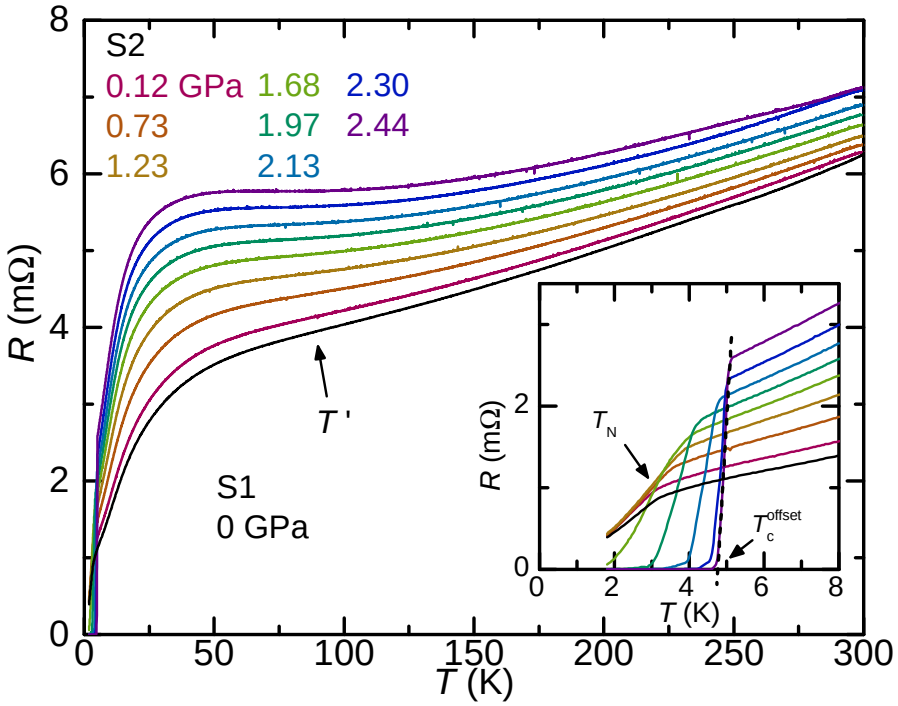

Figure 6.1 Resistance of $CeBi_2$ as a function of temperature at ambient pressure (measured on sample S1) and at different finite pressures up to 2.44 GPa (measured on sample S2). The ambient pressure data for S1 is normalized by extrapolating $p \leq 1.23$ GPa pressure-dependent resistance data, $R(p)$, at 300 K from S2 back to 0 GPa. A broad hump feature is present in all data sets. The inferred crossover temperature T' is exemplarily marked for the data set at 2.44 GPa (for more details, see text). Inset: Blowup of the resistance data at low temperatures showing the magnetic and superconducting transitions. AFM transition temperature T_N is indicated by arrow. Criterion for T_c^{offset} is indicated by arrow.

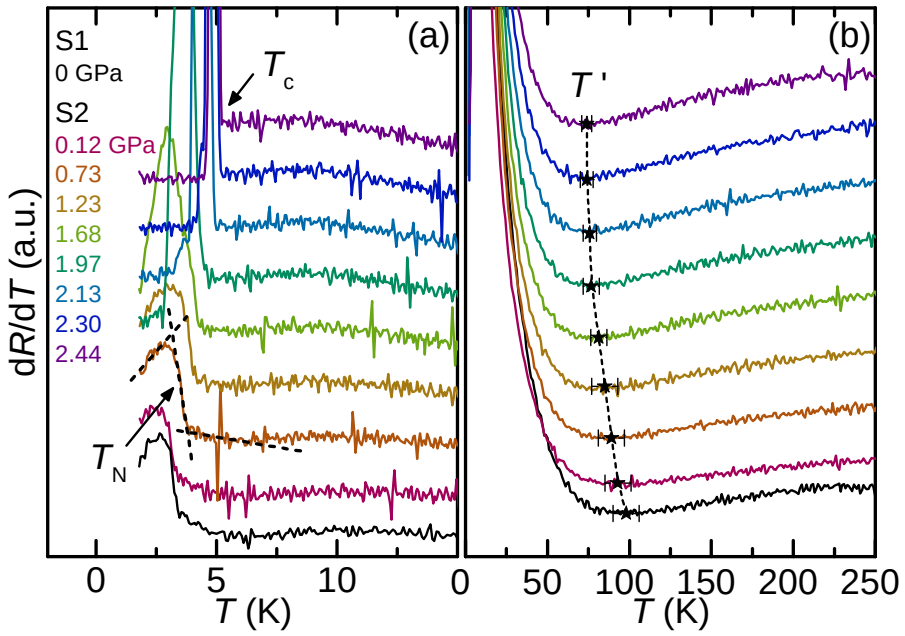

Figure 6.2 (a) Temperature derivative of the resistance,dR/dT, in the low-temperature region ($T \leq 15$ K). The criterion for the determination of the AFM transition temperature T_N is illustrated by dashed lines and marked by the arrow (midpoint of the jump-like feature). At high pressures, the magnetic anomaly is masked by a strong drop of resistance, likely due to spurious SC (see main text). The respective temperature is denoted by T_c (see arrow). (b) Temperature derivative of the resistance,dR/dT, showing the evolution of the temperature associated with the broad hump feature in $R(T)$ curves. T' is determined by the minimum in dR/dT curves. Data sets in (a) and (b) are offset for clarity.

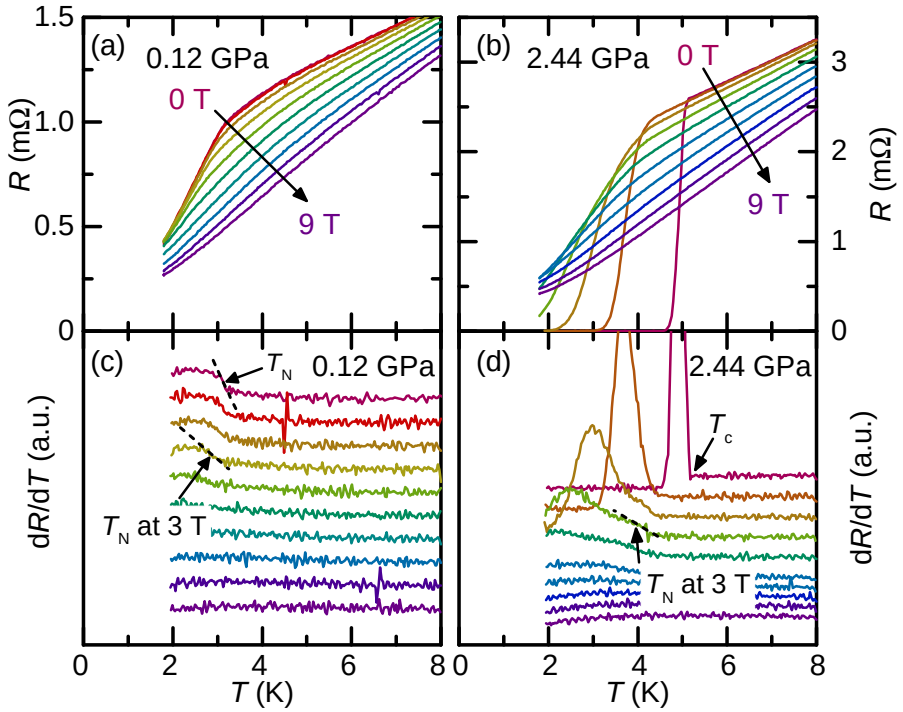

Figure 6.3 (a), (b) Temperature-dependent resistance of $CeBi_2$ S2 under magnetic fields up to 9 T for selected pressures. Fields are applied along the b-axis. (c), (d) Temperature-derivative of the resistance data, taken in applied magnetic fields, shown in (a) and (b), respectively. Data sets are offset for clarity. Criteria for T_N at 0 T and 3 T are indicated by arrows (midpoint of the jump-like feature).

temperature derivative $\mathrm{d}R/\mathrm{d}T$, we first observed a sharp peak associated with the superconducting transition at low magnetic fields. Upon increasing the field, the sharp peak is suppressed and shifted to lower temperatures, at the same time, a second jump-like feature emerges. At even higher fields, both features disappear. By analogy we associate this re-emerged kink-like anomaly in $R(T)$ (jump-like feature in $\mathrm{d}R/\mathrm{d}T$) with the same magnetic transition that is observed at low pressures. The resistance does not become zero at 1.8 K for magnetic field $B \geq$ 2 T indicating a critical field of $\sim$ 2 T at 1.8 K.

To further investigate the overall increase of resistance with pressure, we present in Fig. 6.4 the pressure dependent resistance $R(p)$ at fixed temperatures. As shown in the figure, a change of slope is observed when pressure is increased from 1.68 GPa to 1.97 GPa at 10 K, this feature

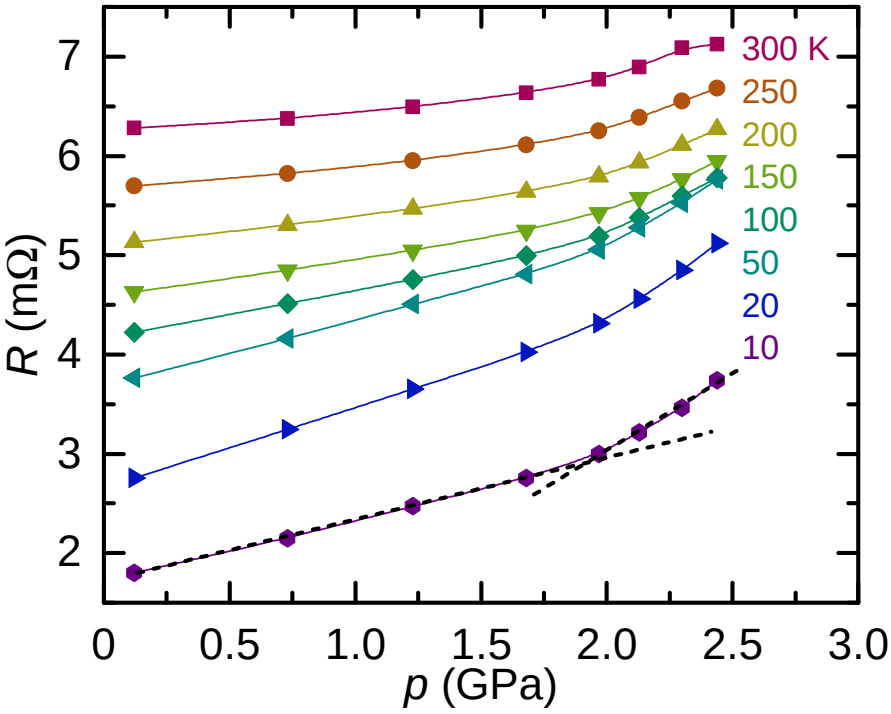

Figure 6.4 Pressure dependence of resistance, $R(p)$, at fixed temperatures for $CeBi_2$. A change of slope between 1.68 GPa and 1.97 GPa is indicated by the cross of the dashed line.

persists up to 300 K, the highest temperature investigated in this study. The strongest pressure responses are for $T \lesssim T'$, suggesting shifts in the Kondo feature around T'. Whereas the $R(p)$ data for 300 K are quite similar to what is found for $LaBi_2$ in Fig. 6.9 (see below).

The observation of a state with zero resistance in $CeBi_2$ calls for a thermodynamic investigation of the temperature-pressure phase diagram. Thus, we studied the specific heat of $CeBi_2$ (sample S3) under pressure and the results are presented in Fig. 6.5 (a). At lowest pressure (0.04 GPa), very close to ambient pressure, the specific heat, $C_p(T)$, nicely reveals a nearly mean-field-like anomaly at $T \sim 3.2$ K, which speaks in favor of a second-order phase transition. The shape, position, and size of the feature is consistent with the specific results of a previous study and therefore allows us to assign this feature to the magnetic transition at T_N. Figures. 6.5 (b) and (c) show the comparison between temperature dependent C_p and $\mathrm{d}R/\mathrm{d}T$ at two sets of nearly identical pressures (0.04 GPa and 0 GPa, 1.28 GPa and 1.23 GPa). As shown in the figure,

temperature-dependent $C_p(T)$ and $\mathrm{d}R/\mathrm{d}T$ exhibit similar jump-like feature at the transition temperature which is consistent with the Fisher-Langer relationFisher and Langer (1968); Alexander et al. (1976). Thus, to determine the transition temperature, T_N, from specific heat measurement, same criterion as in the resistance measurement is used (midpoint of jump-like anomaly as indicated by dashed lines and arrow in Fig. 6.5 (a)). As pressure is increased up to 2.55 GPa, T_N is monotonically increased. At the same time, the jump size of the anomaly does not significantly change indicating that the amount of entropy released at T_N is unchanged. However, we did not observe a second feature at any pressure, thus suggesting that $CeBi_2$ does not undergo any other phase transition than the magnetic one. This includes in particular also a possible superconducting transition for $p > 1.68$ GPa inferred from our resistance data. One might argue that a possible superconducting feature in specific heat is masked by the huge entropy release at the magnetic transition, as T_N and the resistive T_c are very close. However, even at high pressure, at which we expect that T_N and T_c are well separated, no feature in specific heat occurs (see inset of Fig. 6.5 (a)). Another possibility for the apparent absence of a specific heat feature might be that the superconducting jump size is very small and therefore falls below the resolution limit. In the following, we provide estimates for the lower and upper bound of superconducting jump size in $CeBi_2$.

For a phonon-mediated BSC superconductor, the specific heat jump at the superconducting transition can be written as,

$$\Delta C = 1.43\gamma T_c, \tag{6.1}$$

where γ is the electronic Sommerfeld coefficient and T_c is the superconducting transition temperature. To estimate a possible lower limit of ΔC, we first assume that superconductivity is unrelated to the Kondo-lattice-nature of $CeBi_2$. Thus, for the choice of γ, we refer to the nonmagnetic reference $LaBi_2$ which is isostructural to $CeBi_2$. Since $LaBi_2$ has a γ value of 2 mJ/mol K^2Petrovic et al. (2002), with $T_c \sim 4.6$ K from Fig. 6.1, we get ΔC =13.2 mJ/mol K. Compared to the noise level, such value of specific jump (gray vertical line in the inset of Fig. 6.5 (a)) should be resolvable. For an upper limit, we take the γ value of the Kondo-lattice $CeBi_2$, 200

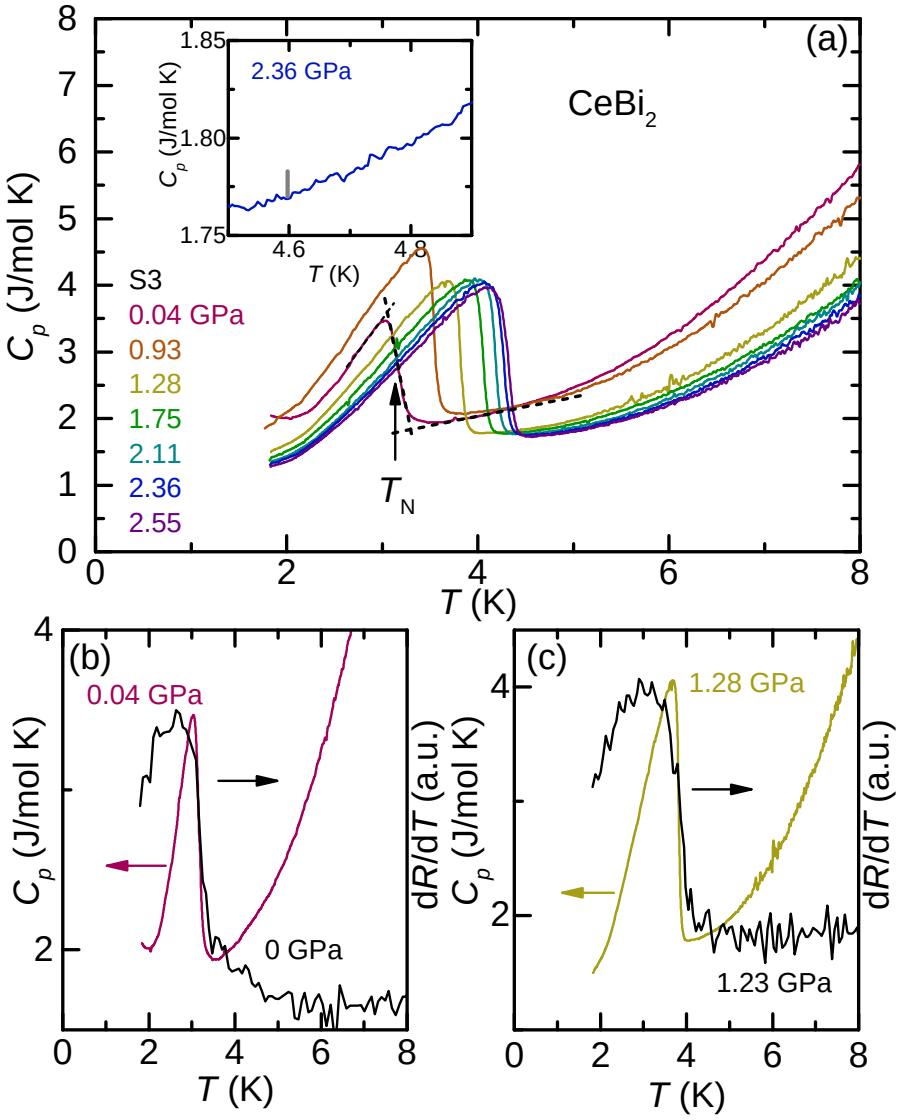

Figure 6.5 (a) Evolution of the temperature-dependent specific heat, $C_p(T)$, with pressure up to 2.55 GPa for $CeBi_2$ S3. Criterion for T_N is indicated by arrow (midpoint of the specific heat jump). The inset shows the data near 4.6 K for 2.36 GPa, the gray vertical line indicates a 13.2 mJ/mol K specific heat jump at 4.6 K (details are discussed in the main text). (b), (c) Temperature-dependent specific heat data and temperature-derivative of the resistance data at two sets of nearly identical pressures ((b) 0.04 GPa and 0 GPa, (c) 1.28 GPa and 1.23 GPa). Note that the midpoint criterion gives same T_N values for both data sets.

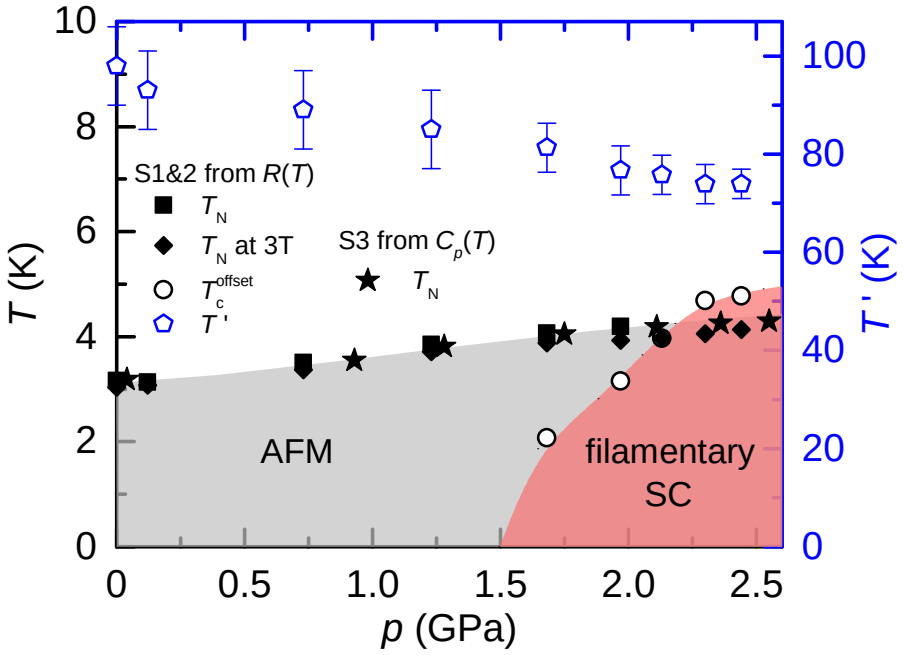

Figure 6.6 Temperature-pressure phase diagram of $CeBi_2$ as determined from resistance and specific heat measurements. Black squares and diamonds represent the magnetic transition T_N determined from resistance measurement for 0 T and 3 T respectively. Black stars represent T_N determined from specific heat measurement. Black open symbols represent the superconducting transition T_c^{offset} determined from resistance measurement. Blue pentagons represent T' determined from resistance measurement (Note the right axis used here for T'). Gray and red areas represent the antiferromagnetically ordered and filamentary-superconducting regions, respectively.

mJ/mol K^2Zhou et al. (2018), we get ΔC =1.32 J/mol K, which would be one hundred times larger than the gray vertical line in the inset of Fig. 6.5 (a). The absence of any resolvable specific heat jump feature, which can be associated with superconductivity, suggests that the pressure-induced superconductivity is likely filamentary rather than bulk. This conclusion will be related to again below after presentation of data on $LaBi_2$.

We summarize our T_N and T' data for $CeBi_2$ as well as our T_c^{offset} (filamentary) data in the temperature-pressure ($T-p$) phase diagram shown in Fig. 6.6. For the magnetic transition, both T_N at zero field and 3 T from resistance measurement (Fig. 6.3) and T_N from zero field specific heat data are included. For superconducting transition, T_c^{offset} is determined from resistance

measurement (Fig. 6.1 (b)). The T_N values, inferred from $R(T,p)$ and $C(T,p)$ agree reasonably well within their experimental resolution. As shown in Fig. 6.6, magnetic field suppresses magnetic transition T_N slightly ($\sim$ 0.2 K by 3 T), as is often the case for antiferromagnets. T_N increases monotonically with pressure with a rate of 0.48 K/GPa up to 2.55 GPa. For superconductivity, it first sets in at $\sim$ 1.68 GPa with a sharp drop in $R(T)$, yet not give rise to zero resistance down to 1.8 K. Upon increasing pressure, the drop in $R(T)$ becomes progressively sharper and zero resistance at low temperature is reached as well. Furthermore, from 1.68 GPa to 2.44 GPa, T_c^{offset} monotonically increases from 2.1 K to 4.8 K, appearing to saturate at our highest pressure. Finally, the temperature T' associated with Kondo coherence scattering or CEF splitting is suppressed upon increasing pressure, with $T' \simeq 98$ K at 0 GPa and 74 K at 2.44 GPa.

6.3.2 $LaBi_2$

Next, we discuss our resistance data for the non-magnetic, $LaBi_2$, member of the RBi_2 family. Figure 6.7 presents the pressure evolution of the temperature-dependent resistance for $LaBi_2$ with pressures 0.60 GPa $\leq p \leq$ 2.52 GPa. For all pressures, resistance decreases upon cooling, showing metallic behavior. For a large temperature range ($T \gtrsim 50$ K), the resistance shows linear dependence on temperature. In the low-temperature region (upper inset of Fig. 6.7), for $p \leq 1.03$ GPa, resistance as a function of temperature is relatively flat suggesting that the low-temperature resistance is dominated by impurity scattering. At 1.68 GPa, $R(T)$ shows a faster drop of resistance below $\sim$ 2.5 K. When pressure is further increased, this drop of resistance becomes more pronounced. At 2.52 GPa, resistance actually drops to zero below 2.7 K, suggesting pressure-induced superconductivity. The drop of resistance, visible for 1.68 GPa $\leq p \leq$ 2.34 GPa, is likely to be associated with traces of superconducting phase. Using the criterion defined in the upper inset of Fig. 6.7, the superconducting transition temperature, T_c^{offset}, can be traced and the results are shown in the bottom inset of Fig. 6.7. As shown in the figure, T_c^{offset} increases from 1.2 K to 3 K when pressure is increased from 2.10 GPa to 2.52 GPa.

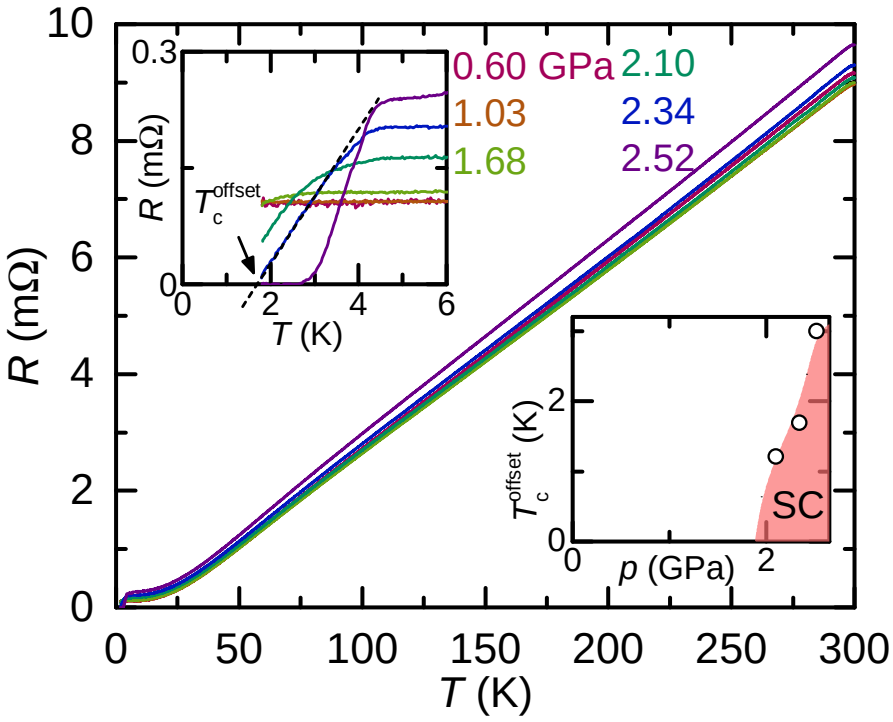

Figure 6.7 Resistance of $LaBi_2$ as a function of temperature at different pressures for 0.60 GPa $\leq p \leq$ 2.52 GPa. Upper inset: blowup of the resistance data at low temperatures showing the superconducting transition. Criterion for T_c^{offset} is indicated by arrow. Bottom inset: superconducting transition temperature, T_c^{offset}, as a function of pressure. Red area represent the superconducting region as inferred from resistance measurement.

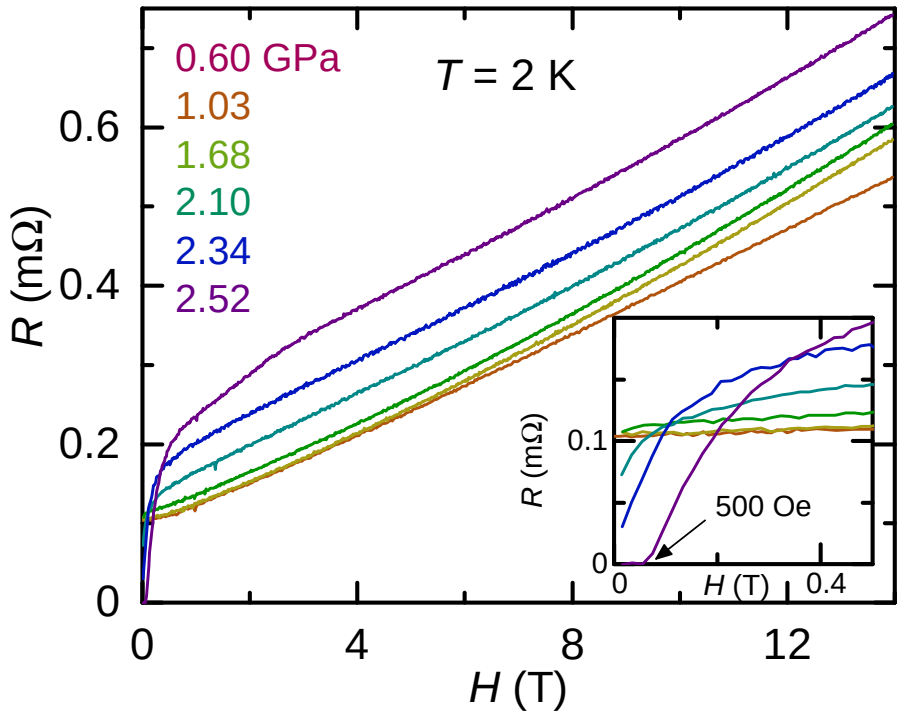

Figure 6.8 Evolution of the field-dependent resistance at 2 K of $LaBi_2$ with pressure 0.60 GPa $\leq p \leq$ 2.52 GPa and fields applied along the b-axis. The lowest pressure data (0 GPa) is not included due to excessive noise. Inset shows the blowups of the low-field region.

The field dependence of the resistance at 2 K was studied and is presented in Fig. 6.8. For $p \leq$1.03 GPa, resistance gradually increases with magnetic field with a slightly up-bending curvature. For $p \geq$1.68 GPa, at low fields, the resistance first undergoes a fast increase upon increasing fields, which is likely due to the suppression of superconductivity. At higher fields, $R(H)$ curves behave similarly with the ones at lower pressures. Moreover, at 2.52 GPa the zero resistance at 2 K is lifted for $H \gtrsim 500$ Oe, indicating a critical field of ~ 500 Oe. Bearing in mind that close to ambient pressure the magnetoresistance clearly deviates from the conventional H^2 behavior, we observe that pressures up to ~ 2.5 GPa do not modify this behavior (besides the lower field effects of superconductivity) in any conspicuous way. The data in Figs. 6.7 and 6.8 are consistent with traces of SC phase, with distributions of T_c values existing in the $LaBi_2$ sample. The mean T_c of these filamentary traces increases with pressure for $p > 1.68$ GPa.

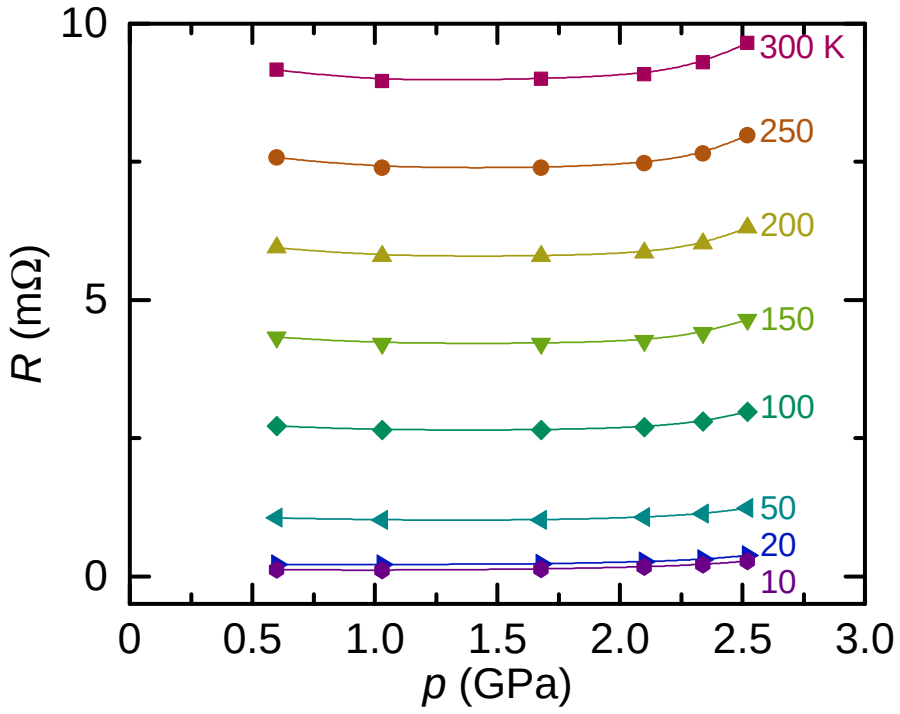

Figure 6.9 Pressure dependence of resistance, $R(p)$, at fixed temperatures for $LaBi_2$. The lowest pressure data (0 GPa) is not included due to excessive noise.

To better visualize the pressure evolution of the higher temperature resistance for $LaBi_2$, Fig. 6.9 presents the pressure-dependent resistance $R(p)$ at fixed temperatures. The resistance of $LaBi_2$ first decreases and then increases with pressure, giving rise to a broad minimum between 1.03 GPa and 1.68 GPa. Compared with the $R(p)$ of $CeBi_2$, $R(p)$ of $LaBi_2$ has a similar higher-pressure, higher-temperature up-turn, but lacks the larger $T \lesssim T'$ pressure dependence seen in $CeBi_2$.

6.4 Discussion

Before discussing the implications of the zero-resistive state, which we observed in $CeBi_2$ and $LaBi_2$ at higher pressures, we first focus on the increase of T_N and decrease of T' under pressure in $CeBi_2$, as this is robustly established by our resistance and specific heat study. The properties of a Kondo lattice system are usually dominated by two characteristic energy scales, which are both susceptible to externally applied pressure: Ruderman-Kittel-Kasuya-Yosida (RKKY) interaction energy $T_{RKKY} \propto J^2$ and Kondo interaction energy $T_K \propto e^{-1/J}$ where J is the exchange interactionRuderman and Kittel (1954); Kasuya (1956); Yosida (1957); Kondo (1964); Hewson (1993). When $T_{RKKY} \gg T_K$, the ground state is magnetic and for $T_K \gg T_{RKKY}$, it is nonmagnetic. The competition between them and the resulting ground state is often described by the Doniach phase diagramDoniach (1977). For Ce-based compounds, the ground state is often magnetic. Applying external pressure can suppress magnetic transition temperature to zero and lead to non-magnetic ground state via a quantum critical pointSteglich et al. (1979); Jaccard et al. (1992); Mathur et al. (1998); Park et al. (2006); Knebel et al. (2006); Jiao et al. (2015). In our study, the AFM transition temperature T_N of $CeBi_2$ is moderately increased by pressure up to ~ 2.5 GPa. This suggests that at ambient pressure, $CeBi_2$ is deeply in its magnetic state and higher pressure is needed to suppress T_NKnebel et al. (2006); Chen et al. (2006); Kimura et al. (2007); Bauer et al. (2010). This is compatible with the Doniach picture, as there is a maximum of T_N due to the explicit functional dependences of T_{RKKY} and T_K. Moreover, in the Doniach picture, when pressurizing a Ce-based Kondo lattice, an increase of T_K is often observed due to

the enhancement of exchange interaction JThompson and Lawrence (1994); Goltsev and Abd-Elmeguid (2005). This, in turn, should give rise to a shift of broad resistive features, associated with T_K, to higher temperatures with pressure. Therefore, a suppression of T' observed in this study suggests that the broad drop/hump feature in $R(T)$ can not be explained by only the Kondo coherence scatteringHegger et al. (2000); Muramatsu et al. (2001); Nicklas et al. (2003).

The resistance measurements for both $CeBi_2$ and $LaBi_2$ reveal a zero-resistive state at high pressures, suggesting a pressure-induced SC phase for these compounds. By comparing their $T-p$ phase diagrams (Figs. 6.6 and 6.7 (a) inset), we see that the two phase diagrams exhibit similar SC phase regions, but with slightly different onset pressures and T_c values. For $CeBi_2$ T_c saturated at $\sim$ 4.8 K by 2.44 GPa whereas T_c of $LaBi_2$ reaches $\sim$ 3 K but seems still rising with pressure. Moreover, at the highest pressures in this study (2.44 GPa for $CeBi_2$ and 2.52 GPa for $LaBi_2$), $CeBi_2$ and $LaBi_2$ have very different critical fields at $\sim$ 2 K ($\sim$ 2 T for $CeBi_2$ and $\sim$ 500 Oe for $LaBi_2$).

Despite the zero-resistive state and relative sharp resistance drop at high pressures for $CeBi_2$ and $LaBi_2$, we would like to argue that the observed SC feature is extrinsic for the following reasons. First of all, specific heat measurement under pressure for $CeBi_2$ does not reveal any SC feature which strongly speaks in favor of filamentary SC. Second, similar T_c values for Ce and La are unlikely in bulk RBi_2. On one hand, if the SC in these two compounds is standard BSC SC, then hybridizing rare earths such as Ce or Yb suppresses T_c aggressivelyMaple et al. (1972); Canfield et al. (1998); Bud'ko and Canfield (2006). On the other hand, if $CeBi_2$ at high pressures becomes a heavy fermion superconductor, the specific heat jump anomaly at T_c should be even bigger. Then similar SC onset pressure and T_c between $LaBi_2$ and $CeBi_2$ are unlikely again as $LaBi_2$ is not a heavy fermion compound.

To speculate about the possible origin of the filamentary SC, we refer to literature. First we notice that similar situation has been found in other Bi compounds as well where SC is attributed to Bi flux or thin films of BiThamizhavel et al. (2003); Mizoguchi et al. (2011); Lin et al. (2013). Moreover, it is know that single-crystalline Bi undergoes sequential structural transitions upon

increasing pressure and possesses rich physics under pressureKlement et al. (1963); Degtyareva et al. (2004); Li et al. (2017). Specifically, at low temperature, Bi-II exists between 2.55 GPa and 2.70 GPa with $T_c \sim 3.9$ K and upper critical field $\mu_0 H_{c2}(2\text{ K}) \sim 0.05$ T, Bi-III exists between 2.70 GPa and 7.7 GPa with $T_c \sim 7$ K and $\mu_0 H_{c2}(2\text{ K}) \sim 3$ TLi et al. (2017). Owing to the very similar T_c of Bi-II to our results on $CeBi_2$ in the almost identical pressure range, we suspect that the filamentary SC we observed in the resistance measurement of $CeBi_2$ originates from traces of Bi flux. It is likely that the SC in $LaBi_2$ is non-bulk and origins from Bi flux as well. Slight differences in onset pressure and $\mu_0 H_{c2}$ could arise from details of the unit cell parameters which could give rise to slightly different strain conditions.

6.5 Conclusion

In conclusion, the resistance of RBi_2 (R = La and Ce) under pressure up to ~ 2.5 GPa and ac specific heat of $CeBi_2$ under pressure up to 2.55 GPa have been studied. Our studies show that for $CeBi_2$ the antiferromagnetic transition temperature, T_N, increases upon increasing pressure with the rate of ~ 0.48 K/GPa. This fits into the Doniach phase diagram and suggests that there might be a maximum of T_N, followed by its decrease and finally a quantum critical point at possibly significantly higher pressures. Resistance and ac specific heat measurements of $CeBi_2$ together suggest that the pressure-induced superconductivity in $CeBi_2$ is likely not bulk. It is likely that the SC phase is filamentary Bi either on the surface or as laminar in the bulk of the sample. We suspect the pressure-induced superconductivity in $LaBi_2$ to arise from a similar extrinsic origin giving that the onset pressure and transition temperature of superconductivity are very similar to that of $CeBi_2$. Further pressure-dependent resistance analyses for $CeBi_2$ and $LaBi_2$ indicate some anomalies in the $R(p)$ curves, a change of slope between 1.68 GPa and 1.97 GPa for $CeBi_2$ and a broad minimum between 1.03 GPa and 1.68 GPa for $LaBi_2$. Taken together, these suggest that the stronger, low-temperature features see near and below T' for $CeBi_2$ are related to the pressure dependent hybridization and crystal electric field splitting of the Ce.

Finally, we would like to point out, again, that when studying the properties of Bi-rich compounds under pressure, one needs to be very careful and mindful for the various phases elemental Bi has and the rich physics they display at different pressuresKlement et al. (1963); Degtyareva et al. (2004); Li et al. (2017).

CHAPTER 7. AVOIDED FERROMAGNETIC QUANTUM CRITICAL POINT IN PRESSURIZED $La_5Co_2Ge_3$

A pressure work on a newly discovered metallic ferromagnetic material, $La_5Co_2Ge_3$ was performed. The following context presents our current measurement results and understanding of the data. Further analysis and interpretation of the data is on-going.

7.1 Introduction

Suppressing a second-order phase transition to zero temperature has been of great interest, since exotic physical phenomena, such as unconventional superconductivity, heavy Fermi-liquid etc., are often found in the proximity of the quantum critical point (QCP)Steglich et al. (1979); Dagotto (1994); Pfleiderer et al. (2001); Paglione and Greene (2010); Canfield and Bud'ko (2016). Whereas antiferromagnetic (AFM) transitions in many metals can be continuously suppressed to zero temperature by a non-thermal tuning parameter, such as pressure, chemical substitution or magnetic fieldGegenwart et al. (2008); Shibauchi et al. (2014), striking differences are observed when suppressing ferromagnetic (FM) transitions in metals. Current theoretical models suggest that, when tuning a second-order FM transition in metals towards zero temperature, the quantum criticality is avoided for general reasons. Possible predicted outcomes in clean metallic systems include that, when tuning a second-order FM transition towards zero temperature, the FM transition either becomes of first-order through a tricritical point, or a long-wavelength AFM phase appearsBelitz et al. (1999); Chubukov et al. (2004); Conduit et al. (2009); Karahasanovic et al. (2012); Pedder et al. (2013); Brando et al. (2016). Whereas a first-order FM transition was experimentally verified in several metallic systemsHuxley et al. (2000); Pfleiderer and Huxley (2002); Uhlarz et al. (2004); Niklowitz et al. (2005); Brando et al. (2016), a modulated magnetic phase was only observed in a few compoundsKotegawa et al. (2013); Cheng et al. (2015); Brando

et al. (2016); Niklowitz et al. (2019). In contrast, it was found that in disordered systems the FM transition remains continuous to low temperaturesBrando et al. (2016). Furthermore, a recent theoretical work proposes that a FM QCP can be realized even in a clean system, when the systems is noncentrosymmetric with a strong spin-orbit interactionKirkpatrick and Belitz (2020). The multiplicity of possible scenarios in itinerant ferromagnets motivated our search for new metallic ferromagnets, in which the (avoided) ferromagnetic criticality is experimentally accessible by using a tuning parameter, which does not introduce any additional disorder, such as hydrostatic pressure.

As part of an ongoing search for fragile magnetic orderingCanfield and Bud'ko (2016), we recently discovered a new itinerant, ferromagnetic compound $La_5Co_2Ge_3$Saunders et al. (2020). $La_5Co_2Ge_3$ belongs to the $R_5Co_2Ge_3$ (R = La - Sm) family which crystallizes in a monoclinic structure ($C2/m$ space group)Lin et al. (2017). At ambient pressure, thermodynamic, transport, and moun spin relaxation (μSR) measurements showed that $La_5Co_2Ge_3$ undergoes a FM transition at $T_C \simeq 3.8\,K$. In addition, the magnetism associated with $La_5Co_2Ge_3$ was found to be itinerant with a low-field saturated moment of $\sim 0.1\,\mu_B$/Co. These properties make $La_5Co_2Ge_3$ a rare, small moment, low T_C compound, which is a promising candidate material for tuning the FM transition towards even lower temperatures.

Motivated by this discovery, in this work we investigate the pressure-temperature phase diagram of $La_5Co_2Ge_3$ up to 5.12 GPa. To this end, magnetization, resistivity as well as specific heat measurements were performed under pressure. Our study demonstrates that T_C is suppressed from $\sim 4\,K$ to $\sim 3\,K$ upon increasing pressure up to $\sim 1.7\,GPa$. Upon further increasing pressure, different resistive and specific heat features are observed. Our results suggest that $La_5Co_2Ge_3$ enters a different, likely magnetic, low-temperature ground state that has an antiferromagnetic component. Therefore, $La_5Co_2Ge_3$ is another example, in which ferromagnetic criticality in metals is avoided by the occurrence of a new phase.

7.2 Experimental details

Single crystals of $La_5Co_2Ge_3$ were grown using a flux method as described in Ref. Saunders et al. (2020). Low-field (25 Oe) dc magnetization measurements on a crystal (with magnetic field applied along a random orientation) under pressure were performed in a Quantum Design Magnetic Property Measurement System (MPMS-3) SQUID magnetometer. The measurements were performed on warming after zero-field-cooling from above the magnetic and superconducting transitions of $La_5Co_2Ge_3$ and Pb manometer respectively. A commercially-available HDM Be-Cu piston-cylinder pressure cellHDM was used to apply pressures up to ~ 1 GPa. Daphne oil 7373, which solidifies at ~ 2.2 GPa at room temperatureYokogawa et al. (2007), was used as a pressure medium, ensuring hydrostatic conditions during the pressure change (see below for details). The superconducting transition temperature of elemental Pb was used as a low-temperature manometerEiling and Schilling (1981).

The resistivity measurements with current applied along the crystallographic b ($j \parallel b$) and c ($j \parallel c$) directions were performed in a Quantum Design Physical Property Measurement System (PPMS) using a 1 mA excitation with frequency of 17 Hz, on cooling using a rate of -0.25 K/min. A standard, linear four-terminal configuration was used. The magnetic field was always applied perpendicular to the bc plane (i.e., along the a^* direction), along which direction the largest saturated magnetization was observed at ambient pressureSaunders et al. (2020). To apply pressures up to ~ 2.3 GPa, a Be-Cu/Ni-Cr-Al hybrid piston-cylinder cell (abbreviated as PCC), similar to the one described in Ref. Bud'ko et al. (1984), was used. A 4:6 mixture of light mineral oil:n-pentane, which solidifies, at room temperature, in the range $3 - 4$ GPaBud'ko et al. (1984); Kim et al. (2011); Torikachvili et al. (2015), was used as pressure medium. To apply higher pressures, up to ~ 5.1 GPa, a modified Bridgman Anvil Cell (mBAC)Colombier and Braithwaite (2007) was used. A 1:1 mixture of iso-pentane:n-pentane, which solidifies at ~ 6.5 GPa at room temperatureTorikachvili et al. (2015) was used as the pressure medium for the mBAC. For both types of pressure cells, pressure values at low temperature were inferred from the $T_c(p)$ of leadBireckoven and Wittig (1988); Xiang et al. (2020a).

Specific heat measurements under pressure up to $\sim 2.4\,\mathrm{GPa}$ were performed using an AC calorimetry technique in a PPMS. Details of the setup used and the measurements protocol are described in Ref. Gati et al. (2019a). The same PCC, with same pressure medium and low-temperature pressure gauge, as in resistivity measurements was used.

For all measurements under pressure, the pressure was changed at room temperature and locked by tightening a lock-nut. The pressure variation across the Pb manometer at low temperature can be estimated from the increase of the superconducting transition width with pressure, that can be as large as 0.06 GPa depending on the cell and absolute pressure. Specifically, for the HDM cell, the PCC and the mBAC with maximum pressures up to $\sim 1\,\mathrm{GPa}$, $\sim 2.3\,\mathrm{GPa}$ and $\sim 5.1\,\mathrm{GPa}$, the pressure variations are up to $\sim 0.01\,\mathrm{GPa}$, $\sim 0.01\,\mathrm{GPa}$ and $\sim 0.06\,\mathrm{GPa}$, respectively. The measurement results shown and discussed in the main text are taken upon increasing pressure. Data taken upon decreasing pressure are shown and discussed in the Appendix.

7.3 Results and discussions

Figure 7.1 shows the temperature-dependent magnetization, $M(T)$, under pressures up to 0.99 GPa. The sharp onset of the diamagnetism at $\sim 7\,\mathrm{K}$ is associated with the superconducting transition of elemental Pb, which was used to determine the low-temperature pressure. With decreasing temperature, a rapid increase of the magnetization is observed at $\sim 4\,\mathrm{K}$ for all pressures, which is associated with a FM ordering. The transition temperature, T_C, is determined from the intersection of the two dashed lines as indicated in Fig. 7.1. The dashed line on the low-temperature side corresponds to a line, which goes through the point of maximum slope of $M(T)$ and whose slope corresponds to this maximum slope. The dashed line on the high-temperature side is a linear fit to the $M(T)$ data in a 1 K-temperature window below the Pb T_c and above the sharp increase of M. In order to estimate the uncertainty of our T_C determination, we have used multiple 1 K windows in this limited temperature range. T_C is suppressed from $\sim 4\,\mathrm{K}$ to $\sim 3.8\,\mathrm{K}$ upon increasing pressure from 0.16 GPa to 0.99 GPa. Finally,

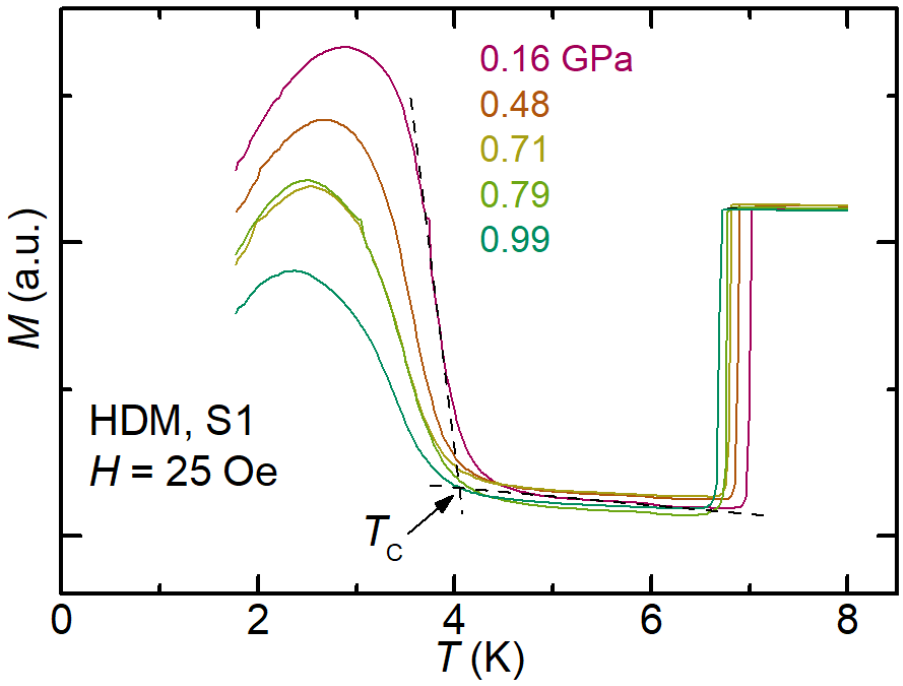

Figure 7.1 Resistance of $CeBi_2$ as a function of temperature at ambient pressure (measured on sample S1) and at different finite pressures up to 2.44 GPa (measured on sample S2). The ambient pressure data for S1 is normalized by extrapolating $p \leq 1.23$ GPa pressure-dependent resistance data, $R(p)$, at 300 K from S2 back to 0 GPa. A broad hump feature is present in all data sets. The inferred crossover temperature T' is exemplarily marked for the data set at 2.44 GPa (for more details, see text). Inset: Blowup of the resistance data at low temperatures showing the magnetic and superconducting transitions. AFM transition temperature T_N is indicated by arrow. Criterion for T_c^{offset} is indicated by arrow.

the decrease of M below $\sim 3\,\text{K}$, observed in low-field magnetization measurements after zero-field cooling, could be related to the formation of ferromagnetic domains in the crystal.

To investigate the phase diagram to higher pressure, resistivity measurements on several specimens were performed utilizing different pressure cells. Specifically, samples S2, S3 and S4 were measured in the PCC, the mBAC and the PCC with $j \parallel c$, $j \parallel c$ and $j \parallel b$, respectively. The results are summarized and presented in Fig. 7.2. At ambient pressure, in agreement with Ref. Saunders et al. (2020), for resistivity measured with $j \parallel b$ and $j \parallel c$, a sharp drop of resistivity is

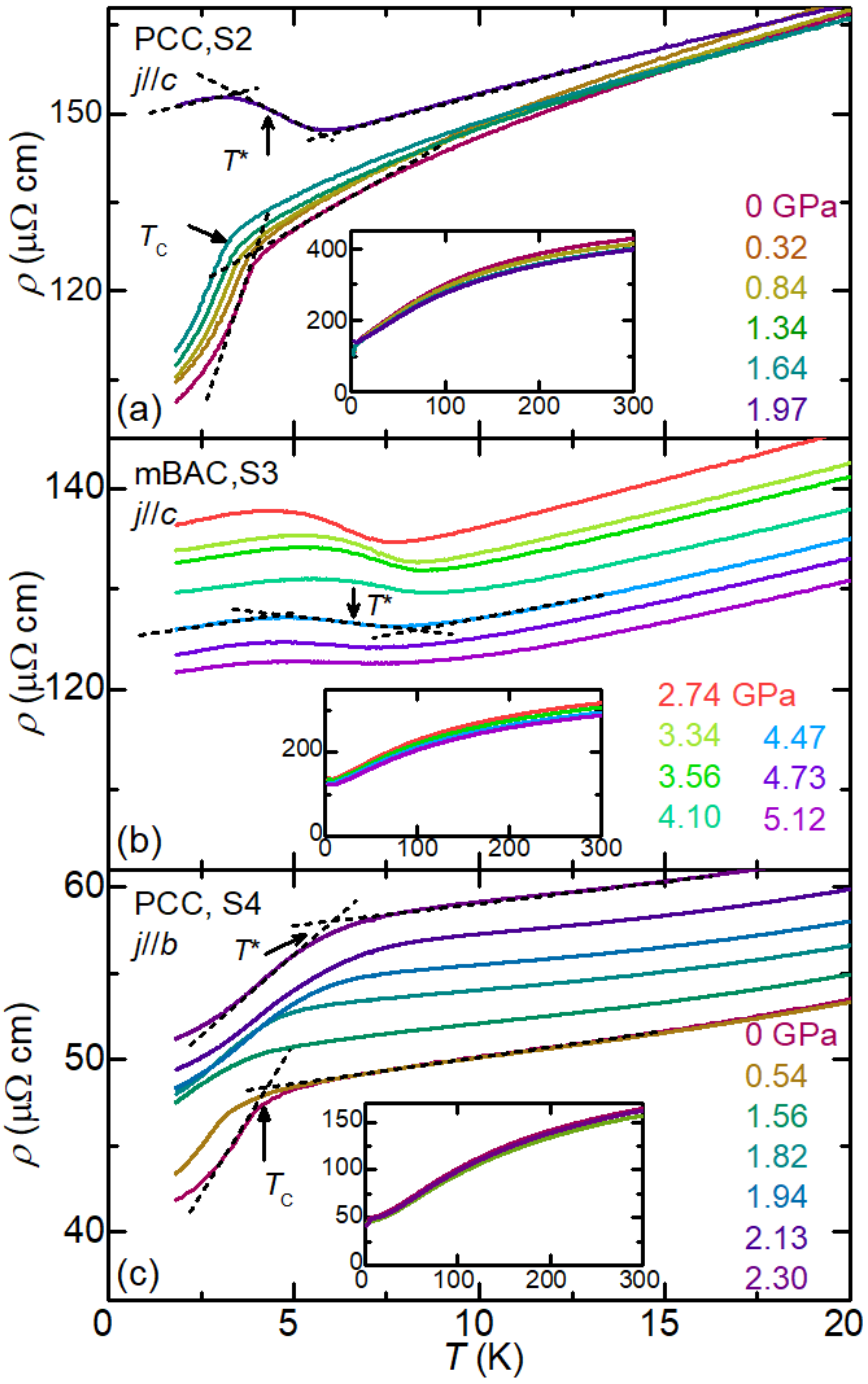

Figure 7.2 Resistivity measurements under pressure on $La_5Co_2Ge_3$. (a-c) Low-temperature resistivity, $\rho(T)$, for sample S2 measured in a piston-cylinder cell with current applied along c (a), for sample S3 measured in a modified Bridgman Anvil cell with current applied along c (b), and for sample S4 measured in a piston-cylinder cell with current applied along b (c). Insets: $\rho(T)$ curves in the full temperature range up to 300 K. Criteria for the determination of the ferromagnetic transition temperature T_C and the transition temperature into new ground state T^* are indicated by dashed lines and arrows in the figures (see text for details). Data curves in the main panels of (a) and (c) are shifted up by 2 $\mu\Omega$ cm for clarity.

observed at $T \sim 4\,\mathrm{K}$ which is associated with the FM transition. In addition, the c-axis resistivity shows a downturn curvature ($\mathrm{d}^2\rho/\mathrm{d}T^2 < 0$) for $T > T_\mathrm{C}$ (see Fig. 7.2 (a) inset), whereas the b-axis resistivity shows a upturn curvature ($\mathrm{d}^2\rho/\mathrm{d}T^2 > 0$) for $T_\mathrm{C} < T \lesssim 50\,\mathrm{K}$ (see Fig. 7.2 (c) inset), suggesting an anisotropic behavior of the c-axis and b-axis resistivity.

For all measured samples, $La_5Co_2Ge_3$ shows metallic behavior in the whole studied pressure range. For sample S2 measured in the PCC (see Fig. 7.2 (a)), the sharp drop of resistivity, associated with the FM transition, persists to pressures as high as 1.64 GPa. The ferromagnetic transition temperature, T_C, is determined from the intersection of the two dashed lines as indicated in Fig. 7.2 (a). The dashed lines are drawn in the same way as described above (with multiple 1 K windows on the high-temperature side over the temperature range of 5 K - 10 K to obtain the uncertainties). Using this criterion, we infer that, T_C is suppressed from $\sim 4\,\mathrm{K}$ to $\sim 3.4\,\mathrm{K}$ upon increasing pressure from 0 to 1.64 GPa. At 1.97 GPa, an anomaly with a different shape is observed at low temperatures. Upon cooling through $T \sim 6\,\mathrm{K}$, the resistivity shows a broad increase which is suggestive of superzone-gap formation. This feature implies that at 1.97 GPa, $La_5Co_2Ge_3$ enters a low-temperature ground state below T^* (defined below), which is different from the FM state at lower pressures. It appears likely that this new state is characterized by an antiferromagnetic component that partially gaps the Fermi surfaceFreeman (1972); Friedel (1987); Bud'ko and Canfield (2000). This superzone-gap-like feature in the resistivity is observed in all temperature-dependent data sets under pressures between 1.97 GPa and 5.12 GPa (see Fig. 7.2 (b) for data on sample S3 for $p \geq 2.74\,\mathrm{GPa}$ taken in the mBAC with $j \parallel c$).

The transition temperature T^*, which is associated with the transition into this new state, is determined from the following construction of three lines in the low-, intermediate- and high-temperature regime as indicated in Figs. 7.2 (a) and (b). The low- and high-temperature lines are linear fits to the $\rho(T)$ data in these temperature regimes, whereas the intermediate-temperature line goes through the point of maximum slope of $\rho(T)$ and the slope corresponds to this maximum slope. T^* is determined as the midpoint of the two intersection

points of the dashed lines and the uncertainties of T^* are obtained from the temperature difference of the two intersections points. Upon increasing pressure, T^* first increases from $\sim$ 4.0 K (2.74 GPa) to $\sim$ 7.4 K (4.10 GPa), then decreases to $\sim$ 6.3 K (4.73 GPa) and finally increases again slightly to $\sim$ 6.4 K (5.12 GPa).

For sample S4, measured with $j \parallel b$, for all data sets under pressure up to 2.30 GPa, resistivity decreases monotonically upon cooling from high temperatures, until it shows a sharp drop of resistivity when cooling through the phase transitions T_{C} and T^* (see Fig. 7.2 (c)). The corresponding transition temperature, T_{C} (T^*), is determined from the intersection of the two dashed lines (drawn in the same way as described above) as indicated in Fig. 7.2 (c). This observation shows that the resistivity at the T^* phase transition displays a distinct directional anisotropy, i.e., resistivity increases (decreases) upon cooling through T^* along the c (b) direction. The proposed superzone-gap formation outlined above is consistent with the $j \parallel c$ and $j \parallel b$ anisotropy of the resistive feature at T^*.

To further study the pressure effect on $La_5Co_2Ge_3$ from a thermodynamic perspective, specific heat measurements under pressure were performed. Figure 7.3 presents the specific heat divided by temperature, C_p/T, as a function of temperature for different pressures. At the lowest pressure measured (0.25 GPa), a clear "λ-shape" anomaly is observed at $\sim$ 3.3 K, which is associated with the ferromagnetic transition. The shape of the anomaly is consistent with the second-order nature of the transitionSaunders et al. (2020). At 0.62 GPa, the "λ-shape" anomaly is suppressed to lower temperature at $\sim$ 3 K and becomes significantly broader. In addition, a second feature at slightly lower temperature ($\sim$ 2.6 K), the origin of which is unclear, is only observed for this pressure. We point out that in the resistivity measurements, shown in Fig. 7.2, such a second feature at a similar pressure and temperature is not observed. We therefore did not include the second feature at 0.62 GPa in the pressure-temperature phase diagram. At 0.98 GPa, a single, broad anomaly is observed. For 1.18 GPa $\leq p \leq$ 1.41 GPa, C_p/T displays a continuous, smooth change upon cooling. The reason for the absence of a clear thermodynamic feature in this pressure range despite the presence of clear resistive features, as presented above, is presently

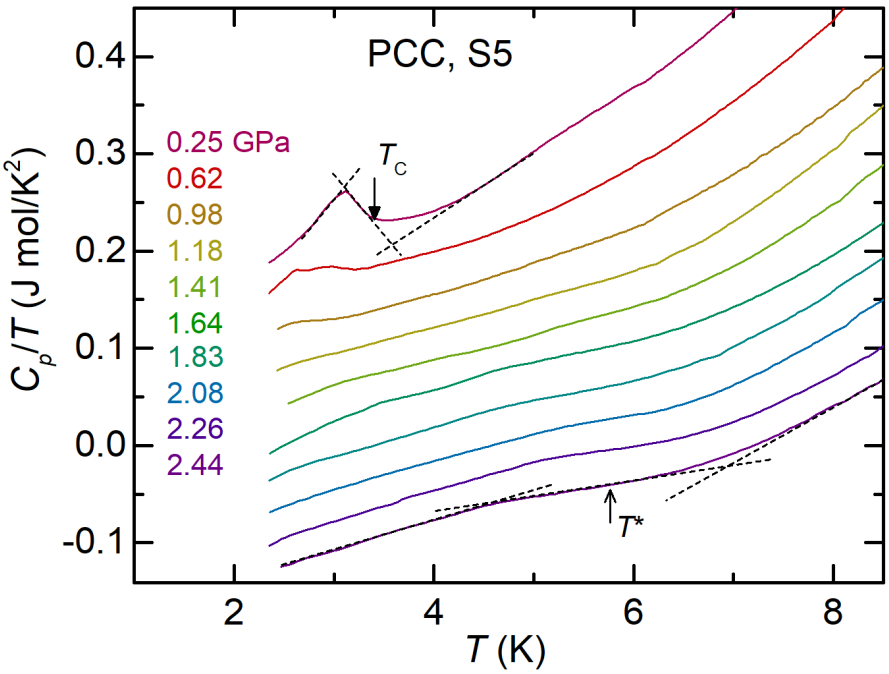

Figure 7.3 Evolution of the temperature-dependent specific heat over temperature, C_p/T, of $La_5Co_2Ge_3$ with pressure up to 2.44 GPa in a piston-cylinder cell for sample S5. Criteria for the determination of the ferromagnetic transition temperature T_C and the transition temperature into new ground state T^* are indicated by dashed lines and arrows in the figures (see text for details). Data curves are shifted down by 0.03 J mol/K^2 for clarity.

unknown. We speculate that in this pressure range, the change of entropy associated with the magnetic transition is broad in temperature and thus the specific heat feature is not resolvable from the non-magnetic background contribution. For $p \geq 1.64\,\mathrm{GPa}$, a broad hump-like feature is observed at $\sim 6\,\mathrm{K}$. Based on our previously-described observations in resistivity measurements, we associate this broad specific heat feature with the phase transition into the new type of order at high pressures. Thus, our thermodynamic, specific heat, measurements are consistent with the proposal that $La_5Co_2Ge_3$ enters a new state in the high-pressure, low-temperature region. The corresponding transition temperatures, T_C and T^*, are determined from the intersections of the three dashed lines as indicated in Fig. 7.3 (constructed following the same way as the lines constructed above in resistivity measurements shown in Fig. 7.2 (b)).

The transition temperatures, T_C and T^*, as determined from the magnetization, resistivity and specific heat measurements are used to construct a pressure-temperature ($p-T$) phase diagram, as shown in Fig. 7.4. Overall, three phase regions exist in the studied $p-T$ phase space, and are separated by the determined phase transition lines $T_C(p)$ and $T^*(p)$. At high temperatures, $La_5Co_2Ge_3$ is in the paramagnetic (PM) state. In the low-temperature (below T_C) and low-pressure ($p \lesssim 1.7\,\mathrm{GPa}$) region, $La_5Co_2Ge_3$ is in the ferromagnetic state. The transition temperature T_C is suppressed from $\sim 4.0\,\mathrm{K}$ to $\sim 3.3\,\mathrm{K}$ upon increasing pressure from 0 GPa to $\sim$ 1.7 GPa. In the low-temperature (below T^*) and high-pressure ($p \gtrsim 1.7$ GPa) region, $La_5Co_2Ge_3$ shows a different type of order. The transition temperature T^* manifests a nonmonotonic dependence on p with a local maximum at $\sim 4.1\,\mathrm{GPa}$ and a local minimum at $\sim 4.7\,\mathrm{GPa}$.

To further investigate the nature of the new type of order at high pressures and low temperatures, we studied the response of the superzone-gap feature to external magnetic fields. Figure 7.5 presents the temperature-dependent resistivity, $\rho(T)$, in magnetic fields up to 90 kOe, applied perpendicular the *bc* plane, for sample S2 at 0 GPa and 1.97 GPa. At low pressures, when magnetic field is increased, the resistive anomaly broadens and shifts to higher temperature. This is consistent with the expectation when the external magnetic field is applied along the ferromagnetic easy axisSaunders et al. (2020). At high fields, the $\rho(T)$ behavior is consistent with

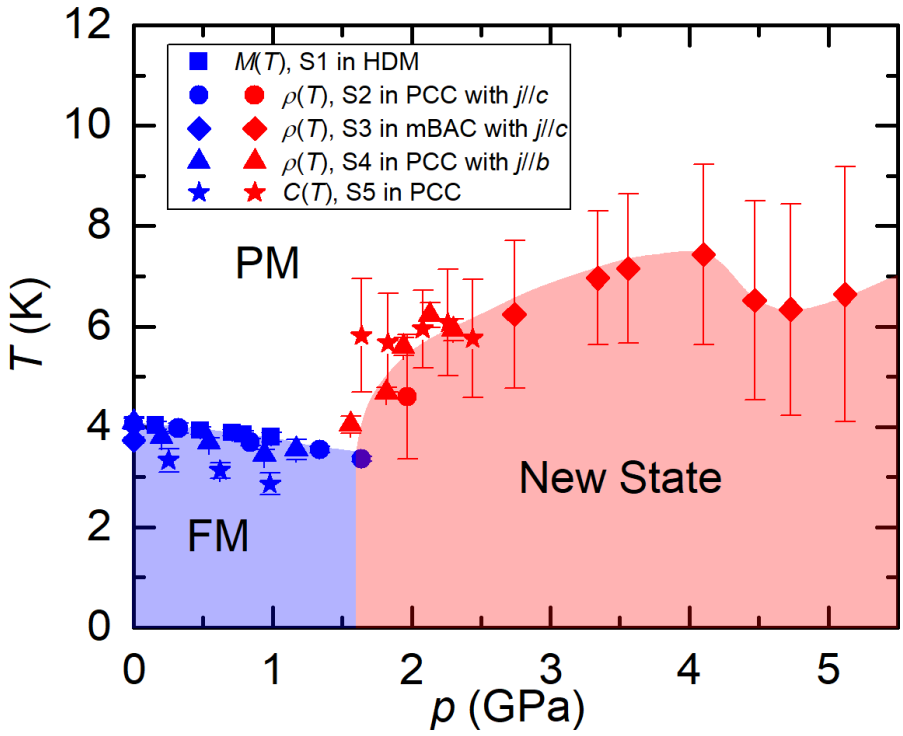

Figure 7.4 Pressure-temperature ($p-T$) phase diagram of $La_5Co_2Ge_3$, as determined from magnetization (sample S1), resistivity (samples S2, S3, S4) as well as specific heat (sample S5) measurements. Transition temperatures T_C (blue symbols) and T^* (red symbols) are determined using the criteria shown in Figs. 7.1-7.3. The determination of the error bars of the transition temperatures are described in detail in the text. The blue-shaded region corresponds to the region of ferromagnetic (FM) order, and the red-shaded region corresponds to the region of a new type of order. PM stands for paramagnetic.

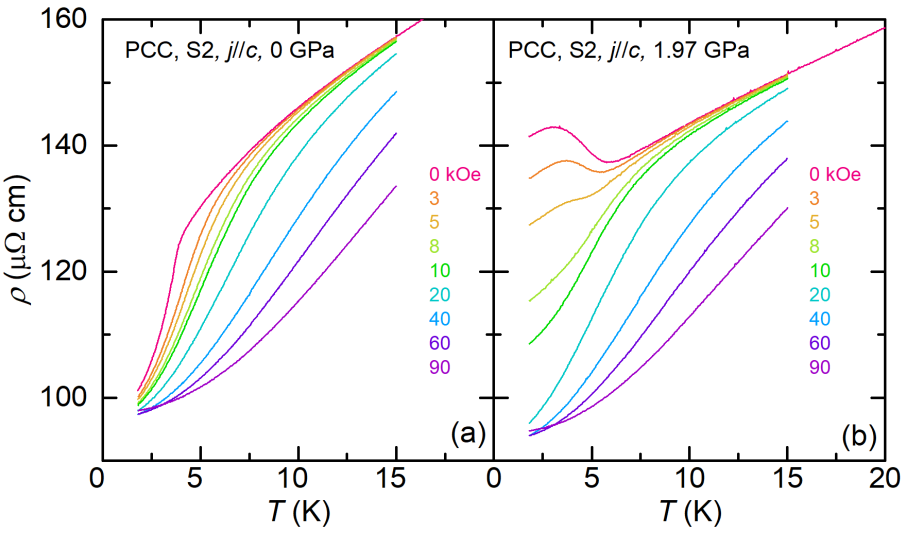

Figure 7.5 Temperature-dependent resistivity of $La_5Co_2Ge_3$ in magnetic fields up to 90 kOe (field was always applied perpendicular to the *bc* plane) for sample S2 at 0 GPa (a) and 1.97 GPa (b). Current is applied along the crystallographic *c* axis.

$La_5Co_2Ge_3$ undergoing a crossover to a fully spin-polarized state upon cooling. At high pressures, where our data demonstrate a phase transition into a state with different type of order, the resistive anomaly is broadened with applying magnetic field but the apparent transition temperature does not shift very much for low fields. At high fields, the resistivity displays a similar temperature dependence compared to that at low pressures and under high magnetic fields. The data in Fig. 7.5 (b), then, are consistent with a low-field antiferromagnetic state that becomes a high-field spin-polarized state when the external field is applied along the antiferromagnetic hard axis.

7.4 Conclusion

In summary, magnetization, resistivity and specific heat measurements under pressure up to 5.12 GPa were performed on single-crystalline $La_5Co_2Ge_3$. The ambient-pressure ferromagnetic transition temperature, T_C, is suppressed upon increasing pressure up to ~1.7 GPa. Instead of T_C being suppressed further upon increasing pressure beyond 1.7 GPa, we find that $La_5Co_2Ge_3$

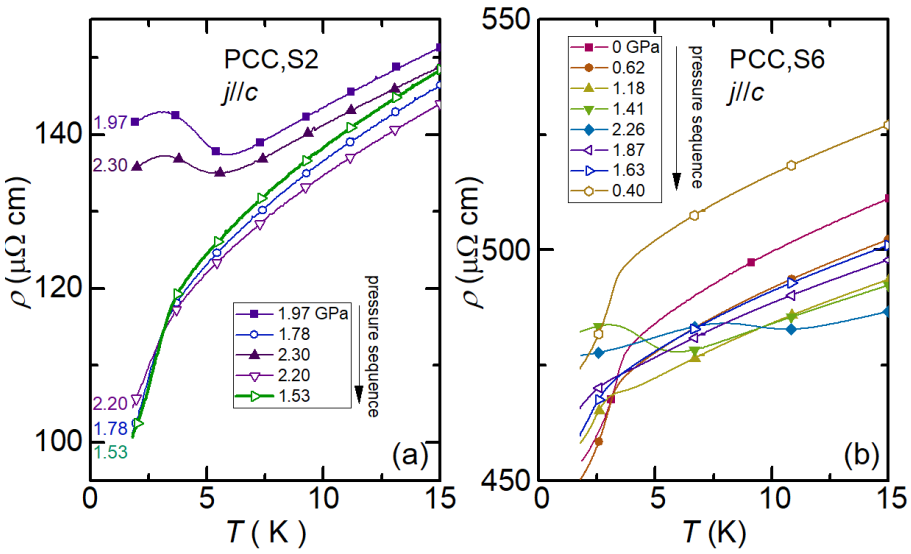

Figure 7.6 Temperature-dependent resistivity for samples S2 (a) and S6 (b) of $La_5Co_2Ge_3$ measured with current applied along c direction in piston-cylinder cell where pressure is changed in a non-monotonic way. Solid (open) symbols correponds to pressure increase (decrease) from a previous measurement. The corresponding pressure change sequences are indicated by arrows in the figures.

enters a different low-temperature ground state. The transition temperature, T^*, into the new state has a non-monotonic dependence on p up to 5.12 GPa. Overall, our study shows that $La_5Co_2Ge_3$ manifests another example of avoided ferromagnetic quantum criticality in a metallic system via the appearance of a new ordered state. Based on our transport data in zero and finite field, it seems likely that this new type of order is magnetic in nature with an antiferromagnetic component. To clarify the exact nature of the new phase, microscopic studies, such as neutron scattering or μSR under pressure, would be needed.

7.5 Appendix

In the following, we present results of further resistivity measurements on $La_5Co_2Ge_3$ under increasing and decreasing pressure. These measurements indicate that whereas $La_5Co_2Ge_3$ enters into a new state in the high-pressure, low-temperature region, the exact critical pressure, which

separates the FM and the new ground state, as well as transition temperature, T^*, can vary somewhat from sample to sample and depends on the history of pressure change.

In the main text, Fig. 7.2 (a) shows the $\rho(T)$ for sample S2 measured in the PCC with $j \parallel c$ where pressure is monotonically increased to 1.97 GPa. Further measurements on this sample were performed where pressure was changed non-monotonically after 1.97 GPa and the results are shown in Fig. 7.6 (a). We start our discussion at 1.97 GPa, where we find clear evidence for the superzone-gap-like feature in resistivity, and now turn to the next pressure point, which was obtained by decreasing pressure to 1.78 GPa. This results, as expected, in a phase transition back into the FM state at low temperatures. Increasing pressure again to 2.30 GPa leads, again, to the observation of the superzone-gap-like feature. Then, surprisingly, when reducing the pressure back to 2.20 GPa, we observe a resistive behavior which we would associate with the low-pressure behavior of FM ordering instead of the superzone-gap-like feature. We would have not expected this result based from our phase diagram. These data suggest that the pressure history seems to affect the critical pressure.

To investigate the dependence of the critical pressure in a more systematic way, sample S6 was measured in the PCC with $j \parallel c$, where pressure is first monotonically increased and then monotonically decreased. The $\rho(T)$ data for selected pressures are presented in Fig. 7.6 (b). We point out that S6 has a higher residual resistivity, ρ_0, compared with other measured samples, indicating a somewhat higher level of disorder in this sample. At low pressures, $\rho(T)$ displays a sharp drop upon cooling, which corresponds to the FM transition. With increasing pressure to 1.41 GPa and higher, a clear increase of ρ upon cooling is observed, suggesting that $La_5Co_2Ge_3$ enters into the new ordered state. When pressure is monotonically decreased from the highest pressure, we see that at 1.63 GPa, the superzone-gap-like feature is lost and a sharp drop of resistive anomaly, which we associate with the FM transition, is observed. Upon further decreasing pressure, sample S6 stays FM at low temperature. These measurement results demonstrate that the critical pressure upon increasing and decreasing pressure are clearly different for S6 ($\sim$ 1.41 GPa and $\sim$ 1.63 GPa with increasing and decreasing pressure). We

further point out that even upon increasing pressure, the critical pressure for S6 ($\sim$ 1.41 GPa) is lower than for S2 ($\sim$ 1.7 GPa).

The corresponding transition temperatures T_{C} and T^*, determined from the measurements on samples S2 and S6 are summarized in Figs. 7.7 (a) and (b), respectively. The transition temperatures determined from resistivity measurements with $j \parallel c$ (samples S2, S3 and S6), where pressure is monotonically increased, are plotted in Fig. 7.7 (c) together for comparison. Whereas the pressure dependence of the FM transition temperature, T_{C}, agrees well with each other for all different samples and experiments, the critical pressure varies from sample to sample and depends on the history of pressure change. In addition, the corresponding transition temperature, T^*, also varies (T^* is $\sim$ 4.6 K and $\sim$ 7.8 K for S2 and S6 respectively, at a pressure of $\sim$ 2 GPa). Overall, whereas the basic features of the $p-T$ phase diagram of $La_5Co_2Ge_3$ are robust among all measurements (i.e., $La_5Co_2Ge_3$ is ferromagnetic in the low-temperature, low-pressure region and enters into a new state in the low-temperature, high-pressure region), the sensitivity of the pressure-induced transition to the super-zone-gapped state to the pressure history as well as possibly small differences in degrees of disorder suggests that there are parameters influencing the precise values of the critical pressure as well as T^* that still need to be understood.

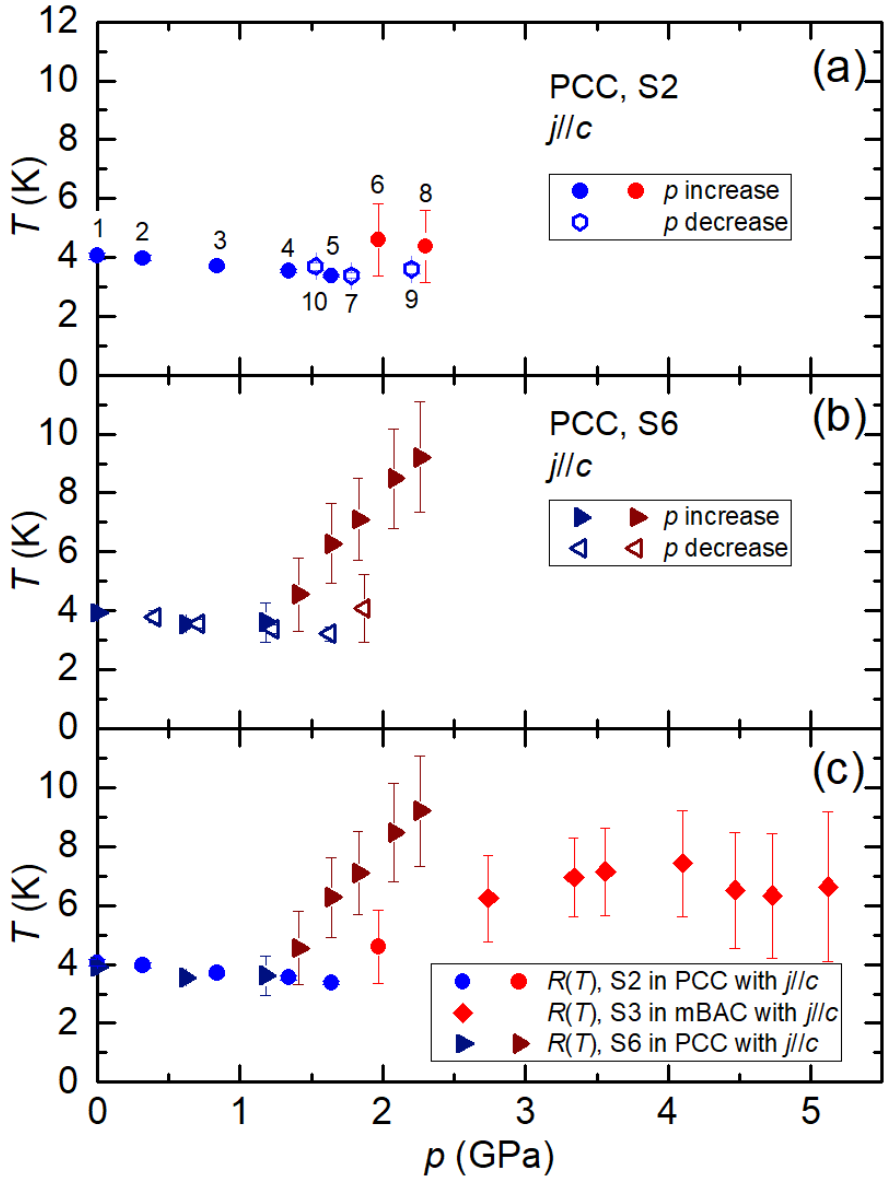

Figure 7.7 Pressure-temperature ($p-T$) phase diagrams of $La_5Co_2Ge_3$ determined from measurements on sample S2 (a), sample S6 (b), samples S2, S3 and S6 (c). Solid (open) symbols correspond to data that were obtained after increasing (decreasing) pressure with respect to the previous measurement. Numbers in (a) indicate the sequence of pressure change.

CHAPTER 8. CHARACTERIZATION OF THE PRESSURE COEFFICIENT OF MANGANIN AND TEMPERATURE EVOLUTION OF PRESSURE IN CONVENTIONAL PISTON-CYLINDER CELLS

The following context is a slightly modified version of the published work in Ref. Xiang et al. (2020a). DOI: https://doi.org/10.1063/5.0022650. Reproduced from [L. Xiang *et. al.*, Review of Scientific Instruments 91, 095103 (2020)], with the permission of AIP.

8.1 Introduction

Pressure, as an external tuning parameter, has been recognized as a powerful tool to modify materials' properties as well as to stabilize new, and sometimes exotic, phasesSchilling (1979); Doniach (1977); Chu and Lorenz (2009); Paglione and Greene (2010); Steglich and Wirth (2016); Mao et al. (2016); Drozdov et al. (2015); Gati et al. (2020a). To put materials under pressure, a sample of interest is typically placed into a pressure cell surrounded by a pressure-transmitting medium (gas, liquid or solid powder). When a force is applied to the medium via a piston or an anvil, pressure is generated and transmitted to the sample. Over decades, various pressure cells were developed to cover different pressure ranges and many measurement techniques were adapted to be used in these cellsBridgman (1952); Jamieson and Lawson (1962); Smith et al. (1966); Jayaraman et al. (1967); Fujiwara et al. (1980); Eremets (1996); Colombier and Braithwaite (2007); Rüetschi and Jaccard (2007); Drozdov et al. (2015). In the area of high-pressure research, it is essential to determine the absolute value of the applied pressure that a material of interest is exposed to. Intuitively, assuming some level of hydrostaticity of the pressure medium, one can calculate the pressure p by $p = \frac{F}{S}$, where F is the applied force and S is the area the force is applied to. However, this method suffers from the ambiguity of determination of the exact experienced force and area (due to friction and dimension changes of

the area which the force is applied to). In addition, the pressure in many pressure cells, particularly in clamp cells, is subject to temperature-induced changes due to differential thermal expansion of the cell materials and media Brandt et al. (1974); Eiling and Schilling (1981); Thompson (1984). Due to these uncertainties, the absolute value of pressure is instead determined from measurements of a physical quantity of a reference system (manometer) where the pressure dependence of the specific physical quantity is per-characterized. For example, pressure can be determined from measuring the p dependence of the superconducting transition temperature T_c of elemental Pb, Sn and InSmith and Chu (1967); Smith et al. (1969); Clark and Smith (1978); Wittig et al. (1979); Bireckoven and Wittig (1988), the p dependence of the resistance of manganinBridgman (1911), the p dependence of the fluorescence lines of ruby (typically used in pressure cells with access for optical measurements, e.g., in diamond anvil cells)Forman et al. (1972); Barnett et al. (1973); Piermarini et al. (1975), the p dependence of the lattice parameters of Au, Cu and Pt (often used in neutron or x-ray diffraction experiments)Fei et al. (2007). The choice of the manometer in a specific experiment often depends on the specific cell design as well as the available measurement techniques.

Among the different types of pressure cells, piston-cylinder clamp cells are among the most commonly used due to their relative ease of usage, their wide covered pressure range (up to $\sim$4 GPa, depending on the specific design and materials) as well as their relatively large sample volumes that allow to perform a variety of measurementsKadomatsu and Fujiwara (1979); Fujiwara et al. (1980); Kamishima et al. (2001); Fujiwara et al. (2007); Gati et al. (2019a, 2020b). In these cells, either superconducting manometers (Pb, Sn or In) are frequently used to determine pressure at low temperatures or resistive manganin sensors are often utilized to infer pressure at different temperatures, given its relatively high, relatively temperature-insensitive and relatively pressure-sensitive resistivity. Using these sensors, several studies were performed to determine the pressure change as a function of temperature in piston-cylinder cells with maximum pressure of 2 - 3 GPaItskevich (1964); Brandt et al. (1974); Eiling and Schilling (1981); Thompson (1984); Fujiwara et al. (2007); Becker et al. (1976). Overall, these studies suggested a pressure drop up to

$\sim 0.3\,\mathrm{GPa}$ - $0.4\,\mathrm{GPa}$ from room temperature to low temperatures, with some differences in details of $p(T)$ behaviorItskevich (1964); Brandt et al. (1974); Eiling and Schilling (1981); Thompson (1984); Fujiwara et al. (2007). Some of these estimates Fujiwara et al. (2007); Brandt et al. (1974); Thompson (1984) relied on the characterization of the pressure-dependent resistance of the manganin sensor at room temperature to obtain the pressure coefficient α, defined via $R_p = (1 + \alpha p)R_0$ where R_0 and R_p are resistance at ambient pressure and finite pressure p, respectively. The room-temperature α was then extended to be used at lower temperatures. In fact, other studies suggested already that α is slightly temperature-dependent and therefore the use of a temperature-independent α would result in an overestimation of the pressure change with temperature Itskevich (1964); Andersson and Sundqvist (1997); Dmowski and Litwin-Staszewska (1999). Specifically, Dmowski *et al.* in Ref. Dmowski and Litwin-Staszewska (1999) carried out a temperature-dependent study of α in the T range from $77\,\mathrm{K}$ up to $350\,\mathrm{K}$. They reported that α decreases linearly with T from $77\,\mathrm{K}$ up to $110\,\mathrm{K}$, then shows a very sharp change of slope and increases linearly with T up to high temperatures. Despite the fact that for many modern complex materials and phenomena there is a need to accurately evaluate pressure behavior not only at room temperature or liquid Helium temperatures, but also at intermediate temperaturesKaluarachchi et al. (2017a); Xiang et al. (2018b); Lamichhane et al. (2018), the temperature dependence of α of manganin has not been widely appreciated and used in investigations of the detailed temperature evolution of pressure in piston-cylinder cells.

The goal of this study is to perform a more detailed and careful characterization of the temperature and pressure dependence of the coefficient $\alpha(T, p)$ of manganin, as well as to utilize it to determine the evolution of pressure with temperature in a piston-cylinder cell. To this end, we first present an analysis of the manganin wire resistance from measurements performed inside a ^{4}He-gas pressure cell, which serve as calibration measurements of the manganin sensor, between $0\,\mathrm{GPa}$ and $0.8\,\mathrm{GPa}$, from room temperature down to the solidification temperature of ^{4}He ($T_{\mathrm{solid}} \sim 50\,\mathrm{K}$ at $0.8\,\mathrm{GPa}$). In this set of experiments, we make use of the fact that the specific design of the ^{4}He-gas pressure setup allows us to readily measure the pressure at low

temperatures via a manganin pressure sensor, which is held at room temperature at all times, as long as the pressure medium ^{4}He is either in its gaseous or liquid state (see below for more details). In a second step, the resistance of the same manganin wire manometer was measured in a piston-cylinder cell from 300 K down to 1.8 K and for pressures between 0 GPa and $\sim$2 GPa. By combining the results of these measurements, the pressure coefficient, $\alpha(T, p)$, is obtained. We find that α shows a non-monotonic behavior as a function of temperature with a broad minimum at $\sim$120 K. We also show that whereas for $T \gtrsim 60$ K α is almost pressure-independent, it has a larger pressure dependence for $T \lesssim 60$ K. Overall, our results emphasize the need to take the temperature and pressure dependence of α into account when using manganin as a secondary manometer. By using the determined $\alpha(T, p)$, we then address the change of pressure with temperature in a piston-pressure cell. We find (i) that pressure decreases with decreasing temperature for all investigated pressures up to $\sim$2 GPa, and (ii) that the pressure difference between room temperature and base temperature, Δp, decreases with increasing pressure. For our specific combination of pressure cell, pressure medium and sample space filling factor, Δp is estimated to be $\simeq$0.47 GPa ($\simeq$0.26 GPa) for lowest (highest) pressure, for which the pressure at low temperature is $\simeq$0.21 GPa ($\simeq$1.86 GPa). We also compare the pressure values from the manganin sensor at $T \simeq 7$ K to those, determined from the superconducting transition temperature of elemental Pb (denoted in the manuscript as Pb-T_c manometer). As a result of this analysis, we offer in the end a "practical" approach for inferring p values for our piston-cylinder cell, pressure medium and sample space filling factor for temperatures below room temperature. We note that in previous studiesEiling and Schilling (1981) the absolute resistance of Pb was also proposed to be used as a manometer for higher temperatures (referred to as Pb-resistive manometer). As we describe in detail in Appendix B, it turns out that the determination of pressure values from a Pb-resistive sensor is somewhat fraught with problems related to the residual resistivity of Pb and the reproducibility of ambient-pressure resistivity values, and therefore a comparison to those values is not included in the main text.

8.2 Experimental Details

The studied manganin manometer was made from a commercial, AWG 44 manganin wire segment (Driver-Harris Co). It has a diameter of ~ 0.05 mm and was wound into a free-standing coil with an outer diameter of ~ 1.5 mm. Prior to taking all data, presented here, the manganin manometer was thermally cycled between 300 K and 1.8 K for more than ten times under different pressures up to 2 GPa. After this thermal cycling process, no significant further aging effect of the manganin wire was observed at room temperature. Specifically, the resistance of manganin at room temperature and ambient pressure was the same within 0.01% before and after a pressure cycle up to $\sim$ 2 GPa . The Pb manometer was made in-house from elemental Pb with purity higher than 99.99%. In a first step, a 0.03 mm thin Pb sheet was formed by rolling a glass vial over the elemental Pb piece. Then a rectangular Pb bar with dimensions around $0.7\times0.1\times0.03\,\mathrm{mm}^3$ was cut from the Pb sheet for electrical resistance measurements.

Resistance measurements of manganin were carried out in the ^{4}He-gas pressure setup under pressure up to ~ 0.8 GPa upon cooling in a ^{4}He VTI cryostat down to 5 K with a cooling rate of -0.2 K/min. A standard four-terminal configuration was used. Contacts for manganin were made by soldering 100 μm diameter Cu wires using a Sn:Pb-60:40 alloy. The manganin wire was supplied with a constant DC current of 10 μA and the resulting voltage was measured using a Keithley 2182A Nanovoltmeter. The current direction was switched once during each measurement to subtract thermoelectric voltage contributions. The pressure cell is manufactured out of CuBe (Unipress, Institute of High-Pressure Physics, Polish Academy of Sciences, Unipress Equipment Division) and is connected via a CuBe capillary (outer/inner diameter: 3 mm/0.3 mm) to a Helium-gas compressor (Unipress), which is held at room temperature, during the entire time of the experiment. The gas compressor is not only used for changing the pressure in the system, but also acts as a large gas reservoir to ensure, to a good approximation, that pressure inside the pressure cell is held constant during temperature sweeps. The pressure is measured by a manganin sensor inside the compressor (calibrated by Unipress), which measures the pressure in the entire system (low-temperature pressure cell, capillary and compressor) and is not subject to

any temperature changes. Throughout the manuscript, we will refer to the pressure value determined from this compressor manometer.

The exact same manganin wire that was measured in the ^{4}He-gas pressure system, together with a piece of Pb was mounted into a CuBe/NiCrAl hybrid piston-cylinder cell (abbreviated in the manuscript as PCC) similar to the one described in Ref. Bud'ko et al. (1984), which has a maximum pressure of ~ 2.5 GPa. Standard four-terminal resistance measurements were performed in a Quantum Design Physical Property Measurement System (PPMS) on warming with a rate of 0.25 K/min and with a current excitation of 1 mA for manganin and 5 mA for Pb. Contacts for Pb were made by spot-welding 25 μm Au wires to the sample. A 4:6 mixture of light mineral oil: n-pentane was used as the pressure medium, which solidifies in the range of 3-4 GPa at room temperatureTorikachvili et al. (2015). Pressure was changed at room temperature and locked by tightening the top lock-nut.

8.3 Results and Discussion

8.3.1 ^{4}He-gas pressure cell measurements

The resistance of the manganin wire, which acts as a secondary manometer, was characterized in a ^{4}He-gas pressure cell under pressure up to ~ 0.8 GPa. Figure 8.1 (a) presents the temperature-dependent resistance, $R(T)$, of manganin for different pressure runs, denoted as $p_{i,He}$, i=1, ...,5. At any temperature, R increases with increasing pressure, and in any pressure run, R decreases with lowering temperature. For all finite pressure runs, kink-like anomalies were observed at low temperatures. The positions of the anomalies (see arrows in Figs. 8.1 (a) and (b)) are pressure-dependent and can be associated with the solidification of ^{4}HePinceaux et al. (1979). The temperature dependence of the pressure in the ^{4}He-gas experiments (see Fig. 8.1 (b)), which was recorded by the compressor manometer, shows that the pressure varies only weakly with temperature; this is enabled by the large gas reservoir, provided by the compressor (Note that a leak in the gas-pressure system was responsible for the strong temperature dependence of $p_{5,He}$)Manna et al. (2012). The minor temperature dependence for $p_{1,He}$ to $p_{4,He}$ can be

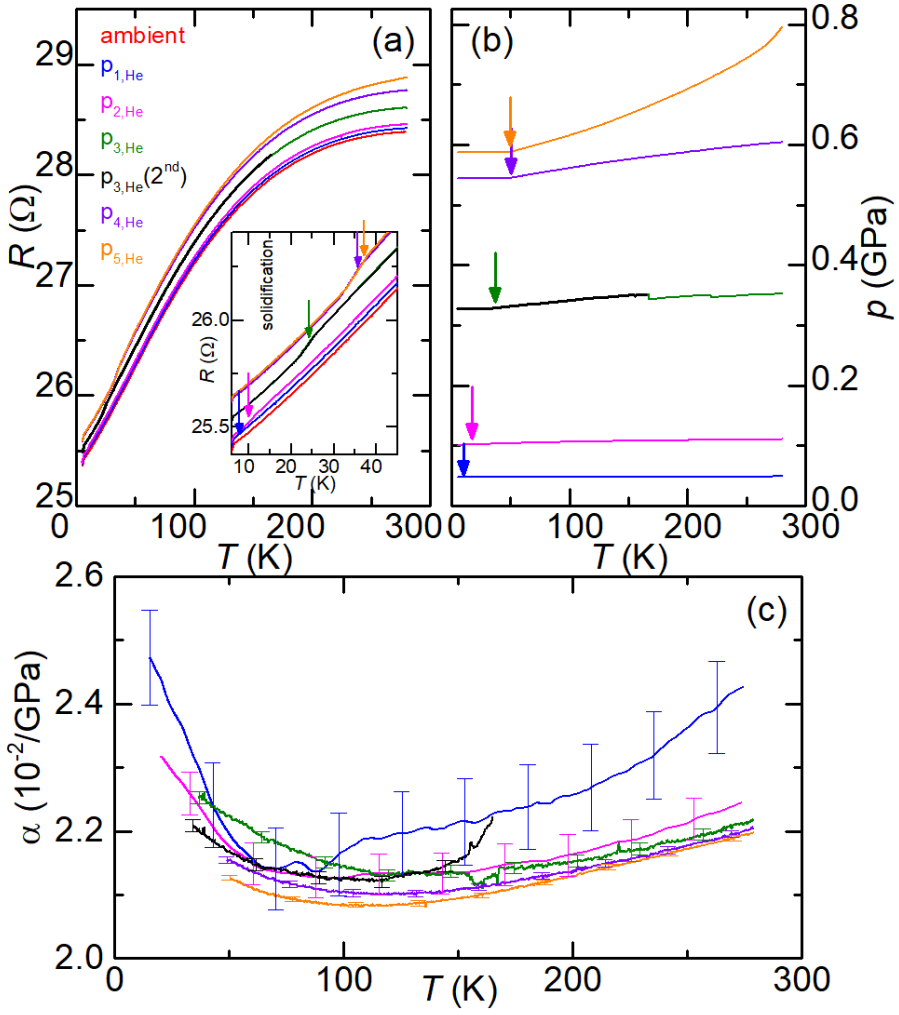

Figure 8.1 (a) Temperature-dependent resistance, $R(T)$, of manganin measured in various pressure runs up to $\approx 0.8\,\mathrm{GPa}$ in a ^{4}He-gas pressure system. The data are labeled according to their run number $\mathrm{p}_{1,\mathrm{He}}$ to $\mathrm{p}_{5,\mathrm{He}}$; Inset: Enlarged view of the low-temperature $R(T)$ data. The kink-like anomalies in $R(T)$ (see arrows) are associated with the solidification of ^{4}He; (b) Temperature-dependent pressure, $p(T)$, for the corresponding pressure runs. Pressure values are determined from a manganin manometer, which is located inside the compressor and held at room temperature (see text for details). The step-like change of pressure at $T \approx 160\,\mathrm{K}$ and $230\,\mathrm{K}$ for the $\mathrm{p}_{3,\mathrm{He}}$ run can be attributed to manual pressure increase via the compressor; (c) Temperature-dependent pressure coefficient, $\alpha(T)$, for various pressure runs. Error bars are a result of an uncertainty of $\pm 0.002\,\mathrm{GPa}$ in the pressure determination of ^{4}He-gas pressure system. Data below ^{4}He-solidification temperature are discarded due to reasons outlined in the main text.

rationalized when considering that the gas reservoir volume is large but finite ($V \sim 1000\,\mathrm{cm}^3$ with piston in lowest positions; for comparison cell volume $V \sim 1\,\mathrm{cm}^3$). Upon cooling, helium atoms are transferred from the reservoir to the pressure cell, leading to an overall minor decrease of the pressure in the entire system with lowering the temperature. As can be intuitively understood from a consideration of ideal gas law, the change of pressure with temperature becomes slightly larger upon decreasing pressure (as seen in Fig. 8.1 (b), $\mathrm{d}p/\mathrm{d}T$ becomes larger upon cooling). In addition, the volume of the gas reservoir is reduced by increasing the absolute pressure of the system, since the piston (in the various pressure stages) is moved to different positions. Thus, temperature-induced changes of the pressure are larger for higher pressures than for lower pressures. As can be seen in Fig. 8.1 (b), these intuitive expectations ($\mathrm{d}p/\mathrm{d}T$ becomes larger upon decreasing T and/or increasing p) are met in our measurements of the $p(T)$ landscape. We would like to stress though, that these effects are fully taken into account in our analysis, since we measure the pressure *in situ* at any temperature. Only when the pressure medium becomes solid at very low temperaturesPinceaux et al. (1979), the compressor and the pressure cell are decoupled since the solid ^{4}He in the capillary blocks the pressure transmission from the reservoir to the pressure cell, and thus, the compressor manometer does not measure the low-temperature pressure (see the plateau in $p(T)$ in Fig. 8.1 (b), particularly clearly for $\mathrm{p}_{4,\mathrm{He}}$ and $\mathrm{p}_{5,\mathrm{He}}$). We therefore refrain from including data below the solidification in our analysis.

With the data presented in Figs. 8.1 (a) and (b), the temperature-dependent pressure coefficient can be calculated via

$$\alpha(T) = \frac{\frac{\Delta R_p}{R_0}}{p} = \frac{(R_p(T) - R_0(T))/R_0(T)}{p} \tag{8.1}$$

where $R_0(T)$ and $R_p(T)$ are the resistances measured at ambient pressure and finite pressure p, respectively. The resulting α values as a function of temperature for various pressure runs are shown in Fig. 8.1 (c). Our calculated α value at room temperature is consistent with previous literature reports of $\alpha(300\,\mathrm{K}) = (2.35 \pm 0.15) \times 10^{-2}/\mathrm{GPa}$Wang (1967); Zeto and Vanfleet (1969); Fujioka et al. (1978); Andersson and Sundqvist (1997); Dmowski and Litwin-Staszewska (1999). For all pressure runs, the overall behavior of $\alpha(T)$ displays a moderate decrease upon cooling in

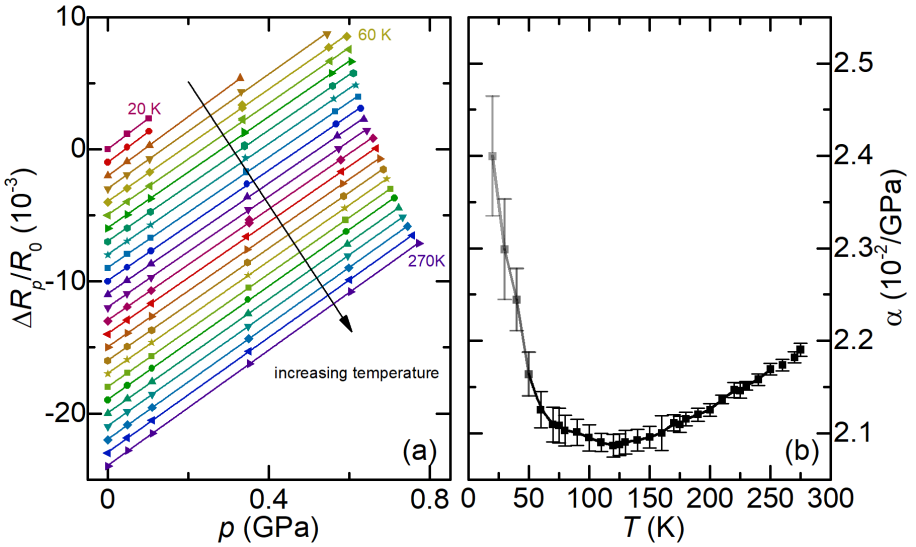

Figure 8.2 (a) Normalized change of resistance, defined as $\frac{\Delta R_p}{R_0} = \frac{R_p - R_0}{R_0}$ where R_0 and R_p are the resistance at ambient pressure and finite pressure p respectively, as a function of pressure, p, for various temperatures from 20 K to 270 K (spacing of 10 K), determined in ^{4}He-gas pressure experiments. Lines are linear fits to the data points. Data curves are vertically shifted (spacing of 10^{-3}) for clarity. For lower temperatures $T < 60\,K$, the high-pressure data points are omitted due to the solidification of the pressure medium (see text); (b) Temperature-dependent pressure coefficient, $\alpha(T)$, obtained by the slope of the linear fit in (a). Error bars correspond to the fitting error of the linear fit. A color gradient for the symbols is used to visualize that the data points result from fitting the data over different pressure ranges, since the solidification of the pressure medium strongly limits the maximum pressure for low temperatures. Black (light grey) symbols indicate that the linear fit was performed up to $\sim$0.7 GPa ($\sim$0.2 GPa).

the high-temperature region and then a increase in the low-temperature region with a broad minimum centered around 120 K. For high temperatures, the α values determined from pressure runs $p_{2,He}$ to $p_{5,He}$ agree with each other very well, whereas the α values for $p_{1,He}$ are clearly larger than the ones from other runs. We speculate that this deviation is related to the fact that the pressure and pressure-induced resistance changes for $p_{1,He}$ are so low that systematic errors in the determination of α are larger.

The temperature dependence of α can be quantified alternatively by analyzing the isothermal pressure dependence of the resistance. Figure 8.2 (a) presents the normalized change of resistance,

$\frac{\Delta R_p}{R_0}$, (defined in Eq. 8.1) as a function of p, as determined from our measurements under ^{4}He-gas pressure. Up to $\sim$0.8 GPa, $\frac{\Delta R_p}{R_0}$ changes linearly with p for 60 K$\leq T \leq$270 K, i.e. α is constant with p within 5%. For $T <$60 K, the limited number of data points does not allow us to make a definitive statement on the linearity of $\frac{\Delta R_p}{R_0}$ with p over a wide pressure range. Based on the assumption of linearity, the $\alpha(T)$ data set is obtained by performing a linear fit of the $\frac{\Delta R_p}{R_0}(p)$ data and the result is shown in Fig. 8.2 (b). The error bars are determined from the error of the linear fits. We relate the larger error bars for $T <$60 K to the fact that less data points are available to perform the linear fit. The overall behavior of α as a function of T resembles the data shown in Fig. 8.1 (c) on a gross level. Note that a non-linear behavior of the $\frac{\Delta R_p}{R_0}(p)$ curve would indicate a p dependence of α. In this case, the α value determined from a linear fit of $\frac{\Delta R_p}{R_0}(p)$ data represents an averaged α value over the fitted pressure range, which can be different from the real α value at a specific pressure.

Compared to literature results on the T dependence of the pressure coefficient α, our $\alpha(T)$ behavior is overall consistent with that reported in Ref. Dmowski and Litwin-Staszewska (1999) in the sense that a local minimum of $\alpha(T)$ is observed at $T \sim$120 K, suggesting that this could be a general behavior of the manganin sensor. However, our results suggest a smooth, continuous change of α with temperature, in contrast to the sharp kink anomaly in $\alpha(T)$ at $T \approx$110 K as reported in Ref. Dmowski and Litwin-Staszewska (1999).

8.3.2 Piston-cylinder cell measurements

Having obtained a calibration of our manganin sensor from the ^{4}He-gas pressure measurements, we proceed and evaluate the temperature dependence of the applied pressure in a piston-cylinder pressure cell. To this end, the characterized manganin sensor, together with Pb-T_c manometer, is utilized to study the pressure behavior in the PCC. Figure 8.3 presents the temperature-dependent resistance of manganin (Fig. 8.3 (a)) and Pb (inset of Fig. 8.3 (b)) for various pressure runs up to $\sim$ 2 GPa. The pressure runs $p_{2,PCC}$ - $p_{9,PCC}$ were taken after the application of a force, ranging from 1000 lbs to 8000 lbs, by a hydraulic press, whereas for

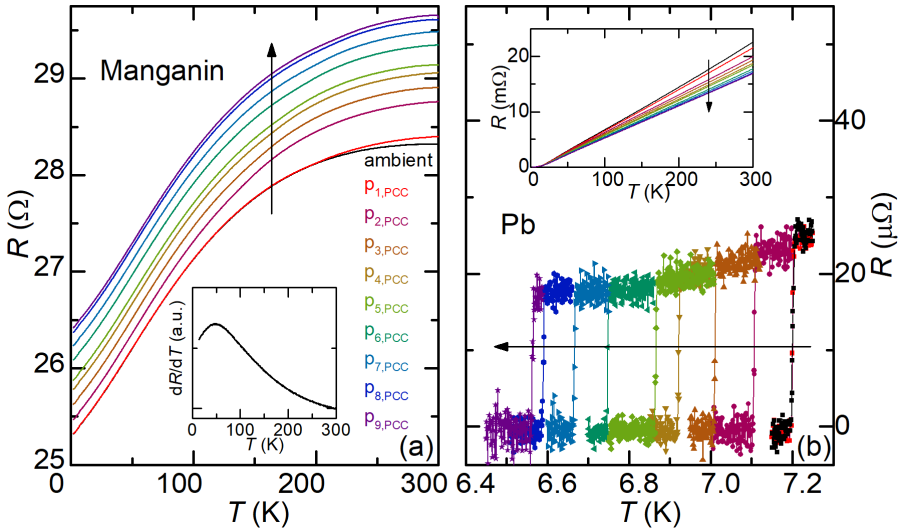

Figure 8.3 (a) Temperature-dependent resistance, $R(T)$, of the manganin for different pressure runs up to ~ 2 GPa measured in a piston-cylinder cell with 4:6 mixture of light mineral oil: n-pentane as a pressure-transmitting medium. Inset: temperature derivative of the manganin resistance, $\mathrm{d}R/\mathrm{d}T$, as a function of temperature at ambient pressure; (b) Temperature-dependent resistance around the superconducting transition of Pb measured in the same experiment. Inset: Temperature-dependent resistance of elemental Pb over the whole temperature range of 1.8 K - 300 K. Arrows in the figure indicate the direction of pressure increase.

$p_{1,PCC}$ the lock-nut was closed hand-tight without the application of external load. The analysis of the $p_{1,PCC}$ data will be discussed in Appendix A. As shown in Fig. 8.3, at any fixed temperature, R of manganin increases upon increasing pressure. The superconducting transition temperature, T_c, of Pb (Fig. 8.3 b) is suppressed upon increasing pressure.

The p values over the full temperature range from 300 K down to low temperature are calculated from the manganin resistance using the pressure coefficient $\alpha(T)$ obtained from the ^{4}He-gas pressure experiments (see Fig. 8.2 (b)). The resulting $p(T)$ curves are shown in Fig. 8.4 by solid lines. Upon cooling from high temperature, $p(T)$ decreases, until at a certain temperature, which depends on the pressure, a pronounced feature (kink) in $p(T)$ occurs (as shown, e.g., by the arrows at 140 K for $p_{2,PCC}$ or at 220 K for $p_{9,PCC}$ in Fig. 8.4 (a)). This feature is associated with the solidification of the pressure medium, since its temperature coincides with previous reports on the solidification temperature of the chosen mediumTorikachvili et al. (2015). Upon further decreasing temperature below the solidification, $p(T)$ still continues to decrease, however the slope, dp/dT, becomes progressively reduced.

Below $T \sim 60$ K a second set of distinct features appears in $p(T)$, as shown in Fig. 8.4 (a). In detail, for low pressures ($p_{2,PCC}$ to $p_{4,PCC}$) $p(T)$ displays a non-monotonic temperature dependence with local minima and maxima below 60 K (see Fig. 8.4 (b) for enlarged view), and for higher pressures ($p_{5,PCC}$ to $p_{9,PCC}$) $p(T)$ shows a rapid decrease below ~ 60 K upon cooling (see Fig. 8.4 (c) for enlarged view of $p_{8,PCC}$ and $p_{9,PCC}$). In contrast to the solidification temperature, the temperature of 60 K does not correspond to any characteristic temperature of the system, since there is, to the best of our knowledge, no drastic change of thermal expansion of any of the cell components Swenson (1997); Ventura G. (2014). Also, since thermal expansion is typically smaller at lower temperatures and is zero at 0 K, it is reasonable to assume that the change of pressure with temperature should become smaller for low temperatures and should smoothly change from a finite dp/dT for finite temperatures to $dp/dT = 0$ at $T = 0$ K. In the following, we will argue that the features in $p(T)$ below ~ 60 K in Fig. 8.4 (a) can be attributed to

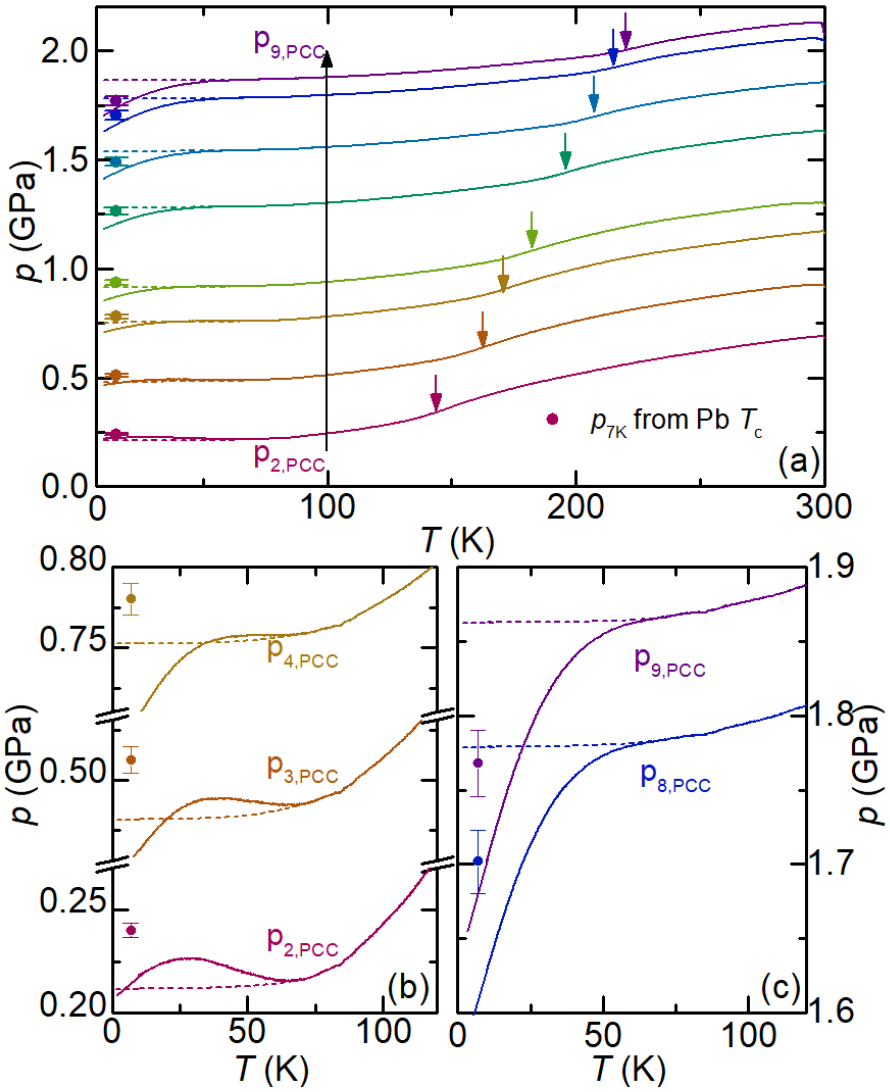

Figure 8.4 (a) Temperature-dependent pressure, $p(T)$, for various pressure runs in piston-cylinder cell. Pressure run $\mathrm{p}_{1,\mathrm{PCC}}$ (hand tight) is discussed separately in Appendix A. Solid lines are $p(T)$ curves determined from $\alpha(T)$ obtained from measurements in ^{4}He-gas cell (Fig. 8.2 (b)) and $R(T)$ of manganin measured in PCC (Fig. 8.3 (a)). Dashed lines correspond to $p(T)$ curves that were extrapolated from high temperatures and represent a physically reasonable $p(T)$ behavior at low temperatures (for details, see text). Circles correspond to pressure values at low temperature, $p_{7\,\mathrm{K}}$, determined from T_c of Pb. Downward arrows indicate a more rapid pressure decrease in $p(T)$ curves which is associated with the solidification of the pressure medium (see text for details); (b, c) Enlarged view of the low-temperature data of $p(T)$ for lowest pressures (b) and highest pressures (c).

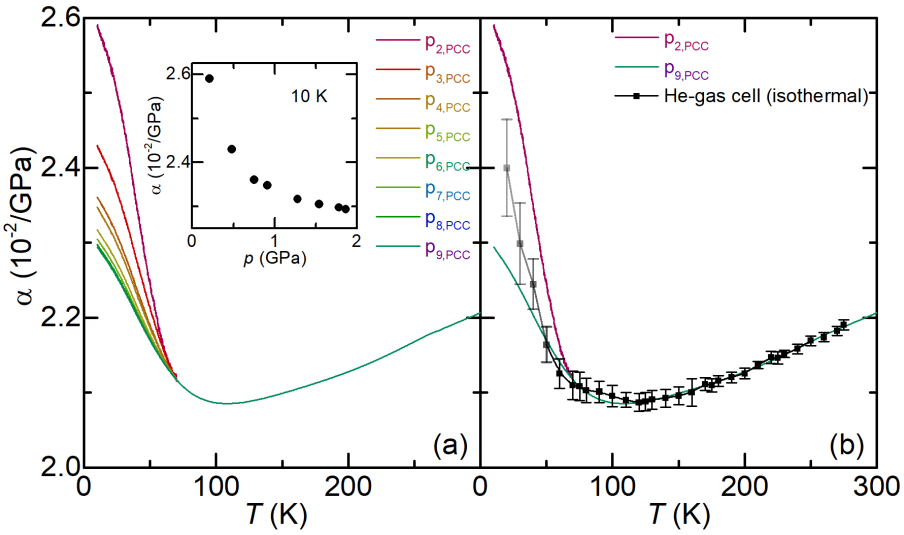

Figure 8.5 (a) The temperature-dependent pressure coefficient, $\alpha(T)$, of manganin determined from modified $p(T)$ in the piston-cylinder cell. Inset: The pressure dependence of α at $T = 10$ K where pressure values at 10 K are obtained from the modified $p(T)$. (b) Comparison of the $\alpha(T)$ determined from the modified $p(T)$ with that determined from ^{4}He-gas pressure cell measurements via linear fit of p-dependent $\frac{\Delta R_p}{R_0}$ data (same plot as in Fig. 8.2 (b)). A color gradient for the symbols is used to visualize that the data points result from fitting the ^{4}He-gas pressure data over different pressure ranges, as explained in caption of Fig. 8.2 and the main text.

a non-negligible pressure dependence of α for low temperatures, which for simplicity has been ignored in the analysis so far.

To this end, we construct $p(T)$ curves below 60 K, which are modified in such a way that they represent a physically more reasonable behavior, and then discuss their implication on the pressure dependence of α. For this construction, we used a simple form of polynomial that simultaneously meets the following criteria: (i) the fit describes our experimental $p(T)$ data for $70\,\mathrm{K} < T < 90\,\mathrm{K}$, (ii) the fit reaches $\mathrm{d}p/\mathrm{d}T = 0$ at 0 K and (iii) $\mathrm{d}p/\mathrm{d}T$ of the fit is always positive. We found that these criteria can be best met by using a polynomial of the order of 4 of the form $p(T) = aT^4 + b$, where a and b are fitting parameters. These fits are shown by the dashed lines in Fig. 8.4.

We can now crosscheck what the implications of our extrapolations of the $p(T)$ behavior for $T < 60\,\mathrm{K}$ are for the behavior of $\alpha(T,p)$. As shown in Fig. 8.5, the corresponding modified $\alpha(T)$ curves for various pressure runs in the piston-cylinder cell are plotted as lines and symbols. The modified $\alpha(T)$ curves at low temperatures agree with that determined from ^{4}He-gas pressure cell measurements on a qualitative level, since for all pressure runs in the piston-cylinder cell α increases rapidly upon cooling below 60 K, and quantitatively, since the absolute values are within a similar range (see Fig. 8.5 (b)). As a result of modifying the $p(T)$ behavior at low temperatures, α shows a clear pressure dependence for low temperatures. For any temperature below $\sim$60 K, α determined from the modified $p(T)$ in the piston-cylinder cell is suppressed upon increasing pressure. Specifically, $\alpha(10\ \mathrm{K})$ is suppressed from $2.59{\times}10^{-2}$/GPa to $2.29{\times}10^{-2}$/GPa when the low-temperature pressure is increased from 0.21 GPa to 1.86 GPa (see Fig. 8.5 (a) inset). Overall, this corresponds to a change of α up to 12% with pressure at low temperatures, which is approximately half of the overall change of α with temperature. Note that the low-pressure, low-temperature α value of $2.59{\times}10^{-2}$/GPa at $p = 0.21$ GPa (pressure run $\mathrm{p}_{2,\mathrm{PCC}}$) and $T = 10\,\mathrm{K}$ agrees well with the value of $2.52{\times}10^{-2}$/GPa, which was determined from the ^{4}He-gas measurements at 10 K up to 0.05 GPa (α could not be determined up to higher pressures in the ^{4}He-gas experiments due to the solidification of the medium). Unfortunately, the solidification of Helium and limitations of the maximum pressure of the gas-pressure setup do not allow us to clearly pin down the exact pressure dependence of α over wider ranges of pressures and temperatures. However, we note that whereas the $\alpha(T)$ data from the ^{4}He-gas experiments (see Fig. 8.1 (c)) seems to be almost independent of pressure for high temperatures, reasonable extrapolations of the ^{4}He-gas pressure α data down to lower temperatures below the solidification of the ^{4}He pressure medium might suggest that the pressure dependence of α becomes more pronounced upon cooling. Overall, our analysis from combining the ^{4}He-gas data with the piston-cylinder cell data, presented here, provides some strong indications that α shows some non-negligible pressure dependence for $T \lesssim 60\,\mathrm{K}$. Although the exact reason behind this observation is unknown for now, we speculate that the stronger p-dependence of α is related to a

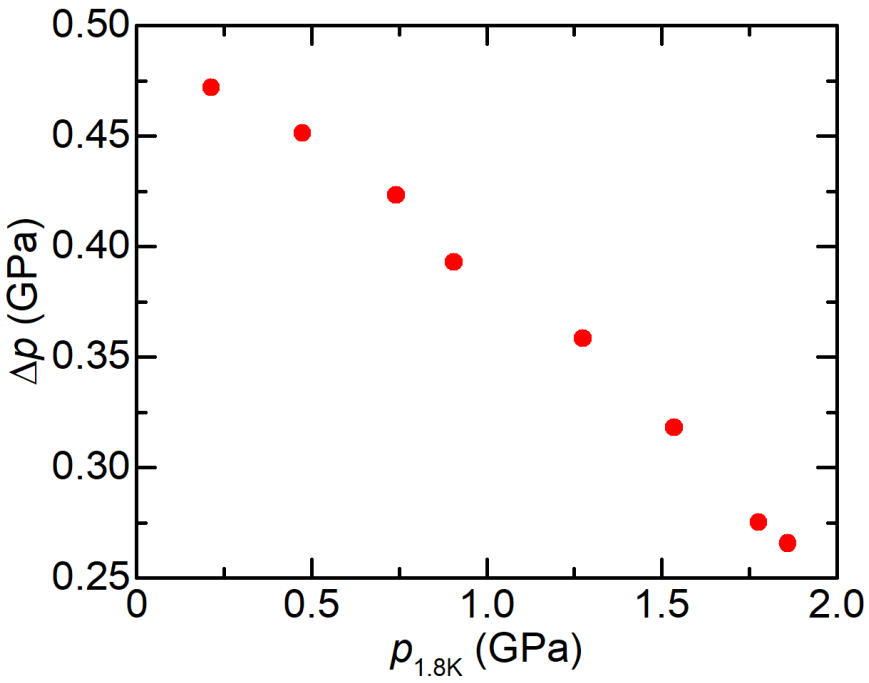

Figure 8.6 Pressure drop between 300 K and 1.8 K, $\Delta p = p_{300\,\mathrm{K}} - p_{1.8\,\mathrm{K}}$, as a function of pressure in the piston-cylinder cell determined from the manganin manometer. Note that the modified $p(T)$ curves (dashed lines in Fig. 8.4) were used to determine $p_{1.8\,\mathrm{K}}$.

possible change of the dominating electron scattering mechanism across $T \sim 50$ K, since a plot of the temperature-dependent $\mathrm{d}R/\mathrm{d}T$ (see Fig. 8.3 (a) inset) shows a broad maximum at ~ 50 K.

Using the modified $p(T)$ data from the manganin sensor, we can now evaluate the pressure dependence of the pressure drop upon cooling from 300 K to 1.8 K, $\Delta p = p_{300\,\mathrm{K}} - p_{1.8\,\mathrm{K}}$, determined from the manganin sensor. As shown in Fig. 8.6, Δp decreases upon increasing pressure, with $\Delta p \simeq 0.47$ GPa for $p_{1.8\,\mathrm{K}} \simeq 0.21$ GPa and $\Delta p \simeq 0.26$ GPa for $p_{1.8\,\mathrm{K}} \simeq 1.86$ GPa. These results are very close to earlier literature results, which found a pressure difference of ~ 0.3 GPa-0.4 GPa between room temperature and liquid-nitrogen temperature for their specific pressure cells, media and sample space filling factors Itskevich (1964); Brandt et al. (1974); Fujiwara et al. (1980); Thompson (1984); Becker et al. (1976); Torikachvili et al. (2015). Also, a previous study of Δp in the same pressure cell with the same pressure medium Torikachvili et al.

(2015) is consistent with our results in terms of the absolute values of Δp as well as its pressure evolution.

We now compare the pressure values from the modified $p(T)$ curves (dashed lines in Fig. 8.4 (a)) with those determined from elemental Pb (i.e., from the Pb-T_c sensor) for low $T \sim 7\,\mathrm{K}$ (solid circles). The Pb-T_c sensor is frequently used in literature to infer the low-temperature pressure Smith and Chu (1967); Smith et al. (1969); Clark and Smith (1978); Wittig et al. (1979); Bireckoven and Wittig (1988). StudiesSmith and Chu (1967); Smith et al. (1969); Clark and Smith (1978); Eiling and Schilling (1981); Bireckoven and Wittig (1988) have shown that, upon increasing pressure up to $\sim 5\,\mathrm{GPa}$, the ambient pressure $T_c = 7.2\,\mathrm{K}$ of Pb is suppressed linearly with a rate between $-0.361\,\mathrm{K/GPa}$ and $-0.386\,\mathrm{K/GPa}$. By taking the suppression rate of -0.365 K/GPa, as determined in Ref. Eiling and Schilling (1981), we determine the pressure at $T \sim 7$ K and depict these pressures by solid circles in Fig. 8.4 (a). The error bars for these data points are obtained using different pressure derivatives of Pb, reported in literatureSmith and Chu (1967); Smith et al. (1969); Clark and Smith (1978); Eiling and Schilling (1981); Bireckoven and Wittig (1988).

Overall, most of the pressure values from Pb-T_c agree very well with those from the manganin sensor, using the extrapolation scheme outlined above (see Fig. 8.4 (a)). This observation supports our modifications of the $p(T)$ curves obtained from manganin. On a more quantitative level, p values at $T \sim 7\,\mathrm{K}$ determined from manganin and Pb-T_c differ by less than 0.025 GPa for $p \lesssim 1.25\,\mathrm{GPa}$ ($\mathrm{p}_{2,\mathrm{PCC}}$ to $\mathrm{p}_{6,\mathrm{PCC}}$). For $p \gtrsim 1.5\,\mathrm{GPa}$, the difference between pressure values inferred from the manganin and Pb-T_c sensors becomes slightly larger, reaching $\sim 0.085\,\mathrm{GPa}$ at 7 K for our highest pressure run ($\mathrm{p}_{9,\mathrm{PCC}}$). The slightly larger difference of the pressure values for higher pressures could be due to the fact that the manganin sensor was only calibrated up to 0.8 GPa in the ^{4}He-gas pressure cell (maximum pressure of the system). Thus, any pressure dependence of α over a wider pressure range, even for $T > 60\,\mathrm{K}$, would directly affect the evaluation of the pressure from the manganin sensor and therefore also its extrapolations.

Given that some small differences between pressure values determined from the manganin sensor and the Pb-T_c are observed, we finally want to offer a practical approach for estimating the absolute pressure value at any given intermediate temperature for this specific combination of pressure cell, pressure medium and sample space filling factor. Since we lack any calibration measurements for the manganin sensor for higher pressures $p > 0.8\,\mathrm{GPa}$ (due to the maximum pressure of our ^{4}He gas setup), we suggest that if a Pb-T_c manometer is present, one refers to the p_{7K} obtained from T_c of Pb for the determination of low-temperature pressure up to 2 GPa. To estimate p at higher temperatures, the $p(T)$ curves determined from manganin in this study can be used as a reference by using a linear interpolation of the nearest $p(T)$ curves, so that the interpolation matches p_{7K} from Pb. If only a manganin sensor is present, $p(T)$ can be obtained by utilizing the $\alpha(T)$ characterized in ^{4}He-gas experiments in this study (see Fig. 8.2 (b)), and $p(T)$ at low temperatures ($T \lesssim 60\,\mathrm{K}$) can possibly be modified similar to the procedure performed in our analysis. This practical approach offered here gives a good estimation of the overall $p(T)$ behavior within the discussed systematic errors, which result from the small differences in the absolute values inferred from the manganin vs. the Pb-T_c manometers. In general, we believe that a similar practical approach could be used to estimate pressure values at intermediate temperatures for other cells, pressure media and/or sample space filling factors as well by performing a separate calibration via a manganin sensor (and utilizing the $\alpha(T, p)$ behavior reported here) and a Pb-T_c sensor.

8.4 Summary

In summary, so as to better characterize the temperature dependence of pressure within a piston-cylinder cell, the resistance of manganin for its use as a manometer was characterized in a ^{4}He-gas pressure system from ambient pressure up to 0.8 GPa and from room temperature down to the solidification temperature of ^{4}He. Subsequently, the same manganin piece was measured in a piston-cylinder cell from ambient pressure up to $\sim 2\,\mathrm{GPa}$ and from room temperature down to 1.8 K. From an analysis of the resistance measurements, the temperature and pressure dependence

of the pressure coefficient $\alpha(T,p)$ was determined. The obtained $\alpha(T,p)$ of manganin was utilized to study the temperature-dependent pressure behavior in a piston-cylinder cell and was compared to the low-temperature pressure, inferred from the superconducting transition temperature of elemental Pb. Our results can be summarized as follows: First, we find that α of manganin is 2.21×10^{-2}/GPa at 300 K, which is in the range of other literature reports, and that α has a non-monotonic temperature dependence. Upon cooling, $\alpha(T)$ first decreases and then increases, thus displaying a broad minimum at $\sim$120 K. In addition, our results suggest that α is almost pressure-independent for 60 K $\lesssim T <$ 300 K, whereas for $T \lesssim$ 60 K it has a non-negligible pressure dependence, i.e., α at a given temperature is suppressed upon increasing pressure. Second, we quantified the $p(T)$ behavior in a piston-cylinder cell. We demonstrate that pressure decreases continuously upon cooling for the whole pressure range up to 2 GPa, and that pressure experiences a more significant drop upon cooling through the medium solidification temperature. The difference in pressure between room temperature and low temperatures decreases upom increasing overall pressure. The low-temperature pressure values inferred from manganin are overall consistent with the ones inferred from the superconducting transition temperature of elemental Pb.

Overall, this work therefore provides two findings, which are important for the pressure community in general. First, we demonstrate that the temperature and pressure dependence of $\alpha(T)$ for manganin has to be taken into account for an accurate determination of $p(T)$ when using manganin as a manometer. Second, we provide a detailed analysis of the $p(T)$ behavior in piston-type pressure cells, which can be readily used in future pressure experiments to estimate the pressure at any given temperature. Whereas this work is done for a specific combination of pressure cell, pressure medium and sample space filling factor, we believe that our results can be used as reference to estimate pressure values at intermediate temperatures for piston-cylinder pressure cells with similar designs. For a more accurate and detailed $p(T)$ behavior analysis in other cells, for other used pressure media and/or other samples space filling factors, a separate

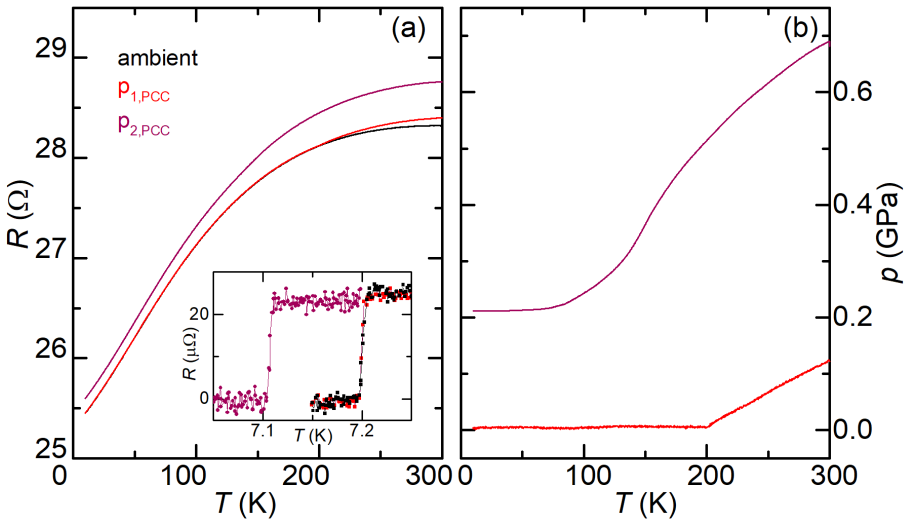

Figure 8.7 (a) $R(T)$ of manganin measured at ambient pressure, $p_{1,PCC}$ (inside the piston-cylinder cell, for which the lock-nut was closed hand-tight without the application of external force) and $p_{2,PCC}$ (inside the piston-cylinder cell and first measurement, for which a finite force of $\sim$ 1000 lbs was applied to the piston prior to the measurement). Inset: $R(T)$ of Pb showing the superconducting transition for ambient pressure, for $p_{1,PCC}$ and for $p_{2,PCC}$; (b) Temperature-dependent pressure, $p(T)$, for $p_{1,PCC}$ and $p_{2,PCC}$ determined from $R(T)$ and $\alpha(T)$ of manganin.

calibration is needed, for which our generic analysis of $\alpha(T, p)$ of the manganin sensor will be useful.

8.5 Appendix

8.5.1 Analysis of pressure run $p_{1,PCC}$ in the piston-cylinder cell

Figure 8.7 (a) presents the temperature-dependent resistance of manganin at ambient pressure outside of the pressure cell, as well as inside the pressure cell without applying a load to the piston ("hand-tight", $p_{1,PCC}$) and inside the pressure cell with a load of 1000 lbs applied to the piston that is locked by tightening the lock-nut ($p_{2,PCC}$). From the ambient pressure run to the $p_{1,PCC}$ run, resistance at any temperature above $\sim$200 K increases. In contrast, no change of the resistance can be observed between the ambient and the $p_{1,PCC}$ run for temperatures below

200 K. From $p_{1,PCC}$ to $p_{2,PCC}$, resistance increases at any temperature with increasing pressure. Figure 8.7 (a) inset shows the resistance of Pb across T_c for the ambient pressure, $p_{1,PCC}$ and $p_{2,PCC}$ runs. We find that T_c is the same for the ambient-pressure and the $p_{1,PCC}$ run, whereas it is distinctly lower for $p_{2,PCC}$. These data suggest that for $p_{1,PCC}$, the pressure at high temperatures is non-zero but becomes zero at low temperatures. We further calculated the temperature-dependent pressure for the $p_{2,PCC}$ run from manganin following the procedure outlined in the main text. As shown in Fig. 8.7 (b), a pressure of 0.12 GPa is obtained at 300 K for $p_{1,PCC}$. Upon cooling pressure decreases, reaches zero at $\sim$200 K and apparently stays unchanged upon further cooling. A very similar result can be reached by using our "practical" approach to determining pressure as well. If we simply shift the $p_{2,PCC}$ curve down to 0.12 GPa at 300 K, we find that it crosses $p = 0$ at $\sim$200 K. In the main text, we demonstrated that a pressure loss of 0.47 GPa occurs for $p_{2,PCC}$ upon cooling. Thus, when the room-temperature pressure is less than 0.47 GPa, such as for $p_{1,PCC}$, the pressure will drop to zero already at an intermediate temperature (200 K for $p_{1,PCC}$). We note that this might result in a inhomogeneous pressure for lower temperatures, since the differential thermal expansion between, e.g., 200 K and low temperatures is still significant. Correspondingly, a minimum pressure of about 0.47 GPa at room temperature is needed to guarantee a well-defined pressure environment down to lowest temperatures.

8.5.2 Determination of pressure values in piston-cylinder cell via Pb-resistance manometer

Similar to the manganin manometer, the resistance of Pb can be utilized to calculate pressure values as well (referred to here as Pb-resistive manometer). A. Eiling and J. S. Schilling in Ref. Eiling and Schilling (1981) investigated the temperature and pressure dependence of resistivity of Pb and utilized the resistivity of Pb to calculate the pressure values in pressure cellsEiling and Schilling (1981). We followed the analysis suggested in Ref. Eiling and Schilling (1981) to carry out a similar determination of temperature-dependent pressure, $p(T)$, in the

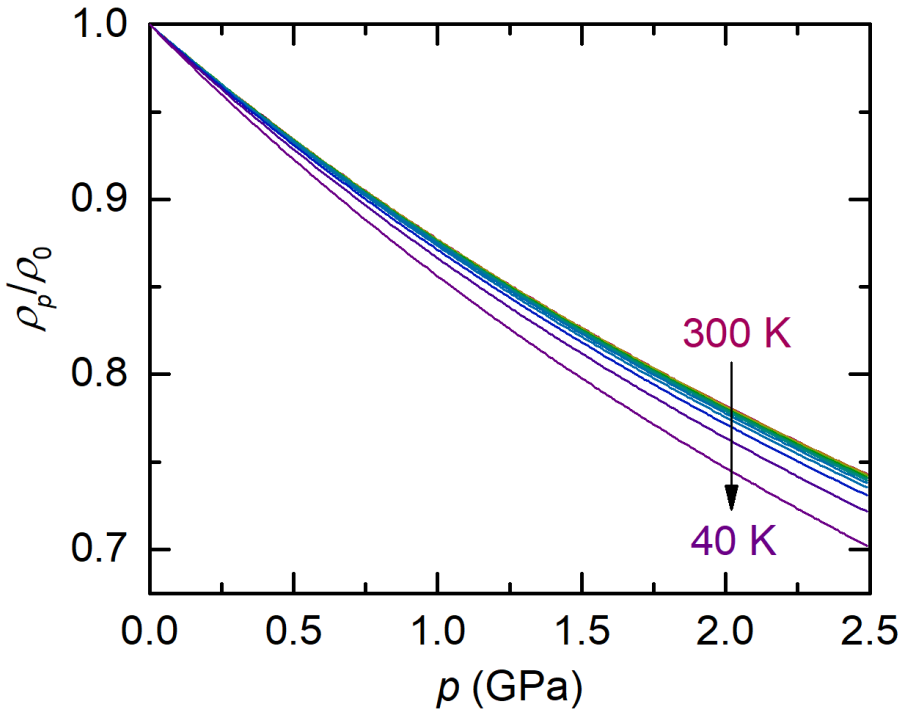

Figure 8.8 Theoretical pressure-dependent resistivity of Pb normalized by ambient-pressure resistivity, ρ_p/ρ_0, at various fixed temperatures from 300 K to 40 K (spacing of 20 K), based on the Bloch-Grüneisen model of Ref. Eiling and Schilling (1981).

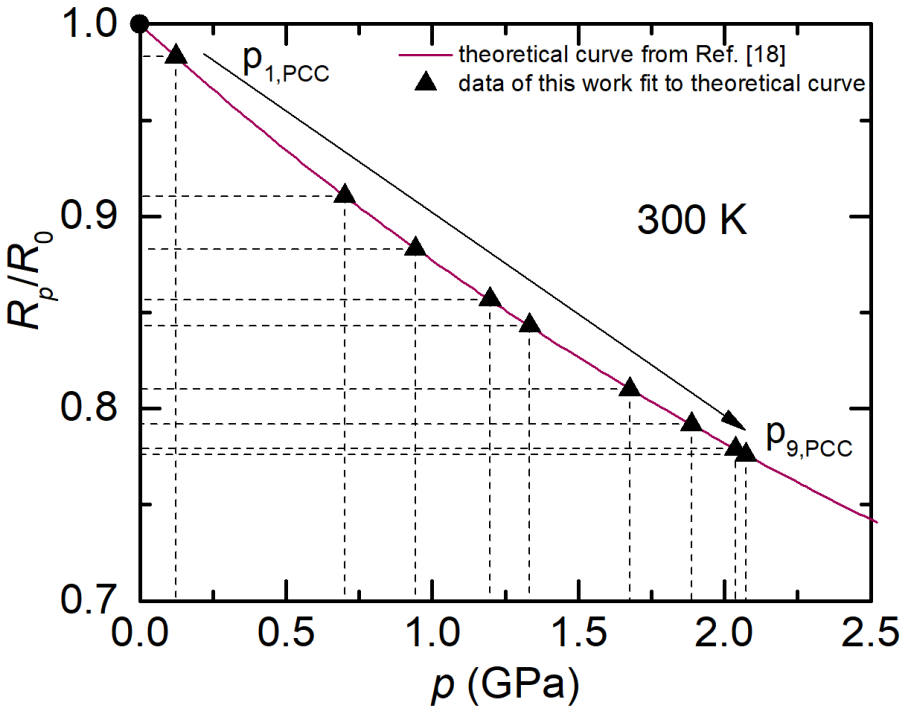

Figure 8.9 Theoretical data of relative resistance, R_p/R_0, of Pb versus pressure at 300 K (solid line), which is reprinted from Ref. Eiling and Schilling (1981), and experimental data from this work (triangles). The circle symbol represents the data at ambient pressure which by definition is at $p = 0$ GPa and $R_p/R_0 = 1$ in the plot. The experimental relative resistance data, is used to calculate pressure values at 300 K for different pressure runs via fitting to the theoretical line.

piston-cylinder cell from the Pb resistance data, which was measured in the present study (see Fig. 8.3 (b) inset) simultaneous to the manganin resistance. The determined pressure values are compared with those from the manganin manometer and the Pb-T_c manometer.

According to the Bloch-Grüneisen analysis outlined in Ref. Eiling and Schilling (1981), resistivity of Pb as a function of temperature and pressure, $\rho_p(T)$, can be calculated in the temperature range $7\,\mathrm{K} \leq T \leq 300\,\mathrm{K}$ and pressure range of $0\,\mathrm{GPa} \leq p \leq 10\,\mathrm{GPa}$. Example theoretical curves of the resistivity, normalized by ambient-pressure resistivity, ρ_p/ρ_0, as a function of pressure at constant temperature are shown in Fig. 8.8. These ρ_p/ρ_0 curves can be used to fit the measured experimental data, R_p/R_0 (assuming that the geometric dimensions of the Pb manometer do not change, in which case $R_p/R_0 = \rho_p/\rho_0$), to calculate the pressure values.

Figure 8.9 illustrates this procedure using the room-temperature data as an example. The solid line in Fig. 8.9 represents the theoretical ρ_p/ρ_0 (R_p/R_0) curve based on Ref. Eiling and Schilling (1981) for $T = 300\,\mathrm{K}$, whereas the solid symbols represent the 300 K experimental data obtained in this study for different pressure runs. Pressure values at 300 K are calculated by fitting the experimental R_p/R_0 values to the theoretical curve. The same procedure was carried out for temperatures between 300 K and 40 K. Below $\sim 40\,\mathrm{K}$ (about half of the Debye temperature), it was suggested in Ref. Eiling and Schilling (1981) that the Bloch-Grüneisen model becomes unreliable. The resulting $p(T)$ curves for various pressure runs ($\mathrm{p}_{2,\mathrm{PCC}}$ to $\mathrm{p}_{9,\mathrm{PCC}}$) are plotted in Fig. 8.10 together with those determined from the manganin and Pb-T_c manometers. The $p(T)$ curves from the Pb-resistive manometer (dotted lines in Fig. 8.10) manifest a continuous decrease of pressure upon cooling. A clear feature in $p(T)$ (as shown by the downward arrows in Fig. 8.10) is associated with the solidification of the pressure mediumTorikachvili et al. (2015). Below $\sim 80\,\mathrm{K}$, a rapid decrease of p upon cooling is observed. Such a rapid decrease of p at low temperatures appears unphysical, following the same arguments, provided in the discussion of the non-modified $p(T)$ curves of manganin in the main text. We assume that this decrease can partially be attributed to a breakdown in the Bloch-Grüneisen modeling of the Pb resistivity at low temperatures. Compared to the pressure values determined from other manometers, $p(T)$ curves from the Pb-resistive manometer (dotted lines) show a slower decrease of p upon cooling (i.e., a smaller $\mathrm{d}p/\mathrm{d}T$) compared with those determined from manganin (solid lines) for $T \gtrsim 80\,\mathrm{K}$. In addition, extrapolations of Pb-resistive $p(T)$ either from above 80 K or from below 80 K down to 7 K result in some discrepancies to the p values determined from the Pb-T_c sensor.

In fact, inferring $p(T)$ from the Pb-resistive manometer is somewhat fraught with problems related to the residual resistivity of a sample as well as the the reproducibility of ambient-pressure resistivity values. To be more explicit, the $p(T)$ inferred from the Bloch-Grüneisen analysis outlined above can vary depending upon the residual resistivity (RRR). Since $p(T)$ is inferred from R_p/R_0 (see Fig. 8.9), changes in RRR affect the inferred $p(T)$. For example, our initial Pb sample has a residual resistivity ratio, RRR $\sim$ 80, at ambient pressure; if we add a relatively small

additional residual resistance (0.2 mΩ) to change the RRR to 8, we find that pressure decreases more rapidly below $T \lesssim 80\,\mathrm{K}$ for $\mathrm{RRR} = 8$, whereas the pressure decreases more moderately for $T \gtrsim 80\,\mathrm{K}$. Another problem is associated with pressure-induced changes of the ambient-pressure resistance, resulting from, e.g., changes in geometry and perfection of the Pb-resistive manometer. In Fig. 8.11 (a) we show the ambient-pressure resistance of the same Pb piece before and after the pressure runs. As can be seen, there is a non-trivial change in the resistance (see also ΔR and $\Delta R/R$ in Fig. 8.11 (b), where ΔR is the difference between the two ambient-pressure Pb resistance data sets). This change cannot simply be related to changes of geometry and cannot simply be related to changes of the defect scattering contribution. Figure 8.11 (c) shows the inferred $p(T)$ for the highest pressure run $\mathrm{p}_{9,\mathrm{PCC}}$ for $40\,\mathrm{K} \leq T \leq 300\,\mathrm{K}$, using the two sets of ambient-pressure resistance before and after the pressure cycle. There is a clear, $\sim 0.2\,\mathrm{GPa}$ pressure difference at room temperature between the two $p(T)$ curves that becomes slightly smaller at lower temperatures. We point out that neither the residual resistance nor the potential change of geometry of the Pb manometer is taken care of in the Bloch-Grüneisen analysis, and that any analysis in terms of the Bloch-Grüneisen model is complicated by potential pressure-induced changes of the ambient-pressure resistivity of Pb. In summary, then, the use of Pb-resistive manometer for determining p values over a wide temperature range is associated with larger uncertainties than the use of the manganin sensor and as such was not used in the main text. This said, it is very important to note that the Pb-T_c value is not affected by these concerns (i.e., changes of RRR, changes of geometry or general changes of ambient-p resistance) and is therefore a much more robust manometer when measuring the pressure values at low temperatures.

8.5.3 Analysis of the resistance of InSb manometers

The change of resistance of InSb under pressure can be used to calculate pressure valuesKraak et al. (1984). In this study, resistance measurements of two commercially-made InSb sensors (SPG-10, heavily n-type doped bulk n-InSb single crystal, purchased from Unipress, Institute of High-Pressure Physics, Polish Academy of Sciences, Unipress Equipment Division)Uni were

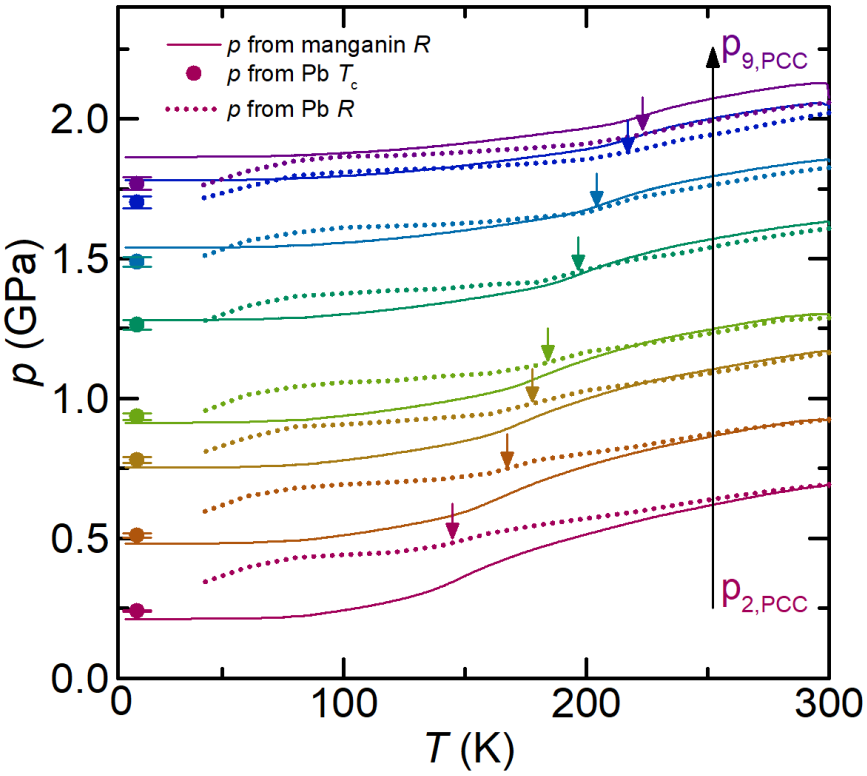

Figure 8.10 Temperature-dependent pressure, $p(T)$, for various pressure runs in piston–cylinder cell. Dotted lines are $p(T)$ curves determined from Pb-resistive manometer, circles correspond to pressure values determined from the Pb-T_c manometer and solid lines are (modified) $p(T)$ curves determined from manganin manometer. Downward arrows indicate a more rapid pressure decrease in $p(T)$ curves which is associated with the solidification of the pressure medium (see text for details).

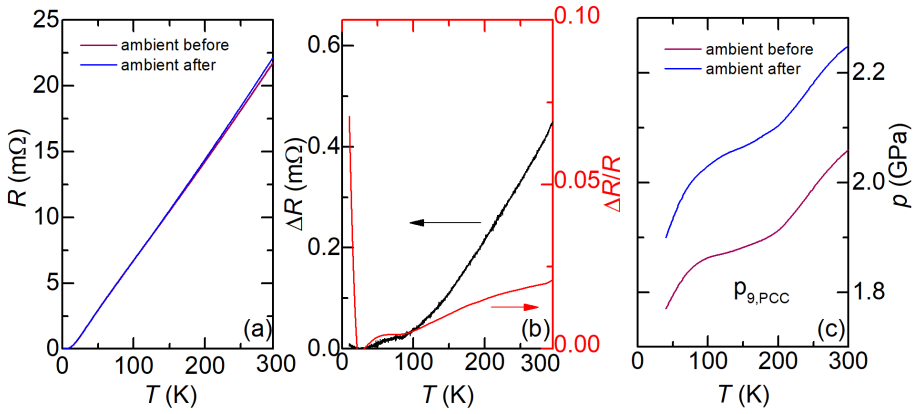

Figure 8.11 (a) Temperature-dependent resistance of Pb at ambient pressure before and after pressure runs $p_{1,PCC}$ to $p_{9,PCC}$. Data curves are labeled as "ambient before" and "ambient after", respectively; (b) The resistance change, ΔR (left axis), between "ambient before" and "ambient after", as well as the relative change, $\Delta R/R$. where for R the "ambient before" data was used (right axis), as a function of temperature; (c) Temperature dependence of pressure, $p(T)$, for pressure run $p_{9,PCC}$ using "ambient before" and "ambient after" data, respectively. See text for details.

carried out in ^{4}He-gas pressure setup and the PCC, together with other manometers as mentioned in the main text. In this section, we present the measurement results and discussions of InSb sensors.

Figures 8.12 summarizes our measurements results of InSb manometers in ^{4}He-gas pressure cell (Figs. 8.12 (a) and (b)) and PCC (Figs. 8.12 (c) and (d)). As shown in Figs. 8.12 (a) and (c), the resistance shows a metallic behavior and $R(T)$ decreases upon cooling for any pressure. Upon increasing pressure, R increases at any given temperature. The pressure values can be calculated for room-temperature, p_{300K}, and temperatures below 77 K, $p_{T\leq 77K}$, using the calibration formulas provided by the user manual,

$$p_{300K} = -5.437 + 8.419(R_p/R_0) - 3.703(R_p/R_0)^2 + 0.723(R_p/R_0)^3 \tag{8.2}$$

$$p_{T\leq 77K} = -3.738 + 5.114(R_p/R_0) - 1.657(R_p/R_0)^2 + 0.281(R_p/R_0)^3 \tag{8.3}$$

where R_0 and R_p are resistance at ambient pressure and finite pressure p. The calculated p as a function of temperature is plotted in Figs. 8.12 (b) and (d) together with $p(T)$ determined from

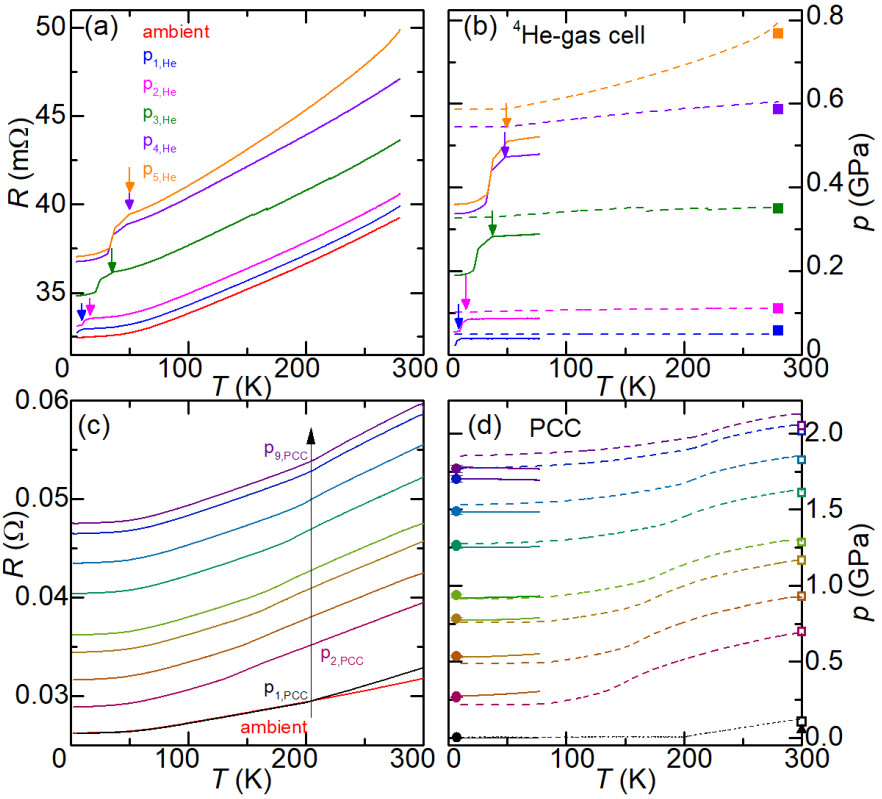

Figure 8.12 (a) Temperature-dependent resistance, $R(T)$, of InSb at various pressure runs measured in ^{4}He-gas pressure system. (b) Temperature-dependent pressure, $p(T)$, for various pressure runs in ^{4}He-gas pressure cell. Dashed lines correspond to the pressure values, which were determined from the compressor manometer at room temperature. Solids lines and squares are pressure values determined from InSb for $T \leq 77$ K and $T = 300$ K, respectively. Arrows in (a) and (b) indicate the pressure-dependent ^{4}He solidification temperature as described in the main text. (c) Temperature-dependent resistance, $R(T)$, of InSb at various pressure runs measured in the piston-cylinder cell. (d) Temperature-dependent pressure, $p(T)$, for various pressure runs in the piston-cylinder cell. Solid lines and open squares are pressure values determined from InSb for $T \leq 77$ K and $T = 300$ K, respectively. Dashed lines and circles are pressure values determined from manganin, Pb-T_c manometer, respectively, as discussed in the main text.

other manometers, which were presented in detail in the main text. For room temperature, the values inferred from InSb agree well with the value inferred from the compressor in the ^{4}He-gas pressure measurements. However, for the low-temperature range $T < 77$ K (and above the ^{4}He solidification temperature as indicated by arrows in the figure), distinct discrepancies between the compressor manometer and the p values from the InSb sensor were observed in ^{4}He-gas pressure measurements (as large as 17% or 0.08 GPa for high pressures in ^{4}He-gas pressure measurements). For the measurements, performed in the PCC, we find that the pressure values at 7 K from the Pb manometer and the InSb manometer are consistent. We would like to note that the InSb sensor did not survive a relative fast pressure relieve. Overall, given the issues in terms of the absolute pressure values in ^{4}He-gas pressure measurements as well as the lacking reproducibility of the InSb sensor in multiple pressure runs in piston-cylinder cell, we would suggest to refrain from using this manometer for high-accuracy determination of pressure. However, the InSb sensor can be very useful, e.g., in ^{4}He-gas pressure measurements to make sure that there is no blocking of the capillary, which would result in a decoupling from the room-temperature compressor manometer.

8.5.4 Evaluation of Zeranin as a resistive manometer

Zeranin is a alloy containing approximate 90.7% Cu, 7% Mn and 2.3% Sn. Studies have suggested that Zeranin can be used as a resistive manometer due to its clear change of resistance with pressure and small temperature dependence of its resistanceBirks and Gall (1973); Rein (1993). In this section, we present a investigation of using Zeranin alloy as a resistive manometer. To begin with, we would like to mention that we failed to purchase commercial-manufactured Zeranin wire from Isabellenhutte with reasonable time and effort. As a result, the Zeranin used in this study was made in-house by melt spinning in the following way. First an alloy ingot with nominal composition $Cu_{90.67}Mn_{8.09}Sn_{1.23}$ and a total mass of $\sim$ 10 g was made by arc melting raw elements in an Ar atmosphere. The alloy ingot was then inductively melted in a quartz crucible in 1/3 atm of high purity He gas and ejected at 1350 °C onto a Cu wheel at wheel speed of 25 m/s.

The resulted melt spun ribbon was then cut into a bar shape for electrical resistance measurements where the contacts were made by spot-welding 25 μm Au wires to the sample surface. The piece of Zeranin, together with a piece of elemental Pb, was mounted into the PCC where another seperate set of resistance measurements under pressure was carried out in PPMS.

To determine pressure values from Zeranin, one can define a pressure coefficient, α_z, of Zeranin as $R_p = (1 + \alpha_z p)R_0$. Then p values can be determined from measurements of Zeranin resistance at ambient pressure, R_0, and finite pressure, R_p, given that α_z is per-characterized. In the following, we report the measurements of the temperature dependent resistance of Zeranin under pressure up to $\sim$ 2 GPa in PCC and discuss briefly the pressure coefficient α_z of Zeranin.

Figure 8.13 summarizes the measurement results of Zeranin in the piston-cylinder cell. As shown in Fig. 8.13 (a), the resistance of Zeranin shows metallic behavior. Upon increasing pressure, R increases at any given temperature, suggesting a postive α_z over the full temperature range. The temperature dependence of α_z can be analyzed by looking at the normalized change of resistance, $\frac{\Delta R_p}{R_0} = \alpha_z p$, as a function of temperature, which is shown in Fig. 8.13 (b) for various pressure runs. For pressure runs p2 to p8, upon cooling, $\frac{\Delta R_p}{R_0}$ first decreases, then goes through a broad minimum at $\sim$ 75 K and increases again towards lower temperatures. Given that pressure decreases monotonically with temperature in this pressure cell as concluded in the main text, such temperature behavior of $\frac{\Delta R_p}{R_0}$ suggests a temperature-dependent pressure coefficient, α_z, of Zeranin. Specifically, α_z should increase upon cooling for $T \lesssim 75$ K to ensure a monotonic decrease of p over the full temperature range. In addition, the pressure-dependent resistance, $R(p)$, can provide information about the behavior of α_z under pressure. $R(p)$ data at 7 K and 300 K are plotted in Fig. 8.13 (c), where $p_{7\mathrm{K}}$ is determined from T_c of Pb (Pb manometer is measured simultaneously with Zeranin in the piston-cylinder cell, data not shown). $p_{300\mathrm{K}}$ is obtained from the practical approach that is offered in the main text, where $p_{7\mathrm{K}}$ from T_c of Pb are used as the reference points. Clear deviations from linear dependence are observed for $R(p)$ at both 7 K and 300 K, indicates that α_z has non-negligible pressure dependence both at room and low temperature in the pressure range of 0 GPa to 2 GPa. Furthermore, the pressure coefficient of

Zeranin, α_z, is calculated for T=7 K and 300 K through $R_p = (1 + \alpha_z p)R_0$ using the data presented in Fig. 8.13. The obtained α_z are plotted as a function of p and presented in Fig. 8.13 (d). As shown in the figure, α_z at both 7 K and 300 K increase upon increasing pressure, and the increase of α_z reaches as large as 36%.

In conclusion, our resistance measurements of Zeranin in PCC suggest both a non-negligible temperature and pressure dependence of the pressure coefficient α_z. Thus, we point out that the temperature and pressure dependence of resistance of Zeranin, if it is to be used as a resistive manometer, needs further and careful study.

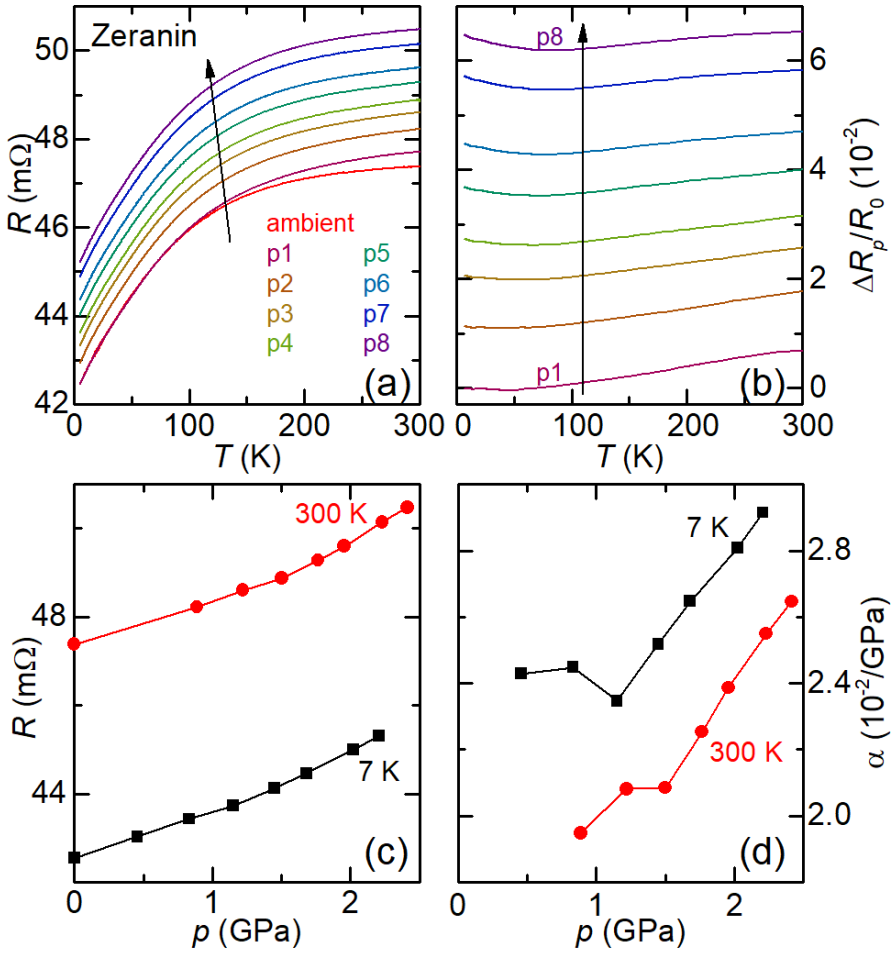

Figure 8.13 (a) Temperature-dependent resistance, $R(T)$, of Zeranin at various pressure runs measured in piston-cylinder cell. (b) Normalized change of resistance, $\frac{\Delta R_p}{R_0}$, as a function of temperature at various pressure runs. (c) Pressure-dependent resistance at 7 K (black) and 300 K (red). $p_{7\mathrm{K}}$ is determined from T_c of Pb. $p_{300\mathrm{K}}$ is obtained from the practical approach that is offered in the main text, where $p_{7\mathrm{K}}$ from T_c of Pb are used as the reference points. (d) Pressure dependence of the pressure coefficient of Zeranin, α_z, at 7 K (black) and 300 K (red). α_z is calculated through $R_p = (1 + \alpha_z p)R_0$, where R_p, R_0 and p are the data presented in (c).

CHAPTER 9. GENERAL CONCLUSION

Physical pressure, via directly changing the lattice parameters of materials, provides a great opportunity to modify materials' properties and induce novel ground states. Through the pressure-tuning process, various physical phenomena such as superconductivity and quantum phase transitions can be investigated. Having studied the pressure response of several different correlated electron systems, this thesis presents in the first part (Chaps. 3-5) the study on selected Fe-based superconductors S-substituted FeSe, Ni-substituted $CaKFe_4As_4$ and $EuRbFe_4As_4$. In the second part, a Kondo heavy system $CeBi_2$ is investigated and understood in the context of the Doniach phase diagram (Chap. 6) and in Chap. 7 a newly discovered metallic ferromagnet $La_5Co_2Ge_3$ is studied under pressure. The third part of the thesis is different and focuses on improving laboratory use and measurement of pressure as a function of temperature in self-clamping pressure cells. In Chap. 8, a systematic study of the pressure coefficient of the manganin manometer is presented and we provide a detailed investigation of the temperature evolution of the pressure in a piston-cylinder cell.

The combination of physical pressure and chemical pressure (Sulfur substitution) on the FeSe provides the access to a detailed substitution-pressure phase space. In Chap. 3, the pressure dependence (up to around 1.8 GPa) of the structural, magnetic and superconducting transitions and of the superconducting upper critical field were studied in sulfur-substituted $Fe(Se_{1-x}S_x)$ ($(x$=0.043, 0.096, 0.12)) to illustrate the effects of chemical and physical pressure on $Fe(Se_{1-x}S_x)$. We demonstrate that on increasing sulfur content, magnetic order in the low-pressure regime is strongly suppressed, whereas, the structural transition temperature, T_s, is much less suppressed by sulfur substitution. The superconducting transition temperature, T_c, of $Fe(Se_{1-x}S_x)$ exhibits similar non-monotonic pressure dependence with a local maximum and a local minimum present in the low pressure range for all x. The local maximum in T_c coincides with the emergence of the

magnetic order above T_c, suggesting a competition relation between superconductivity and magnetism in this pressure region. At this pressure the slope of the upper critical field decreases abruptly, which may indicate a Fermi-surface reconstruction.

The Fe-based superconductor $CaKFe_4As_4$ belongs to the recently discovered "1144" family. Whereas it shares many properties with the archetype $BaFe_2As_2$ system, it possesses some unique physics. i) Ni- or Co-substituted $CaKFe_4As_4$ is the first example of an Fe-based superconductor with spin-vortex-crystal-type magnetic ordering, ii) A new type of structural transition, the half-collapsed-tetragonal phase transition, is identified in $CaKFe_4As_4$ under pressure. These new phenomena together with superconductivity are investigated under the combination of physical and chemical pressure. Resistance measurements were performed on single crystals $CaK(Fe_{1-x}Ni_x)_4As_4$ ($x = 0.033, 0.050$) under pressures up to 5.12 GPa. We demonstrate that, for both compositions, magnetic transition temperatures, T_{N}, are suppressed at a higher rate compared with the superconducting transition temperatures T_{c}, i.e. $|\mathrm{d}T_{\mathrm{N}}/\mathrm{d}p| > |\mathrm{d}T_{\mathrm{c}}/\mathrm{d}p|$. This can be understood on the basis of an itinerant model for competing superconducting and spin-density wave orderMachida (1981); Gati et al. (2020a). In the picture of competing orders, both orders are allowed to be suppressed with pressure, as long as $|\mathrm{d}T_{\mathrm{N}}/\mathrm{d}p| > |\mathrm{d}T_{\mathrm{c}}/\mathrm{d}p|$, when superconductivity is the order, which is promoted by the application of pressure. This then gives rise to an "effective" suppression of T_{N} with respect to T_{c}. In the vicinity of the crossing of T_{N} and T_{c}, a small superconducting dome is observed for $x = 0.050$, further suggesting the competition relation between SC and magnetism. Furthermore, the pressure where the T_{N} and T_{c} lines cross coincides with a minimum in the normalized slope of the superconducting upper critical field, consistent with a likely Fermi-surface reconstruction associated with the loss of magnetic ordering. Finally, at $p \sim 4$ GPa, both Ni-substituted $CaK(Fe_{1-x}Ni_x)_4As_4$ samples likely go through a half-collapsed-tetragonal (hcT) phase transition, similar to the parent compound $CaKFe_4As_4$Kaluarachchi et al. (2017b).

In Chap. 5, we present a pressure study on single crystalline $EuRbFe_4As_4$. As another member of the "1144" family, $EuRbFe_4As_4$ is different from the majority of the Fe-based

superconductors in the sense that the magnetism in $EuRbFe_4As_4$ also comes from the local Eu^{2+} magnetic moment. The pressure dependencies of the magnetic and superconducting transitions, as well as that of the superconducting upper critical field are studied. Resistance measurements were performed under pressures up to 6.21 GPa and magnetization measurements were performed under pressures up to 1.24 GPa. A pressure-temperature phase diagram was constructed from these measurements. Our results show that superconducting transition temperature, T_c, is monotonically suppressed upon increasing pressure. Magnetic transition, T_M, is linearly increased up to 1.24 GPa. For the studied pressure range, no signs of the crossing of T_M and T_c lines are observed. The normalized slope of the superconducting upper critical field is gradually suppressed with increasing pressure, which may be due to the continuous change of Fermi-velocity v_F with pressure.

In Chap. 6, the electrical transport properties of RBi_2 (R = La, Ce) under hydrostatic pressure up to $\sim$ 2.5 GPa are presented. These measurements are complemented by thermodynamic measurements of the specific heat on $CeBi_2$ at different pressures up to 2.55 GPa. For $CeBi_2$, we find a moderate increase of the antiferromagnetic transition, T_N, from 3.3 K to 4.4 K by pressures up to 2.55 GPa. Notably, resistance measurements for both $CeBi_2$ and $LaBi_2$ show signatures of superconductivity for pressures above $\sim$ 1.7 GPa. However, the absence of superconducting feature in specific heat measurements for $CeBi_2$ indicates that superconductivity in $CeBi_2$ (and most likely $LaBi_2$ as well) is not bulk and likely originates from traces of Bi flux, either on the surface of the plate-like samples, or trapped inside the sample as laminar inclusions. Finally, we point out that extra caution should be exercised when claiming superconductivity based just on transport measurements, especially for Bi-containing compounds.

Chapter. 7 presents a pressure study on a newly discovered ferromagnetic compound $La_5Co_2Ge_3$. Magnetization, electrical transport as well as specific heat measurements were performed up to the highest pressure of 5.12 GPa. Our measurements demonstrate that in the low pressure regime ($p \lesssim$1.7 GPa), the ferromagnetic transition temperature, T_C, is monotonically suppressed upon increasing pressure. Before T_C is suppressed to zero, $La_5Co_2Ge_3$ enters into a

new ground states for the high pressure regime ($p \gtrsim 1.7$ GPa). Our results suggest that this system manifests another example of avoided FM QCP, but further analysis of the data is on-going.

In high pressure research, the manganin manometer is one of the most commonly used resistive manometers and is often used to determine the pressure values at room temperature in gas-, piston-cylinder, and large volume anvil cells. To extend the usage of the manganin manometer to lower temperatures, we present in Chap. 8 a study of the temperature- and pressure-dependent resistance, $R(T, p)$, of a manganin manometer in a ^{4}He-gas pressure setup (from room temperature down to the solidification temperature of ^{4}He and for pressures between 0 GPa and ~ 0.8 GPa) and a piston-cylinder cell (from 300 K down to 1.8 K and for pressures between 0 GPa to ~ 2 GPa). From these measurements, we infer the temperature and pressure dependence of the pressure coefficient, $\alpha(T, p)$, of manganin, where α is defined as $R_p = (1 + \alpha p)R_0$ with R_p and R_0 being the resistance at finite pressure p and ambient pressure, respectively. Our results indicate that upon cooling α first decreases, then goes through a broad minimum at ~ 120 K and increases again towards lower temperatures. In addition, we find that α is almost pressure-independent for $T \gtrsim 60$ K up to $p \sim 2$ GPa, but shows a pronounced p dependence for $T \lesssim 60$ K. Using this manganin manometer, we provide a detailed study of the temperature evolution of the pressure in the piston-cylinder cell. It is demonstrated that p overall decreases with decreasing temperature in the piston-cylinder cell for the full pressure range, and that pressure experiences a more significant drop upon cooling through the medium solidification temperature. The size of the pressure difference between room temperature and low temperatures ($T = 1.8$ K), Δp, decreases with increasing pressure. We also compare the pressure values inferred from the manganin manometer with the low-temperature pressure, determined from the superconducting transition temperature of elemental lead (Pb). As a result of these data and analysis we propose a practical algorithm to infer the evolution of pressure with temperature in a piston-cylinder cell in the end.

As a whole, this thesis demonstrates the power and versatility of using pressure as a tuning parameter. It allows for control of, and insight into, diverse systems with electronic, magnetic

and/or structural transitions. As more measurement techniques are adapted to more ready use under applied pressures, experimental and then theoretical details of complex materials and their competing ground states will become better understood, and perhaps even mastered.

REFERENCES

Abrikosov, A. A. and Gor'kov, L. P. (1960). Contribution to the theory of superconducting alloys with paramagnetic impurities. *Zhur. Eksptl'. i Teoret. Fiz.*, 39.

Albedah, M. A., Nejadsattari, F., Stadnik, Z. M., Liu, Y., and Cao, G.-H. (2018). Mössbauer spectroscopy measurements on the 35.5 K superconductor $Rb_{1-\delta}EuFe_4As_4$. *Phys. Rev. B*, 97:144426.

Alexander, S., Helman, J. S., and Balberg, I. (1976). Critical behavior of the electrical resistivity in magnetic systems. *Phys. Rev. B*, 13(1):304–315.

Alireza, P. L., Ko, Y. T. C., Gillett, J., Petrone, C. M., Cole, J. M., Lonzarich, G. G., and Sebastian, S. E. (2009). Superconductivity up to 29 K in $SrFe_2As_2$ and $BaFe_2As_2$ at high pressures. *Journal of Physics: Condensed Matter*, 21(1):012208.

Anderson, P. W. (1961). Localized Magnetic States in Metals. *Phys. Rev.*, 124(1):41–53.

Andersson, O. E. and Sundqvist, B. (1997). Low temperature calibration of Manganin pressure gauges. *Review of Scientific Instruments*, 68(2):1344–1345.

Andrei, N. (1980). Diagonalization of the Kondo Hamiltonian. *Phys. Rev. Lett.*, 45(5):379–382.

Aoki, D., Huxley, A., Ressouche, E., Braithwaite, D., Flouquet, J., Brison, J.-P., Lhotel, E., and Paulsen, C. (2001). Coexistence of superconductivity and ferromagnetism in URhGe. *Nature*, 413:613.

Arsenijević, S., Hodovanets, H., Gaál, R., Forró, L., Bud'ko, S. L., and Canfield, P. C. (2013). Signatures of quantum criticality in the thermopower of $Ba(Fe_{1-x}Co_x)_2As_2$. *Phys. Rev. B*, 87:224508.

Baek, S.-H., Efremov, D. V., Ok, J. M., Kim, J. S., van den Brink, J., and Büchner, B. (2014). Orbital-driven nematicity in FeSe. *Nat. Mater.*, 14:210–214.

Bao, J.-K., Willa, K., Smylie, M. P., Chen, H., Welp, U., Chung, D. Y., and Kanatzidis, M. G. (2018). Single Crystal Growth and Study of the Ferromagnetic Superconductor $RbEuFe_4As_4$. *Crystal Growth & Design*, 18(6):3517–3523.

Bardeen, J., Cooper, L. N., and Schrieffer, J. R. (1957a). Microscopic Theory of Superconductivity. *Phys. Rev.*, 106(1):162–164.

Bardeen, J., Cooper, L. N., and Schrieffer, J. R. (1957b). Theory of Superconductivity. *Phys. Rev.*, 108(5):1175–1204.

Barnett, J. D., Block, S., and Piermarini, G. J. (1973). An Optical Fluorescence System for Quantitative Pressure Measurement in the Diamond-Anvil Cell. *Review of Scientific Instruments*, 44(1):1–9.

Basov, D. N. and Chubukov, A. V. (2011). Manifesto for a higher Tc. *Nature Physics*, 7(4):272–276.

Bauer, E. D., Lee, H. O., Sidorov, V. A., Kurita, N., Gofryk, K., Zhu, J.-X., Ronning, F., Movshovich, R., Thompson, J. D., and Park, T. (2010). Pressure-induced superconducting state and effective mass enhancement near the antiferromagnetic quantum critical point of $CePt_2In_7$. *Phys. Rev. B*, 81(18):180507(R).

Becker, W. M., Hoo, K., and Winchell, P. G. (1976). Comparison of pressures at 300 K and liquid helium temperatures using a clamp type bomb. *Review of Scientific Instruments*, 47(5):587–591.

Bednorz, J. G. and Müller, K. A. (1986). Possible highTc superconductivity in the BaLaCuO system. *Zeitschrift für Physik B Condensed Matter*, 64(2):189–193.

Belitz, D., Kirkpatrick, T. R., and Vojta, T. (1999). First Order Transitions and Multicritical Points in Weak Itinerant Ferromagnets. *Phys. Rev. Lett.*, 82(23):4707–4710.

Bendele, M., Amato, A., Conder, K., Elender, M., Keller, H., Klauss, H.-H., Luetkens, H., Pomjakushina, E., Raselli, A., and Khasanov, R. (2010). Pressure Induced Static Magnetic Order in Superconducting $FeSe_{1-x}$. *Phys. Rev. Lett.*, 104:087003.

Bendele, M., Ichsanow, A., Pashkevich, Y., Keller, L., Strässle, T., Gusev, A., Pomjakushina, E., Conder, K., Khasanov, R., and Keller, H. (2012). Coexistence of superconductivity and magnetism in $FeSe_{1-x}$ under pressure. *Phys. Rev. B*, 85:064517.

Bilbro, G. and McMillan, W. L. (1976). Theoretical model of superconductivity and the martensitic transformation in $A15$ compounds. *Phys. Rev. B*, 14(5):1887–1892.

Bireckoven, B. and Wittig, J. (1988). A diamond anvil cell for the investigation of superconductivity under pressures of up to 50 GPa: Pb as a low temperature manometer. *Journal of Physics E: Scientific Instruments*, 21(9):841.

Birks, A. W. and Gall, C. A. (1973). Design and development of Manganin and other wire sensors together with a resistance strain gauge transducer for use at pressures up to 200000 lbf/in2 (1.38 GN/m2). *Strain*, 9(2):60–65.

Böhmer, A. E., Arai, T., Hardy, F., Hattori, T., Iye, T., Wolf, T., Löhneysen, H. v., Ishida, K., and Meingast, C. (2015). Origin of the Tetragonal-to-Orthorhombic Phase Transition in FeSe: A Combined Thermodynamic and NMR Study of Nematicity. *Phys. Rev. Lett.*, 114:027001.

Böhmer, A. E., Taufour, V., Straszheim, W. E., Wolf, T., and Canfield, P. C. (2016). Variation of transition temperatures and residual resistivity ratio in vapor-grown FeSe. *Phys. Rev. B*, 94:024526.

Borisov, V., Canfield, P. C., and Valentí, R. (2018). Trends in pressure-induced layer-selective half-collapsed tetragonal phases in the iron-based superconductor family $AeAFe_4As_4$. *Phys. Rev. B*, 98:064104.

Brando, M., Belitz, D., Grosche, F. M., and Kirkpatrick, T. R. (2016). Metallic quantum ferromagnets. *Rev. Mod. Phys.*, 88:025006.

Brandt, N. B. and Ginzburg, N. I. (1969). Superconductivity at high pressures. *Contemporary Physics*, 10(4):355–386.

Brandt, N. B., Kuvshinnikov, S. V., Minina, N. Y., and Skipetrov, E. P. (1974). A method of increasing the hydrostatic nature of the compression at low temperatures in fixed pressure bombs. *Cryogenics*, 14(8):464–466.

Bridgman, P. W. (1911). The Measurement of Hydrostatic Pressures up to 20,000 Kilograms per Square Centimeter. *Proc. Am. Acad. Arts Sci.*, 47(11):321–343.

Bridgman, P. W. (1941). Explorations toward the Limit of Utilizable Pressures. *Journal of Applied Physics*, 12(6):461–469.

Bridgman, P. W. (1952). The Resistance of 72 Elements, Alloys and Compounds to 100,000 Kg/Cm**2**. *Proceedings of the American Academy of Arts and Sciences*, 81(4):165–251.

Bud'ko, S. L. and Canfield, P. C. (2000). Rotational tuning of H_{c2} anomalies in erni$_2$b$_2$C : angular-dependent superzone gap formation and its effect on the superconducting ground state. *Phys. Rev. B*, 61:R14932–R14935.

Bud'ko, S. L. and Canfield, P. C. (2006). Magnetism and superconductivity in rare earth-nickel-borocarbides. *C. R. Physique*, 7(1):56–67.

Bud'ko, S. L., Kogan, V. G., Prozorov, R., Meier, W. R., Xu, M., and Canfield, P. C. (2018). Coexistence of superconductivity and magnetism in CaK$(Fe_{1-x}Ni_x)_4As_4$ as probed by ^{57}Fe Mössbauer spectroscopy. *Phys. Rev. B*, 98(14):144520.

Bud'ko, S. L., Voronovskii, A. N., Gapotchenko, A. G., and ltskevich, E. S. (1984). The Fermi surface of cadmium at an electron-topological phase transition under pressure. *Zh. Eksp. Teor. Fiz. 86, 778.*

Bud'ko, S. L., Xiang, L., Hu, C., Shen, B., Ni, N., and Canfield, P. C. (2020). Pressure tuning of structural and magnetic transitions in $EuAg_4As_2$. *Phys. Rev. B*, 101(19):195112.

Bulaevskii, L. N., Buzdin, A. I., Kulić, M. L., and Panjukov, S. V. (1985). Coexistence of superconductivity and magnetism theoretical predictions and experimental results. *Advances in Physics*, 34(2):175–261.

Canfield, P. C. and Bud'ko, S. L. (2010). FeAs-Based Superconductivity: A Case Study of the Effects of Transition Metal Doping on $BaFe_2As_2$. *Annu. Rev. Condens. Matter Phys.*, 1(1):27–50.

Canfield, P. C. and Bud'ko, S. L. (2016). Preserved entropy and fragile magnetism. *Reports on Progress in Physics*, 79(8):084506.

Canfield, P. C., Bud'ko, S. L., and Cho, B. K. (1996). Possible co-existence of superconductivity and weak ferromagnetism in $ErNi_2B_2C$. *Physica C: Superconductivity*, 262(3):249–254.

Canfield, P. C. and Fisk, Z. (1992). Growth of single crystals from metallic fluxes. *Philosophical Magazine B*, 65(6):1117–1123.

Canfield, P. C., Gammel, P. L., and Bishop, D. J. (1998). New Magnetic Superconductors: A Toy Box for Solid-State Physicists. *Physics Today*, 51:10, 40.

Canfield, P. C., Kong, T., Kaluarachchi, U. S., and Jo, N. H. (2016). Use of frit-disc crucibles for routine and exploratory solution growth of single crystalline samples. *Philosophical Magazine*, 96(1):84–92.

Chen, G., Zhu, X., Yang, H., and Wen, H. (2017). Highly anisotropic superconducting gaps and possible evidence of antiferromagnetic order in FeSe single crystals. *arXiv:1703.08680*.

Chen, G. F., Matsubayashi, K., Ban, S., Deguchi, K., and Sato, N. K. (2006). Competitive Coexistence of Superconductivity with Antiferromagnetism in $CeRhIn_5$. *Phys. Rev. Lett.*, 97(1):017005.

Chen, Y. L., Analytis, J. G., Chu, J.-H., Liu, Z. K., Mo, S.-K., Qi, X. L., Zhang, H. J., Lu, D. H., Dai, X., Fang, Z., Zhang, S. C., Fisher, I. R., Hussain, Z., and Shen, Z.-X. (2009). Experimental Realization of a Three-Dimensional Topological Insulator, Bi_2Te_3. *Science*, 325(5937):178.

Cheng, J.-G., Matsubayashi, K., Wu, W., Sun, J. P., Lin, F. K., Luo, J. L., and Uwatoko, Y. (2015). Pressure Induced Superconductivity on the border of Magnetic Order in MnP. *Phys. Rev. Lett.*, 114(11):117001.

Cheon, K. O., Fisher, I. R., and Canfield, P. C. (1999). Boron isotope effect in single-crystal YNi2B2C and LuNi2B2C superconductors. *Physica C: Superconductivity*, 312(1):35–39.

Christianson, A. D., Goremychkin, E. A., Osborn, R., Rosenkranz, S., Lumsden, M. D., Malliakas, C. D., Todorov, I. S., Claus, H., Chung, D. Y., Kanatzidis, M. G., Bewley, R. I., and Guidi, T. (2008). Unconventional superconductivity in $Ba_{0.6}K_{0.4}Fe_2As_2$ from inelastic neutron scattering. *Nature*, 456:930.

Christianson, A. D., Lumsden, M. D., Nagler, S. E., MacDougall, G. J., McGuire, M. A., Sefat, A. S., Jin, R., Sales, B. C., and Mandrus, D. (2009). Static and Dynamic Magnetism in Underdoped Superconductor $BaFe_{1.92}Co_{0.08}As_2$. *Phys. Rev. Lett.*, 103:087002.

Chu, C. W. and Lorenz, B. (2009). High pressure studies on Fe-pnictide superconductors. *Physica C: Superconductivity*, 469(9):385–395.

Chubukov, A. (2012). Pairing Mechanism in Fe-Based Superconductors. *Annu. Rev. Condens. Matter Phys.*, 3(1):57–92.

Chubukov, A. V., Khodas, M., and Fernandes, R. M. (2016). Magnetism, Superconductivity, and Spontaneous Orbital Order in Iron-Based Superconductors: Which Comes First and Why? *Phys. Rev. X*, 6:041045.

Chubukov, A. V., Pépin, C., and Rech, J. (2004). Instability of the Quantum-Critical Point of Itinerant Ferromagnets. *Phys. Rev. Lett.*, 92(14):147003.

Clark, M. J. and Smith, T. F. (1978). Pressure dependence of Tc for lead. *Journal of Low Temperature Physics*, 32(3):495–503.

Clogston, A. M. (1962). Upper Limit for the Critical Field in Hard Superconductors. *Phys. Rev. Lett.*, 9(6):266–267.

Coldea, A. I., Blake, S. F., Kasahara, S., Haghighirad, A. A., Watson, M. D., Knafo, W., Choi, E. S., McCollam, A., Reiss, P., Yamashita, T., Bruma, M., Speller, S., Matsuda, Y., Wolf, T., Shibauchi, T., and Schofield, A. J. (2016). Evolution of the Fermi surface of the nematic superconductors $FeSe_{1-x}S_x$. *arXiv:1611.07424*.

Colombier, E. and Braithwaite, D. (2007). Simple adaptation of the Bridgman high pressure technique for use with liquid media. *Review of Scientific Instruments 78, 093903*.

Colombier, E., Bud'ko, S. L., Ni, N., and Canfield, P. C. (2009). Complete pressure-dependent phase diagrams for $SrFe_2As_2$ and $BaFe_2As_2$. *Phys. Rev. B*, 79:224518.

Colombier, E., Torikachvili, M. S., Ni, N., Thaler, A., Bud'ko, S. L., and Canfield, P. C. (2010). Electrical transport measurements under pressure for $BaFe_2As_2$ compounds doped with Co, Cr, or Sn. *Superconductor Science and Technology*, 23(5):054003.

Conduit, G. J., Green, A. G., and Simons, B. D. (2009). Inhomogeneous Phase Formation on the Border of Itinerant Ferromagnetism. *Phys. Rev. Lett.*, 103(20):207201.

Cooper, L. N. (1956). Bound Electron Pairs in a Degenerate Fermi Gas. *Phys. Rev.*, 104(4):1189–1190.

Cvetkovic, V. and Vafek, O. (2013). Space group symmetry, spin-orbit coupling, and the low-energy effective Hamiltonian for iron-based superconductors. *Phys. Rev. B*, 88:134510.

Dagotto, E. (1994). Correlated electrons in high-temperature superconductors. *Rev. Mod. Phys.*, 66(3):763–840.

Dai, J., Si, Q., Zhu, J.-X., and Abrahams, E. (2009). Iron pnictides as a new setting for quantum criticality. *Proceedings of the National Academy of Sciences*, 106(11):4118–4121.

Dai, P. (2015). Antiferromagnetic order and spin dynamics in iron-based superconductors. *Rev. Mod. Phys.*, 87:855–896.

de Haas, W. J., de Boer, J., and van dën Berg, G. J. (1934). The electrical resistance of gold, copper and lead at low temperatures. *Physica*, 1(7):1115–1124.

Degtyareva, O., Mcmahon, M. I., and Nelmes, R. J. (2004). High-pressure structural studies of group-15 elements. *High Pressure Research*, 24(3):319–356.

Dhaka, R. S., Hahn, S. E., Razzoli, E., Jiang, R., Shi, M., Harmon, B. N., Thaler, A., Bud'ko, S. L., Canfield, P. C., and Kaminski, A. (2013). Unusual Temperature Dependence of Band Dispersion in $Ba(Fe_{1-x}Ru_x)_2As_2$ and its Consequences for Antiferromagnetic Ordering. *Phys. Rev. Lett.*, 110:067002.

Dmowski, L. H. and Litwin-Staszewska, E. (1999). The variation of the pressure coefficient of manganin sensors at low temperatures. *Measurement Science and Technology*, 10(5):343–347.

Doniach, S. (1977). The Kondo lattice and weak antiferromagnetism. *Physica B & C*, 91:231 – 234.

Drozdov, A. P., Eremets, M. I., Troyan, I. A., Ksenofontov, V., and Shylin, S. I. (2015). Conventional superconductivity at 203 kelvin at high pressures in the sulfur hydride system. *Nature*, 525(7567):73–76.

Drozdov, A. P., Kong, P. P., Minkov, V. S., Besedin, S. P., Kuzovnikov, M. A., Mozaffari, S., Balicas, L., Balakirev, F. F., Graf, D. E., Prakapenka, V. B., Greenberg, E., Knyazev, D. A., Tkacz, M., and Eremets, M. I. (2019). Superconductivity at 250 K in lanthanum hydride under high pressures. *Nature*, 569(7757):528–531.

Dubrovinsky, L., Dubrovinskaia, N., Bykova, E., Bykov, M., Prakapenka, V., Prescher, C., Glazyrin, K., Liermann, H.-P., Hanfland, M., Ekholm, M., Feng, Q., Pourovskii, L. V., Katsnelson, M. I., Wills, J. M., and Abrikosov, I. A. (2015). The most incompressible metal osmium at static pressures above 750 gigapascals. *Nature*, 525(7568):226–229.

Dynes, R. C. (1972). McMillan's equation and the T_c of superconductors. *Solid State Communications*, 10(7):615–618.

Eichler, A. and Wittig, J. (1968). Pressure dependence of the superconducting transition temperature of lead.

Eiling, A. and Schilling, J. S. (1981). Pressure and temperature dependence of electrical resistivity of Pb and Sn from 1-300K and 0-10 GPa-use as continuous resistive pressure monitor accurate over wide temperature range; superconductivity under pressure in Pb, Sn and In. *Journal of Physics F: Metal Physics*, 11(3):623.

Eliashberg, G. (1960). Interactions between electrons and lattice vibrations in a superconductor. *Sov. Phys. - JETP (Engl. Transl.); (United States)*, 11:3.

Eremets, M. I. (1996). *High Pressure Experimental Methods*. Oxford University Press.

Fei, Y., Ricolleau, A., Frank, M., Mibe, K., Shen, G., and Prakapenka, V. (2007). Toward an internally consistent pressure scale. *Proc Natl Acad Sci USA*, 104(22):9182.

Fernandes, R. M., Chubukov, A. V., and Schmalian, J. (2014). What drives nematic order in iron-based superconductors? *Nat Phys*, 10(2):97–104.

Fernandes, R. M., Kivelson, S. A., and Berg, E. (2016). Vestigial chiral and charge orders from bidirectional spin-density waves: Application to the iron-based superconductors. *Phys. Rev. B*, 93:014511.

Fernandes, R. M., Pratt, D. K., Tian, W., Zarestky, J., Kreyssig, A., Nandi, S., Kim, M. G., Thaler, A., Ni, N., Canfield, P. C., McQueeney, R. J., Schmalian, J., and Goldman, A. I. (2010). Unconventional pairing in the iron arsenide superconductors. *Phys. Rev. B*, 81:140501.

Fernandes, R. M. and Schmalian, J. (2012). Manifestations of nematic degrees of freedom in the magnetic, elastic, and superconducting properties of the iron pnictides. *Supercond. Sci. Technol.*, 25(8):084005.

Fertig, W. A., Johnston, D. C., DeLong, L. E., McCallum, R. W., Maple, M. B., and Matthias, B. T. (1977). Destruction of Superconductivity at the Onset of Long-Range Magnetic Order in the Compound $ErRh_4B_4$. *Phys. Rev. Lett.*, 38:987–990.

Finnemore, D. K., Hopkins, D. C., and Palmer, P. E. (1965). Coexistence of Antiferromagnetism and Superconductivity. *Phys. Rev. Lett.*, 15(23):891–893.

Fischer, Ø. (1990). *Handbook of Magnetic Materials*, volume 5. North Holland, 1st edition.

Fisher, M. E. and Langer, J. S. (1968). Resistive Anomalies at Magnetic Critical Points. *Phys. Rev. Lett.*, 20(13):665–668.

Forman, R. A., Piermarini, G. J., Barnett, J. D., and Block, S. (1972). Pressure Measurement Made by the Utilization of Ruby Sharp-Line Luminescence. *Science*, 176(4032):284.

Freeman, A. J. (1972). *Magnetic Properties of Rare Earth Metals*. Springer US.

Friedel, J. (1987). *Low-Dimensional Conductors and Superconductors*. Springer US.

Friedrich, J. (2016). Methods for Bulk Growth of Inorganic Crystals: Crystal Growth. In *Reference Module in Materials Science and Materials Engineering*. Elsevier.

Fujioka, N., Mishima, O., Endo, S., and Kawai, N. (1978). Electrical resistance of Manganin under high static pressures. *Journal of Applied Physics*, 49(9):4830–4832.

Fujiwara, H., Kadomatsu, H., and Tohma, K. (1980). Simple clamp pressure cell up to 30 kbar. *Review of Scientific Instruments*, 51(10):1345–1348.

Fujiwara, N., Matsumoto, T., Nakazawab, K., Hisada, A., and Uwatoko, Y. (2007). Fabrication and efficiency evaluation of a hybrid NiCrAl pressure cell up to 4GPa. *Review of Scientific Instruments*, 78(7):073905.

Fujiwara, N., Uwatoko, Y., and Matsumoto, T. (2014). A NiCrAl pressure cell up to 4.6 GPa and its application to cuprate and pnictide superconductors. *Journal of Physics: Conference Series*, 500(3):032008.

Funamori, N. and Sato, T. (2008). A cubic boron nitride gasket for diamond-anvil experiments. *Review of Scientific Instruments*, 79(5):053903.

Gati, E., Drachuck, G., Xiang, L., Wang, L.-L., Bud'ko, S. L., and Canfield, P. C. (2019a). Use of Cernox thermometers in AC specific heat measurements under pressure. *Review of Scientific Instruments*, 90(2):023911.

Gati, E., Köhler, S., Guterding, D., Wolf, B., Knöner, S., Ran, S., Bud'ko, S. L., Canfield, P. C., and Lang, M. (2012). Hydrostatic-pressure tuning of magnetic, nonmagnetic, and superconducting states in annealed $Ca(Fe_{1-x}Co_x)_2As_2$. *Phys. Rev. B*, 86(22):220511.

Gati, E., Xiang, L., Bud'ko, S. L., and Canfield, P. C. (2019b). Role of the Fermi surface for the pressure-tuned nematic transition in the $BaFe_2As_2$ family. *Phys. Rev. B*, 100(6):064512.

Gati, E., Xiang, L., Bud'ko, S. L., and Canfield, P. C. (2020a). Hydrostatic and Uniaxial Pressure Tuning of Iron-Based Superconductors: Insights into Superconductivity, Magnetism, Nematicity, and Collapsed Tetragonal Transitions. *ANNALEN DER PHYSIK*, n/a(n/a):2000248.

Gati, E., Xiang, L., Bud'ko, S. L., and Canfield, P. C. (2020b). Measurements of elastoresistance under pressure by combining in-situ tunable quasi-uniaxial stress with hydrostatic pressure. *Review of Scientific Instruments*, 91(2):023904.

Gati, E., Xiang, L., Wang, L.-L., Manni, S., Canfield, P. C., and Bud'ko, S. L. (2018). Effect of pressure on the physical properties of the superconductor $NiBi_3$. *Journal of Physics: Condensed Matter*, 31(3):035701.

Gavriliuk, A. G., Mironovich, A. A., and Struzhkin, V. V. (2009). Miniature diamond anvil cell for broad range of high pressure measurements. *Review of Scientific Instruments*, 80(4):043906.

Ge, J.-F., Liu, Z.-L., Liu, C., Gao, C.-L., Qian, D., Xue, Q.-K., Liu, Y., and Jia, J.-F. (2015). Superconductivity above 100 K in single-layer FeSe films on doped $SrTiO_3$. *Nat Mater*, 14(3):285–289.

Gegenwart, P., Si, Q., and Steglich, F. (2008). Quantum criticality in heavy-fermion metals. *Nature Physics*, 4(3):186–197.

Ginzburg, V. L. and Landau, L. D. (1950). On the Theory of superconductivity. *Zh. Eksp. Teor. Fiz.*, 20:1064–1082.

Glasbrenner, J. K., Mazin, I. I., Jeschke, H. O., Hirschfeld, P. J., Fernandes, R. M., and Valenti, R. (2015). Effect of magnetic frustration on nematicity and superconductivity in iron chalcogenides. *Nat Phys*, 11(11):953–958.

Goltsev, A. V. and Abd-Elmeguid, M. M. (2005). Origin of the pressure dependence of the Kondo temperature in Ce- and Yb-based heavy-fermion compounds. *Journal of Physics: Condensed Matter*, 17(11):S813–S821.

Gooch, M., Lv, B., Lorenz, B., Guloy, A. M., and Chu, C.-W. (2009). Evidence of quantum criticality in the phase diagram of $K_xSr_{1-x}Fe_2As_2$ from measurements of transport and thermoelectricity. *Phys. Rev. B*, 79:104504.

Gooch, M., Lv, B., Lorenz, B., Guloy, A. M., and Chu, C. W. (2010). Critical scaling of transport properties in the phase diagram of iron pnictide superconductors $K_xSr_{1-x}Fe_2As_2$ and $K_xBa_{1-x}Fe_2As_2$. *Journal of Applied Physics*, 107(9):09E145.

Goto, T., Shindo, Y., Ogawa, S., and Harada, T. (1998). Magnetic properties of $Co(S_{1-x}Se_x)_2$ under high magnetic field and high pressure. *International Conference on Magnetism*, 177-181:579–580.

Hasan, M. Z. and Kane, C. L. (2010). Colloquium: Topological insulators. *Rev. Mod. Phys.*, 82:3045–3067.

Hassinger, E., Gredat, G., Valade, F., de Cotret, S. R., Cyr-Choinière, O., Juneau-Fecteau, A., Reid, J.-P., Kim, H., Tanatar, M. A., Prozorov, R., Shen, B., Wen, H.-H., Doiron-Leyraud, N., and Taillefer, L. (2016). Expansion of the tetragonal magnetic phase with pressure in the iron arsenide superconductor $Ba_{1-x}K_xFe_2As_2$. *Phys. Rev. B*, 93:144401.

Hassinger, E., Gredat, G., Valade, F., de Cotret, S. R., Juneau-Fecteau, A., Reid, J.-P., Kim, H., Tanatar, M. A., Prozorov, R., Shen, B., Wen, H.-H., Doiron-Leyraud, N., and Taillefer, L. (2012). Pressure-induced Fermi-surface reconstruction in the iron-arsenide superconductor $Ba_{1-x}K_xFe_2As_2$: Evidence of a phase transition inside the antiferromagnetic phase. *Phys. Rev. B*, 86:140502.

Haug, T., Heimonen, H., Dumke, R., Kwek, L.-C., and Amico, L. (2019). Aharonov-Bohm effect in mesoscopic Bose-Einstein condensates. *Phys. Rev. A*, 100(4):041601.

Hegger, H., Petrovic, C., Moshopoulou, E. G., Hundley, M. F., Sarrao, J. L., Fisk, Z., and Thompson, J. D. (2000). Pressure-Induced Superconductivity in Quasi-2D $CeRhIn_5$. *Phys. Rev. Lett.*, 84(21):4986–4989.

Helfand, E. and Werthamer, N. R. (1964). Temperature and Purity Dependence of the Superconducting Critical Field, H_{c2}. *Phys. Rev. Lett.*, 13(23):686–688.

Helfand, E. and Werthamer, N. R. (1966). Temperature and Purity Dependence of the Superconducting Critical Field, H_{c2}. II. *Phys. Rev.*, 147(1):288–294.

Herring, C. (1958). Spin exchange in superconductors. *Physica*, 24:S184.

Hertz, J. A. (1976). Quantum critical phenomena. *Phys. Rev. B*, 14(3):1165–1184.

Hewson, A. C. (1993). *The Kondo Problem to Heavy Fermions*. Cambridge Studies in Magnetism. Cambridge University Press.

Hodder, R. E. (1969). Pressure Effects on the Superconducting Transition Temperature of Pb. *Phys. Rev.*, 180(2):530–534.

Hor, Y. S., Williams, A. J., Checkelsky, J. G., Roushan, P., Seo, J., Xu, Q., Zandbergen, H. W., Yazdani, A., Ong, N. P., and Cava, R. J. (2010). Superconductivity in $Cu_xBi_2Se_3$ and its Implications for Pairing in the Undoped Topological Insulator. *Phys. Rev. Lett.*, 104:057001.

Hosoi, S., Matsuura, K., Ishida, K., Wang, H., Mizukami, Y., Watashige, T., Kasahara, S., Matsuda, Y., and Shibauchi, T. (2016). Nematic quantum critical point without magnetism in $FeSe_{1-x}S_x$ superconductors. *Proc. Natl. Acad. Sci. U.S.A.*, 113(29):8139–8143.

Huang, Q., Qiu, Y., Bao, W., Green, M. A., Lynn, J. W., Gasparovic, Y. C., Wu, T., Wu, G., and Chen, X. H. (2008). Neutron-Diffraction Measurements of Magnetic Order and a Structural Transition in the Parent $BaFe_2As_2$ Compound of FeAs-Based High-Temperature Superconductors. *Phys. Rev. Lett.*, 101(25):257003.

Huxley, A., Sheikin, I., and Braithwaite, D. (2000). Metamagnetic behavior near the quantum critical point in UGe_2. *Physica B: Condensed Matter*, 284-288:1277–1278.

Huy, N. T., Gasparini, A., de Nijs, D. E., Huang, Y., Klaasse, J. C. P., Gortenmulder, T., de Visser, A., Hamann, A., Görlach, T., and Löhneysen, H. v. (2007). Superconductivity on the Border of Weak Itinerant Ferromagnetism in UCoGe. *Phys. Rev. Lett.*, 99:067006.

Isaeva, A., Rasche, B., and Ruck, M. (2013). Bismuth based candidates for topological insulators: Chemistry beyond Bi_2Te_3. *Phys. Status Solidi RRL*, 7(1-2):39–49.

Ishikawa, M. and Fischer, . (1977). Destruction of superconductivity by magnetic ordering in $Ho_{1.2}Mo_6S_8$. *Solid State Communications*, 23(1):37–39.

Itskevich, E. S. (1964). A high pressure bomb for work at low temperatures. *Cryogenics*, 4(6):365–367.

Iyo, A., Kawashima, K., Kinjo, T., Nishio, T., Ishida, S., Fujihisa, H., Gotoh, Y., Kihou, K., Eisaki, H., and Yoshida, Y. (2016). New-Structure-Type Fe-Based Superconductors: $CaAFe_4As_4$ (A = K, Rb, Cs) and $SrAFe_4As_4$ (A = Rb, Cs). *Journal of the American Chemical Society*, 138(10):3410–3415.

Jaccard, D., Behnia, K., and Sierro, J. (1992). Pressure induced heavy fermion superconductivity of $CeCu_2Ge_2$. *Physics Letters A*, 163(5):475–480.

Jackson, D. E., VanGennep, D., Bi, W., Zhang, D., Materne, P., Liu, Y., Cao, G.-H., Weir, S. T., Vohra, Y. K., and Hamlin, J. J. (2018). Superconducting and magnetic phase diagram of $RbEuFe_4As_4$ and $CsEuFe_4As_4$ at high pressure. *Phys. Rev. B*, 98:014518.

Jaeger, G. (1998). The Ehrenfest Classification of Phase Transitions: Introduction and Evolution. *Archive for History of Exact Sciences*, 53(1):51–81.

Jamieson, J. C. and Lawson, A. W. (1962). X-Ray Diffraction Studies in the 100 Kilobar Pressure Range. *Journal of Applied Physics*, 33(3):776–780.

Jayaraman, A., Hutson, A. R., McFee, J. H., Coriell, A. S., and Maines, R. G. (1967). Hydrostatic and Uniaxial Pressure Generation using Teflon Cell Container in Conventional Piston-Cylinder Device. *Review of Scientific Instruments*, 38(1):44–49.

Jeevan, H. S., Hossain, Z., Kasinathan, D., Rosner, H., Geibel, C., and Gegenwart, P. (2008). Electrical resistivity and specific heat of single-crystalline $EuFe_2As_2$: A magnetic homologue of $SrFe_2As_2$. *Phys. Rev. B*, 78:052502.

Jiang, S., Luo, Y., Ren, Z., Zhu, Z., Wang, C., Xu, X., Tao, Q., Cao, G., and Xu, Z. (2009a). Metamagnetic transition in $EuFe_2As_2$ single crystals. *New Journal of Physics*, 11(2):025007.

Jiang, S., Xing, H., Xuan, G., Ren, Z., Wang, C., Xu, Z.-a., and Cao, G. (2009b). Superconductivity and local-moment magnetism in $Eu(Fe_{0.89}Co_{0.11})_2As_2$. *Phys. Rev. B*, 80:184514.

Jiang, S., Xing, H., Xuan, G., Wang, C., Ren, Z., Feng, C., Dai, J., Xu, Z., and Cao, G. (2009c). Superconductivity up to 30 K in the vicinity of the quantum critical point in $BaFe_2(As_{1-x}P_x)$. *J. Phys. Condens. Matter*, 21(38):382203.

Jiao, L., Chen, Y., Kohama, Y., Graf, D., Bauer, E. D., Singleton, J., Zhu, J.-X., Weng, Z., Pang, G., Shang, T., Zhang, J., Lee, H.-O., Park, T., Jaime, M., Thompson, J. D., Steglich, F., Si, Q., and Yuan, H. Q. (2015). Fermi surface reconstruction and multiple quantum phase transitions in the antiferromagnet $CeRhIn_5$. *Proc Natl Acad Sci USA*, 112(3):673.

Jiao, W.-H., Tao, Q., Bao, J.-K., Sun, Y.-L., Feng, C.-M., Xu, Z.-A., Nowik, I., Felner, I., and Cao, G.-H. (2011). Anisotropic superconductivity in $Eu(Fe_{0.75}Ru_{0.25})_2As_2$ ferromagnetic superconductor. *EPL (Europhysics Letters)*, 95(6):67007.

Jiao, W.-H., Zhai, H.-F., Bao, J.-K., Luo, Y.-K., Tao, Q., Feng, C.-M., Xu, Z.-A., and Cao, G.-H. (2013). Anomalous critical fields and the absence of Meissner state in $Eu(Fe_{0.88}Ir_{0.12})_2As_2$ crystals. *New Journal of Physics*, 15(11):113002.

Jin, W. T., Li, W., Su, Y., Nandi, S., Xiao, Y., Jiao, W. H., Meven, M., Sazonov, A. P., Feng, E., Chen, Y., Ting, C. S., Cao, G. H., and Brückel, T. (2015). Magnetic ground state of superconducting $Eu(Fe_{0.88}Ir_{0.12})_2As_2$: A combined neutron diffraction and first-principles calculation study. *Phys. Rev. B*, 91:064506.

Jin, W. T., Nandi, S., Xiao, Y., Su, Y., Zaharko, O., Guguchia, Z., Bukowski, Z., Price, S., Jiao, W. H., Cao, G. H., and Brückel, T. (2013). Magnetic structure of superconducting $Eu(Fe_{0.82}Co_{0.18})_2As_2$ as revealed by single-crystal neutron diffraction. *Phys. Rev. B*, 88:214516.

Jo, N. H., Xiang, L., Kaluarachchi, U. S., Masters, M., Neilson, K., Downing, S. S., Canfield, P. C., and Bud'ko, S. L. (2017). Pressure induced change in the electronic state of $Ta_4Pd_3Te_{16}$. *Phys. Rev. B*, 95:134516.

Johnston, D. C. (2010). The puzzle of high temperature superconductivity in layered iron pnictides and chalcogenides. *Advances in Physics*, 59(6):803–1061.

Kadomatsu, H. and Fujiwara, H. (1979). The Curie temperature and the effect of pressure of Ni-based alloys (Ni-Cu, -Pd, -Pt and -Rh). *Solid State Communications*, 29(3):255–258.

Kaluarachchi, U. S. (2018). *"Pressure effects on magnetism and superconductivity"*. PhD thesis, Iowa State University.

Kaluarachchi, U. S., Deng, Y., Besser, M. F., Sun, K., Zhou, L., Nguyen, M. C., Yuan, Z., Zhang, C., Schilling, J. S., Kramer, M. J., Jia, S., Wang, C.-Z., Ho, K.-M., Canfield, P. C., and Bud'ko, S. L. (2017a). Highly responsive ground state of $PbTaSe_2$: Structural phase transition and evolution of superconductivity under pressure. *Phys. Rev. B*, 95:224508.

Kaluarachchi, U. S., Taufour, V., Böhmer, A. E., Tanatar, M. A., Bud'ko, S. L., Kogan, V. G., Prozorov, R., and Canfield, P. C. (2016). Nonmonotonic pressure evolution of the upper critical field in superconducting FeSe. *Phys. Rev. B*, 93:064503.

Kaluarachchi, U. S., Taufour, V., Sapkota, A., Borisov, V., Kong, T., Meier, W. R., Kothapalli, K., Ueland, B. G., Kreyssig, A., Valentí, R., McQueeney, R. J., Goldman, A. I., Bud'ko, S. L., and Canfield, P. C. (2017b). Pressure-induced half-collapsed-tetragonal phase in $CaKFe_4As_4$. *Phys. Rev. B*, 96:140501.

Kaluarachchi, U. S., Xiang, L., Ying, J., Kong, T., Struzhkin, V., Gavriliuk, A., Bud'ko, S. L., and Canfield, P. C. (2018). Collapse of the Kondo state and ferromagnetic quantum phase transition in $YbFe_2Zn_{20}$. *Phys. Rev. B*, 98(17):174405.

Kamihara, Y., Watanabe, T., Hirano, M., and Hosono, H. (2008). Iron-Based Layered Superconductor La[O1-xFx]FeAs (x = 0.050.12) with Tc = 26 K. *Journal of the American Chemical Society*, 130(11):3296–3297.

Kamishima, K., Hagiwara, M., and Yoshida, H. (2001). Investigation of a strong titanium alloy KS15-5-3 and the application to a high pressure apparatus for magnetization measurements. *Review of Scientific Instruments*, 72(2):1472–1476.

Karahasanovic, U., Krüger, F., and Green, A. G. (2012). Quantum order-by-disorder driven phase reconstruction in the vicinity of ferromagnetic quantum critical points. *Phys. Rev. B*, 85(16):165111.

Kasahara, S., Shibauchi, T., Hashimoto, K., Ikada, K., Tonegawa, S., Okazaki, R., Shishido, H., Ikeda, H., Takeya, H., Hirata, K., Terashima, T., and Matsuda, Y. (2010). Evolution from non-Fermi- to Fermi-liquid transport via isovalent doping in $BaFe_2(As_{1-x}P_x)_2$ superconductors. *Phys. Rev. B*, 81:184519.

Kasap, S. (2006). *Principles of Electronic Materials and Devices*. McGraw-Hill, Inc., New York, NY, USA, 3 edition.

Kasuya, T. (1956). A Theory of Metallic Ferro-and Antiferromagnetism on Zener's Model. *Progress of Theoretical Physics*, 16(1):45.

Kawashima, K., Ishida, S., Oka, K., Kito, H., Takeshita, N., Fujihisa, H., Gotoh, Y., Kihou, K., Eisaki, H., Yoshida, Y., and Iyo, A. (2018). Superconducting state in $(Eu_{1-x}Ca_x)RbFe_4As_4$ with 1144-type Structure. *Journal of Physics: Conference Series*, 969(1):012027.

Kawashima, K., Kinjo, T., Nishio, T., Ishida, S., Fujihisa, H., Gotoh, Y., Kihou, K., Eisaki, H., Yoshida, Y., and Iyo, A. (2016). Superconductivity in Fe-Based Compound $EuAFe_4As_4$ (A = Rb and Cs). *J. Phys. Soc. Jpn.*, 85(6):064710.

Kim, S. (2013). *Pressure effects on selected correlated electron systems*. PhD thesis, Iowa State University.

Kim, S. K., Torikachvili, M. S., Colombier, E., Thaler, A., Bud'ko, S. L., and Canfield, P. C. (2011). Combined effects of pressure and Ru substitution on $BaFe_2As_2$. *Phys. Rev. B*, 84:134525.

Kimber, S. A. J., Kreyssig, A., Zhang, Y.-Z., Jeschke, H. O., Valentí, R., Yokaichiya, F., Colombier, E., Yan, J., Hansen, T. C., Chatterji, T., McQueeney, R. J., Canfield, P. C., Goldman, A. I., and Argyriou, D. N. (2009). Similarities between structural distortions under pressure and chemical doping in superconducting $BaFe_2As_2$. *Nature Materials*, 8:471.

Kimura, N., Muro, Y., and Aoki, H. (2007). Normal and Superconducting Properties of Noncentrosymmetric Heavy Fermion $CeRhSi_3$. *J. Phys. Soc. Jpn.*, 76(5):051010.

Kinjo, T., Kajino, S., Nishio, T., Kawashima, K., Yanagi, Y., Hase, I., Yanagisawa, T., Ishida, S., Kito, H., Takeshita, N., Oka, K., Eisaki, H., Yoshida, Y., and Iyo, A. (2016). Superconductivity in $LaBi_3$ with $AuCu_3$ -type structure. *Superconductor Science and Technology*, 29(3):03LT02.

Kirkpatrick, T. R. and Belitz, D. (2020). Ferromagnetic Quantum Critical Point in Noncentrosymmetric Systems. *Phys. Rev. Lett.*, 124(14):147201.

Klement, W., Jayaraman, A., and Kennedy, G. C. (1963). Phase Diagrams of Arsenic, Antimony, and Bismuth at Pressures up to 70 kbars. *Phys. Rev.*, 131(2):632–637.

Klintberg, L. E., Goh, S. K., Kasahara, S., Nakai, Y., Ishida, K., Sutherland, M., Shibauchi, T., Matsuda, Y., and Terashima, T. (2010). Chemical Pressure and Physical Pressure in $BaFe_2(As_{1-x}P_x)_2$. *J. Phys. Soc. Jpn.*, 79(12):123706.

Knebel, G., Aoki, D., Braithwaite, D., Salce, B., and Flouquet, J. (2006). Coexistence of antiferromagnetism and superconductivity in $CeRhIn_5$ under high pressure and magnetic field. *Phys. Rev. B*, 74(2):020501(R).

Kogan, V. G. and Prozorov, R. (2012). Orbital upper critical field and its anisotropy of clean one- and two-band superconductors. *Rep. Prog. Phys.*, 75(11):114502.

Kogan, V. G. and Prozorov, R. (2014). Changing the type of superconductivity by magnetic and potential scattering. *Phys. Rev. B*, 90:180502.

Kondo, J. (1964). Resistance Minimum in Dilute Magnetic Alloys. *Progress of Theoretical Physics*, 32(1):37.

Kostrzewa, M., Szcześniak, K. M., Durajski, A. P., and Szcześniak, R. (2020). From LaH10 to room-temperature superconductors. *Scientific Reports*, 10(1):1592.

Kotegawa, H., Taufour, V., Aoki, D., Knebel, G., and Flouquet, J. (2011). Evolution toward Quantum Critical End Point in UGe_2. *J. Phys. Soc. Jpn.*, 80(8):083703.

Kotegawa, H., Toyama, T., Kitagawa, S., Tou, H., Yamauchi, R., Matsuoka, E., and Sugawara, H. (2013). Pressure-Temperature-Magnetic Field Phase Diagram of Ferromagnetic Kondo Lattice CeRuPO. *J. Phys. Soc. Jpn.*, 82(12):123711.

Kothapalli, K., Böhmer, A. E., Jayasekara, W. T., Ueland, B. G., Das, P., Sapkota, A., Taufour, V., Xiao, Y., Alp, E., Bud'ko, S. L., Canfield, P. C., Kreyssig, A., and Goldman, A. I. (2016). Strong cooperative coupling of pressure-induced magnetic order and nematicity in FeSe. *Nat. Commun.*, 7:12728.

Kraak, W., Schaller, U., and Herrmann, R. (1984). Sensitive Pressure Gauge on the Basis of Pure n-InSb. *phys. stat. sol. (a)*, 85(2):K183–K187.

Kreyssig, A., Green, M. A., Lee, Y., Samolyuk, G. D., Zajdel, P., Lynn, J. W., Bud'ko, S. L., Torikachvili, M. S., Ni, N., Nandi, S., Leão, J. B., Poulton, S. J., Argyriou, D. N., Harmon, B. N., McQueeney, R. J., Canfield, P. C., and Goldman, A. I. (2008). Pressure-induced volume-collapsed tetragonal phase of $CaFe_2As_2$ as seen via neutron scattering. *Phys. Rev. B*, 78:184517.

Kushwaha, S. K., Krizan, J. W., Xiong, J., Klimczuk, T., Gibson, Q. D., Liang, T., Ong, N. P., and Cava, R. J. (2014). Superconducting properties and electronic structure of NaBi. *Journal of Physics: Condensed Matter*, 26(21):212201.

Labat, D. and Paul, I. (2017). Pairing instability near a lattice-influenced nematic quantum critical point. *arXiv:1703.04146*, page 1703.04146.

Lamichhane, T. N., Xiang, L., Lin, Q., Pandey, T., Parker, D. S., Kim, T.-H., Zhou, L., Kramer, M. J., Bud'ko, S. L., and Canfield, P. C. (2018). Magnetic properties of single crystalline itinerant ferromagnet $AlFe_2B_2$. *Phys. Rev. Materials*, 2:084408.

Landau, L. (1936). The Theory of Phase Transitions. *Nature*, 138(3498):840–841.

Landau, L. D. (1937). On the theory of phase transition. I. *Zh. Eksp. Teor. Fiz.*, 11:19.

Lederer, S., Schattner, Y., Berg, E., and Kivelson, S. A. (2015). Enhancement of Superconductivity near a Nematic Quantum Critical Point. *Phys. Rev. Lett.*, 114:097001.

Li, Y., Wang, E., Zhu, X., and Wen, H.-H. (2017). Pressure-induced superconductivity in Bi single crystals. *Phys. Rev. B*, 95(2):024510.

Lin, J.-Y., Hsieh, Y. S., Chareev, D. A., Vasiliev, A. N., Parsons, Y., and Yang, H. D. (2011). Coexistence of isotropic and extended s-wave order parameters in FeSe as revealed by low-temperature specific heat. *Phys. Rev. B*, 84:220507.

Lin, Q., Aguirre, K., Saunders, S. M., Hackett, T. A., Liu, Y., Taufour, V., Paudyal, D., Bud'ko, S., Canfield, P. C., and Miller, G. J. (2017). Polar Intermetallics $Pr_5Co_2Ge_3$ and $Pr_7Co_2Ge_4$ with Planar Hydrocarbon-Like Metal Clusters. *Chem. Eur. J.*, 23(44):10516–10521.

Lin, X., Straszheim, W. E., Bud'ko, S. L., and Canfield, P. C. (2013). Anisotropic magnetization and resistivity of single crystalline $RNi_{1-x}Bi_{2\pm y}$ (R=La-Nd, Sm, Gd-Dy). *Journal of Alloys and Compounds*, 554:304–311.

Liu, C., Kondo, T., Ni, N., Palczewski, A. D., Bostwick, A., Samolyuk, G. D., Khasanov, R., Shi, M., Rotenberg, E., Bud'ko, S. L., Canfield, P. C., and Kaminski, A. (2009a). Three- to Two-Dimensional Transition of the Electronic Structure in $CaFe_2As_2$: A Parent Compound for an Iron Arsenic High-Temperature Superconductor. *Phys. Rev. Lett.*, 102:167004.

Liu, G., Liu, H., Zhao, L., Zhang, W., Jia, X., Meng, J., Dong, X., Zhang, J., Chen, G. F., Wang, G., Zhou, Y., Zhu, Y., Wang, X., Xu, Z., Chen, C., and Zhou, X. J. (2009b). Band-structure reorganization across the magnetic transition in $BaFe_2As_2$ seen via high-resolution angle-resolved photoemission. *Phys. Rev. B*, 80:134519.

Liu, X.-Y. (2017). Chapter 5 - High Pressure Synthesis and Preparation of Inorganic Materials. In Xu, R. and Xu, Y., editors, *Modern Inorganic Synthetic Chemistry (Second Edition)*, pages 105–141. Elsevier, Amsterdam.

Liu, Y., Liu, Y.-B., Tang, Z.-T., Jiang, H., Wang, Z.-C., Ablimit, A., Jiao, W.-H., Tao, Q., Feng, C.-M., Xu, Z.-A., and Cao, G.-H. (2016). Superconductivity and ferromagnetism in hole-doped $RbEuFe_4As_4$. *Phys. Rev. B*, 93:214503.

Liu, Y., Liu, Y.-B., Yu, Y.-L., Tao, Q., Feng, C.-M., and Cao, G.-H. (2017). $RbEu(Fe_{1-x}Ni_x)_4As_4$: From a ferromagnetic superconductor to a superconducting ferromagnet. *Phys. Rev. B*, 96:224510.

London, F. and London, H. (1935). Supraleitung und diamagnetismus. *Physica*, 2(1):341–354.

London, F., London, H., and Lindemann, F. A. (1935). The electromagnetic equations of the supraconductor. *Proceedings of the Royal Society of London. Series A - Mathematical and Physical Sciences*, 149(866):71–88.

Lorenz, B. and Chu, C. W. (2005). High Pressure Effects on Superconductivity. In *Frontiers in Superconducting Materials*, pages 459–497. Springer Berlin Heidelberg, Berlin, Heidelberg.

Luo, H., Zhang, R., Laver, M., Yamani, Z., Wang, M., Lu, X., Wang, M., Chen, Y., Li, S., Chang, S., Lynn, J. W., and Dai, P. (2012). Coexistence and Competition of the Short-Range Incommensurate Antiferromagnetic Order with the Superconducting State of $BaFe_{2-x}Ni_xAs_2$. *Phys. Rev. Lett.*, 108(24):247002.

Machida, K. (1981). Spin Density Wave and Superconductivity in Highly Anisotropic Materials. *J. Phys. Soc. Jpn.*, 50(7):2195–2202.

Maeda, H., Tanaka, Y., Fukutomi, M., and Asano, T. (1988). A New High-TcOxide Superconductor without a Rare Earth Element. *Japanese Journal of Applied Physics*, 27(Part 2, No. 2):L209–L210.

Maiwald, J., Jeevan, H. S., and Gegenwart, P. (2012). Signatures of quantum criticality in hole-doped and chemically pressurized $EuFe_2As_2$ single crystals. *Phys. Rev. B*, 85:024511.

Manna, R. S., Wolf, B., de Souza, M., and Lang, M. (2012). High-resolution thermal expansion measurements under helium-gas pressure. *Review of Scientific Instruments*, 83(8):085111.

Mao, H.-K., Chen, B., Chen, J., Li, K., Lin, J.-F., Yang, W., and Zheng, H. (2016). Recent advances in high-pressure science and technology. *Matter and Radiation at Extremes*, 1(1):59–75.

Maple, M. B. (1968). The superconducting transition temperature of $La_{1-x}Gd_xAl_2$. *Physics Letters A*, 26(10):513–514.

Maple, M. B. (1970). Dependence of s-f exchange on atomic number in rare earth dialuminides. *Solid State Communications*, 8(22):1915–1917.

Maple, M. B. (1976). Superconductivity. *Applied physics*, 9(3):179–204.

Maple, M. B., Fertig, W. A., Mota, A. C., DeLong, L. E., Wohlleben, D., and Fitzgerald, R. (1972). The re-entrant superconducting-normal phase boundary of the Kondo system (La, Ce)Al_2. *Solid State Communications*, 11(6):829–834.

Mathur, N. D., Grosche, F. M., Julian, S. R., Walker, I. R., Freye, D. M., Haselwimmer, R. K. W., and Lonzarich, G. G. (1998). Magnetically mediated superconductivity in heavy fermion compounds. *Nature*, 394(6688):39–43.

Matsuura, K., Mizukami, Y., Arai, Y., Sugimura, Y., Maejima, N., Machida, A., Watanuki, T., Fukuda, T., Yajima, T., Hiroi, Z., Yip, K. Y., Chan, Y. C., Niu, Q., Hosoi, S., Ishida, K. andMukasa, K., Watashige, T., Kasahara, S., Cheng, J.-G., Goh, S. K., Matsuda, Y., Uwatoko, Y., and Shibauchi, T. (2017). Maximizing T_c by tuning nematicity and magnetism in $FeSe_{1-x}S_x$ superconductors. *arXiv:1704.02057*.

Matthias, B. T. and Hulm, J. K. (1952). A Search for New Superconducting Compounds. *Phys. Rev.*, 87:799–806.

Matthias, B. T., Suhl, H., and Corenzwit, E. (1958). Spin Exchange in Superconductors. *Phys. Rev. Lett.*, 1(3):92–94.

Mazin, I. I. (2010). Superconductivity gets an iron boost. *Nature*, 464(7286):183–186.

McMillan, W. L. (1968). Transition Temperature of Strong-Coupled Superconductors. *Phys. Rev.*, 167(2):331–344.

McQueen, T. M., Williams, A. J., Stephens, P. W., Tao, J., Zhu, Y., Ksenofontov, V., Casper, F., Felser, C., and Cava, R. J. (2009). Tetragonal-to-Orthorhombic Structural Phase Transition at 90 K in the Superconductor $Fe_{1.01}Se$. *Phys. Rev. Lett.*, 103:057002.

Meier, W. R., Ding, Q.-P., Kreyssig, A., Bud'ko, S. L., Sapkota, A., Kothapalli, K., Borisov, V., Valentí, R., Batista, C. D., Orth, P. P., Fernandes, R. M., Goldman, A. I., Furukawa, Y., Böhmer, A. E., and Canfield, P. C. (2018). Hedgehog spin-vortex crystal stabilized in a hole-doped iron-based superconductor. *npj Quantum Materials*, 3(1):5.

Meier, W. R., Kong, T., Bud'ko, S. L., and Canfield, P. C. (2017). Optimization of the crystal growth of the superconductor $CaKFe_4As_4$ from solution in the $FeAs{-}CaFe_2As_2{-}KFe_2As_2$ system. *Phys. Rev. Materials*, 1:013401.

Meier, W. R., Kong, T., Kaluarachchi, U. S., Taufour, V., Jo, N. H., Drachuck, G., Böhmer, A. E., Saunders, S. M., Sapkota, A., Kreyssig, A., Tanatar, M. A., Prozorov, R., Goldman, A. I., Balakirev, F. F., Gurevich, A., Bud'ko, S. L., and Canfield, P. C. (2016). Anisotropic thermodynamic and transport properties of single-crystalline $CaKFe_4As_4$. *Phys. Rev. B*, 94:064501.

Meissner, W. and Ochsenfeld, R. (1933). Ein neuer Effekt bei Eintritt der Supraleitfähigkeit. *Naturwissenschaften*, 21(44):787–788.

Millis, A. J. (1993). Effect of a nonzero temperature on quantum critical points in itinerant fermion systems. *Phys. Rev. B*, 48(10):7183–7196.

Miyoshi, K. (2014). Enhanced Superconductivity on the Tetragonal Lattice in FeSe under Hydrostatic Pressure. *J. Phys. Soc. Jpn.*, 83(1):013702.

Mizoguchi, H., Matsuishi, S., Hirano, M., Tachibana, M., Takayama-Muromachi, E., Kawaji, H., and Hosono, H. (2011). Coexistence of Light and Heavy Carriers Associated with Superconductivity and Antiferromagnetism in $CeNi_{0.8}Bi_2$ with a Bi Square Net. *Phys. Rev. Lett.*, 106(5):057002.

Mizuguchi, Y., Tomioka, F., Tsuda, S., Yamaguchi, T., and Takano, Y. (2009). Substitution Effects on FeSe Superconductor. *J. Phys. Soc. Jpn.*, 78(7):074712.

Moriya, T. (1985). *Spin Fluctuations in Itinerant Electron Magnetism*. Springer-Verlag Berlin Heidelberg.

Mou, D., Kong, T., Meier, W. R., Lochner, F., Wang, L.-L., Lin, Q., Wu, Y., Bud'ko, S. L., Eremin, I., Johnson, D. D., Canfield, P. C., and Kaminski, A. (2016). Enhancement of the Superconducting Gap by Nesting in $CaKFe_4As_4$: A New High Temperature Superconductor. *Phys. Rev. Lett.*, 117:277001.

Munevar, J., Micklitz, H., Agüero, J., Tan, G., Zhang, C., Dai, P., and Baggio-Saitovitch, E. (2013). Superconductivity and antiferromagnetism in $Ba_{0.75}K_{0.25}Fe_2As_2$ single crystals as seen by ^{57}Fe Mössbauer spectroscopy. *Phys. Rev. B*, 88(18):184514.

Muramatsu, T., Tateiwa, N., Kobayashi, T., Shimizu, K., Amaya, K., Aoki, D., Shishido, H., Haga, Y., and Ōnuki, Y. (2001). Superconductivity of $CeRhIn_5$ under High Pressure. *J. Phys. Soc. Jpn.*, 70(11):3362–3367.

Nandi, S., Kim, M. G., Kreyssig, A., Fernandes, R. M., Pratt, D. K., Thaler, A., Ni, N., Bud'ko, S. L., Canfield, P. C., Schmalian, J., McQueeney, R. J., and Goldman, A. I. (2010). Anomalous Suppression of the Orthorhombic Lattice Distortion in Superconducting $Ba(Fe_{1-x}Co_x)_2As_2$ Single Crystals. *Phys. Rev. Lett.*, 104:057006.

Nereson, N. and Arnold, G. (1971). Magnetic Properties of CeBi, NdBi, TbBi, and DyBi. *Journal of Applied Physics*, 42(4):1625–1627.

Ni, N. and Bud'ko, S. L. (2011). Tuning the ground state of $BaFe_2As_2$: Phase diagrams and empirical trends. *MRS Bulletin*, 36(8):620–625.

Nicklas, M., Borth, R., Lengyel, E., Pagliuso, P. G., Sarrao, J. L., Sidorov, V. A., Sparn, G., Steglich, F., and Thompson, J. D. (2001). Response of the heavy-fermion superconductor CeCoIn5 to pressure: roles of dimensionality and proximity to a quantum-critical point. *Journal of Physics: Condensed Matter*, 13(44):L905–L912.

Nicklas, M., Sidorov, V. A., Borges, H. A., Pagliuso, P. G., Petrovic, C., Fisk, Z., Sarrao, J. L., and Thompson, J. D. (2003). Magnetism and superconductivity in Ce_2RhIn_8. *Phys. Rev. B*, 67:020506(R).

Niklowitz, P. G., Beckers, F., Lonzarich, G. G., Knebel, G., Salce, B., Thomasson, J., Bernhoeft, N., Braithwaite, D., and Flouquet, J. (2005). Spin-fluctuation-dominated electrical transport of Ni_3Al at high pressure. *Phys. Rev. B*, 72(2):024424.

Niklowitz, P. G., Hirschberger, M., Lucas, M., Cermak, P., Schneidewind, A., Faulhaber, E., Mignot, J.-M., Duncan, W. J., Neubauer, A., Pfleiderer, C., and Grosche, F. M. (2019). Ultrasmall Moment Incommensurate Spin Density Wave Order Masking a Ferromagnetic Quantum Critical Point in $NbFe_2$. *Phys. Rev. Lett.*, 123(24):247203.

Nowik, I., Felner, I., Ren, Z., Cao, G. H., and Xu, Z. A. (2011). Coexistence of ferromagnetism and superconductivity: magnetization and Mössbauer studies of $EuFe_2(As_{1-x}P_x)_2$. *Journal of Physics: Condensed Matter*, 23(6):065701.

O'Halloran, J., Agterberg, D. F., Chen, M. X., and Weinert, M. (2017). Stabilizing the spin vortex crystal phase in two-dimensional iron-based superconductors. *Phys. Rev. B*, 95:075104.

Onnes, H. K. (1911). The resistance of pure mercury at helium temperatures. *Commun. Phys. Lab. Univ. Leiden*, 12.

Ovchenkov, Y. A., Chareev, D. A., Presnov, D. E., Volkova, O. S., and Vasiliev, A. N. (2016). Superconducting Properties of $FeSe_{1-x}S_x$ Crystals for x up to 0.19. *J. Low Temp. Phys.*, 185(5):467–473.

Ozaki, M.-a. and Machida, K. (1989). Superconducting classes of heavy-fermion materials. *Phys. Rev. B*, 39(7):4145–4163.

Paglione, J. and Greene, R. L. (2010). High-temperature superconductivity in iron-based materials. *Nat Phys*, 6(9):645–658.

Park, T., Ronning, F., Yuan, H. Q., Salamon, M. B., Movshovich, R., Sarrao, J. L., and Thompson, J. D. (2006). Hidden magnetism and quantum criticality in the heavy fermion superconductor $CeRhIn_5$. *Nature*, 440(7080):65–68.

Pedder, C. J., Krüger, F., and Green, A. G. (2013). Resummation of fluctuations near ferromagnetic quantum critical points. *Phys. Rev. B*, 88(16):165109.

Petrovic, C., Bud'ko, S. L., and Canfield, P. C. (2002). Anisotropic properties of rare-earth dibismites. *Journal of Magnetism and Magnetic Materials*, 247(3):270–278.

Petrovic, C., Pagliuso, P. G., Hundley, M. F., Movshovich, R., Sarrao, J. L., Thompson, J. D., Fisk, Z., and Monthoux, P. (2001). Heavy-fermion superconductivity in $CeCoIn_5$ at 2.3 K. *Journal of Physics: Condensed Matter*, 13(17):L337–L342.

Pfleiderer, C. and Huxley, A. D. (2002). Pressure Dependence of the Magnetization in the Ferromagnetic Superconductor UGe_2. *Phys. Rev. Lett.*, 89(14):147005.

Pfleiderer, C., Uhlarz, M., Hayden, S. M., Vollmer, R., Löhneysen, H. v., Bernhoeft, N. R., and Lonzarich, G. G. (2001). Coexistence of superconductivity and ferromagnetism in the d-band metal $ZrZn_2$. *Nature*, 412:58.

Piermarini, G. J., Block, S., Barnett, J. D., and Forman, R. A. (1975). Calibration of the pressure dependence of the R1 ruby fluorescence line to 195 kbar. *Journal of Applied Physics*, 46(6):2774–2780.

Pinceaux, J.-P., Maury, J.-P., and Besson, J.-M. (1979). Solidification of helium, at room temperature under high pressure. *J. Physique Lett.*, 40(13):307–308.

Pratt, D. K., Tian, W., Kreyssig, A., Zarestky, J. L., Nandi, S., Ni, N., Bud'ko, S. L., Canfield, P. C., Goldman, A. I., and McQueeney, R. J. (2009). Coexistence of Competing Antiferromagnetic and Superconducting Phases in the Underdoped $Ba(Fe_{0.953}Co_{0.047})_2As_2$ Compound Using X-ray and Neutron Scattering Techniques. *Phys. Rev. Lett.*, 103:087001.

Putzke, C., Walmsley, P., Fletcher, J. D., Malone, L., Vignolles, D., Proust, C., Badoux, S., See, P., Beere, H. E., Ritchie, D. A., Kasahara, S., Mizukami, Y., Shibauchi, T., Matsuda, Y., and Carrington, A. (2014). Anomalous critical fields in quantum critical superconductors. *Nat. Commun.*, 5:5679.

Qi, X.-L. and Zhang, S.-C. (2011). Topological insulators and superconductors. *Rev. Mod. Phys.*, 83:1057–1110.

Ramadana, A., Gouldb, R., and shoura, A. (1994). On the Van der Pauw method of resistivity measurements. *Thin Solid Films*, 239:2.

Ran, S., Bud'ko, S. L., Straszheim, W. E., Soh, J., Kim, M. G., Kreyssig, A., Goldman, A. I., and Canfield, P. C. (2012). Control of magnetic, nonmagnetic, and superconducting states in annealed $Ca(Fe_{1-x}Co_x)_2As_2$. *Phys. Rev. B*, 85(22):224528.

Rana, K., Xiang, L., Wiecki, P., Ribeiro, R. A., Lesseux, G. G., Böhmer, A. E., Bud'ko, S. L., Canfield, P. C., and Furukawa, Y. (2020). Impact of nematicity on the relationship between antiferromagnetic fluctuations and superconductivity in $FeSe_{0.91}S_{0.09}$ under pressure. *Phys. Rev. B*, 101(18):180503.

Rein, C. (1993). The pressure-temperature dependence of the electrical resistance of Zeranin in the temperature range 160-370 K and at pressures up to 1 GPa. *Measurement Science and Technology*, 4(11):1194–1200.

Ren, Z. A., Che, G. C., Dong, X. L., Yang, J., Lu, W., Yi, W., Shen, X. L., Li, Z. C., Sun, L. L., Zhou, F., and Zhao, Z. X. (2008). Superconductivity and phase diagram in iron-based arsenic-oxides ReFeAsO1-δ (Re = rare-earth metal) without fluorine doping. *EPL (Europhysics Letters)*, 83(1):17002.

Rüetschi, A.-S. and Jaccard, D. (2007). Adaptation of the Bridgman anvil cell to liquid pressure mediums. *Review of Scientific Instruments*, 78(12):123901.

Roberts, B. W. (1976). Survey of superconductive materials and critical evaluation of selected properties. *Journal of Physical and Chemical Reference Data*, 5(3):581–822.

Rotter, M., Tegel, M., and Johrendt, D. (2008). Superconductivity at 38 K in the Iron Arsenide $(Ba_{1-x}K_x)Fe_2As_2$. *Phys. Rev. Lett.*, 101:107006.

Ruderman, M. A. and Kittel, C. (1954). Indirect Exchange Coupling of Nuclear Magnetic Moments by Conduction Electrons. *Phys. Rev.*, 96:99–102.

Sachdev, S. (2000). Quantum Criticality: Competing Ground States in Low Dimensions. *Science*, 288(5465):475.

Sachdev, S. (2011). *Quantum Phase Transitions*. Cambridge University Press, Cambridge, 2 edition.

Sachdev, S. and Keimer, B. (2011). Quantum criticality. *Physics Today*, 64(2):29–35.

Sambongi, T. (1971). Superconductivity of LiBi. *J. Phys. Soc. Jpn.*, 30(1):294–294.

Saunders, S. M., Xiang, L., Khasanov, R., Kong, T., Lin, Q., Bud'ko, S. L., and Canfield, P. C. (2020). Exceedingly small moment itinerant ferromagnetism of single crystalline $La_5Co_2Ge_3$. *Phys. Rev. B*, 101(21):214405.

Saxena, S. S., Agarwal, P., Ahilan, K., Grosche, F. M., Haselwimmer, R. K. W., Steiner, M. J., Pugh, E., Walker, I. R., Julian, S. R., Monthoux, P., Lonzarich, G. G., Huxley, A., Sheikin, I., Braithwaite, D., and Flouquet, J. (2000). Superconductivity on the border of itinerant-electron ferromagnetism in UGe_2. *Nature*, 406:587.

Schilling, A., Cantoni, M., Guo, J. D., and Ott, H. R. (1993). Superconductivity above 130 K in the Hg-Ba-Ca-Cu-O system. *Nature*, 363(6424):56–58.

Schilling, J. S. (1979). Pressure as a parameter in the study of dilute magnetic alloys. *Advances in Physics*, 28(5):657–715.

SEIDEN, P. E. (1969). Pressure Dependence of the Superconducting Transition Temperature. *Phys. Rev.*, 179(2):458–462.

Shao, D. F., Luo, X., Lu, W. J., Hu, L., Zhu, X. D., Song, W. H., Zhu, X. B., and Sun, Y. P. (2016). Spin-orbit coupling enhanced superconductivity in Bi-rich compounds ABi_3 (A=Sr and Ba). *Scientific Reports*, 6:21484.

Sheng, Z. Z. and Hermann, A. M. (1988). Bulk superconductivity at 120 K in the Tl-Ca/Ba-Cu-O system. *Nature*, 332(6160):138–139.

Shibauchi, T., Carrington, A., and Matsuda, Y. (2014). A Quantum Critical Point Lying Beneath the Superconducting Dome in Iron Pnictides. *Annu. Rev. Condens. Matter Phys.*, 5(1):113–135.

Shrivastava, K. N. and Sinha, K. P. (1984). Magnetic superconductors: Model theories and experimental properties of rare-earth compounds. *Physics Reports*, 115(3):93–149.

Smit, W. A. and Vertogen, G. (1973). Coexistence of superconductivity and magnetism. *Physics Letters A*, 43(5):455–456.

Smith, F. A., Bradley, C. C., and Bacon, G. E. (1966). A neutron diffraction investigation of Au2Mn under pressure. *Journal of Physics and Chemistry of Solids*, 27(6):925–930.

Smith, T. F. (1972). Pressure dependence of the superconducting transition temperature for vanadium. *Journal of Physics F: Metal Physics*, 2(5):946–956.

Smith, T. F. and Chu, C. W. (1967). Will Pressure Destroy Superconductivity? *PR*, 159(2):353–358.

Smith, T. F., Chu, C. W., and Maple, M. B. (1969). Superconducting manometers for high pressure measurement at low temperature. *Cryogenics*, 9(1):53–56.

Smylie, M. P., Willa, K., Bao, J.-K., Ryan, K., Islam, Z., Claus, H., Simsek, Y., Diao, Z., Rydh, A., Koshelev, A. E., Kwok, W.-K., Chung, D. Y., Kanatzidis, M. G., and Welp, U. (2018). Anisotropic superconductivity and magnetism in single-crystal $RbEuFe_4As_4$. *Phys. Rev. B*, 98:104503.

Sondhi, S. L., Girvin, S. M., Carini, J. P., and Shahar, D. (1997). Continuous quantum phase transitions. *Rev. Mod. Phys.*, 69(1):315–333.

Steglich, F., Aarts, J., Bredl, C. D., Lieke, W., Meschede, D., Franz, W., and Schäfer, H. (1979). Superconductivity in the Presence of Strong Pauli Paramagnetism: $CeCu_2Si_2$. *Phys. Rev. Lett.*, 43(25):1892–1896.

Steglich, F. and Wirth, S. (2016). Foundations of heavy-fermion superconductivity: lattice Kondo effect and Mott physics. *Reports on Progress in Physics*, 79(8):084502.

Stolyarov, V. S., Casano, A., Belyanchikov, M. A., Astrakhantseva, A. S., Grebenchuk, S. Y., Baranov, D. S., Golovchanskiy, I. A., Voloshenko, I., Zhukova, E. S., Gorshunov, B. P., Muratov, A. V., Dremov, V. V., Vinnikov, L. Y., Roditchev, D., Liu, Y., Cao, G.-H., Dressel, M., and Uykur, E. (2018). Unique interplay between superconducting and ferromagnetic orders in $EuRbFe_4As_4$. *Phys. Rev. B*, 98:140506.

Suhl, H. and Matthias, B. T. (1959). Impurity Scattering in Superconductors. *Phys. Rev.*, 114(4):977–988.

Sun, J. P., Matsuura, K., Ye, G. Z., Mizukami, Y., Shimozawa, M., Matsubayashi, K., Yamashita, M., Watashige, T., Kasahara, S., Matsuda, Y., Yan, J. Q., Sales, B. C., Uwatoko, Y., Cheng, J. G., and Shibauchi, T. (2016). Dome-shaped magnetic order competing with high-temperature superconductivity at high pressures in FeSe. *Nat. Commun.*, 7:12146.

Sun, J. P., Ye, G. Z., Shahi, P., Yan, J.-Q., Matsuura, K., Kontani, H., Zhang, G. M., Zhou, Q., Sales, B. C., Shibauchi, T., Uwatoko, Y., Singh, D. J., and Cheng, J.-G. (2017). High-T_c Superconductivity in FeSe at High Pressure: Dominant Hole Carriers and Enhanced Spin Fluctuations. *Phys. Rev. Lett.*, 118:147004.

Swenson, C. A. (1997). Linear thermal expansivity (1.5-300 K) and heat capacity (1.2-90 K) of Stycast 2850FT. *Review of Scientific Instruments*, 68(2):1312–1315.

Takahashi, H., Igawa, K., Arii, K., Kamihara, Y., Hirano, M., and Hosono, H. (2008). Superconductivity at 43K in an iron-based layered compound $LaO_{1-x}F_xFeAs$. *Nature*, 453:376.

Tanatar, M. A., Böhmer, A. E., Timmons, E. I., Schütt, M., Drachuck, G., Taufour, V., Kothapalli, K., Kreyssig, A., Bud'ko, S. L., Canfield, P. C., Fernandes, R. M., and Prozorov, R. (2016). Origin of the Resistivity Anisotropy in the Nematic Phase of FeSe. *Phys. Rev. Lett.*, 117:127001.

Tanatar, M. A., Ni, N., Samolyuk, G. D., Bud'ko, S. L., Canfield, P. C., and Prozorov, R. (2009). Resistivity anisotropy of AFe_2As_2 ($A = Ca$, Sr, Ba): Direct versus Montgomery technique measurements. *Phys. Rev. B*, 79:134528.

Tateiwa, N., Kobayashi, T. C., Hanazono, K., Amaya, K., Haga, Y., Settai, R., and Onuki, Y. (2000). Pressure-induced superconductivity in a ferromagnet UGe_2. *Journal of Physics: Condensed Matter*, 13(1):L17–L23.

Taufour, V., Foroozani, N., Tanatar, M. A., Lim, J., Kaluarachchi, U., Kim, S. K., Liu, Y., Lograsso, T. A., Kogan, V. G., Prozorov, R., Bud'ko, S. L., Schilling, J. S., and Canfield, P. C. (2014). Upper critical field of KFe_2As_2 under pressure: A test for the change in the superconducting gap structure. *Phys. Rev. B*, 89:220509.

Taufour, V., Kaluarachchi, U. S., Khasanov, R., Nguyen, M. C., Guguchia, Z., Biswas, P. K., Bonfà, P., De Renzi, R., Lin, X., Kim, S. K., Mun, E. D., Kim, H., Furukawa, Y., Wang, C.-Z., Ho, K.-M., Bud'ko, S. L., and Canfield, P. C. (2016). Ferromagnetic Quantum Critical Point Avoided by the Appearance of Another Magnetic Phase in $LaCrGe_3$ under Pressure. *Phys. Rev. Lett.*, 117:037207.

Taufour, V., Thimmaiah, S., March, S., Saunders, S., Sun, K., Lamichhane, T. N., Kramer, M. J., Bud'ko, S. L., and Canfield, P. C. (2015). Structural and Ferromagnetic Properties of an Orthorhombic Phase of MnBi Stabilized with Rh Additions. *Phys. Rev. Applied*, 4:014021.

Tencé, S., Janson, O., Krellner, C., Rosner, H., Schwarz, U., Grin, Y., and Steglich, F. (2014). $CoBi_3$-the first binary compound of cobalt with bismuth: high-pressure synthesis and superconductivity. *Journal of Physics: Condensed Matter*, 26(39):395701.

Terashima, T., Kikugawa, N., Kasahara, S., Watashige, T., Shibauchi, T., Matsuda, Y., Wolf, T., Böhmer, A. E., Hardy, F., Meingast, C., v. Löhneysen, H., and Uji, S. (2015). Pressure-Induced Antiferromagnetic Transition and Phase Diagram in FeSe. *J. Phys. Soc. Jpn.*, 84(6):063701.

Terashima, T., Kikugawa, N., Kiswandhi, A., Graf, D., Choi, E.-S., Brooks, J. S., Kasahara, S., Watashige, T., Matsuda, Y., Shibauchi, T., Wolf, T., Böhmer, A. E., Hardy, F., Meingast, C., Löhneysen, H. v., and Uji, S. (2016). Fermi surface reconstruction in FeSe under high pressure. *Phys. Rev. B*, 93:094505.

Thaler, A., Ni, N., Kracher, A., Yan, J. Q., Bud'ko, S. L., and Canfield, P. C. (2010). Physical and magnetic properties of $Ba(Fe_{1-x}Ru_x)_2As_2$ single crystals. *Phys. Rev. B*, 82:014534.

Thamizhavel, A., Galatanu, A., Yamamoto, E., Okubo, T., Yamada, M., Tabata, K., C Kobayashi, T., Nakamura, N., Sugiyama, K., Kindo, K., Takeuchi, T., Settai, R., and Ōnuki, Y. (2003). Low Temperature Magnetic Properties of $CeTBi_2$ (T: Ni, Cu and Ag) Single Crystals. *J. Phys. Soc. Jpn.*, 72(10):2632–2639.

Thompson, J. D. (1984). Low-temperature pressure variations in a self-clamping pressure cell. *Review of Scientific Instruments*, 55:231.

Thompson, J. D. and Lawrence, J. M. (1994). Chapter 133 High pressure studies – physical properties of anomalous Ce, Yb and U compounds. In *Handbook on the Physics and Chemistry of Rare Earths*, volume 19, pages 383–478. Elsevier.

Torikachvili, M. S., Bud'ko, S. L., Ni, N., and Canfield, P. C. (2008a). Effect of pressure on the structural phase transition and superconductivity in $(Ba_{1-x}K_x)Fe_2As_2$ ($x = 0$ and 0.45) and $SrFe_2As_2$ single crystals. *Phys. Rev. B*, 78:104527.

Torikachvili, M. S., Bud'ko, S. L., Ni, N., and Canfield, P. C. (2008b). Pressure Induced Superconductivity in $CaFe_2As_2$. *Phys. Rev. Lett.*, 101:057006.

Torikachvili, M. S., Kim, S. K., Colombier, E., Bud'ko, S. L., and Canfield, P. C. (2015). Solidification and loss of hydrostaticity in liquid media used for pressure measurements. *Rev. Sci. Instrum.*, 86:123904.

Uhlarz, M., Pfleiderer, C., and Hayden, S. M. (2004). Quantum Phase Transitions in the Itinerant Ferromagnet $ZrZn_2$. *Phys. Rev. Lett.*, 93(25):256404.

Umeo, K., Kadomatsu, H., and Takabatake, T. (1996). Transition from magnetic to nonmagnetic ground state in a heavy-fermion compound Ce_7Ni_3 under high pressure. *Phys. Rev. B*, 54(2):1194–1198.

van der Pauw, L. (1958). A method of measuring the resistivity and Hall coefficient on lamellae of arbitrary shape. *Philips Research Reports*, 20:220.

Ventura G., P. M. (2014). *Thermal Properties of Solids at Room and Cryogenic Temperatures*, chapter Data of Thermal Expansion, pages 121–127. Springer, Dordrecht.

Vojta, M. (2003). Quantum phase transitions. *Reports on Progress in Physics*, 66(12):2069–2110.

Walker, I. R., Grosche, F. M., Freye, D. M., and Lonzarich, G. G. (1997). The normal and superconducting states of $CeIn_3$ near the border of antiferromagnetic order. *Materials and Mechanisms of Superconductivity High Temperature Superconductors V*, 282-287:303–306.

Wang, C. (1967). Electrical Resistance of Manganin Coil to 7 kbar and 200°C. *Review of Scientific Instruments*, 38(1):24–26.

Wang, F., Kivelson, S. A., and Lee, D.-H. (2015). Nematicity and quantum paramagnetism in FeSe. *Nat Phys*, 11(11):959–963.

Wang, Z., Hu, W.-J., and Nevidomskyy, A. H. (2016). Spin Ferroquadrupolar Order in the Nematic Phase of FeSe. *Phys. Rev. Lett.*, 116:247203.

Watson, M. D., Kim, T. K., Haghighirad, A. A., Blake, S. F., Davies, N. R., Hoesch, M., Wolf, T., and Coldea, A. I. (2015a). Suppression of orbital ordering by chemical pressure in $FeSe_{1-x}S_x$. *Phys. Rev. B*, 92:121108.

Watson, M. D., Kim, T. K., Haghighirad, A. A., Davies, N. R., McCollam, A., Narayanan, A., Blake, S. F., Chen, Y. L., Ghannadzadeh, S., Schofield, A. J., Hoesch, M., Meingast, C., Wolf, T., and Coldea, A. I. (2015b). Emergence of the nematic electronic state in FeSe. *Phys. Rev. B*, 91:155106.

Wentorf, R. H. (1967). Modern very-high-pressure research. *British Journal of Applied Physics*, 18(7):865–882.

Werthamer, N. R., Helfand, E., and Hohenberg, P. C. (1966). Temperature and Purity Dependence of the Superconducting Critical Field, H_{c2}. III. Electron Spin and Spin-Orbit Effects. *Phys. Rev.*, 147(1):295–302.

Wiegmann, P. B. (1981). Exact solution of the s-d exchange model (Kondo problem). *Journal of Physics C: Solid State Physics*, 14(10):1463–1478.

Wilhelm, H., Alami-Yadri, K., Revaz, B., and Jaccard, D. (1999). Detailed investigation of the magnetic phase diagram of $CeRu_2Ge_2$ up to 11 GPa. *Phys. Rev. B*, 59(5):3651–3660.

Wilson, K. G. (1975). The renormalization group: Critical phenomena and the Kondo problem. *Rev. Mod. Phys.*, 47(4):773–840.

Winiarski, M. J., Wiendlocha, B., Gołab, S., Kushwaha, S. K., Wiśniewski, P., Kaczorowski, D., Thompson, J. D., Cava, R. J., and Klimczuk, T. (2016). Superconductivity in $CaBi_2$. *Phys. Chem. Chem. Phys.*, 18(31):21737–21745.

Wittig, J., Probst, C., Schmidt, F. A., and Gschneidner, K. A. (1979). Superconductivity in a New High-Pressure Phase of Scandium. *Phys. Rev. Lett.*, 42(7):469–472.

Xia, Y., Qian, D., Hsieh, D., Wray, L., Pal, A., Lin, H., Bansil, A., Grauer, D., Hor, Y. S., Cava, R. J., and Hasan, M. Z. (2009). Observation of a large-gap topological-insulator class with a single Dirac cone on the surface. *Nature Physics*, 5:398.

Xiang, L., Bud'ko, S. L., Bao, J.-K., Chung, D. Y., Kanatzidis, M. G., and Canfield, P. C. (2019a). Pressure-temperature phase diagram of the $EuRbFe_4As_4$ superconductor. *Phys. Rev. B*, 99(14):144509.

Xiang, L., Gati, E., Bud'ko, S. L., Ribeiro, R. A., Ata, A., Tutsch, U., Lang, M., and Canfield, P. C. (2020a). Characterization of the pressure coefficient of manganin and temperature evolution of pressure in piston-cylinder cells. *Review of Scientific Instruments*, 91(9):095103.

Xiang, L., Gati, E., Neilson, K., Bud'ko, S. L., and Canfield, P. C. (2019b). Physical properties of $R\mathrm{Bi}_2$ ($R = \mathrm{La}, \mathrm{Ce}$) under pressure. *Phys. Rev. Materials*, 3(9):095006.

Xiang, L., Kaluarachchi, U. S., Böhmer, A. E., Taufour, V., Tanatar, M. A., Prozorov, R., Bud'ko, S. L., and Canfield, P. C. (2017). Dome of magnetic order inside the nematic phase of sulfur-substituted FeSe under pressure. *Phys. Rev. B*, 96:024511.

Xiang, L., Meier, W. R., Xu, M., Kaluarachchi, U. S., Bud'ko, S. L., and Canfield, P. C. (2018a). Pressure-temperature phase diagrams of $CaK(\mathrm{Fe}_{1-x}\mathrm{Ni}_x)_4\mathrm{As}_4$ superconductors. *Phys. Rev. B*, 97:174517.

Xiang, L., Ribeiro, R. A., Kaluarachchi, U. S., Gati, E., Nguyen, M. C., Wang, C.-Z., Ho, K.-M., Bud'ko, S. L., and Canfield, P. C. (2018b). Pressure-induced multiple phase transformations of the $BaBi_3$ superconductor. *Phys. Rev. B*, 98(21):214509.

Xiang, L., Ryan, D. H., Straszheim, W. E., Canfield, P. C., and Bud'ko, S. L. (2020b). Tuning of charge density wave transitions in $LaAu_xSb_2$ by pressure and Au stoichiometry. *Phys. Rev. B*, 102(12):125110.

Yokogawa, K., Murata, K., Yoshino, H., and Aoyama, S. (2007). Solidification of High-Pressure Medium Daphne 7373. *Japanese Journal of Applied Physics*, 46(6R):3636.

Yosida, K. (1957). Magnetic Properties of Cu-Mn Alloys. *Phys. Rev.*, 106:893–898.

Yu, G., Li, Y., Motoyama, E. M., and Greven, M. (2009a). A universal relationship between magnetic resonance and superconducting gap in unconventional superconductors. *Nature Physics*, 5:873.

Yu, R. and Si, Q. (2015). Antiferroquadrupolar and Ising-Nematic Orders of a Frustrated Bilinear-Biquadratic Heisenberg Model and Implications for the Magnetism of FeSe. *Phys. Rev. Lett.*, 115:116401.

Yu, W., Aczel, A. A., Williams, T. J., Bud'ko, S. L., Ni, N., Canfield, P. C., and Luke, G. M. (2009b). Absence of superconductivity in single-phase $CaFe_2As_2$ under hydrostatic pressure. *Phys. Rev. B*, 79:020511.

Zeto, R. J. and Vanfleet, H. B. (1969). Pressure Calibration to 60 kbar Based on the Resistance Change of a Manganin Coil under Hydrostatic Pressure. *Journal of Applied Physics*, 40(5):2227–2231.

Zhou, W., Xu, C. Q., Li, B., Sankar, R., Zhang, F. M., Qian, B., Cao, C., Dai, J. H., Lu, J., Jiang, W. X., Qian, D., and Xu, X. (2018). Kondo behavior and metamagnetic phase transition in the heavy-fermion compound $\mathbf{CeBi_2}$. *Phys. Rev. B*, 97:195120.

https://www.qdusa.com/sitedocs/productBrochures/High_Pressure_Cell_for_Magnetometry_Brochure.pdf.

https://www.unipress.waw.pl/.

https://www.ceramics.net/ceramic-materials-solutions/silicates/lava-grade-a.

https://www.betsa.fr/accessories.html.

https://advancedabrasives.com/index.cfm?page=sap-cbn-powder#:~:text=Superabrasive%20Powders-,cBNP%20Cubic%20Boron%20Nitride%20Powder,ideal%20for%20high%20temperature%20applications.

https://www.alfa.com/en/catalog/A11662/.

APPENDIX A. ASSEMBLING THE PISTON-CYLINDER CELL

The piston-cylinder cell (PCC) is one the most commonly used pressure cells in high pressure research. The PCC used for my research has a maximum pressure of ~ 2.5 GPa and is typically used for electrical transport measurements. The schematic diagram and various individual components are shown in Fig. 2.1. In the following, a detailed description of the assembling process is provided.

Step 1: Preparing the feed-through The feed-through is one of the most complex and potentially fragile parts of the PCC, it allows for the electrical connection with the specimen and the manometer inside the sample area. As such, the feed-through can have a pressure difference of up to 2.5 GPa across it and, simultaneously have up to a dozen or more insulated wires passing through it. To clean a feed-through from a previous usage in case a leak or broken wires were observed, the Stycast needs to be completely removed with the help of the Epoxy Stripping Agent (the stripping agent contains Methylene Chloride, Formic Acid and Phenol, see Fig. A.1 (a)). Put the feed-through inside a glass beaker and pour in enough agent so that the feed-through is submerged. The agent will slowly etch/soften the Stycast. The glass beaker can be put into an ultrasonic cleaner to speed up the etching/softening process. From time to time take out the feed-through and use a needle to poke the Stycast so that the underneath Stycast can be etched/softened. Refill or exchange the agent as needed if the etching/softening process is too slow. Eventually the needle can poke all the way through the hole of the feed-though. Then the feed-through is further put back into the agent to make sure that Stycast is completely removed. For the last step, clean the feed-through with ethanol. Note that when handling the agent, chemical gloves should be worn.

With the cleaned feed-through (Figs. A.2 (a) and (b)), we now refill the hole with new Stycast and Cu wires passing through the hole. The exact number of Cu wires can be adjusted

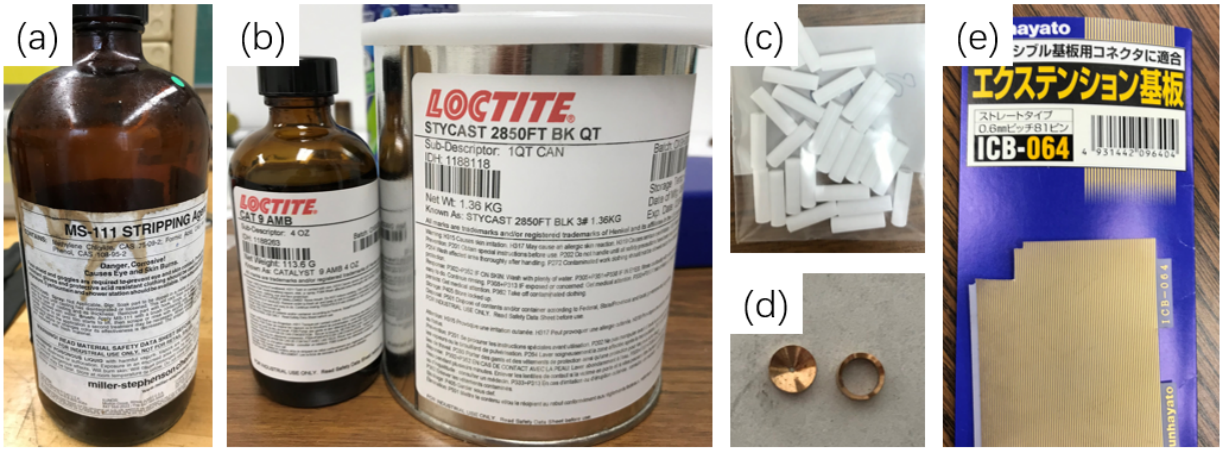

Figure A.1 Various objects that are used when assembling a PCC. (a) The MS-111 Epoxy Stripping Agent (stripping agent contains Methylene Chloride, Formic Acid and Phenol) that is used to remove the Stycast. (b) Stycast 2850 FT BK and Catalyst 9 that are used to make new Stycast mixture. (c) Teflon cups (machined by Ames Laboratory machine shop) that are used to contain pressure transimitting medium. (d) Top (left) and bottom (right) anti-extrusion rings (machined by Ames Laboratory machine shop). (e) The plastic/metal strip sheet (metal strip spacing 0.6 mm) that is used to make specimen and manometer stages.

according the desired measurements (gauge sizes #34, #36 and #38 Cu wires are often used). In the case of measuring standard four-terminal resistance of one specimen, a typical number of ten Cu wires are used (four for specimen, four for the Pb manometer and two for backup). A maximum number of twenty Cu wires (gauge sizes #45) were used for a particularly designed set up which enables elastoresistance measurements under pressure (See Ref. Gati et al. (2020b) for details). With all the Cu wires passing through the hole, they should be able to move freely without much friction against the inside wall of the hole. Next, prepare the Stycast. Stycast 2850FT BK is mixed with Catalyst 9 (Fig. A.1 (b)) in the ratio of 100 : 3.5 by weight. Apply some amount of the Stycast mixture to the top side of the feed-though. Slowly move the Cu wires up and down with a small "amplitude" while dragging down the Cu wires so that the Stycast flows inside the hole. Re-apply Stycast on top of the feed-through as the Stycast flows in. Repeat this process until Stycast is seen on the Cu wires from the bottom side. Then the hole is completely filled with Stycast. Subsequently, tighten up the Cu wires from the top side of the feed-through with a thin bundle (the tightened part is buried inside the Stycast, a manganin wire with diameter $\sim 67 \mu$m or gauge #44 is often used for this purpose. After the Stycast is cured, the unburied part of the bundle is removed from the feed-through, see below for details). The purpose of this bundle is to keep the Cu wires from moving down due to gravity during the curing period the Stycast. With these, the Stycast is left overnight to cure completely (Figs. A.2 (c) and (d)).

Step 2: Preparing sample and manometer stages After the Stycast is cured, cut off the unburied part of manganin wire off the feed-through. Arrange the positions of the Cu wires and cut them to the proper length. Remove the insulating layer of the Cu wires on both ends. On top of the feed-through, the Cu wires are soldered to the specimen and Pb-manometer platforms (Figs. A.2 (e) and (f)). These platforms are cut from plastic sheets with evenly spaced metal strips (Fig. A.1 (e)) into dimension of around 2.0×1.5 mm^2. These platforms provide extra mechanical strength and soldering stages to connect Cu wires with contact leads.

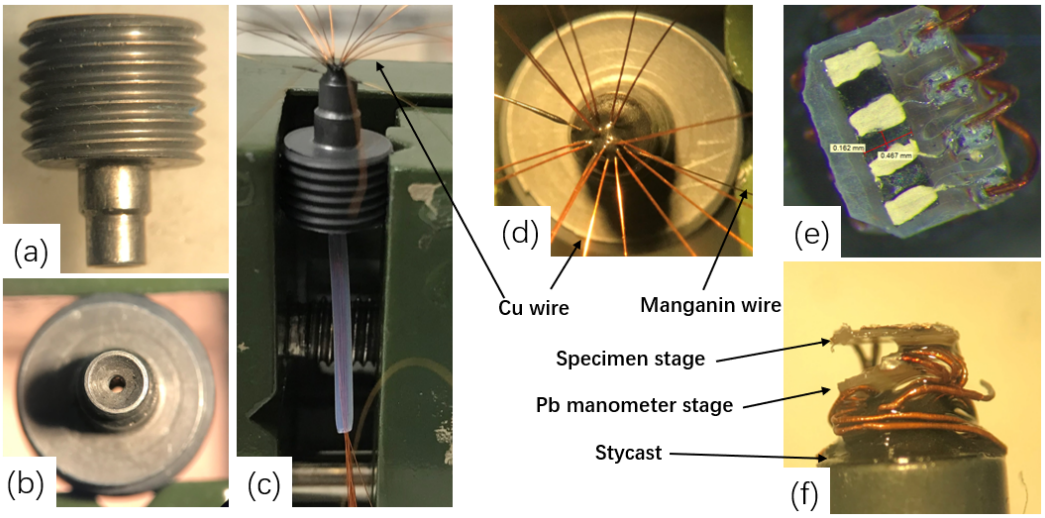

Figure A.2 (a), (b) Side view and top view of the piston-cylinder cell feed-through. (c) Feed-through on a clamp. Cu wires pass through the hole of the feed-through which is filled with Stycast. Plastic tubing is used the protect the Cu wires from bending/getting hurt by packing and pressurizing processs. (d) Top view of the feed-through. Cu wires spread out from the feed-through. A manganin wire is used to tighten the Cu wires and keep them from falling during the Stycast curing process. After the Stycast is completely cured, the unburied part of the manganin wire is cut off from the feed-through (e) Top view of a specimen stage that is soldered to the Cu wires. A specimen (on the left side) is then mounted on the specimen stage. For this specific example, contacts of the specimen are made by silver paint. (f) Side view of the feed-through showing the specimen stage and the Pb manometer stage.

Step 3: Mounting the Pb manometer and specimen To measure the pressure inside the pressure cell at low temperature, a Pb manometer, for which the four-contact resistance is measured, is usually used. The pressure dependence of the superconducting transition temperature, $T_c(p)$ can be used to calculate the pressure values at low temperatures Bireckoven and Wittig (1988). A thin Pb ribbon with dimension around $1.0\times0.2\times0.03$ mm^3 is used to fit into the sample space. To make such Pb ribbon, elemental Pb is first made into Pb sheet by rolling a glass vial over the elemental Pb (use the side surface of the vial to roll over the Pb). The surface is then brushed with a tooth pick wrapped with paper tissue until the surface is shiny in silver color. Finally, rectangular Pb sample (ribbon) can be easily cut from the sheet into the required dimension by a razor blade. To make electrical contacts on the the Pb manometer, we spot weld Au wires (diameter of 12.5 μm) onto the surface of Pb. To make the contacts mechanically stronger, tiny amount of silver epoxy is used to cover the contact spots and cured at 120 °C for $\sim$ 20 mins. A Pb manometer with contacts and Au wires is shown in Fig. A.3.

The sample to be measured needs to be formed into a bar with typical dimension of around $1.5\times0.2\times0.1$ mm^3 (the dimensions of the specimen can be adjusted, as long as it fits in the sample space). Contacts of leads can be made with silver epoxy, spot welding or soldering (silver paint is sometimes used for air-sensitive samples where the whole mounting process needs to be done in an insert-gas glove box).

With the prepared manometer and specimen, they are then mounted on the the platforms with the contacts leads soldered to the metal strips/Cu wires (Fig. A.2 (e)). Once all this soldering is done the sample and Pb manometer are ready for checking the ambient-pressure resistance. This is important to do before closing the cell (see below) since bad contacts are easier to fix now rather than later.

Step 4: Closing the cell With the specimen and manometer mounted, the rest of the cell can be assembled and closed. First put the bottom anti-extrusion ring (Fig. A.1 (d)) on the feed-through. Polish the extrusion ring prior if needed so that the inner and outer diameters fit

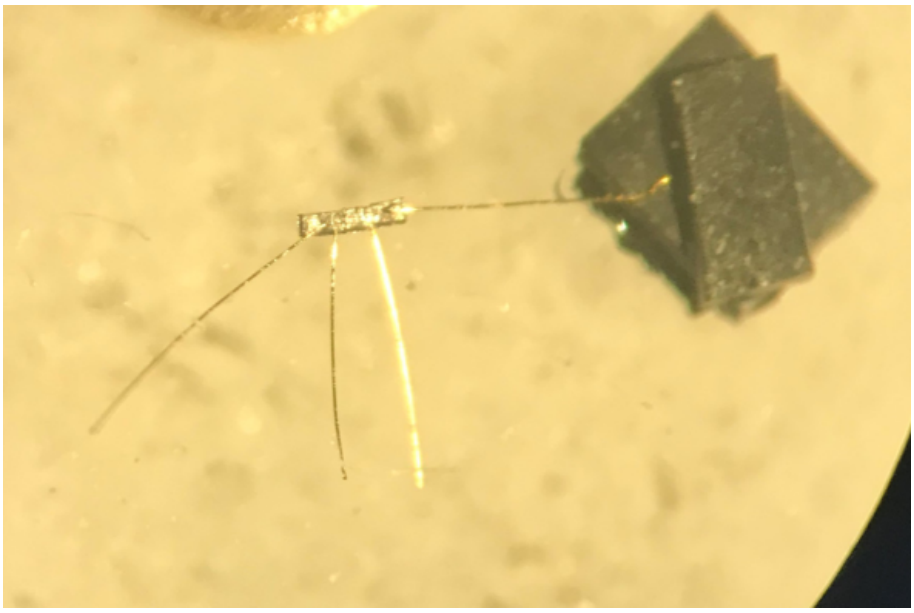

Figure A.3 A prepared Pb manometer that is used to determine pressure in pressure cells. Dimension of the Pb bar is around $1.0\times0.2\times0.03$ mm^3. Contacts are made by spot welding Au wires (12.5 μm diameter) and re-enforced by silver epoxy.

well with the feed-through and the inner diameter of the cell body, respectively. Then fill the Teflon cup with the pressure transmitting medium (mixture of 4:6 light mineral oil: n-pentane) using a syringe (Fig. A.4 (a)). Check under the microscope to make sure there is no air bubble in the pressure medium. Hold the feed-though upside down and carefully insert the feed-through into the pressure medium filled Teflon cup (Fig. A.4 (b)). Alternatively, the assembly on top of the feed-through (Cu wires, sample and Pb manometer stages) can be pre-wetted with the pressure medium before being inserted into the Teflon cup with the idea that this can help reduce the chance of bubbles forming/attaching to all of the wires. Then insert the Teflon cup/feed-through into the cell body column from the bottom side (Fig. A.4 (c)). Tighten the bottom lock nut firmly. Now from the top side of the cell body, the top of the Teflon cup can be seen. Place the top anti-extrusion ring on top of the Teflon cup (Fig. A.4 (d)). Put the piston on top of the anti-extrusion ring (Fig. A.4 (e)). Put on the Ni-Cr-Al disk

and tighten the top lock nut (Fig. A.4 (f)). See Fig. 2.1 (b) in Chap. 2 Sec. 2.1 for the relative positions of individual parts of the PCC.

With the cell closed, further electrical connection to the measurement systems can be done through the Cu wires (for example wiring the cell to a Quantum Design PPMS puck). To increase pressure, the PCC is put in a hydraulic press where load is applied and the position of the piston is locked (e.g. "self-clamping") by tightening the top lock nut (Fig. A.4 (g)). The maximum load that can be applied is typically around 9000 lbs. A successfully assembled feed-through can be used multiple times before the Cu wires on the high-pressure side of the feed-through starts to break and/or the Stycast becomes aged and can not hold the pressure well. In this case, the feed-through needs be re-assembled following the steps described above.

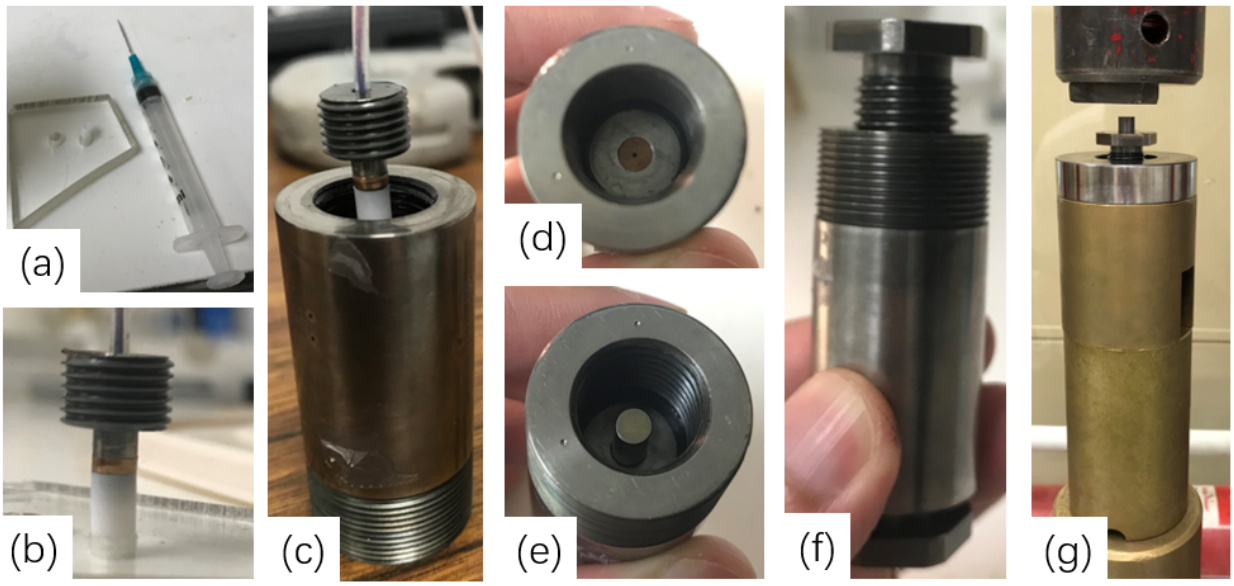

Figure A.4 Steps of assembling a PCC, using a cell where the body is made of Ti alloy as an example. (a) Teflon cup and the syringe that is used to fill the pressure transimitting medium. (b) Insert the feed-through into the Teflon cup. Note that a bottom anti-extrusion ring is put on the feed-through prior. (c) Insert the feed-through/Teflon cup into the column of the cell body from the bottom side. The feed-through is then tightened by the bottom lock nut. (d) From the top side of the cell body place the top anti-extrusion ring into the column. (e) Place the WC piston on top of the extrusion ring. (f) Put on the top lock nut. (g) Increase the load of PCC under a hydraulic press.

APPENDIX B. ASSEMBLING THE MODIFIED BRIDGMAN ANVIL CELL

The modified Bridgman Anvil Cell (mBAC) was frequently used to investigate materials' properties under hydrostatic pressure up to $\sim$ 6 GPa during my research. The following sections describe the detailed steps of assembling a mBAC including making various cells components (gaskets, manometers, electrical wiring etc.) as well as assembling a working pressure cell for electrical transport measurement. These steps are described based on a mBAC with tungsten carbide (WC) anvil culet size of 3.2 mm (maximum pressure $\sim$ 6 GPa). For different culet size of WC anvil, dimensions of certain components (gaskets, Teflon rings) can be rescaled accordingly. A video of these processes is recorded for reference.

B.1 Pre-preparation of certain cell components

Various cell components including gaskets, Teflon rings as well as Pb manometers can be pre-made prior to the assembling of mBAC.

B.1.1 Gasket

Pyrophyllite is used as the gasket material for the pressure cell for the reasons outlined in Chap. 2, Sec. 2.2. For a mBAC with anvil culet size of 3.2 mm diameter, the required gasket dimension is 3.2 mm outer diameter (OD), 1.8 mm inner diameter (ID) and (0.183$\pm$0.001) mm thickness (thickness is measured with a micrometer caliper as will be described in details below).

OD 3.2 mm Begin with a pyrophyllite rod (see Fig. B.1 (a), purchased from Superior Techical Ceramics "Grade A Lava Rock Lav" and cut into $1'' \times 1'' \times 12''$ rods by Ames Laboratory machine shop). The rod is first shaped into approximate round shape in cross section using a shaft grinder shown in Fig. B.1 (b). To do that, use the drilling bit to polish the

rectangular corners to a roughly round shape while rotating. Then the pyrophyllite rod is fixed in a chuck of the lathe (Fig. B.1 (d)) for further machining. With a rotating speed of 400 rpm, decrease the diameter of the pyrophyllite rod in a step-shape manner (to increase mechanical strength, see Fig. B.1 (c)) where the tip part of the pyrophyllite rod has a diameter of 3.2 mm (length of the tip-rod is 5 - 7 mm, it easily breaks if too long). During this process, keep using the digital caliper to monitor the diameter of the pyrophyllite rod.

ID 1.8 mm To make the ID of 1.8 mm, the rod from the previous step is kept fixed in the chuck. Then different drill bits are used to drill inner hole to the rod with the rod rotating at 400 rpm (Fig. B.1 (e)). Start with the drill bit with the diameter of 1.05 mm (Fig. B.1 (e)). The drill bit is fixed to a moving stage where it can be moved slowly and steady towards or away from the chuck of the lathe. Align the drill bit with the pyrophyllite rod so that it drills in the center of the pyrophyllite rod. Bring the drill bit slowly toward the pyrophyllite rod that is fixed the the chuck until the drill bit drills the pyrophyllite rod. Keep moving to drill deeper. Pay attention that the drill bit needs to be retracted from time to time to allow the pyrophyllite powder to come out from the hole (otherwise the powder can accumulate into the hole and break the pyrophyllite rod). Also do not drill too deep into the pyrophyllite rod (typically depth of $\sim$ 7 mm) otherwise it easily breaks. Following the steps of the hole-drilling, slowly work the way to the drilling rod with the diameter of 1.8 mm so the resulting ID of the pyrophyllite rod is 1.8 mm as required.

Raw gasket disks After the previous step, a pyrophyllite tube with 3.2 mm OD and 1.8 mm ID is obtained on the end of the larger, stepped down rod (see above). Now we cut the tube part into disks with thickness $\sim$ 0.5 mm. With the rod still being fixed in the chuck of the lathe and rotating at 400 rpm, a cutter (Fig. B.1 (f)) is slowly brought in from the side to cut the pyrophyllite tube. Use a soft container (usually a paper boat) underneath the pyrophyllite rod to catch the cut-off disk so that the disk does not fall off and breaks. With the typical

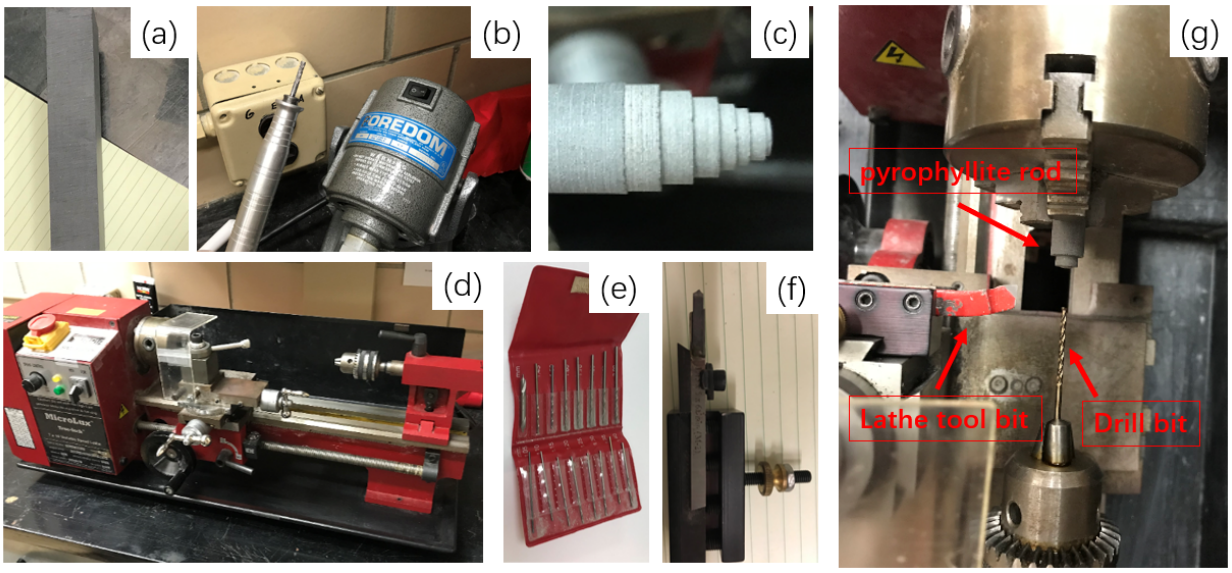

Figure B.1 (a) Square cross-section raw pyrophyllite rod. (b) A shaft grinder used to make square-shape pyrophyllite rod roughly round shape. (c) Step-shape of the pyrophyllite rod when making the pyrophyllite rod the desired outer diameter (very tip of the rod has the outer diameter of 3.2 mm). (d) Mini-lathe for preparing gasket and Teflon rings. (e) The dril bits that used to drill the inner hole of the pyrophyllite rod. (f) A lathe cutter that is used to cut raw pyrophyllite disks from pyrophyllite tube. (g) Enlarged view of the lathe with the pyrophyllite rod, drill bit and lathe tool bit. The lathe tool bit is replaced with the cutter shown in (g) when cutting raw pyrophyllite disks.

length of 5 - 6 mm of the tube and thickness of 0.5 mm of the disk, $\sim$ 10 raw gasket disks can be obtained (Fig. B.2 (a)).

Thickness 0.183 mm In this step, the raw gasket disk is carefully polished down the required thickness (0.183 mm) using different grid sandpapers and an in-house-made (Ames Lab machine shop) polishing stage. The polishing stage is made of brass cylinder where the center has a movable stage of which the height can be adjusted by turning a set-screw on the backside of the brass cylinder (Fig. B.2 (b)). When the raw gasket disk is placed on the movable stage, the height of the stage is adjusted so that the top surface of the disk is slightly above the surface of the brass cylinder. To polish, simply put the disk on top of the moving

stage. Then the surface of the disk can be polished by pushing and moving a sandpaper over against the surface of the disk. In the beginning, sandpaper with larger grit size (for example a 320 grit) can be used to decrease the thickness more efficiently, as approaching the desired thickness, smaller grit size sandpaper (a 2500 grit) is used to polish slower as well as obtaining a smoother surface of the gasket (both sides of the gasket needs to be polished with the 2500 grit sandpaper to have smooth surfaces). Flip the gasket from time to time to make sure that both sides of the gasket are evenly polished. Use the digital micrometer caliper (Fig. B.2 (e)) during the polishing process to measure the thickness of the gasket from time to time to avoid over-polishing. To flip or move the gasket from the polishing stage to the caliper, a "eyebrow" tool (Fig. B.2 (d)) is used. To measure the thickness of the gasket, the gasket is carefully placed on the anvil of the caliper and measured by rotating the thimble until the spindle gently presses the gasket (see Fig. B.2 (f). The caliper clicks when the spindle presses the gasket/anvil). **DO NOT** use tweezers to grab the gasket as it can break the gasket. Any gasket that drops to the ground from the table should not be used for assemble mBAC (possible small cracks develop when hitting the hard ground). Gaskets with thickness (0.183±0.001) mm can be reliably used to assemble a working mBAC (historically, gaskets with thickness ranging from 0.181 mm to 0.184 mm have been successfully used to assemble a working mBAC). An example of the prepared gasket is shown in Fig. B.2 (c).

B.1.2 Teflon ring

For a mBAC, two Teflon rings are stacked together inside the pyrophyllite gasket and serve as part of the liquid barrier. They are machined from a Teflon rod and the required dimensions are 1.8 mm OD, 1.3 ID and 0.06 to 0.09 mm in thickness (thickness of the Teflon ring is measured in the same way as measuring the thickness of the gasket).

OD 1.8 mm Begin with a Teflon rod (Fig. B.3 (a)) in the lab, the first step is to make a Teflon rod with diameter $\sim$ 1.65 mm as measured by the caliper. **Note** that this is different from the required OD 1.8 mm of Teflon ring. The reason is that the Teflon ring will expand

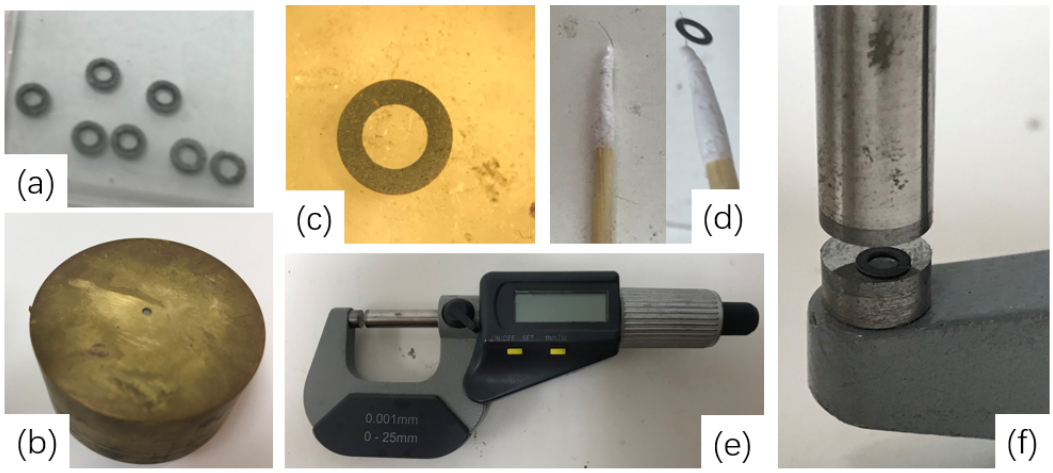

Figure B.2 (a) Raw gasket disks with OD 3.2 mm, ID 1.8 mm and thickness $\sim$ 0.5 mm. (b) In-house-made polishing stage that is used to polish the cross-section area of the raw gasket disk to decrease the thickness. (c) Final result of gasket with desired dimension, OD 3.2 mm, ID 1.8 mm and thickness $\sim$ 0.183 mm. (d) A "eyebrow" tool (left) that is used for handling the gasket (right). The "eyebrow" tool is made by gluing (by superglue) a eyebrow on to a toothpick. This "eyebrow" tool is also frequently used to handle Teflon rings (see below), apply tiny amount of silver paint, silver epoxy, epoxy etc. (e) The micrometer caliper (resolution 0.001 mm) that is used to measure the diameter of the pyrophyllite rod, Teflon rod (see below), thickness of the gaskets, thickness of the Teflon rings (see below). (f) A picture of measuring the thickness of a polished gasket using the micrometer caliper. The gasket is carefully placed on top of the anvil, and the spindle is brought towards the gasket/anvil by rotating the thimble. The caliper clicks when the spindle gently presses the gasket/anvil. The thickness is read from the LED display.

during the process of polishing down to the required thickness (which will be described in the following), and a diameter of $\sim$ 1.65 mm rod will give a final Teflon ring that best fits into the gasket. The process of making the Teflon rod is very similar with that described for making a pyrophyllite rod but different in the last step to reach the desired diameter. Since Teflon is a very soft material, attempts of decreasing the diameter by less than 0.25 mm using a lathe tool bit will simply cause the rod to bend rather than being cut. Thus, when turning the Teflon rod, the diameter of the rod needs to be decreased by no less than 0.25 mm (corresponding to 10 ticks of the micrometer of the lathe) in one cut. If the diameter from the last step is slightly

larger than the desired diameter, a piece of sandpaper (2500 grit paper) is used instead to polish the rod down the desired diameter by pushing the sandpaper against the rod while the rod is rotating with 400 rpm.

Raw Teflon disks After the Teflon rod is made, then Teflon disks are cut out from the rod with thickness of $\sim$ 0.5 mm (see Fig. B.3). The process is similar with that described for making raw gasket disks, where a blade is used (Fig. B.3 (d)).

ID 1.3 mm The Teflon disks from last step now need to be made into a ring with ID 1.3 mm. The disk is first glued onto a in-house-made drilling stage (Ames Laboratory machine shop) using super glue. The drilling stage is designed so that it has a recess on the top surface to allow the Teflon disk to fit in and a hole slightly larger than 1.3 mm so it allows/guides the drill bit to drill the Teflon disk in the center (Figs. B.4 (a) and (c)). After the glue is completely dried, one inserts the drill bit (Fig. B.4 (b)) into the hole of the stage and drill the Teflon disk by hand, spinning the bit between you thumb and finger. Start from the thinnest drill bit and move progressively to the final drill bit with the diameter of 1.3 mm. After the inner hole is done, raw Teflon rings (Fig. B.4 (e)) are removed and clean in Acetone from the drilling stage.

Thickness 0.06 to 0.09 mm In this step, the Teflon rings resulted from the last steps are polished down to the required thickness. Teflon rings are glued to a polishing puck of the South Bay Technology polishing fixture (Fig. B.4 (d)) by super glue then polished with sandpaper (grit 2500 paper). Both sides of the Teflon ring needs to be polished to obtain smooth surfaces. One can first polish one side of the Teflon ring to have a flat and smooth surface and then flip the Teflon ring to polish the other side of the surface directly to the required thickness. Be careful not to over-polishing when polishing the first side. Small Cu or Pt wires (with diameter 50 μm, 90 μm, 120 μm or 180μm) can be glued together with the Teflon ring to prevent over-polishing as well as to estimate the thickness during the polishing process by watching how much the wires have (have not) been polished.

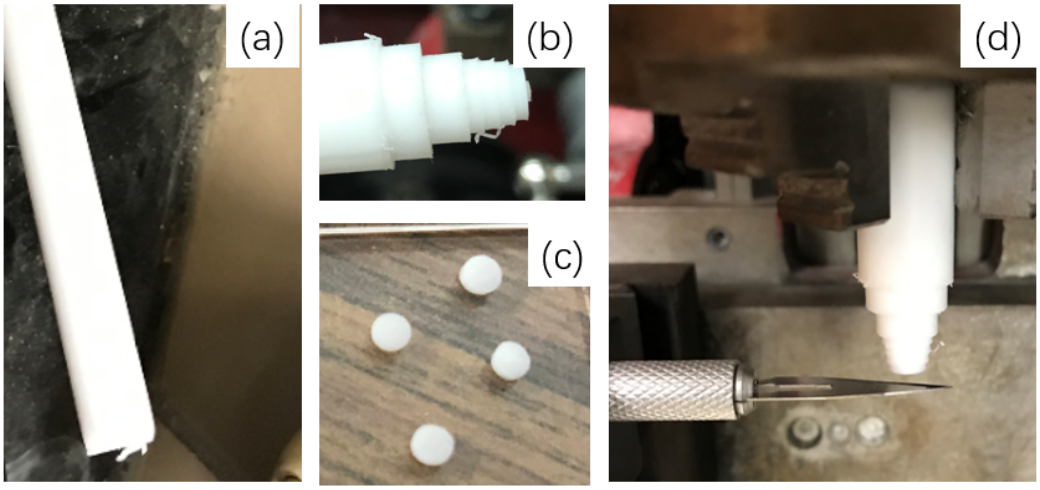

Figure B.3 (a) Raw Teflon rod material. (b) Step-shape of the Teflon rod when making the pyrophyllite rod the desired outer diameter. (c) Teflon disks with diameter of $\sim$ 1.65 mm and thickness $\sim$ 0.5 mm. (d) A picture showing that a blade is used to cut raw Teflon disks from the Teflon rod. The blade is fixed to the same position as that of the lathe tool bit as shown in Fig. B.1 (g)

B.1.3 Pb manometer

To measure the pressure inside the pressure cell at low temperature, a Pb manometer is typically used. The Pb manometer is prepared in the same way as described in the Appx. A with the difference being that the dimension of the Pb ribbon used for the mBAC is around $0.7\times0.15\times0.03$ mm^3 so as to fit into the sample space.

B.2 Process of assembling the mBAC

Step 1: Assemble WC anvils With the various components prepared as described above, the mBAC can be assembled. To begin with, clean throughout the individual components of mBAC including cell body, anvil holders, WC anvils. Any leftover glue from the last usage needs to be removed (scratch off mechanically if needed) and followed by cleaning with Kimwipes soaked in Ethanol or Acetone. The anvils are then inserted into the anvil holders (see Fig. B.5 (a) and (b), make sure the anvil sits tightly in the anvil holder). An epoxy

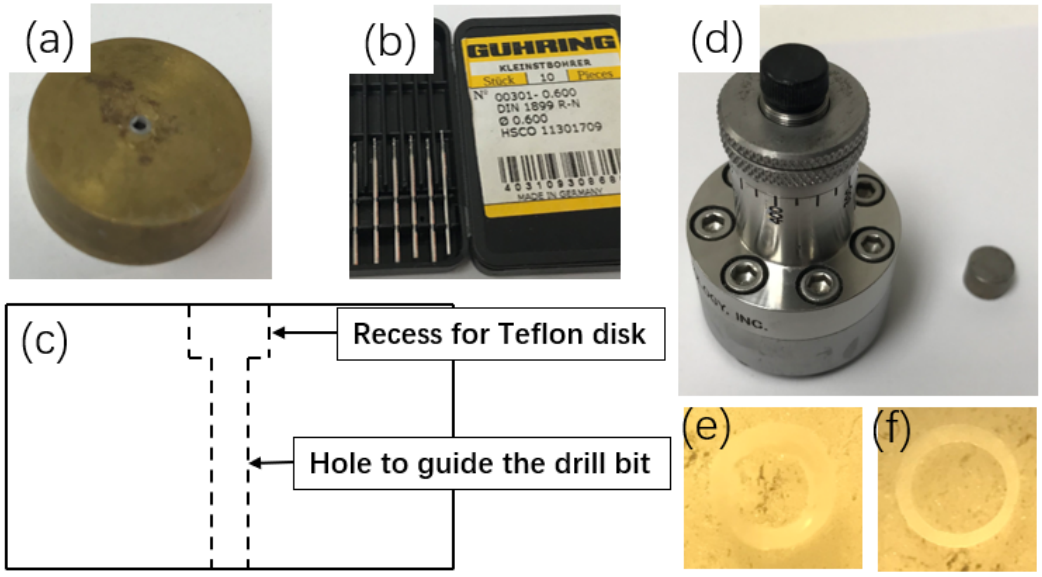

Figure B.4 (a) In-house-made drilling stage to make the inner diameter of 1.3 mm of Teflon rings. (b) Drill bits that are used to drill the hole on the Teflon disk. (c) A schematic diagram of the in-house-made drilling stage. During the drilling process, the raw Teflon disk is glued inside the recess. The drill bits are inserted through the hole of the drilling stage so that it drills at the center of the Teflon disk. (d) South Bay Technology polishing puck that is used to polish the raw Teflon ring. (e) Raw Teflon ring after drilling hole. (f) Final result of the Teflon ring with OD $\sim$ 1.8 mm, ID $\sim$ 1.3 mm and thickness ranging from 0.06 - 0.09 mm.

(Blue Araldite, working time around 60 mins) is gently applied into the space between the anvil and the holder. The epoxy is typically left over night to cure. After that, the anvils are then checked for levelness. The height of the flat surface of the anvil can differ by no more than 5 μm across the area of the culet to ensure a decent success rate. If the height difference is larger than 5 μm, two scenarios are often observed. In the first case one side of the culet is higher/lower than the other side, it is likely that the WC anvil is tilted slightly in the anvil holder (anvil not sitting tightly enough in the anvil holder), then the anvil needs to be removed from the holder and glued again. In the other case the outside area of the culet is higher than the inside area of the culet, this typically means that WC anvil culet surface is already deformed (typically inner part gets dented under pressure) after being used for a long time.

Then this anvil needs to disposed and new anvil needs to be used. A Mitutoyo Absolute Digimatic Indicator (Fig. B.5 (c)) is used to measure this height difference.

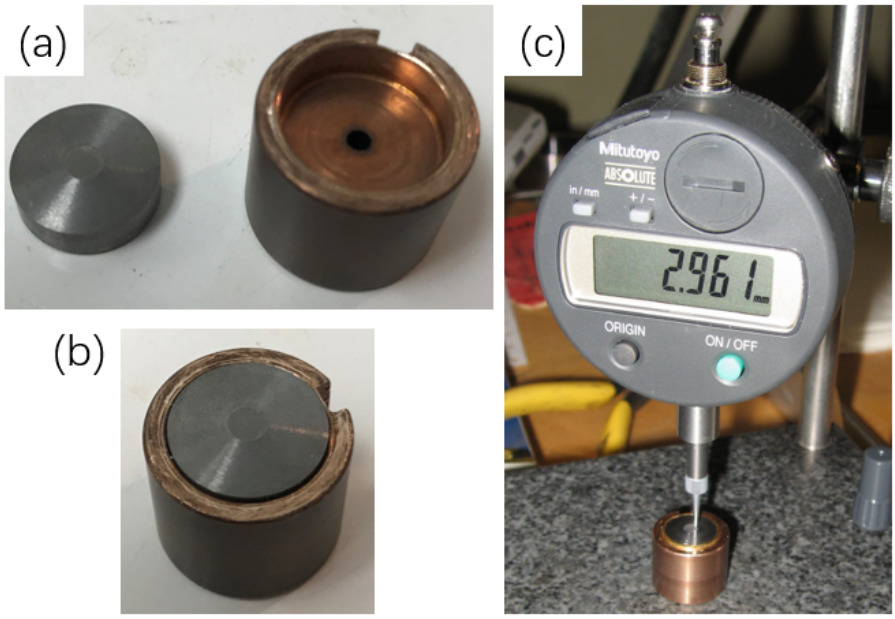

Figure B.5 (a) A WC anvil and a top anvil holder. (b) A WC anvil sitting in the top anvil holder. (c) A Mitutoyo digital thickness gauge used to check the levelness of the culet of the anvil seated in the anvil holder.

Small square soldering pads (cut from the plastic/metal strip sheet as shown in Fig. A.1 (e)) are glued (Blue Araldite) on the top of the bottom anvil holder (Fig. B.6 (a)). The height of the soldering pads should not exceed the height of the anvil center. These soldering pads provide contact points for the copper wires that go into the sample space and that connect to the PPMS puck.

Copper wires (American Wire Gauge AWG 34) are twisted in pairs and then encased in plastic tubing. These are then fed through the side holes in the bottom BeCu screw (Fig. B.6 (b)). Then the PPMS puck is glued to the bottom of the BeCu using GE varnish. The copper wire is affixed to the holes by applying a small amount of epoxy. Then the copper wires are soldered to the bottom of the PPMS puck and to the soldering pads. This provides the electrical connection between the soldering pads and the PPMS puck.

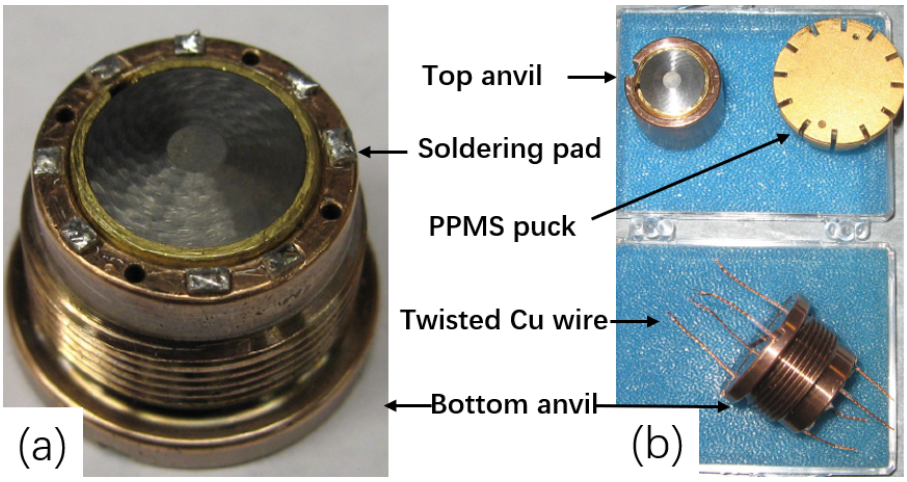

Figure B.6 (a) Bottom WC anvil sitting inside a anvil holder. Small soldering pads are attached to the anvil holder for later electrical connection. (b) Top WC anvil sitting inside a anvil holder, a PPMS puck and twisted Cu wires within the bottom anvil holder for electrical connection.

Step 2: Attaching gaskets and Teflon ring to the bottom anvil Make sure the WC surface is clean. Bake the pyrophyllite gasket in furnace at 120 °C for 12 hours to remove moisture in the gasket (this treatment has been empirically proven to increase the successful rate) Kim (2013). Apply a small amount of diluted GE varnish (mixture of the thick, as purchased, GE varnish and Ethanol at a ratio of $\sim$ 1:30 by volume) on the surface of the bottom anvil, then quickly and carefully center the pyrophyllite gasket in the middle of the culet. This procedure needs to be performed under the microscope to make sure that gasket is well aligned with culet surface of the anvil. After the pyrophyllite gasket is laid down, put a small metal tube (a Ti tube with OD 3.16 mm, ID 2.35 mm and mass 1.34 g. The side that is placed on the gasket is polished flat) on top of the gasket to press the gasket against the anvil (Fig. B.7 (a)). This will make a stronger gluing when the GE varnish is drying. Allow $\sim$ 10 mins for the GE varnish to be completely dry, then use a fresh new scalpel blade to remove all remaining GE varnish on the surface of the anvil (both outside and inside of the gasket) except those underneath the gasket.

The rest of the surface area of the bottom anvil is coated with epoxy (Blue Araldite). Outside the gasket, epoxy is applied over the whole surface of the anvil with some epoxy dragged up the side of the gasket (Figs. B.7 (b) and (c)) to provide some support to the gasket. Inside the gasket, a very thin layer of epoxy is applied to cover the surface of the anvil. To do that, typically a tiny drop of epoxy is put on the surface of the anvil inside the gasket, then a "eyebrow" tool is used to spread the epoxy to evenly cover the surface area. The epoxy serves as an insulating layer. Before the epoxy is cured, the bottom Teflon ring is placed inside the gasket and glued down to the anvil by the epoxy (Fig. B.7 (e)).

Given that the (Blue Araldite) epoxy is already prepared, one can use this epoxy to coat the top anvil. Similar to the bottom anvil, the surface of the top anvil is coated with the epoxy everywhere (both inside and outside of the gasket) except the area that is going to be in contact with gasket. Since there is no gasket attached to the top anvil during the assembling process, one needs to estimate the inside surface area within the gasket when applying the epoxy on the culet. To make sure the proper surface area is coated, after the epoxy is cured, a second gasket can be placed on top of the culet of the top anvil to check the coated area. Epoxy can be re-applied to coat the missed area or over-coated area can be scratched off by a scalpel blade. Since the coating of the top anvil is a completely separated process with the bottom anvil, one can also choose to do this at a different convenient time.

Step 3: Assembling Cu wires for electrical connections In this step, eight Cu wires are mounted to provide electrical connections from the sample space to the soldering pads (four for sample, four for Pb manometer). To begin with, we prepare eight slits on top of the gasket which allows Cu wires to go into the sample space from the outside. After the epoxy from previous step is cured overnight, eight small triangles, evenly surrounding the gasket are first cut out from the epoxy (Fig. B.7 (d)). The epoxy for the triangle area is cut all the way through to actually expose the underneath WC anvil surface. The exposed triangle areas are then re-covered with thin layer of fast drying epoxy (Red Araldite, working time $\sim$ 5 mins). These triangles provide space that allows the Cu wires to go into the sample space horizontally

without bending. A homemade blade tool (Fig. B.7 (f)) is then used to carve eight narrow slits on the gasket (Fig. B.7 (e)). The location of slits corresponds to the eight triangles. The width of the slits is $\sim 50\,\mu$m so that Cu wires can fit in. The depth of the slits is determined to ensure that the Cu wire, when placed in the slit, is at the same height as the bottom Teflon ring. However, the depth of the slits should not exceed 2/3 of the gasket thickness, i.e. $120\,\mu$m. The pyrophyllite powders from the curving is removed by a dust blower. Note that the homemade blade tool (see Fig. B.7 (f)) has a proper sharpness so that when carving from above, the slit has roughly a round shape to fit the Cu wire. If one feels like the slit is too V-shaped, then the bottom part of the slit needs to be rounded by carving with a tilted angle. The baseline is, when placing the Cu wire in the slit, there should not be a gap between the Cu wire and the wall of the slit at the bottom part.

Next step, we prepare the Cu wires. Cu wires with diameter of $50\,\mu$m are cut into proper length. The insulating coating at two ends of the Cu wire is removed. On the side of the Cu wire that goes into the sample space, the exposed part of the Cu wire is flatted via being rolled over by the side surface of a glass vial. This can make the surface area of the exposed part bigger so that the contact between the Cu wire and leads of specimen or Pb manometer is easier to make. The length of the exposed part is adjusted (usually too long and needs to be cut shorter by razor blade) so that when the Cu wire is placed in the slit, the exposed area only sits within the surface area of the Teflon ring, whereas the part of the Cu wire that sits in the slit is still insulating-coated (Fig. B.7 (g), see the Cu wire part that goes above the Teflon ring). In addition, try to confine the flattened part only to the exposed area of the Cu wire so that the insulating part (which fits in the slit) is still round shape.

The prepared Cu wires are then soldered to the soldering pads. The other end of the Cu wires are then carefully guided near the slits and fitted into the slits. Note that the electrically exposed part of the Cu wires (i.e. the flatted part as described before) should locate within the area of the Teflon ring (Fig. B.7 (g)). Again, the Cu wire should be enamel covered and round where it fits in the cut slits through the gasket. Fix the positions of the Cu wires by small

pieces of black electric tape (Fig. B.7 (h)). The slits in the gaskets (with the Cu wires fitted in) are then refilled with a dense mixture of epoxy (Red Araldite) and pyrophyllite powder (the powder is obtained by scratching a pyrophyllite rod with razor blade). Increasing amounts of pyrophyllite powder is mixed into the epoxy until it appears very dry. This ensures that the epoxy will not seep into the gasket. The homemade blade is used to gently push the mixture inside the slits so that they are firmly refilled. Note that when refilling, an extra amount of the mixture is used to make sure the slit is properly refilled (Fig. B.7 (h)). After the mixture is cured ($\sim$ 30 mins at room temperature), the Cu wires are firmly buried inside the gasket. The excess mixture is removed by scalpel blade so that the gasket is flat and clean again. After the "cleaning", typically the refilled mixture is transparent enough to be able to actually see the Cu wire inside (Fig. B.8). Note that the mixture may need to be re-made several times if it becomes too dry during the process.

Step 4: Placing sample and Pb manometer into sample space The sample and Pb manometer are placed within the Teflon ring. The flatted ends of the Cu wires are bent to cover the respective Au or Pt wires of the sample and Pb (Au or Pt wires of the sample and Pb can also be bent as necessary). This provides mechanical contacts under pressure. To further safeguard the connection and prevent sample or Pb from moving during any later process, a small amount of silver paint is applied to the connections. The top Teflon ring is then affixed by applying a small drop of epoxy (Red Araldite) on the bottom Teflon ring at a location that is away from any Au or Pt wire. At this point, the ambient-pressure, room-temperature resistance of sample and Pb can be measured. If any open or bad contacts are detected attempts to fix them can be made (primarily by checking the Ag-paint joints). If necessary, the slits can be unfilled by slowly pulling the Cu wire out from the slit (this usually does not kill the gasket assembly and the slit can be refilled again).

Step 5: Fill pressure medium and close the cell The BeCu body is screwed on the bottom anvil stage, held by a clamp and placed on a stand (Fig. B.9 (a)). Pressure medium (1:1

mixture of n-pentane : iso-pentane) is inserted using a pasteur pipette. Put the tip of the pasteur pipette against the inside wall of the cell body so that the pressure medium flows down along the wall (See Fig. B.9 (b). **DO NOT** drop the liquid medium directly on the sample space as it can destroy your assembly in the sample space). Excessive liquid is added so that the liquid level is higher than the top of the gasket (fill the liquid to roughly half the height of the cell body). Then a visual check under the microscope is made to confirm everything inside the sample space is still held in position and that the liquid is no longer bubbling within the gasket. Gently tap the cell body to speed up the releasing of any bubbles, do not exceed 30 s for this process. Empirically, once the gasket is soaked in the pressure medium, waiting too long before closing the cell has higher explosion rate when applying the initial load (see below). Then the top anvil is carefully lowered into the cell body with the help of a wooden stick (Fig. B.9 (c)). Sudden movements during this process can caused shift of the top Teflon ring which causes failure in the end. Then the BeCu disc is placed on top and the top lock nut is screwed on gently (Fig. B.9 (d)). The cell with a press piston is placed in the hydraulic press. The load is applied using a hydraulic press with a slow, continuous motion (Fig. B.9 (e)). A initial load of no less than 2500 lbs needs to be applied to ensure proper sealing by the Teflon rings. Typically a load of 2500 lbs is applied which results in an initial pressure of $\sim$ 2 GPa. Such a initial load will typically result in a final maximum pressure of $\sim$ 5.5 GPa with the maximum load of 9000 lbs. To target for a higher final maximum pressure, a initial load of 3000 - 4000 lbs can be used and the final maximum pressure can reach $\sim$ 6 - 6.5 GPa with 9000 lbs. However, it is worth noting that the performance of a working mBAC depends on many factors (perfectness of gasket or Teflon ring, whether there is bubble inside the sample space etc.), and with the same load applied, the pressure can vary by as much $\sim$ 1 GPa.

If an initial load is reached without a rupture of the gasket (which sounds like a "puff", in which case contacts of sample and Pb manometer are often lost as well), then a torque wrench (Fig. B.9 (f)) is used to turn in the top lock nut. The typical relationship between the load and the torque wrench setting is n$\times$1000 lbs load=n$\times$10 N m. Once the torque wrench locks (it

clicks when the designated torque is achieved), the load from the hydraulic press can be slowly decreased. Check again the resistance of the sample and Pb can be measured and the values are reasonable.

Note that for this step, prepare all tools for closing the cell in advance so that once the liquid medium is inserted in, cell can be closed as quickly as possible, for the reason that we do not want the gasket to be soaked in the pressure medium for too long time before the cell is closed and a initial load is applied.

With the cell successfully closed, the electrical properties of the sample can be investigated under pressure. After the pressure is locked in, 3 hours of relaxation time is needed for the pressure medium of 1:1 mixture of n-pentane : iso-pentane. This relaxation time is determined by measuring the resistance of the Pb or sample at room temperature over time. Initially, resistance slows changes over time and then gradually saturates after $\sim$ 3 hours.

B.3 Summary

Assembling a successful mBAC is an time intensive process which needs patience and caution. Every individual component needs to be prepared with care and patience. Often, one can prepare the gaskets, Teflon rings as well as Pb manometers in large quantities. With these prepared prior, one can assemble a mBAC in two days. Statistically, a success rate of $\sim$ 50% was reached during my PhD research. I can say, with no false modesty, this can be considered to be an excellent success rate to strive for.

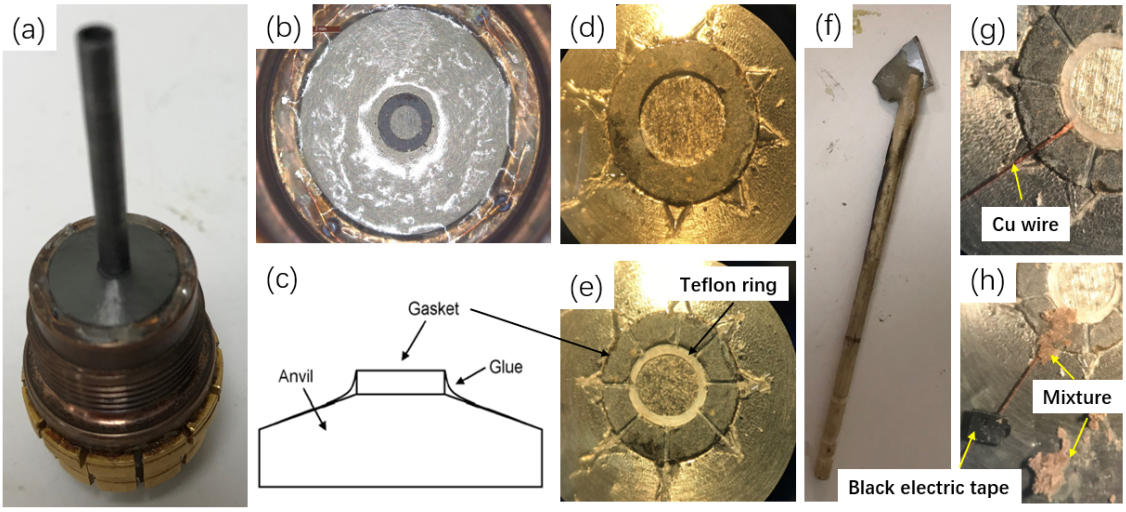

Figure B.7 (a) Glue a gasket to the anvil using GE varnish. A small metal tube is put on the gasket to ensure good adherence between the gasket and the anvil. (b) Cover the surface of the anvil with epoxy. (c) Schematic diagram of applying epoxy. (d) Eight small triangles surrounding the gasket that are cut out from the epoxy (the triangle area of the epoxy is removed completely to expose the surface of the anvil), providing space for the Cu wires. (e) Anvil surface inside the triangles and the gasket are covered with thin layer of epoxy for electrical insulating. A Teflon ring is placed inside the gasket and glued with epoxy. Eight slits are carved on the gasket for Cu wires to pass through. (f) Homemade blade tool (a broken piece of razor blade glued to a toothpick by Red Araldite epoxy) used to carve the slits. The tool can be used as long as the blade has a decent sharpness to carve the gasket. (g) Example of a Cu wire on top of the anvil and passing through the slit. (h) Example of a slit refilled by a mixture of epoxy and pyrophyllite powder with Cu wire inside. Some mixture is placed beside the gasket to be easily taken to fill the slits, which is removed after all slits are refilled. Extra amount of mixture is used to ensure that the slit is properly filled with mixture. The excess amount will be removed after the mixture is cured (see Fig. B.8 for after removing the excess mixture).

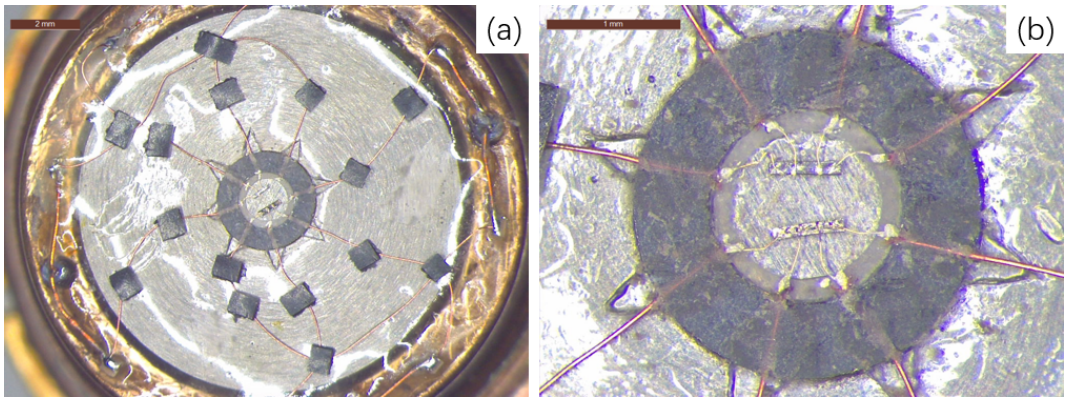

Figure B.8 (a) Assembled sample space within the gasket and Teflon ring. Sample and Pb manometer are mounted within the sample space. Electrical connections are made via Cu wires. (b) Enlarged view of the sample space showing the connection between Cu wires and contact leads of sample and Pb manometer, as well as Cu wires going through the gasket. Note that the refilled epoxy/pyrophyllite mixture is actually transparent enough to be able to see Cu wires inside.

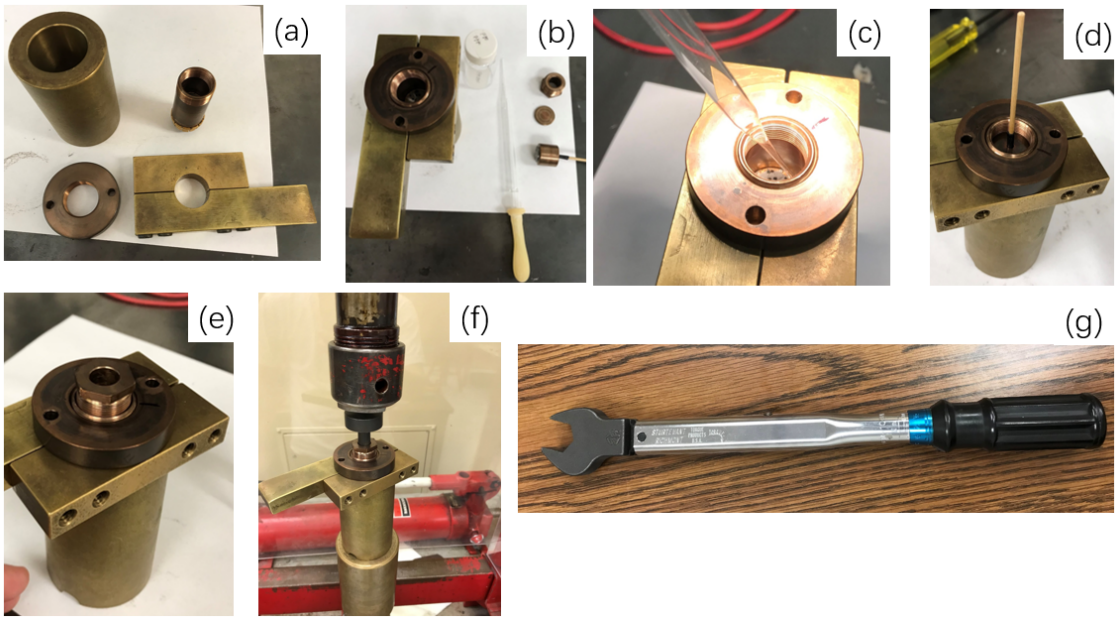

Figure B.9 Steps of closing a mBAC with an initial load of 2500 lbs. (a) Various components that are used to support the mBAC including a brass-cylinder stand, a band screw ring and a cylinder clmap. With the band screw ring attached to the cell body, mBAC can be supported by the cylinder stand. The cylinder clamp provides extra fixing of the cell body so that when using a wrench to turn the lock nut, the cell body does not turn together with the lock nut. (b) Various components that are prepared for closing a mBAC including a cell body already clamped on the supporting stage, pressure medium, pasteur pipette that is used to fill pressure medium, CuBe disk, CuBe lock nut and top anvil/holder. Note that the top anvil/holder is attached to a wooden stick so that it can be slowly inserted into the cell body without sudden drop. (c) Using pasteur pipette to fill pressure medium through the inside wall of cell body. (d) Insert the top anvil/holder slowly using a wooden stick. (e) Close the cell by putting in the CeBe disk and tightening the lock nut. (f) Apply a initial load via the hydraulic press. (g) Tighten the lock nut using a torque wrench.

APPENDIX C. ASSEMBLING THE MINIATURE DIAMOND ANVIL CELL

Diamond anvil cells (DAC) are often used to reach even higher pressures in the range of tens to hundreds of GPa. The design of the DAC is very similar to the mBAC, but using two diamonds as opposing anvils instead of the WC that was used in the mBAC, and thus can generate and maintain higher pressures. However, sample space in pressure cells typically becomes smaller as maximum pressure gets higher. In a DAC, sample space size is usually sub-millimeter or even smaller, making experiments, especially transport measurements, very challenging. During my thesis work, a miniature diamond Anvil Cell (mDAC) was borrowed from Geophysics Lab and was used to perform electrical transport measurements under pressure up to $\sim$ 30 GPa. In the following sections, I will describe the detailed steps of assembling the mDAC. I would like to acknowledge Dr. V. Struzhkin and Dr. J. Ying for the support of me and my colleague G.D.M (a.k.a Dr. Udhara Kaluarachchi) in learning this technique at Geophysical Laboratory, Carnegie Institution of Washington.

The detailed description of the design of the DAC is reported in Gavriliuk et al. (2009). The schematic diagram as well as example pictures of the miniature Diamond Anvil Cell (mDAC) is shown in Fig. C.1. This cell is 10 mm in diameter, small (miniature) enough to fit with the dilution-refrigerator insert of the QD PPMS. The main components of the cell body are a piston and cylinder (C.1), which are manufactured from a hardened, non-magnetic Ni-Cr-Al alloy (40HNU) Eremets (1996). Diamonds with culet size about 350 μm are mounted on the top cylinder and bottom piston to generate pressures up to $\sim$ 30 GPa. In the following, the detailed steps of assembling a mDAC are provided.

Step 1: Glue diamond anvils In the first step, the two diamond anvils are glued to the cylinder and piston. To begin with, clean the cell body and the diamond anvils. Leftover

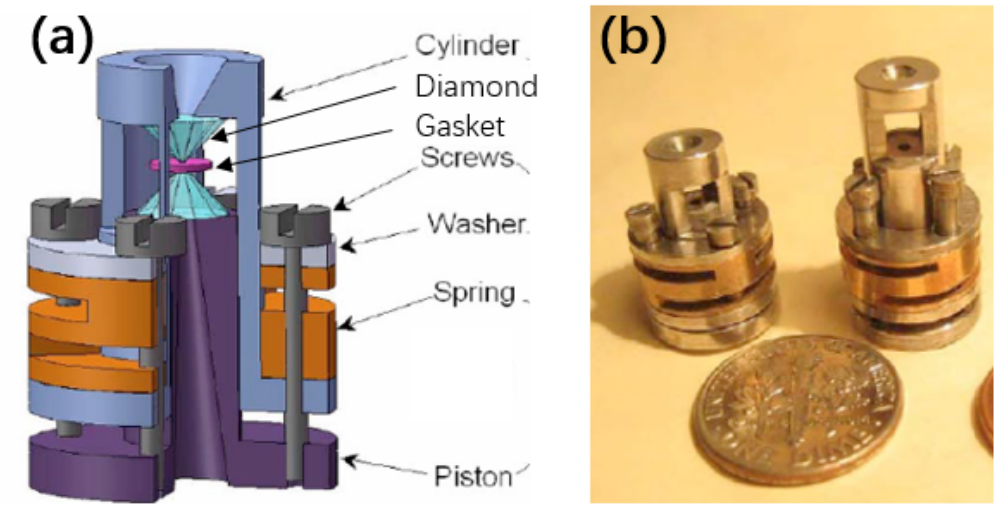

Figure C.1 (a) Schematic drawings of a miniature Diamond Anvil Cell (mDAC). The external spring serves for controlled and uniform application of force, and also compensates temperature-driven stresses, which appear at low temperatures. The force applied to the spring is clamped by four screws. (b) The photograph of cells with slightly different dimensions. Figures are adapted from Ref. Gavriliuk et al. (2009).

Stycast from previous usage needs to be cleaned off throughly. For this cell, scratching mechanically usually removes the Stycast efficiently. Heating up to 140 °C will make the Stycast easier to come off from the cell body.

The diamond anvil on the cylinder is glued first. Put the cylinder upside down and place the diamond anvil inside the cylinder. Glue a small piece of a wooden stick (make sure the two sides of the wooden stick are flat by polishing using sandpaper) on top of the piston via double-side tape (Fig. C.2 (a)). Then assemble the pressure cell (with gentle force) so that the wooden stick is pushing the diamond against the cylinder (Fig. C.2 (b)). Check the position of the diamond under a microscope and align the diamond with the cylinder as best as you can (with a top-light of the microscope, make sure that the circular shape of the optical window and the diamond culet are in the middle). Apply Stycast (Stycast 2850FT BK mixed with Catalyst 9 with the ratio of 100 : 3.5 by weight) between the diamond and cylinder to glue

them together (Fig. C.2 (c)). The Stycast is applied to cover up to half of the height of the diamond to ensure a rigid gluing of the diamond and to expose the culet as well as its surrounding area for later assembling process. In addition, always pay attention not to glue the cylinder and piston together. Make sure the alignment is still good right after applying Stycast and adjust position of the diamond if needed. Then the Stycast was left overnight to cure. After the diamond and cylinder are glued rigidly, remove the wooden stick, double-side tape and clean the piston. The second diamond is then placed on top of the piston. Cell is assembled again (with gentle force) with a small piece of double-side tape put between the two diamonds to avoid direct pushing of the diamonds against each other (Fig. C.2 (d)). Under a microscope (using back-light), align the two diamonds so that the culets of the two diamonds match with each other (Figs. C.2 (e) and (f)). Then apply Stycast to glue the diamond with the piston (Fig. C.2 (g)). Again Stycast is applied to cover up to half of the height of the diamond and be careful not to glue the cylinder and piston together.

Step 2: Make metal gasket A supporting metal gasket is made by indenting a rhenium metal sheet under pressure up to $\sim 15\,\mathrm{GPa}$ (about half of the maximum pressure of the mDAC) via the mDAC after which the middle part is cut off to provide sample space. First spread some ruby spheres (diameter $\sim 5\,\mu\mathrm{m}$ purchased from BETSA BET) on the culet of the bottom diamond anvil (ruby spheres are used for pressure calibration). Then a circular-shape rhenium sheet (diameter of ~6.6 mm, thickness of ~200 μm) (Fig. C.3 (a)) is first attached to the bottom diamond anvil (the diamond anvil on the piston) via small amount of clay. Spread some ruby spheres on top of the rhenium again. The cell is assembled (Fig. C.3 (b)) and force is applied through an external press (see Fig. C.4 (a)) by evenly tightening the four screw on the press and subsequently tightening the four screws on the mDAC to lock the force. Apply force in several steps to reach the desired pressure and measure the pressure values each time after force is increased. An in-house optical system (Fig. C.4 (b)) is used to measure the Ruby fluorescence to determine the pressure values (make multiple measurements to achieve an average pressure value) Piermarini et al. (1975). Once the pressure reaches $\sim$ 15

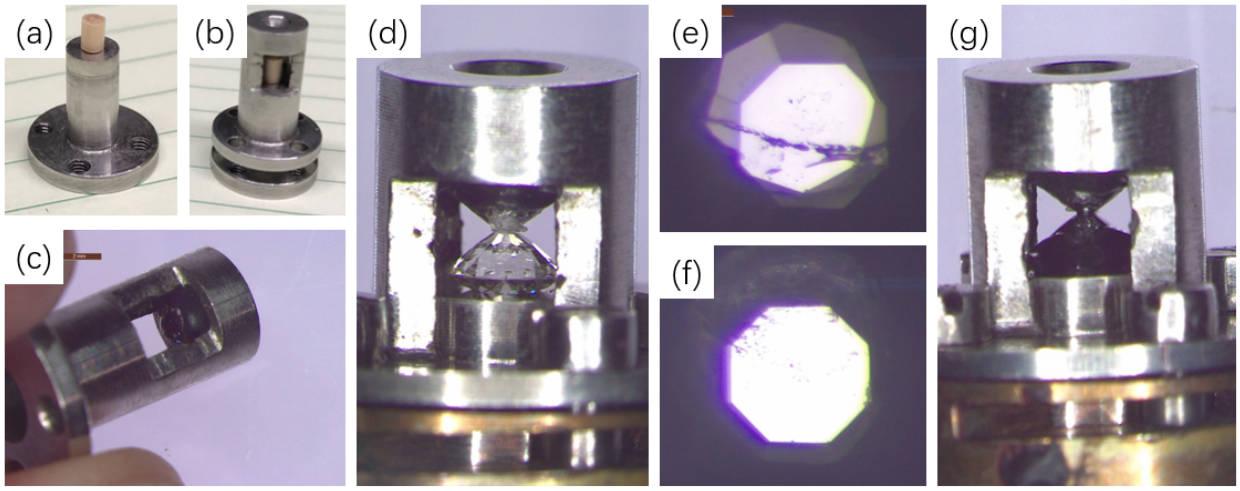

Figure C.2 Steps of gluing diamond anvils. (a) A small piece of wooden stick is glued to the piston via a piece of double-side tape. (b) Put cylinder and piston together with gentle force so that the diamiond anvil is pushed against the cylinder by the wooden stick. (c) One diamond anvil glued to the cylinder by Stycast. (d) The other diamond anvil sitting on top of the piston. Cylinder and piston are put together with gentle force so that two diamond anvils are pushed against each other but seperated by a piece of double side tape. (e) Image of the culets of the two diamonds under a microscope with a backlight. Image clearly domonstrates that the culets of the two diamonds are not aligned well. (f) Image of the culets aligned well. (g) Bottom diamond anvil glued to the piston via Stycast.

GPa, make marks on the metal gasket and cell body so that the relative position of the metal gasket to the cell is recorded. Then open the cell and take out the indented rhenium sheet. Take the indented metal gasket and cut a hole in the middle (Fig. C.3 (a)) using a laser-driller system (procedure done at Geophysical Laboratory). Note that the hole is as large as possible but must not exceed the area of the diamond culet ($\sim 300\,\mu$m in diameter). After cutting, the metal gasket is put back onto the top anvil (align the marks so that the position of the metal gasket relative to the cell body is the same as previously) for later BN gasket making.

In this step, multiple metal gaskets can be prepared for later usage.

Step 3: Make BN gasket A BN gasket is constructed within the Re-gasket to serve the mechanical as well as electrical insulating purposes. The laser-drilled hole of the metal gasket is first filled with a c-BN/epoxy mixture. The c-BN/epoxy mixture is prepared by mixing c-BN powder (grain size about 1μm, purchased from Advanced Abrasive BN) with epoxy (Epoxy Technology, part No. 353ND) at about the ratio of 10:1=c-BN:epoxy by weight Funamori and Sato (2008), which is then dried in air over night at room temperature. The mDAC is then assembled and the BN is compressed with a pressure of 20-25 GPa (see Fig. C.3 (d). Pressure values are determined by the Ruby fluorescence as described above). Subsequently, the gasket part is taken out and another hole of 100 μm is drilled from the BN (laser-drilling performed at Geophysical Laboratory) to form the sample space. In the end, the gasket is put back onto the bottom anvil and glued to the anvil by Stycast (Stycast 2850FT BK mixed with Catalyst 9 with the ratio of 100 : 3.5 by weight). The remaining metal part of the gasket is coved with Stycast to prevent electrical shorts.

At this stage, the gasket part of the mDAC is completed. Note that multiple gaskets can be constructed for later usage by repeating the last two steps.

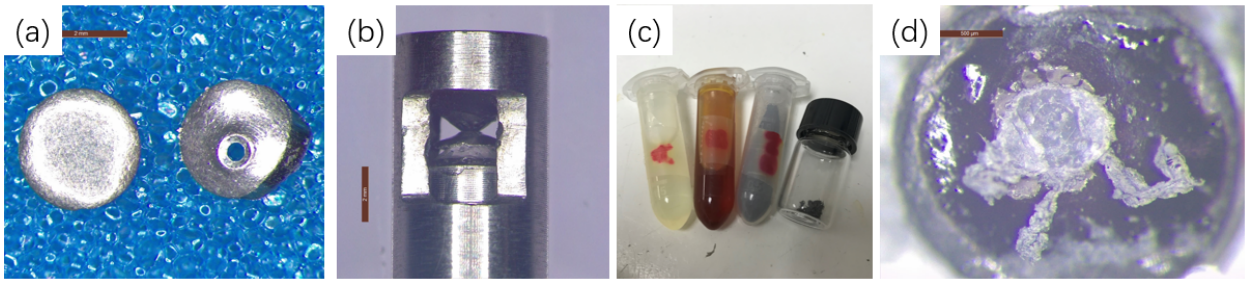

Figure C.3 (a) Left: Rhenium metal disk (diameter of ∼6.6 mm and thickness of ∼200 μm) that is used to make metal gasket. Right: metal disk after compressing with mDAC and hole cutting (diameter of the hole is ∼ 300 μm). (b) Metal disk compressed in between the diamond anvils to make metal gasket. (c) Individual components including epoxy (Part A and B are mixed with the ratio of 10:1 by weight), c-BN powder (grain size about 1μm, purchased from Advanced Abrasive BN) and the c-BN/epoxy mixture (in the glass vial) that are used to make c-BN/epoxy mixture. (d) BN gasket after compressing with mDAC.

Step 4: Fill pressure medium In the mDAC used for thesis work, solid pressure transmitting medium (KCl) was used. The solid KCl (Purchased from Alfa Aesar KCl, purity better than 99%) is in single crystalline form (cubic shape). To choose the proper sized KCl single crystal, the sample volume is calculated. With the diameter of 100 μm and thickness of $\sim$ 30 μm. The volume $V = \pi \times (100\,\mu m/2)^2 \times 30\,\mu m \simeq 235500\,\mu m^3$. Thus, a cubic KCl crystal with length of $(235500\,\mu m^3)^{1/3} \simeq 62\,\mu m$ is required. Measure the length of the cubic KCl under the microscope and choose a proper sized one, then put the KCl in the sample area within the gasket. Assemble the pressure cell and apply a small force to break the cubic KCl into smaller powder.

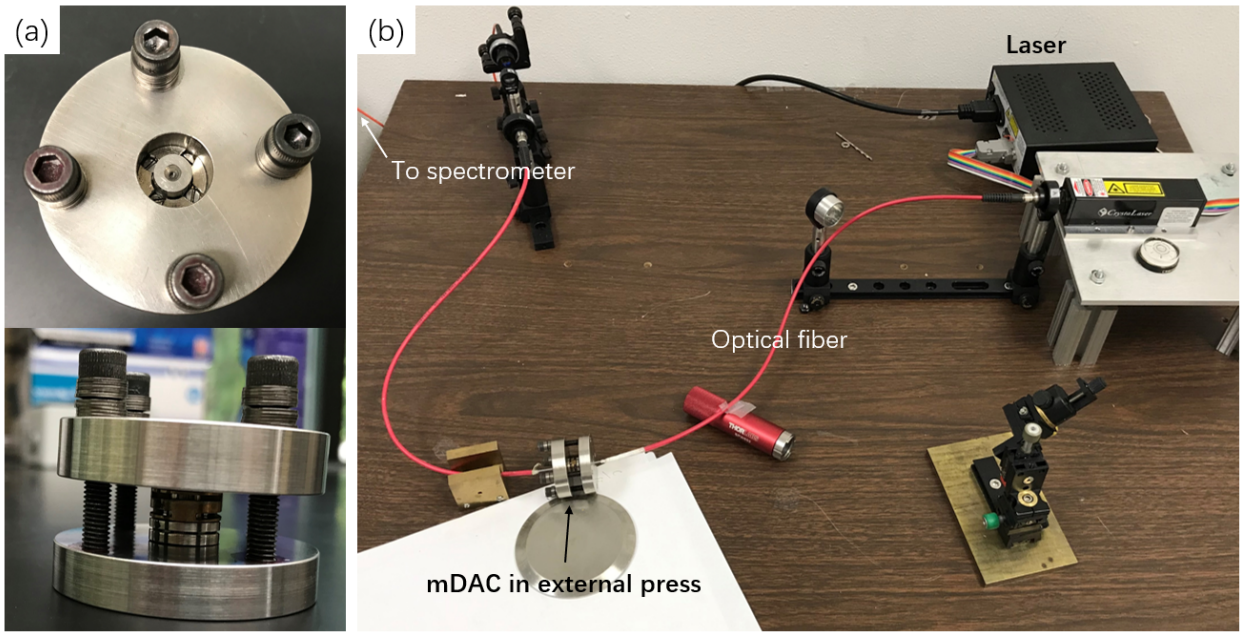

Figure C.4 (a) External press that is used to increase pressure on mDAC. (b) Optical system that is used to determine the pressure in mDAC via Ruby fluorescence Piermarini et al. (1975).

Step 5: Mount sample and make electrical contacts Sample is first polished and cut into a size that is small enough to fit into the sample space. A typical dimension is $70\times70\times15\,\mu m^3$. To reached the desired thickness, sample is polished using the polishing puck as

described in Appx. B.1.1 with the final polishing via a 0.3 μm Alumina sandpaper. For brittle materials, it is impossible to cut the sample into the desired dimension, instead, the polished sample is simply broken into tiny pieces among which a proper sized piece is chosen to be used for measurements. The chosen specimen is then carefully placed in the middle of the sample area, cell is assemble and a gentle force is applied to compress the specimen into the pressure medium. Ruby spheres are spread surrounding the sample area for later pressure determination. The electrical contact is done by a mechanical contact of Pt sheet with the specimen surface. Due to the small dimension of the sample, the electrical transport measurements are done through the van der Pauw method van der Pauw (1958); Ramadana et al. (1994). As shown in Fig. C.5 (a), four pieces of Pt sheets (with typical dimension of $120\times30\times4\,\mu m^3$) are cut, with one end of the Pt sheet cut into a triangle shape so to have a pointy tip. The four pieces of the Pt sheets are then carefully positioned in the sample area so that the tips of the Pt sheet overlap with four places on the sample surface. Cell is assembled again with gentle force to compress the Pt sheets into the pressure medium/BN gasket so that the positions of the four Pt sheets are fixed. To extend the electrical contacts outside of the sample area, Cu wire where one end is soldered to a thin Pt strip is used (Fig. C.5 (b)). The Cu wire is attached to the surrounding area of the metal gasket. The position is adjusted so that the Pt strip goes into the sample area and the end of the Pt strip overlaps with the Pt sheet that contacts with the specimen surface. By doing this, an electrical contact is formed between the two Pt sheets as they mechanically touch each other when cell is closed. Then the far end of the Cu wire can be used to connect with external measurement systems.

Step 6: Close cell and determine pressure To close the cell, carefully put the cylinder and piston together and then hand-tighten the four screws evenly. Check the electrical contacts through the four Cu wires to make sure of good electrical contacts. To measure the pressure inside the pressure cell, place the mDAC in the optical system (Fig. C.5 (b)). Laser light is transmitted through the diamonds, sample space, picked up by a spectrometer and the Ruby fluorescence is analyzed determine the pressure values via the pressure-dependent

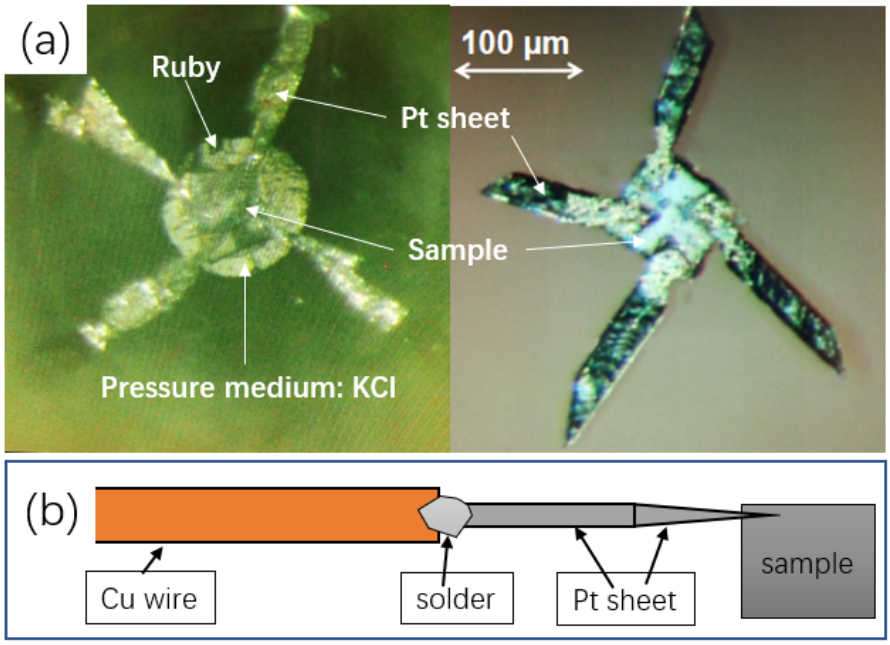

Figure C.5 (a) The $YbFe_2Zn_{20}$ samples prepared for the pressure experiment. The sample size is about $70\times70\times15\,mum^3$ and the van der Pauw contact geometry was used to measure the resistance van der Pauw (1958); Ramadana et al. (1994). Leads are cut from $4\,\mu$m Pt foil (Pt foil is obtained by rolling over the 25μm diameter Pt wire with a glass vial). (b) Schematic diagram showing how contacts are made to the specimen inside the sample area.

fluorescence lines. With an initial hand-tight, pressure of several GPa can be reached. To reach for higher pressures, the external press is used to compress the cylinder against the piston, where the position of them are locked by hand-tightening the screws subsequently. Once the desired pressure is achieved, the mDAC can then be removed from the optical system and used for desired measurements.

APPENDIX D. SUMMARY OF OTHER PROJECTS AND PUBLICATION LIST

During my PhD, I also led or was involved in the following projects which I will summarize briefly in the following.

D.1 Pressure induced change in the electronic state of $Ta_4Pd_3Te_{16}$

In this work, we present measurements of superconducting transition temperature, resistivity, magnetoresistivity and temperature dependence of the upper critical field of $Ta_4Pd_3Te_{16}$ under pressures up to 16.4 kbar. All measured properties have an anomaly at $\sim$ 2 - 4 kbar pressure range, in particular there is a maximum in T_C and upper critical field, $H_{c2}(0)$, and minimum in low temperature, normal state resistivity. Qualitatively, the data can be explained considering the density of state at the Fermi level as a dominant parameter.
In this project, I conducted the electrical transport measurement under pressure and was partly involved in the data analysis. This work is published in Ref. Jo et al. (2017).

D.2 Magnetic properties of single crystalline itinerant ferromagnet $AlFe_2B_2$

In this work, single crystals of $AlFe_2B_2$ have been grown using the self flux growth method and then the structural properties, temperature and field dependent magnetization, and temperature dependent electrical resistivity were measured at ambient as well as high pressure. The Curie temperature of $AlFe_2B_2$ is determined to be 274 K. The measured saturation magnetization and the effective moment for paramagnetic Fe-ion indicate the itinerant nature of the magnetism with a Rhode-Wohlfarth ratio $\frac{M_c}{M_{sat}} \approx 1.14$. Temperature dependent resistivity measurements under hydrostatic pressure shows that transition temperature T_C is suppressed down to 255 K for $p = 2.24$ GPa pressure with a suppression rate of $\sim$ 8.9 K/GPa.

The anisotropy fields and magnetocrystalline anisotropy constants are in reasonable agreement with density functional theory calculations.

In this project, I conducted the electrical transport measurement under pressure to investigate the pressure tunability of the ferromagnetic state. This work is published in Ref. Lamichhane et al. (2018).

D.3 Collapse of Kondo state and ferromagnetic quantum phase transition in $YbFe_2Zn_{20}$

In this work, we present the electrical resistivity data under application of pressures up to ~ 26 GPa and down to 50 mK temperatures on $YbFe_2Zn_{20}$. We find a pressure induced magnetic phase transition with an onset at $p_c = 18.2 \pm 0.8$ GPa. At ambient pressure, $YbFe_2Zn_{20}$ manifests a heavy fermion, nonmagnetic ground state and the Fermi liquid behavior at low temperatures. As pressure is increased, the power law exponent in resistivity, n, deviates significantly from Fermi liquid behavior and tends to saturate with n = 1 near p_c. A pronounced resistivity maximum, $T_{\max}$, which scales with Kondo temperature is observed. $T_{\max}$ decreases with increasing pressure and flattened out near p_c indicating the suppression of Kondo exchange interaction. For $p > p_c$, $T_{\max}$ shows a sudden upward shift, most likely becoming associated with crystal electric field scattering. Application of magnetic field for $p > p_c$ broadens the transition and shifts it toward the higher temperature, which is a typical behavior of the ferromagnetic transition. The magnetic transition appears to abruptly develop above p_c, suggesting probable first-order (with changing pressure) nature of the transition; once stabilized, the ordering temperature does not depend on pressure up to ~ 26 GPa. Taken as a whole, these data suggest that $YbFe_2Zn_{20}$ has a quantum phase transition at $p_c = 18.2$ GPa associated with the avoided quantum criticality in metallic ferromagnets.

In this project, I was heavily involved in the electrical transport measurement under pressure using the mDAC and in the data analysis. This work is published in Ref. Kaluarachchi et al. (2018).

D.4 Effect of pressure on the physical properties of the superconductor $NiBi_3$

In this work, we present an experimental study of the superconducting properties of $NiBi_3$ as a function of pressure by means of resistivity and magnetization measurements and combine our results with density functional theory calculations of the band structure under pressure. We find a moderate suppression of the critical temperature T_c from ≈4.1 K to ≈3 K by pressures up to 2 GPa. By taking into account the change of the band structure as a function of pressure, we argue that the decrease in T_c is consistent with conventional, phonon-mediated BCS type superconductivity.

In this project, I helped to perform high pressure tranport measurements and partly involved in the data analysis. This work is published in Ref. Gati et al. (2018).

D.5 Pressure-induced multiple phase transformations of the $BaBi_3$ superconductor

In this work, measurements of temperature-dependent resistance and magnetization under hydrostatic pressures up to 2.13 GPa are reported for single-crystalline, superconducting BaBi3. A temperature-pressure phase diagram is determined and the results suggest three different superconducting phases α, β, and γ in the studied pressure range. We further show that the occurrence of the three superconducting phases is intuitively linked to phase transitions at higher temperature, which are likely first order and structural in nature. With the α phase being the ambient-pressure tetragonal structure (P4/mmm), our first-principles calculations suggest the phase has a cubic structure (Pm-3m) and the γ phase has a distorted tetragonal structure where the Bi atoms are moved out of the face-centered position. Finally, an analysis of the evolution of the superconducting upper critical field with pressure further confirms these transitions in the superconducting state and suggests a possible change of band structure or a Lifshitz transition near 1.54 GPa in γ phase. Given the large atomic numbers of

both Ba and Bi, our results establish $BaBi_3$ as a good candidate for the study of the interplay of structure with superconductivity in the presence of strong spin-orbit coupling.
In this project which I led, I grew single crystals of $BaBi_3$ via high temperature solution method, conducted XRD measurement, performed electrical transport measurement under pressure and data analysis. Note that $BaBi_3$ is air sensitive, thus XRD measurements and electrical contacts were performed in the glovebox with ambient pressure N_2 gas condition. This work is published in Ref. Xiang et al. (2018b).

D.6 Use of Cernox thermometers in AC specific heat measurements under pressure

In this work, we report on the resistance behavior of bare-chip Cernox thermometers under pressures up to 2 GPa, generated in a piston-cylinder pressure cell. Our results clearly show that Cernox thermometers, frequently used in low-temperature experiments due to their high sensitivity, remain highly sensitive even under applied pressure. We show that these thermometers are therefore ideally suited for measurements of heat capacity under pressure utilizing an ac oscillation technique up to at least 150 K. Our Cernox-based system is very accurate in determining changes of the specific heat as a function of pressure as demonstrated by measurements of the heat capacity on three different test cases: (i) the superconducting transition in elemental Pb ($T_c = 7.2$ K), (ii) the antiferromagnetic transition in the rare-earth compound $GdNiGe_3$ ($T_N = 26$ K) and (iii) the structural/magnetic transition in the iron-pnictide $BaFe_2As_2$ ($T_{s,N} = 130$ K). The chosen examples demonstrate the versatility of our technique for measuring the specific heat under pressure of various condensed matter systems with very different transition temperatures as well as amounts of removed entropy.
In this project, I was involved in setting up the AC specific heat measurement assembly based on the piston cylinder cell. This work is published in Ref. Gati et al. (2019a).

D.7 Role of the Fermi surface for the pressure-tuned nematic transition in the $BaFe_2As_2$ family

The tetragonal-to-orthorhombic phase transition at T_s, which precedes the antiferromagnetic phase transition at T_N in many iron-based superconductors, is considered one of the manifestations of electronic *nematic* order. By constructing temperature-pressure phase diagrams of pure and Co-doped $BaFe_2As_2$, we study the relation of T_s and T_N under pressure p. Our data reveal two qualitatively different regimes in which $\Delta T = T_s - T_N$ either increases or decreases with p. We provide experimental evidence that the transition between the two regimes may be associated with sudden changes of the Fermi surface topology. Therefore, our results not only support the electronic origin of the structural order, but also emphasize the importance of details of the Fermi surface for the evolution of nematic order under pressure. In this work, I carried out the Hall coefficient measurement of Co-doped $BaFe_2As_2$ under pressure and the data analysis. This work is published in Ref. Gati et al. (2019b).

D.8 Measurements of elastoresistance under pressure by combining in-situ tunable quasi-uniaxial stress with hydrostatic pressure

Uniaxial stress, as well as hydrostatic pressure are often used to tune material properties in condensed matter physics. In this work, we presented a setup which allows for the study of the combined effects of quasi-uniaxial stress and hydrostatic pressure. Following earlier designs for measurements under finite stress at ambient pressure (e.g., Chu *et al.*, Science 337, 710 (2012)), the present setup utilizes a piezoelectric actuator to change stress in situ inside the piston-cylinder pressure cell. We show that the actuator can be operated over the full temperature (from 30 K up to 260 K) and pressure range (up to $\approx$ 2 GPa), resulting in a clear and measurable quasi-uniaxial strain. To demonstrate functionality, measurements of the elastoresistance (i.e., the change of resistance of a sample as a response to quasi-uniaxial strain) under finite hydrostatic pressure on the iron-based compound $BaFe_2As_2$ are presented as a proof-of-principle example, and discussed in the framework of electronic nematicity. Overall,

this work introduces the combination of *in situ* tunable quasi-uniaxial stress and large (up to ≈ 2 GPa) hydrostatic pressure as a powerful combination in the study of novel electronic phases. In addition, it also points towards further technical advancements which can be made in the future.

In this project, I was heavily involved in setting up the elestroresistance measurement assembly based on the piston cylinder cell, performing measurements as well as data analysis. The first two authors: Elena Gati and Li Xiang equally contributed to this work. This work is published in Ref. Gati et al. (2020b).

D.9 Impact of Nematicity on the Relationship between Antiferromagnetic Fluctuations and Superconductivity in $FeSe_{0.91}S_{0.09}$ Under Pressure

The sulfur substituted FeSe system, $FeSe_{1-x}S_x$, provides a versatile platform for studying the relationship between nematicity, antiferromagnetism, and superconductivity. In this work, by nuclear magnetic resonance (NMR) and resistivity measurements up to 4.73 GPa on $FeSe_{0.91}S_{0.09}$, we established the pressure(p)-temperature(T) phase diagram in which the nematic state is suppressed with pressure showing a nematic quantum phase transition (QPT) around $p = 0.5$ GPa, two SC regions, separated by the QPT, appear and antiferromagnetic (AFM) phase emerges above ∼3.3 GPa. From the NMR results up to 2.1 GPa, AFM fluctuations are revealed to be characterized by the stripe-type wavevector which remains the same for the two SC regions. Furthermore, the electronic state is found to change in character from non-Fermi liquid to Fermi liquid around the nematic QPT and persists up to ∼ 2.1 GPa. In addition, although the AFM fluctuations correlate with T_c in both SC states, demonstrating the importance of the AFM fluctuations for the appearance of SC in the system, we found that, when nematic order is absent, T_c is strongly correlated with the AFM fluctuations, whereas T_c weakly depends on the AFM fluctuations when nematic order is present. Our findings on $FeSe_{0.91}S_{0.09}$ were shown to be applied to the whole $FeSe_{1-x}S_x$ system and also provide a new insight into the relationship between AFM fluctuations and SC in Fe-based superconductors.

In this project, I carried out electrical transport measurements of $FeSe_{0.91}S_{0.09}$ under pressure up to 4.73 GPa via the mBAC as well as the data analysis. This work is published in Ref. Rana et al. (2020).

D.10 Pressure tuning of structural and magnetic transitions in $EuAg_4As_2$

In this work, we report temperature dependent measurements of ambient pressure specific heat, magnetic susceptibility, anisotropic resistivity and thermal expansion as well as in-plane resistivity under pressure up to 20.8 kbar on single crystals of $EuAg_4As_2$. Based on thermal expansion and in-plane electrical transport measurements at ambient pressure this compound has two, first order, structural transitions in 80 - 120 K temperature range. Ambient pressure specific heat, magnetization and thermal expansion measurements show a cascade of up to seven transitions between 8 and 16 K associated with the ordering of the Eu^{2+} moments. In-plane electrical transport is able to detect more prominent of these transitions: at 15.5, 9.9, and 8.7 K as well as a weak feature at 11.8 K at ambient pressure. Pressure dependent electrical transport data show that the magnetic transitions shift to higher temperatures under pressure, as does the upper structural transition, whereas the lower structural transition is suppressed and ultimately vanishes. A jump in resistivity, associated with the upper structural transition, decreases under pressure with an extrapolated disappearance (or a change of sign) by 30-35 kbar. In the 10 - 15 kbar range a kink in the pressure dependency of the upper structural transition temperature as well as the high and low temperature in-plane resistivities suggest that a change in the electronic structure may occur in this pressure range. The results are compared with the literature data for $EuAg_4As_2$.

In this project, I carried out the resistivity measurement under pressure up to 20.8 kbar using the piston cylinder cell and corresponding data analysis. This work is published in Ref. Bud'ko et al. (2020).

D.11 Exceedingly Small Moment Itinerant Ferromagnetism of Single Crystalline $La_5Co_2Ge_3$

In this work, single crystals of monoclinic $La_5Co_2Ge_3$ were grown using a self-flux method and were characterized by room-temperature powder X-ray diffraction, anisotropic temperature and field dependent magnetization, temperature dependent resistivity, specific heat, and muon spin rotation. $La_5Co_2Ge_3$ has a Curie temperature (T_C) of 3.8 K and clear signatures of ferromagnetism in magnetization and μSR data, as well as a clear loss of spin disorder scattering in resistivity data and a sharp specific heat anomaly. The magnetism associated with $La_5Co_2Ge_3$ is itinerant, has a change in the entropy at T_C of $\simeq$0.05 R ln2 per mol-Co, and has a low-field saturated moment of $\sim 0.1\mu_B$/Co, making it a rare, itinerant, small moment, low T_C compound.

In this project, I was partly involved with the synthesis of the $La_5Co_2Ge_3$ single crystals, electrical transport measurements as well as data analysis. This work is published in Ref. Saunders et al. (2020).

D.12 Tuning of charge density wave transitions in $LaAu_xSb_2$ by pressure and Au-stoichiometry

In this work, two charge density wave transition can be detected in $LaAu_xSb_2$ at $\sim$ 110 and $\sim$ 90 K by careful electrical transport measurements. Whereas control of the Au site occupancy in $LaAu_xSb_2$ (for $0.9 < x < 1.0$) can suppress each of these transitions by $\sim$ 80 K, the application of hydrostatic pressure can completely suppress the lower transition by $\sim$ 10 kbar and the upper transition by $\sim$ 17 kbar. Clear anomalies in the resistance as well as the magnetoresistance are observed to coincide with the pressures at which the charge density wave transitions are driven to zero.

In this project, I carried out the resistivity measurement under pressure up using the piston cylinder cell and partially data analysis. This work is Published in Ref. Xiang et al. (2020b).